

AD-A132 136

TARGETED BASIC STUDIES OF FERROELECTRIC AND
FERROELASTIC MATERIALS FOR PI. (U) PENNSYLVANIA STATE
UNIV UNIVERSITY PARK MATERIALS RESEARCH LA.

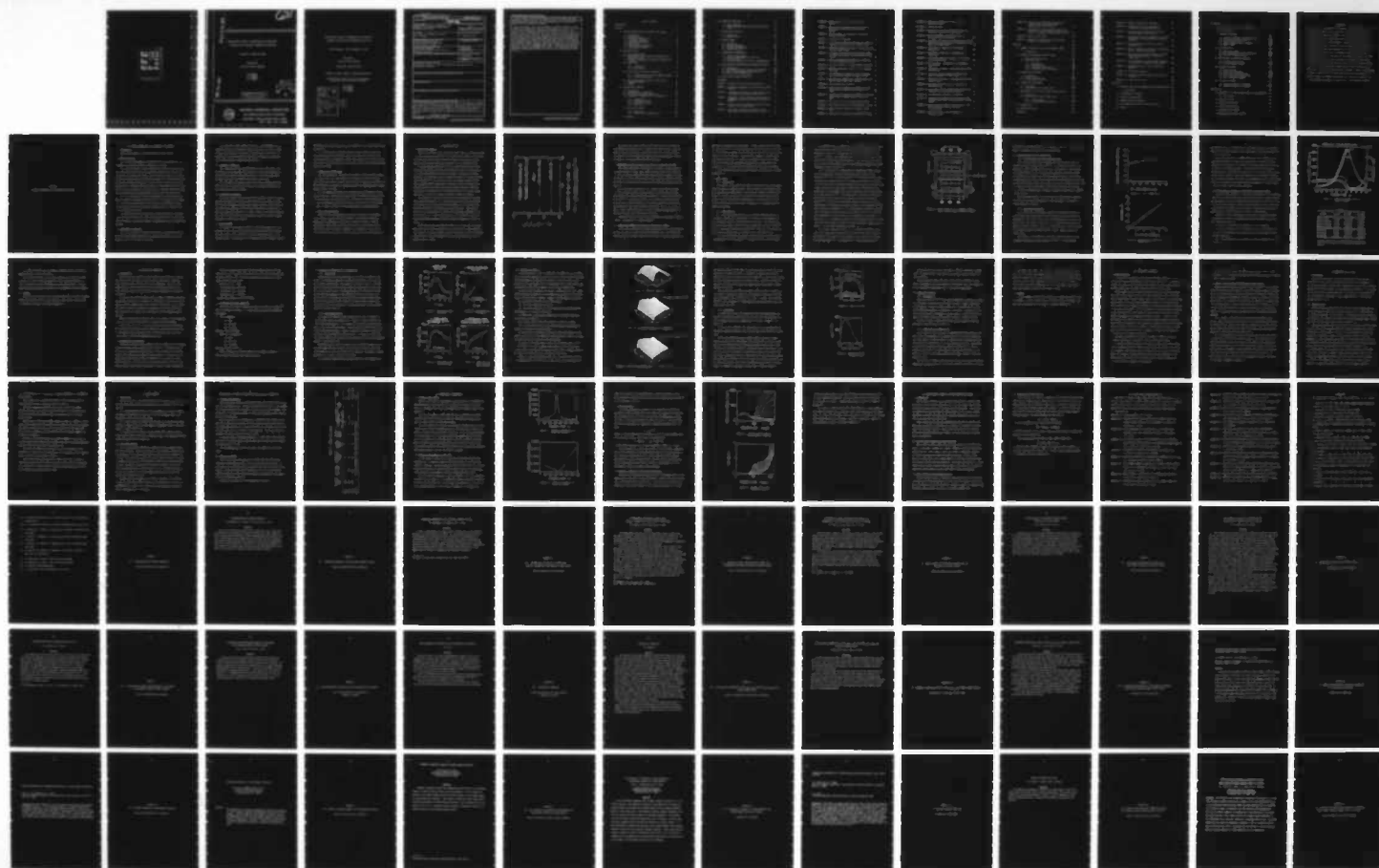
1/4

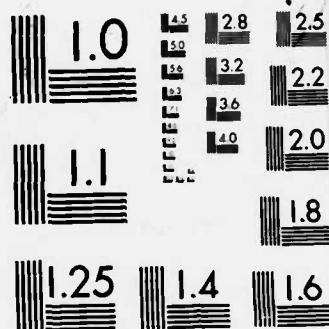
UNCLASSIFIED

L E CROSS ET AL. MAR 83 N00014-78-C-0291

F/G 9/1

NL





MICROCOPY RESOLUTION TEST CHART
NATIONAL BUREAU OF STANDARDS-1963-A

ADA 132136

72

TARGETED BASIC STUDIES OF FERROELECTRIC AND FERROELASTIC
MATERIALS FOR PIEZOELECTRIC TRANSDUCER APPLICATIONS

Contract No. N00014-78-C-0291

Sponsored by

The Office of Naval Research

L.E. Cross
R.E. Newnham
G.R. Barsch
J.V. Biggers

DTIC FILE COPY

DTIC
ELECTE
SEP 7 1983
S D

DISTRIBUTION STATEMENT A

Approved for public release;
Distribution Unlimited



MATERIALS RESEARCH LABORATORY

THE PENNSYLVANIA STATE UNIVERSITY

UNIVERSITY PARK, PENNSYLVANIA 16802

83 09 06 053

TARGETED BASIC STUDIES OF FERROELECTRIC AND FERROELASTIC
MATERIALS FOR PIEZOELECTRIC TRANSDUCER APPLICATIONS

Period December 1, 1981 to December 31, 1982

Final Report

OFFICE OF NAVAL RESEARCH

Contract No. N00014-78-C-0291

APPROVED FOR PUBLIC RELEASE — DISTRIBUTION UNLIMITED

Reproduction in whole or in part is permitted for
any purpose of the United States Government

L.E. Cross
R.E. Newnham
G.R. Barsch
J.V. Biggers

Accession For	
NTIS GRA&I	<input checked="checked" type="checkbox"/>
DTIC TAB	<input type="checkbox"/>
Unannounced	<input type="checkbox"/>
Justification	
By	
Distribution/	
Availability Codes	
Dist	Avail and/or Special
A	



Unclassified

SECURITY CLASSIFICATION OF THIS PAGE (When Data Entered)

REPORT DOCUMENTATION PAGE		READ INSTRUCTIONS BEFORE COMPLETING FORM
1. REPORT NUMBER	2. GOVT ACCESSION NO. A132136	3. RECIPIENT'S CATALOG NUMBER
4. TITLE (and Subtitle) TARGETED BASIC STUDIES OF FERROELECTRIC AND FERROELASTIC MATERIALS FOR PIEZOELECTRIC TRANSDUCER APPLICATIONS		5. TYPE OF REPORT & PERIOD COVERED Final Dec. 1, 1982 - Dec. 31, 1983
7. AUTHOR(s) L.E. Cross, R.E. Newnham, G.R. Barsch and J.V. Biggers		6. PERFORMING ORG. REPORT NUMBER
9. PERFORMING ORGANIZATION NAME AND ADDRESS Materials Research Laboratory The Pennsylvania State University University Park, PA 16802		8. CONTRACT OR GRANT NUMBER(s) N00014-78-C-0291
11. CONTROLLING OFFICE NAME AND ADDRESS Office of Naval Research Room 619 Ballston Tower, 800 N. Quincy St. Arlington, VA 22217		10. PROGRAM ELEMENT, PROJECT, TASK AREA & WORK UNIT NUMBERS
14. MONITORING AGENCY NAME & ADDRESS (if different from Controlling Office)		12. REPORT DATE March 1983
		13. NUMBER OF PAGES
		15. SECURITY CLASS. (of this report) UNCLASSIFIED
		15a. DECLASSIFICATION/DOWNGRADING SCHEDULE
16. DISTRIBUTION STATEMENT (of this Report) Reproduction in whole or in part is permitted for any purpose of the United States Government		
17. DISTRIBUTION STATEMENT (of the abstract entered in Block 20, if different from Report)		
18. SUPPLEMENTARY NOTES		
19. KEY WORDS (Continue on reverse side if necessary and identify by block number)		
20. ABSTRACT (Continue on reverse side if necessary and identify by block number) The work reported covers the fifth and final year of the program of "Targeted Basic Studies of Ferroelectric and Ferroelastic Materials for Piezoelectric Transducer Applications." The report delineates the new progress made in the final year and discusses the major accomplishments of the full five year program both in the basic science and in the spin off to practical transducer applications. Possible new areas of study which are suggested by the present studies are briefly reported. (Continued on the back)		

Over the course of the five year program, more than 130 papers have been published in refereed journals, 27 invited and almost 100 contributed papers have been presented at national and international meetings and 10 invention disclosures are being processed for patents.

Major achievements include the development of a physical approach to understanding active composites, leading to the development of several new families of PZT:polymer piezoelectric composites for hydrophone application. New advances in the phenomenology and microscopic theory of electrostriction, and the evolution of a new family of high strain ferroelectric relaxor materials for practical application. New basic understanding of the polarization mechanisms in ferroelectric relaxors has been aided by the study of order-disorder of the cation arrangement in lead scandium tantalate, and the results correlate well with studies of relaxor behavior, and of shape memory effects in PLZT ceramics. Low temperature studies on pure and doped PZTs have given the first clear indication of the intrinsic (averaged) single domain response and correlate exceedingly well with earlier phenomenological theory. Crystal growth and ceramic processing studies have developed 'hand-in-hand' with program needs providing new forms of conventional materials, new grain oriented structures and single crystals.

TABLE OF CONTENTS

INTRODUCTION.	1
SECTION I	2
1.0 STUDIES ACCOMPLISHED IN THE CONTRACT YEAR 1982-83	3
1.1 Introduction	3
1.2 Electrostriction	3
1.3 Piezoelectric Composites	3
1.4 Pyroelectric Materials	4
1.5 Ferroelectric Bicrystals	4
1.6 Crystal Growth	4
1.7 Thermodynamic Phenomenology.	5
1.8 Grain Oriented Ceramics.	5
2.0 ELECTROSTRICTION.	6
2.1 Precise Measurements	6
2.2 Measurements of the Converse Electrostriction in Perovskite Halides	8
2.3 Temperature Dependence of Dielectric Permittivity in KMnF_3	8
2.4 Basic Theory	9
2.4.1 Introduction.	9
2.4.2 Major Results	9
2.5 Electrostriction in High K Dielectrics	12
2.5.1 Ultradilatometer for Wide Temperature Range .	12
2.5.2 Ferroelectric Relaxors.	12
2.6 Poling and Depoling Behavior in PLZT 8:65:35 Transparent Ceramic.	14
2.7 Summary.	16
3.0 PIEZOELECTRIC COMPOSITES.	17
3.1 Introduction	17
3.2 Piezoelectric 3-3 Composites	17
3.3 Perforated PZT-Polymer Composites.	18
3.4 Piezoelectric Composites of 1:3 Connectivity	19
3.4.1 Introduction.	19
3.4.2 Experimental Studies.	19
3.4.3 Theoretical Analysis.	21
3.4.4 Discussion.	23
3.5 Polar Glass Ceramics	25
3.5.1 Introduction.	25
3.5.2 Application of Piezoelectrics	25
3.6 Summary.	26

4.0	PYROELECTRIC MATERIALS.	27
4.1	Micro Composites	27
4.2	'Doped' Tungsten Bronze and TGS Structure Single Crystals	28
5.0	FERROELECTRIC BICRYSTALS.	29
5.1	Introduction	29
5.2	Summary of Work.	29
6.0	CRYSTAL GROWTH.	31
6.1	Introduction	31
6.2	Lead Barium Niobate.	31
6.3	Fresnoite and Analogues.	32
6.4	Perovskite Halides	32
7.0	THERMODYNAMIC PHENOMENOLOGY	34
7.1	Dielectric Measurements.	34
7.2	Dielectric Measurements on 'Soft' PZT.	34
7.3	PLZT Relaxations	36
7.4	Dielectric Properties of PZTs at Low Temperature . .	36
8.0	GRAIN ORIENTED CERAMICS AND OTHER PREPARATIVE STUDIES . .	39
8.1	Introduction	39
8.2	Grain Oriented Bismuth Oxide Layer Structures. . . .	39
8.3	Grain Oriented Tungsten Bronze Materials	39
8.4	Fabrication of $\text{PbMg}_{1/3}\text{Nb}_{2/3}\text{O}_3$	40
9.0	RECENT STUDIES NEARING COMPLETION	41
	REFERENCES	43
	APPENDIX 1 Electrostriction in Fluoride Perovskites	45
	APPENDIX 2 Temperature Dependence of the Dielectric Constant of KMnF_3	47
	APPENDIX 3 Thermodynamic Definition of Higher Order Elastic, Piezoelectric and Dielectric Coefficients.	49
	APPENDIX 4 Propagation of Small Amplitude Elastic Waves in a Homogeneously Stressed and Polarized Dielectric Medium	51
	APPENDIX 5 Lattice Theory of the Nonpolar Nonlinear Elastic Dielectric in the Shell Model.	53
	APPENDIX 6 Shell Model Calculation of Electrostriction Coefficients of Rocksalt-Type Alkali Halides	55

APPENDIX 7	Temperature Variation of Electrostriction of SrTiO_3	57
APPENDIX 8	Polarization and Depolarization Behavior of Hot Pressed Lead Lanthanum Zirconate Titanate Ceramics	59
APPENDIX 9	New Developments in Piezoelectric and Electrostrictive Materials.	61
APPENDIX 10	Piezoelectric Composites.	63
APPENDIX 11	The Dielectric Properties of $\text{Pb}(\text{Sc}_{1/2}\text{Ta}_{1/2})\text{O}_3$ and $\text{Pb}(\text{Sc}_{1/2}\text{Ta}_{1/4}\text{Nb}_{1/4})\text{O}_3$ Ceramics Under DC Bias. . .	65
APPENDIX 12	Reversible Pyroelectric Effect in $\text{Pb}(\text{Sc}_{1/2}\text{Ta}_{1/2})\text{O}_3$ Ceramics Under DC Bias.	67
APPENDIX 13	The Growth and Properties of a New Alanine and Phosphate Substituted Triglycine Sulphate (ATGSP) Crystal	69
APPENDIX 14	Domain Configuration and Piezoelectric Behavior of Lithium Niobate Bicrystals	71
APPENDIX 15	Dielectric Behavior of Lithium Niobate Bicrystals	73
APPENDIX 16	Thermally Stimulated Current in Lithium Niobate Bicrystals.	75
APPENDIX 17	The Influence of Piezoelectric Grain Resonance on the Dielectric Spectra of LiNbO_3 Ceramics. . .	77
APPENDIX 18	Ferroelectric Properties of Tungsten Bronze Lead Barium Niobate (PBN) Single Crystals.	79
APPENDIX 19	Low Field Poling of Soft PZTs	81
APPENDIX 20	Dielectric and Piezoelectric Properties of Pure Lead Titanate Zirconate Ceramics from 4.2 to 300°K	83
APPENDIX 21	Dielectric and Piezoelectric Properties of Modified Lead Titanate Zirconate Ceramics from 4.2 to 300°K	85
APPENDIX 22	Fabrication of Grain-Oriented Bi_2WO_6 Ceramics . .	87
APPENDIX 23	Fabrication of Grain Oriented $\text{PbBi}_2\text{Nb}_2\text{O}_6$ Ceramics	89
APPENDIX 24	Grain Oriented Piezoelectric Ceramics at Penn State	91
APPENDIX 25	Fabrication of Perovskite Lead Magnesium Niobate.	93

APPENDIX 26	Dielectric Properties of Pyrochlore Lead Magnesium Niobate	95
APPENDIX 27	Electrostriction.	97
APPENDIX 28	Electrostriction and Its Relationship to Other Properties in Perovskite-Type Crystals.	99
APPENDIX 29	Direct Measurement of Electrostriction in Perovskite Type Ferroelectrics.	101
APPENDIX 30	The Effects of Various B-Site Modifications on the Dielectric and Electrostrictive Properties of Lead Magnesium Niobate Ceramics.	103
APPENDIX 31	Perforated PZT Composites for Hydrophone Applications.	105
APPENDIX 32	Transversely Reinforced 1-3 Piezoelectric Composites.	107
APPENDIX 33	PZT-Polymer Composite Transducers for Ultrasonic Medical Applications.	109
APPENDIX 34	Glass-Ceramics: New Materials for Hydrophone Applications.	111
APPENDIX 35	Pyroelectric Property of $\text{Pb}(\text{Sc}_{1/2}\text{Ta}_{1/2})\text{O}_3$ Ceramics Under DC Bias	113
APPENDIX 36	Electrical Poling and Depoling Studies on the Relaxor-Ferroelectric 8:65:35 PLZT.	115
APPENDIX 37	Pyroelectric Properties of the Modified Triglycine Sulphate (TGS).	117
APPENDIX 38	Pyroelectric and Piezoelectric Properties of SbSI:Composites	119
APPENDIX 39	A New Family of Grain Oriented Glass-Ceramics for Piezoelectric and Pyroelectric Devices.	121
APPENDIX 40	Low Temperature Pyroelectric Properties	123
APPENDIX 41	The Growth and Properties of a New Alanine and Phosphate Substituted Triglycine Sulphate (ATGSP) Crystal	125
APPENDIX 42	Some Interesting Properties of Dislocation Free Single Crystals of Pure and Modified $\text{Sr}_{0.5}\text{Ba}_{0.5}\text{Nb}_2\text{O}_6$	127
APPENDIX 43	The Ferroic Phase Transition Behavior of $\text{Pb}(\text{Zr}_{0.6}\text{Ti}_{0.4})\text{O}_3$	129

APPENDIX 44	Dielectric and Piezoelectric Properties of Tungsten Bronze Lead Barium Niobate ($\text{Pb}_x\text{Ba}_{1-x}\text{Nb}_2\text{O}_6$) Single Crystals	131
APPENDIX 45	Relationship of Crystallographic Polarity to Piezoelectric, Pyroelectric and Chemical Etching Effects in Li_2GeO_3 and LiGaO_2 Single Crystals . .	133
APPENDIX 46	Specific Heat of SbSI	135
APPENDIX 47	Magnetic-Field Dependence of the Soft-Mode Frequency in KTaO_3 at 20K	137
SECTION II.	139
1.0	SUMMARY OF WORK OVER THE FIVE YEAR CONTRACT PERIOD. . . .	140
1.1	Introduction	141
2.0	IMPORTANT CONTRIBUTIONS IN BASIC SCIENCE.	142
2.1	Composite Piezoelectrics	142
2.2	Electrostriction	143
2.2.1	Introduction.	143
2.2.2	Theoretical Work.	143
2.2.3	Experimental Observation.	144
2.2.4	Electrostriction in Perovskites	144
3.0	FERROELECTRIC BICRYSTALS.	146
3.1	Introduction	146
3.2	Bicrystal Studies.	146
3.3	Lithium Niobate Ceramics	146
4.0	FERROELASTIC SHAPE MEMORY	148
4.1	Introduction	148
4.2	Shape Memory in PLZT Compositions.	148
5.0	DEVELOPMENT OF A FULL ELASTIC GIBBS FUNCTION FOR PZT. . .	149
5.1	Introduction	149
5.2	New Data for PZT Family Compositions	150
5.2.1	Thermal Changes	150
5.2.2	Low Temperature Measurements.	150
6.0	PYROELECTRICS	153
7.0	PREPARATIVE STUDIES	154
REFERENCES	155

APPENDIX 2.1	Composite Piezoelectric Transducers.	157
APPENDIX 2.2	Perforated PZT-Polymer Composites for Piezoelectric Transducer Applications.	172
APPENDIX 2.3	Landau-Devonshire Theory with Rotationally Invariant Expansion Coefficients	182
APPENDIX 2.4	A High-Sensitivity AC Dilatometer for the Direct Measurement of Piezoelectricity and Electro- striction.	187
APPENDIX 2.5	Large Electrostrictive Effects in Relaxor Ferroelectrics	195
APPENDIX 2.6	Review: Electrostrictive Effect in Perovskites and Its Transducer Applications.	201
APPENDIX 2.7	The Role of B-Site Cation Disorder in Diffuse Phase Transition Behavior of Perovskite Ferroelectrics	212
APPENDIX 2.8	The Influence of Piezoelectric Grain Resonance on the Dielectric Spectra of LiNbO_3 Ceramic. . .	218
APPENDIX 2.9	Shape-Memory Effect in PLZT Ferroelectric Ceramics	239
APPENDIX 2.10	Polar Glass Ceramics.	258
APPENDIX 2.11	$\text{BaTiGe}_2\text{O}_8$ and $\text{Ba}_2\text{TiSi}_2\text{O}_8$ Pyroelectric Glass- Ceramic	263
APPENDIX 2.12	Densification in PZT.	270
SECTION III	275
1.0	PRACTICAL INDUSTRIAL DEVELOPMENTS BASED ON CONTRACT WORK.	276
1.1	Introduction	276
2.0	ELECTROSTRICTIVE CERAMICS	277
3.0	COMPOSITE PIEZOELECTRICS.	278
4.0	PIEZOELECTRIC GLASS CERAMICS.	280
5.0	NEW FERROELECTRIC CRYSTALS FOR ELECTRO-OPTICS	281
6.0	PATENTS	282

SECTION IV-A.	284
1.0 TOPICS AND OPPORTUNITIES FOR FUTURE STUDY	285
1.1 Introduction	285
2.0 COMPOSITES STRUCTURES	286
2.1 Creative Techniques for Scale Reduction.	286
2.2 Alternative Polymer Components	286
2.3 Active Matching Layers	286
2.4 Ferroic Composite Sound Absorbers.	287
2.5 Model Studies.	287
3.0 ELECTROSTRICTION.	288
3.1 Microscopic Theory	288
3.2 Basic Experiments in Electrostriction.	288
3.3 Practical Electrostrictors	288
4.0 CONVENTIONAL PIEZOELECTRIC CERAMICS	290
4.1 Theoretical Description.	290
4.2 New Experimental Studies	290
5.0 PREPARATIVE STUDIES	292
5.1 Organic Methods.	292
5.2 Fast Firing Techniques	292
5.3 New PbTiO_3 Based Compositions.	292
5.4 Low Firing Relaxor Combinations.	292
5.5 Grain Orientation Methods.	293
6.0 FLEXIBLE ELECTRODES	294
6.1 Contact to Composite Structures.	294
6.2 Electrode:Dielectric Interface	294
SECTION IV-B.	295
1.0 RELEVANCE OF THE WORK TO OTHER AREAS OF ELECTROCERAMICS .	296
1.1 Introduction	296
2.0 ELECTROSTRICTION.	297
3.0 COMPOSITE STRUCTURES.	299
4.0 RELAXOR FERROELECTRICS.	300
5.0 PHENOMENOLOGICAL THEORY	301
6.0 PREPARATION AND CRYSTAL GROWTH.	302

INTRODUCTION

This report on the program of "Targeted Basic Studies of Ferroelectric and Ferroelastic Materials for Piezoelectric Transducer Applications" covers the 5th and final year of the program. The format of the report differs significantly from that established in earlier years of the contract and the presentation is made in 4 major sections. Section I covers work in the final year (1982). Highlights of the results are discussed, but to conserve space, only abstracts of papers published over the year are presented. Section II which comprises the major part of the report summarizes the most important achievements over the full five years of the program. Key papers which represent critical steps in the forward progress are presented in the appendix. Section III discusses the more practical spin offs from the contract studies, indicating the areas where ideas evolved under the basic contract are now being taken up for practical exploitation in industry. Section IV underscores a number of opportunities for future study which have been outlined by the current program, and attempts to delineate the relevance of a number of the contract studies to progress in related areas of electroceramics research.

SECTION I

STUDIES ACCOMPLISHED IN THE CONTRACT YEAR 1982-83

1.0 STUDIES ACCOMPLISHED IN THE CONTRACT YEAR 1982-83

1.1 Introduction

Major accomplishments in the work over the last year include:

1.2 Electrostriction

(a) In precise measurements of electrostriction, we have the first clear evidence of a frequency dependence in measured Q_{11} values.

(b) From the theoretical studies, general relations have been derived for converting coefficients derived in conventional formulation to those of the rotationally invariant Toupin theory. In the microscopic theory, it has been shown that anharmonic many-body perturbation theory in the quasi-harmonic perturbation theory of Bruce and Cowley^(1.1), with a realistic model for the interatomic forces, is adequate for the calculation of room temperature value of the electrostrictive Q constants in perovskites but is completely unable to account for the experimentally observed temperature variation of electrostriction.

(c) A new simpler capacitance ultradilatometer has been constructed to measure temperature dependence of electrostriction in high permittivity solids, so as to provide additional data for verification of the theoretical models. This new system has been used to explore electrostriction in a number of new relaxor ferroelectric solids.

(d) Detailed examination of the poling and depoling behavior in 8:65:35 PLZTs with relaxor character has given convincing evidence for the super paraelectric behavior of polar micro regions at temperatures close to the dielectric maximum.

1.3 Piezoelectric Composites

(a) For 3:1 polymer:PZT composites, the effects of transverse reinforcement upon the hydrophone performance has been explored in detail, and a more complete theory for the behavior developed.

(b) Polar glass ceramic composites have now been investigated in more detail and shown to have hydrophone figures of merit close to those of PVDF. The very high stiffness of these materials (greater than single phase PZT) suggest that they may have important application in bimorph configurations, and in coupling electric fields into glass fibers.

1.4 Pyroelectric Materials

(a) Examination of lead scandiumtantalate crystals and ceramics with disordered B site cations shows clear evidence of an extrinsic component in the pyroelectric response which may be traced to a quasi-reversible order-disorder in the polar micro regions under weak DC bias fields.

(b) New studies of modified tungsten bronze $\text{Ba}_{0.5}\text{Sr}_{0.5}\text{Nb}_2\text{O}_6$ show that small additions of rare earth ions can have a very marked effect enhancing the reversible pyroelectric effect.

1.5 Ferroelectric Bicrystals

Work on the LiNbO_3 bicrystals has now been completed. Etching, dielectric, transport and thermally stimulated current studies have been used to examine the nature of the defect structure at the bonding interface. Modifications to the piezoelectric response in head-to-head bonded crystals has been used to model the piezoelectric dispersion in ceramic LiNbO_3 , and by computer modelling give the first clear proof of the piezoelectric nature of the high frequency dispersion in ferroelectric ceramics.

1.6 Crystal Growth

(a) Tungsten bronze structure crystals in the $\text{Ba}_x\text{Pb}_{1-x}\text{Nb}_2\text{O}_6$ family with compositions very close to the tetragonal orthorhombic morphotropic boundary have been grown, and are being used to verify a thermodynamic model of the structure family. Crystals just on the tetragonal side of the boundary exhibit

exceedingly high values of d_{15} and r_{41} the piezoelectric and linear electro-optic coefficients.

(b) Single crystals of barium titanium silicate (Fresnoite) and barium titanium germanate have been grown. A new first order phase change near 0°C is being explored in the germanate crystal. Both germanate and silicate exhibit most unusual pyroelectric behavior in both single crystal and oriented polycrystal glass ceramic forms.

1.7 Thermodynamic Phenomenology

(a) New measurements of the weak field response in the paraelectric phase for a soft PZT 501 give clear evidence of diffuse phase transition behavior. This is consistent with the very low heat of transition reported for compositions near morphotropic and requires a new modification of our phenomenological thermodynamic analysis for PZTs.

(b) Low temperature studies have confirmed that the differences in piezoelectric activity, coupling constant and permittivity between differently doped PZTs are extrinsic and freeze out at 4°K . Extending our original phenomenology to very low temperature confirms the need for a higher value of Curie constant C , which is again consistent with the observed diffuse transition behavior.

1.8 Grain Oriented Ceramics

Recent work has concentrated upon preparative techniques for developing micro crystals with very high shape anisotropy in the families $\text{PbBi}_2\text{Nb}_2\text{O}_9$, PbNb_2O_6 and $\text{Pb}_{1-x}\text{Ba}_x\text{Nb}_2\text{O}_6$ by the molten salt synthesis technique. Powders developed for these systems are being oriented for sintering by tape casting, and are being used as the active component in 0:3 composites to improve the filling factor over that which is possible with near spherical grain materials.

2.0 ELECTROSTRICTION

2.1 Precise Measurements

Work has continued with the high precision capacitance dilatometer designed originally by Uchino and Cross^(2.1,2.2) to ascertain the reason for the unrealistically high values of electrostriction constants determined for several alkali halides, and for the lack of reproducibility in the measured data.

A proper kinematic mounting^(2.3) for the spring loaded mounting of the halide crystal improved the level and reproducibility but still some values 2 to 5 times those expected were regularly observed. Reviewing differences between our own technique and that of Bohaty and Haussühl^(2.4) and more recent work of Luymens^(2.5), we note that both the latter glued the sample firmly into the mounting before measurement. Replacing our own spring mounting by glueing the halide into place with conductive expoxy produced an immediate improvement in reproducibility of the experimental data, but values for NaCl measured at 7 Hz were still almost twice those of Bohaty and Haussul.

In an attempt to reconcile the data, we have now extended the frequency range of our measurements. It is first necessary to calibrate the equipment using quartz and our rotating capacitance standard, so as to eliminate the frequency dependence of the detector gain characteristics. After careful correction for these effects, we observe a clear frequency dependence of M_{11} for NaCl (Fig. 2.1). Since dispersion of K_1 in these crystals is very weak, the strong frequency dependence implies a frequency dependence of the Q_{11} constant.

It may be noted that our measured dispersion in M reconciles our earlier data with that of Bohaty and Haussühl which was measured at higher frequency in the range 80 to 160 Hz and suggests a possible explanation for the disagreement with the earlier data from Zheludev^(2.6) which was again measured at still a higher frequency (6 kHz).

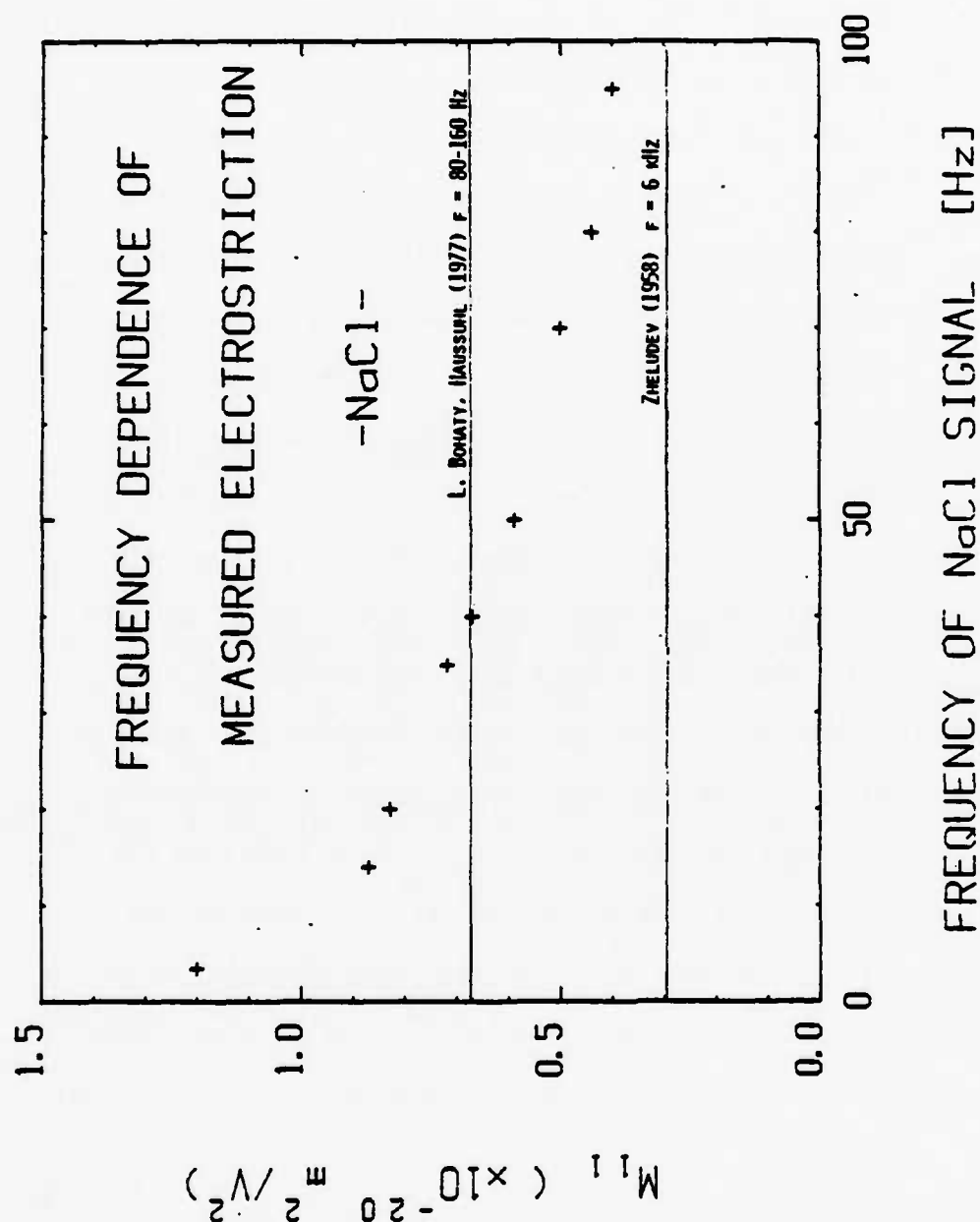


Figure 2.1. Direct measurement of electrostriction coefficient M_{11} as a function of applied frequency.

The present data certainly points up the clear need for more extensive measurements of electrostriction in simple solids which can cover a wider frequency range, and the danger of using numbers which are currently available to judge the validity of theoretical descriptions of the phenomenon. This will be taken up in the discussion of possible future work.

2.2 Measurement of the Converse Electrostriction in Perovskite Halides

The pressure dependence of the dielectric stiffness χ has been measured in single crystals of KMgF_3 , KCaF_3 , KMnF_3 and KZnF_3 grown in this laboratory. The very low electrical capacitance which can be achieved in samples of these low permittivity solids required the design of a rigorously guarded 3 terminal enclosure for the dielectric pressure cell with total stray capacitance below .0001 pF.

In all the samples measured χ vs p is negative and slightly nonlinear. The Q_h have values of order $0.1 \text{ m}^4/\text{c}$ a factor of 10 larger than the oxide perovskites, but in good agreement with the empirical relation derived earlier by Uchino^(2.7). The weak nonlinearity is too large to be explained by nonlinearity in the elastic properties of the halide perovskites, and requires the existence of sixth order electrostriction terms. The $\phi_h = \phi_{111} + \phi_{123} + 2\phi_{122} + \phi_{121}$ in matrix notation, are all positive and of the same order as in the alkali fluorides and alkaline earth fluorides.

A paper describing this work is being submitted to the Journal of Applied Physics. The abstract is included as Appendix 1.

2.3 Temperature Dependence of Dielectric Permittivity in KMnF_3

In the course of examining the converse electrostriction in the perovskite halides, the dielectric permittivities were measured over a wide temperature range to ascertain any phase transitions which might be driven by pressure and

perturbs the electrostriction measurement. In KMnF_3 a transition takes place at 186°K (-37°C)^(2.8-2.10) closely analagous to the 110°K transition in SrTiO_3 . Unlike the titanate, however, we were surprised to find a peak in the dielectric permittivity at the transition. Since the lower temperature state is tetragonal I4/mcm and twinned, it is difficult to comment in detail, but repeated cycling gives remarkably reproducible dielectric data suggesting that the twinning is on a fine enough scale to average out the tetragonal anisotropy.

A paper describing this work has been prepared. The abstract is included as Appendix 2.

2.4 Basic Theory

2.4.1 Introduction

The objective of this work on the theory of electrostriction was to understand the effect of crystal structure, chemical composition and temperature on the electrostriction coefficients of ionic crystals, especially ferroelectric materials, in order to optimize the electrostriction coefficients and, ultimately, in order to maximize the electromechanical coupling factors of ferroelectric materials derived from centric prototypes via a systematic molecular engineering approach.

2.4.2 Major Results

(i) It has been demonstrated that the microscopic approach employed for calculating electrostriction coefficients is suitable for understanding the role of cohesive factors in determining electrostriction. The theoretically calculated static values of electrostriction coefficients of alkali halides^(2.11) and of several perovskite oxide compounds^(2.12,2.13) are the first such calculations based on adequate theoretical models for the interatomic forces.

(ii) Use of anharmonic many-body perturbation theory in the quasiharmonic approximation of Bruce and Cowley^(2.14) in connection with a realistic model

for the interatomic forces is adequate for calculating room temperature values of electrostriction coefficients in perovskites provided experimental room temperature values of the soft mode zone center frequency are used as input data^(2.15). However, this theoretical approach is unable to account for the experimentally observed temperature variation of the electrostriction coefficients, even when experimental values for the temperature dependent soft mode frequency are used as input^(2.15).

(iii) On the basis of a phenomenological thermodynamic analysis and by utilizing rotationally invariance conditions of the nonlinear elastic dielectric^(2.16,2.17), it has been shown^(2.17-2.19) that the nonlinear constitutive relations commonly used in the literature and expressed, for example, in terms of the elastic displacement gradient and the electric field are inconsistent and involve nonlinear elastic, piezoelectric and electrostriction coefficients of lower symmetry than normally belongs to the associated higher rank tensor quantities^(2.10). On the other hand, a consistent formulation of the nonlinear elastic dielectric has been given on the basis of Toupin's theory^(2.16) in terms of the thermodynamic tensions and the electric field thermodynamically conjugate to the material measure of polarization^(2.17-2.19). These results are consequential for the Landau-Devonshire theoretical description of ferroelectric transition with strain present, such as, e.g. when the strain dependence of the ferroelectric Curie temperature is considered. In these cases it is, for example, necessary to use the material measure of polarization as order parameter, instead of the usual polarization vector, which in general is not a proper thermodynamic variable.

(iv) Based on the above results (iii), a consistent theoretical framework for the experimental determination of electrostriction coefficients from measurements of the electric field dependence of the piezoelectric constants has been developed^(2.19). This method could provide an alternative to the

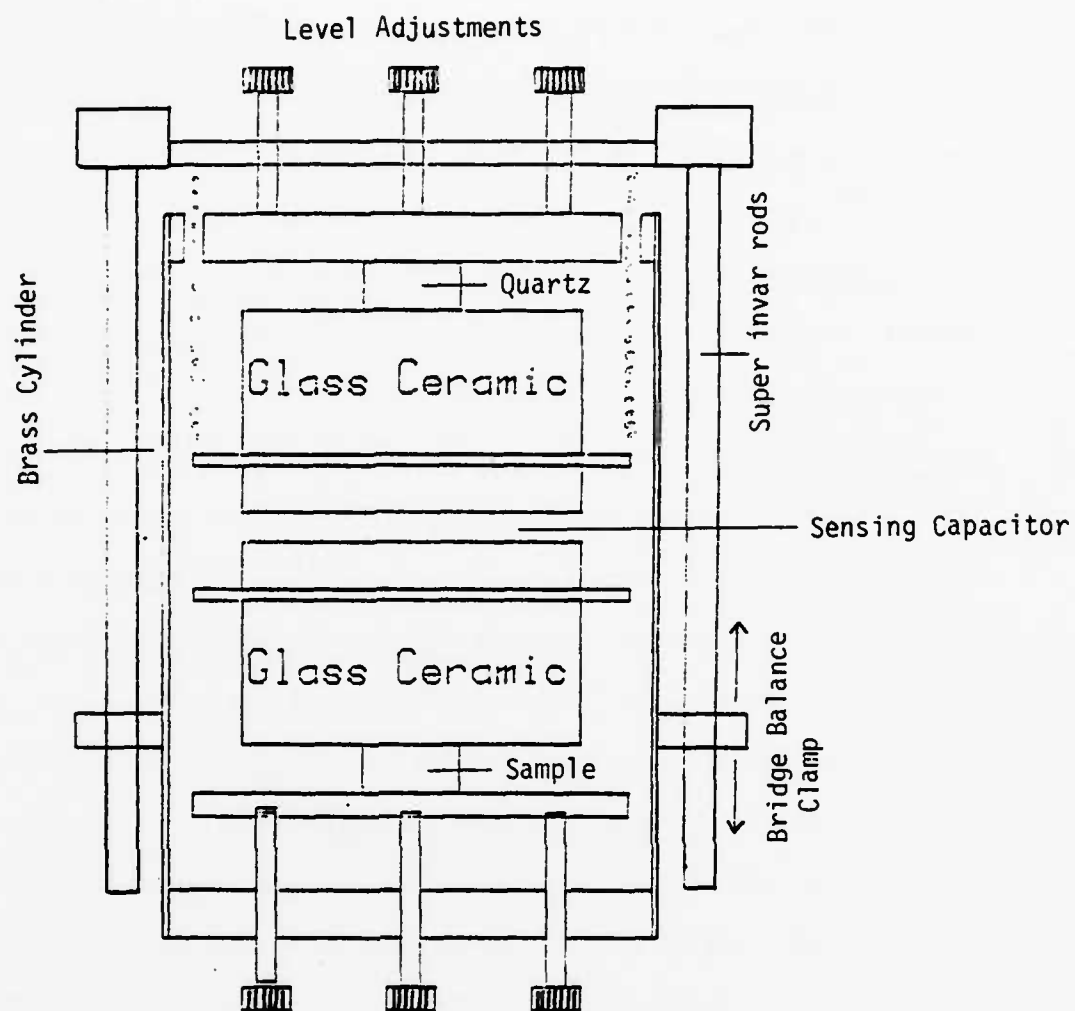


Figure 2.2. Sample holder for AC dilatometer showing Invar: Brass bridge for expansion balance.

dilatometric technique presently in use and perhaps contribute to resolving some of the difficulties encountered with this method.

2.5 Electrostriction in High K Dielectrics

2.5.1 Ultradilatometer for Wide Temperature Range

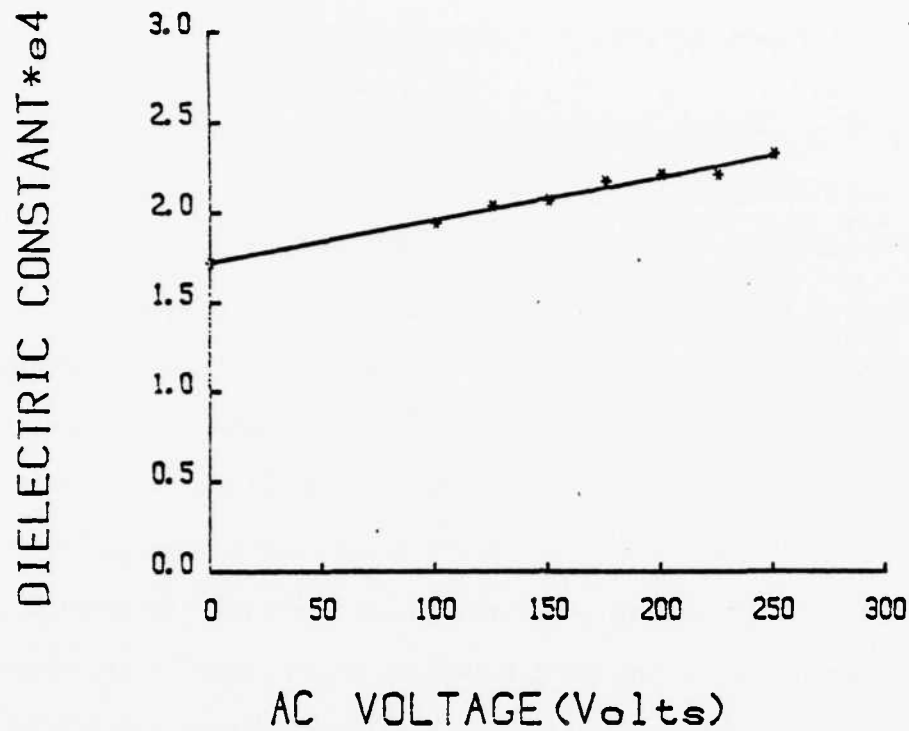
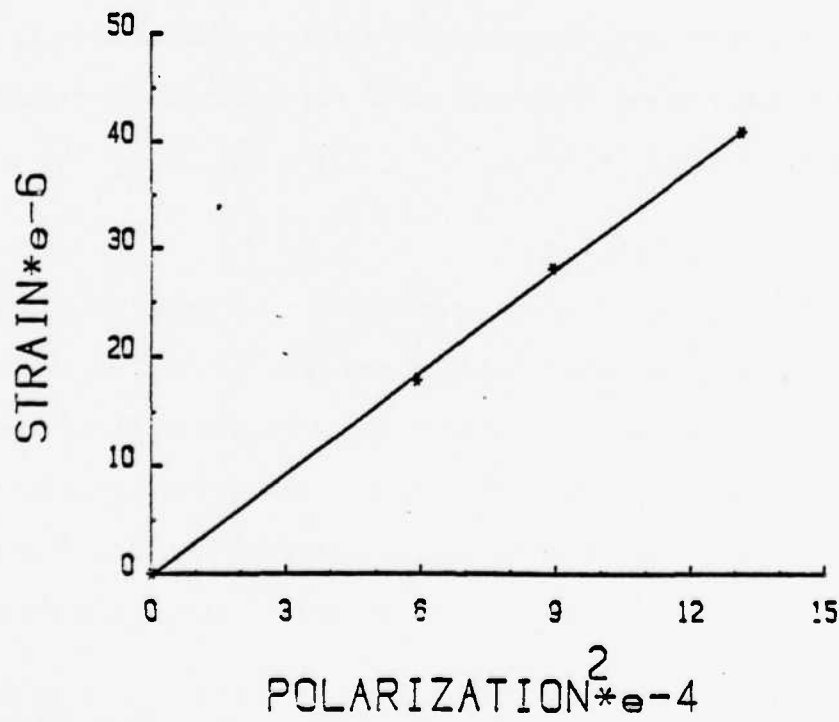
A new simplified capacitance dilatometer has been constructed based on the original design of Uchino and Cross^(2.1). To alleviate the need for a DC feedback for stabilizing the measuring circuit, and to permit a wider temperature range of operation, (1) all plastic parts have been replaced by ceramic or machinable glass ceramics, (2) the sample support structure is designed as a thermal expansion bridge circuit in which one arm of the bridge can be balanced by replacing the brass support with a super invar of very low expansion (Fig. 2.2); (3) guarded 3 terminal measurement of the sensing capacitance is preserved, but all plastic screened cable is replaced by ceramic insulated coaxial supports in the head unit.

With these modifications, the minimum resolvable displacement is reduced to 0.01A, but the temperature range over which measurements can be made is raised from -180°C to +250°C.

2.5.2 Ferroelectric Relaxors

To calibrate the new dilatometer, samples of lead magnesium niobate 10% lead titanate solid solution which had been measured by Jang and Uchino were re-measured. Even at the low field used in the dilatometer (2 kv/cm max) the permittivity is not strictly linear (Fig. 2.3). Correcting the polarization, however, excellent linearity of P^2 vs x_{11} is observed (Fig. 2.4) and the value of the measured coefficient (PMN:10PT STD) in Table agrees closely with Jang's value.

Improvements in the processing of PMN:10PT by Shrout and Swartz in this laboratory (see Section II) have resulted in materials with much reduced

Figure 2.3. ϵ vs V in PMN:10% PT.Figure 2.4. Electrostrictive strain vs P^2 in PMN:10% PT.

contamination with the low permittivity pyrochlore structure phase. Measurements of these samples (Table 2.1) show improvements in the M and Q coefficients by up to a factor of 3.

Due to the courtesy of Dr. Yonezawa at Nippon Electric Company, we were supplied with samples of the lead iron niobate:lead iron tungstate PFN:PFW composition which NEC uses as a dielectric in multilayer capacitors with silver or high silver palladium electrodes. The NEC material has the dielectric characteristics of a ferroelectric relaxor (Fig. 2.5) and gives M and Q values close to those of PMN:PT. The PFN:PFW material has the advantage of compatibility with Ag electrodes, but suffers the disadvantage of a more sharply peaked permittivity leading to much sharper temperature dependence of the M_{11} coefficients, and rather lower insulation resistance.

2.6 Poling and Depoling Behavior in PLZT 8:65:35 Transparent Ceramic

A detailed study (Appendix 3) of the poling and depoling of PZT transparent ceramics at the 7:65:35 and 8:65:35 compositions shows that in freshly thermally depoled samples cooled to low temperature then subjected to weak DC bias, there is a new dielectric anomaly on heating which correlates with a loss of dispersive character only regained at the so-called $\alpha:\beta$ transition which occurs at a temperature well below the dielectric maximum in these materials.

Pyroelectric current measurements show that the low temperature anomaly corresponds to a build up of macro-polarization and the upper transition to a loss of macro-polarization.

The result is, we believe, most important in that it suggests

(a) That the change at the $\alpha:\beta$ transition is not a phase change in the usual sense, but corresponds to an ordering of polar micro regions disordered at higher temperature.

(b) That the materials can be 'frozen' into the disordered state by cooling without field.

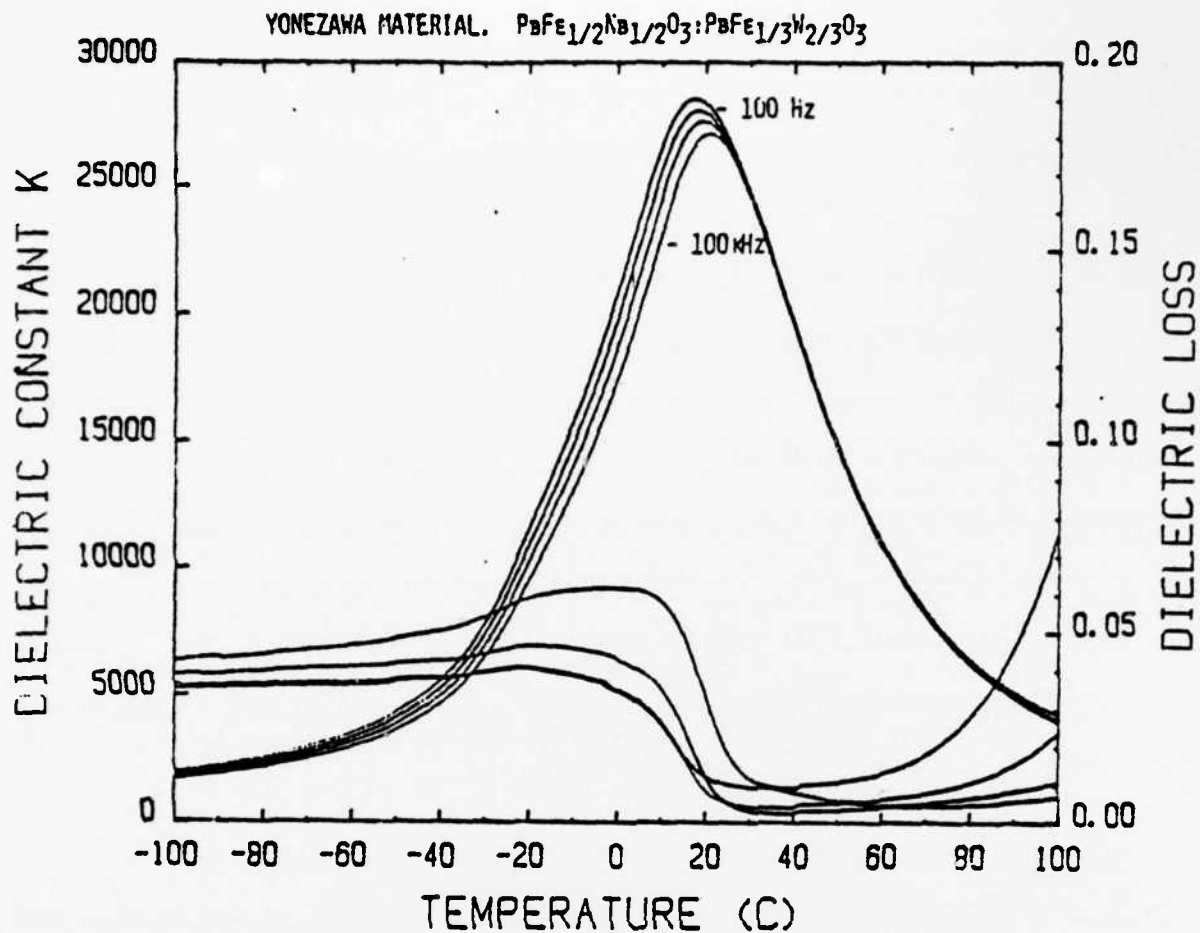


Figure 2.5. Dielectric behavior of typical PFeN:PFeW ceramic.

Table 2.1.

SAMPLE	$\epsilon_R \times 10^3$	$M_{11} \left(\frac{\text{m}^2}{\text{V}^2} \right)$	$Q_{11} \left(\frac{\text{m}^4}{\text{C}^2} \right)$
PMN-10 PT-STD	17.232	7.17×10^{-16}	2.3×10^{-2}
PMN-10 PT-2% PbO	17.289	6.64×10^{-16}	1.4×10^{-2}
PMN-10 PT-2% MgO	19.730	2.31×10^{-15}	3.9×10^{-2}
PMN-10 PT-5% MgO	17.850	1.31×10^{-15}	4.1×10^{-2}
PFW-PFN-#12	25.392	1.383×10^{-15}	1.85×10^{-2}
PFW-PFN-#42	25.386	7.00×10^{-16}	0.975×10^{-2}
PFW-PFN-#43	26.233	1.81×10^{-15}	2.98×10^{-2}

Maximum permittivity, electrostrictive M_{11} and electrostrictive Q_{11} constants for various PMN:PT and PFeW:PFeN samples.

(c) That the disorder can be overcome by moderate fields (1-10 kv/cm) at temperatures much below the α - β anomaly.

On the Smolenskii model for the relaxor behavior, the result would speak strongly for a super paraelectric component in the dispersive permittivity since if domains break down *SPONTANEOUSLY* into polar micro regions, the micro region must be being thermally disordered at the temperature of the α - β anomaly.

2.7 Summary

Electrostrictive studies at Penn State were summarized in the joint US:Japan seminar on Electronic Ceramics held in Rappongi, Tokyo, May 23 - June 4, 1982. An abstract of this paper is included as Appendix 9.

3.0 PIEZOELECTRIC COMPOSITES

3.1 Introduction

Over the past year, effort has been focused upon compiling more extensive and reliable data for a number of the two phase and three phase composites which have the potential for high sensitivity hydrophones. The task is not simple because of the viscoelastic nature of the polymer phase and the non-linear hysteretic nature of the PZT which are major components in the system of interest.

To provide data which mimic more closely the needs of transducer designers, we have turned to using a low frequency A.C. measurement of the g_h which can be made in a pressure chamber under static pressures up to 1000 psi (over 6.5 MPa). The objective has been to authenticate systems which retain high sensitivity under pressures up to 1,000 psi for frequencies in the low frequency range of interest.

Recent intercomparison of data for some of our systems with values obtained by Dr. Ting at the calibration facility in Orlando show good agreement.

In the case of the 1:3, 1:3:0 and transversely reinforced 1:3 composites, the more detailed evaluation has been accompanied by a more complete modelling of the structure which gives a much better understanding of the role of the Poisson ratio in limiting the hydrophone sensitivity.

3.2 Piezoelectric 3-3 Composites

Piezoelectric ceramic-polymer composites with 3:3 connection have been made using the processing technique developed by Shrout^(3.1). The method consists of mixing in an appropriate volume fraction of plastic spheres into the green ceramic, then burning out the polymer in such a manner as to develop an interconnected skeletal structure of pores connected in all 3 dimensions. After careful sintering, a porous equivalent 3 dimensional skeleton of PZT is formed which can then be back filled by the polymer of choice by vacuum impregnation.

Using this method, samples with PZT:polymer volume fractions over the range 70:30 to 30:70 have been fabricated and their dielectric and piezoelectric properties measured. Best results were obtained with a 50:50 PZT:silicone rubber combination which gave

$$\text{Permittivity } K_3 = 450$$

$$\text{Piezoelectric } d_{33} = 150 \text{ pC/N}$$

$$\text{Piezoelectric } g_h = 45 \text{ mVm/N}$$

$$\text{Piezoelectric } d_h = 180 \text{ pC/N}$$

and thus a $d_h g_h$ product of $8,100 \cdot 10^{-15} \text{ m}^2/\text{N}$.

3.3 Perforated PZT-Polymer Composites

Composites of 3-1 and 3-2 connectivity have been fabricated by Safari^(3.2) using a technique of drilling. For typical samples optimized for hydrophone performance

In 3:1 composites

$$K_3 = 600$$

$$d_h = 230 \text{ pC/N}$$

$$g_h = 34 \text{ mVm/N}$$

and $d_h g_h = 7,800 \cdot 10^{-15} \text{ m}^2/\text{N}$.

While for 3:2 composites

$$K_3 = 300$$

$$d_h = 372 \text{ pC/N}$$

$$g_h = 123 \text{ mVm/N}$$

and $g_h d_h = 45,000 \cdot 10^{-15} \text{ m}^2/\text{N}$.

These composites are extremely rugged and show almost no change with hydrostatic pressures up to more than 6 MPa (1,000 psi).

3.4 Piezoelectric Composites of 1:3 Connectivity

3.4.1 Introduction

Recent studies have concentrated upon the possibility of improving the simple 1:3 PZT:polymer composite for hydrophone application by the technique of transverse reinforcement. The reason for the study is that it is evident even from very simple stress analysis, that the effective axial stress transfer to the PZT rods in the 1:3 configuration can be very adversely effected by the transverse components of the hydrostatic stress acting through the Poisson ratio of the supporting three dimensionally connected polymer phase. Since particularly the soft polyurethane and silicone rubber polymers have high Poisson ratio, it is composites involving these phases which may benefit most from transverse support.

3.4.2 Experimental Studies

The experimental data have been presented earlier, but for comparison with the model studies are repeated here. Figure 3.1 shows the influence of glass fiber reinforcement on a 1:2:3 composite of PZT 501:glass:spurs epoxy resin at the 5% PZT volume fraction. Figure 3.2 shows the same figure but for a Devcon polyurethane polymer. Figure 3.3 shows the influence of foaming the polymer to soften and reduce the Poisson ratio. In Figure 3.4, additional transverse stiffening has been effected by encapsulating the Devcon polyurethane sample in a rigid epoxy case.

Measurements were in each case made by the DC charge release method but for each sample more than 10 runs up to 100 psi were carried out before the final measuring run so as to eliminate initial depoling. The number of samples measured for each family is given on the figure.

No irreversible degradation was observed after the initial depolarization.

1. SPURRS EPOXY
(5% PZT)

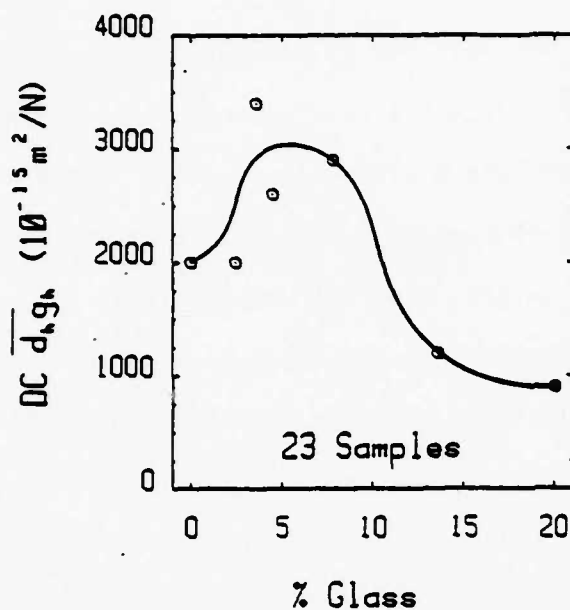


Figure 3.1. Experimental data
PZT:spurrs.

2. DEVCON POLYURETHANE
(5% PZT)

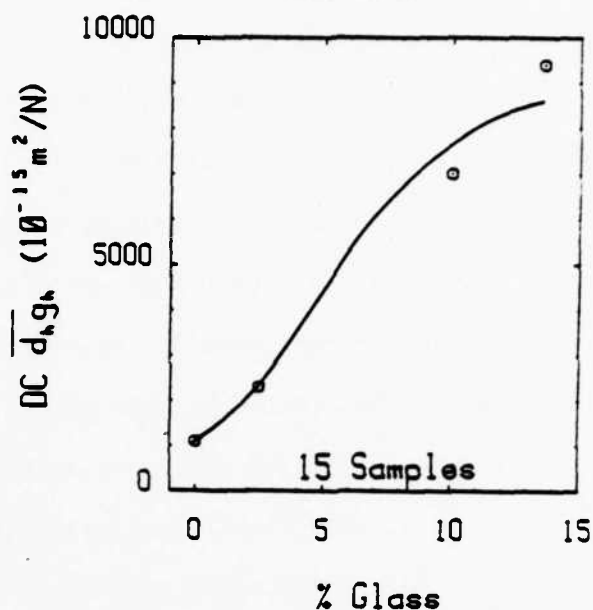


Figure 3.2. Experimental data
PZT:Devcon.

3. FOAMED DEVCON
POLYURETHANE (5% PZT)

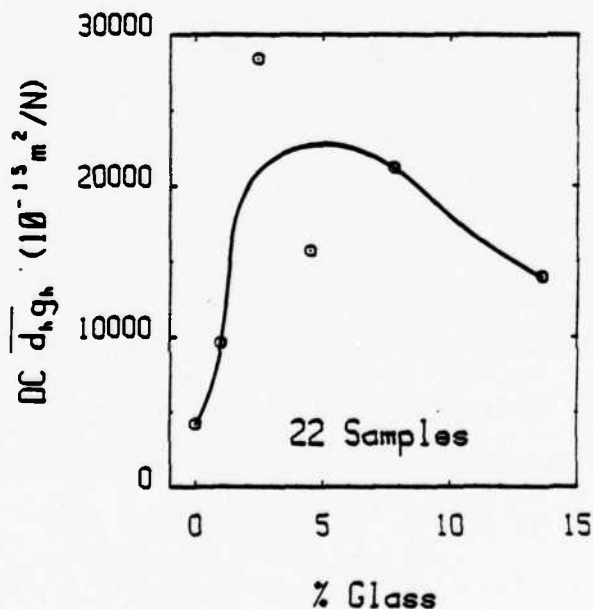


Figure 3.3. Experimental data
PZT:Devcon:foam.

4. ENCAPSULATED FOAMED
DEVCON POLYURETHANE (5% PZT)

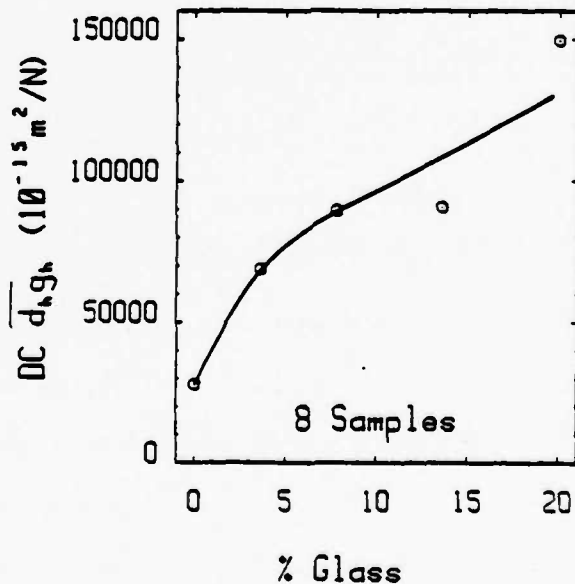


Figure 3.4. Experimental data
epoxy reinforced
PZT:Devcon:foam.

3.4.3 Theoretical Analysis

In earlier analysis of the 1:3 composites, the polymer phase was assumed to be so much more compliant than the PZT that its stiffness could be neglected. These early models also neglected the effects of internal stresses in the polymer and not surprisingly predicted enhancement of the figure of merit $d_h g_h$ significantly higher than was measured in real material combinations.

A new more complete modeling has now been accomplished by M. Haun. Again perfect bonding of polymer and PZT are assumed, and the condition of constant strain in the two phases is assumed. However, the model does take account of

- (a) The elastic properties of the polymer phase.
- (b) The elastic properties of the PZT.
- (c) The elastic properties of a glass fiber used to provide transverse reinforcement in a 1:2:3 phase connection.
- (d) Modification of the elastic properties of the polymer phase which can be effected by foaming.
- (e) Internal stress effects due to Poisson's ratio are included.
- (f) To simplify calculations, both reinforcing phase and porosity are taken on an equivalent rectangular volume.

To see directly the effects of changing the fiber reinforcement and the volume fraction of PZT in the composites, three dimensional surfaces have been calculated for several of the more interesting cases.

In Figure 3.5, the $\bar{d}_h \bar{g}_h$ figure of merit for a PZT:epoxy composite ($P_s = 2.9 \cdot 10^{-10} \text{ m}^2/\text{N}$, $P_v = 0.35$) is mapped on the vertical axis as a function of volume fraction of PZT and volume fraction of glass fibers. Maximum sensitivity of $11,100 \times 10^{-15} \text{ m}^2/\text{N}$ occurs for 10.8% PZT and 10.2% glass.

Figure 3.6 plots the theoretical sensitivity for a polyurethane:glass:PZT 1:2:3 composite ($P_s = 1.10^{-8} \text{ m}^2/\text{N}$, $P_v = 0.48$). Notice now that because of the

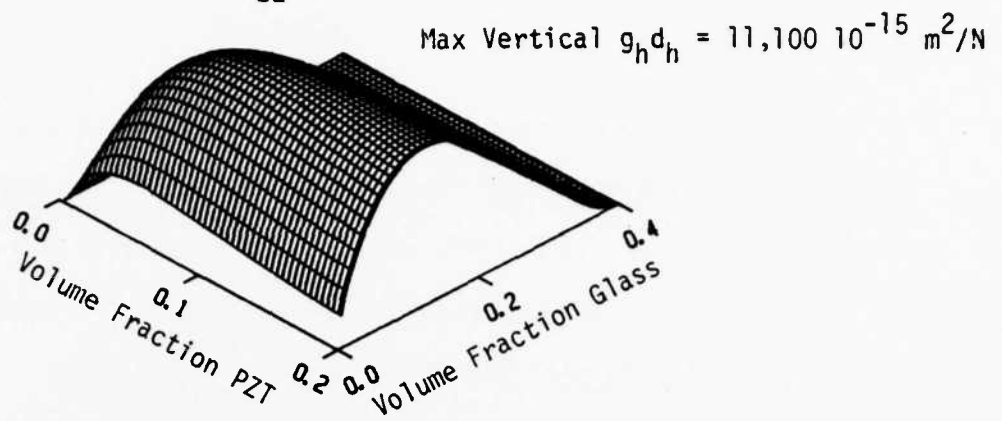


Figure 3.5. PZT:epoxy composite.

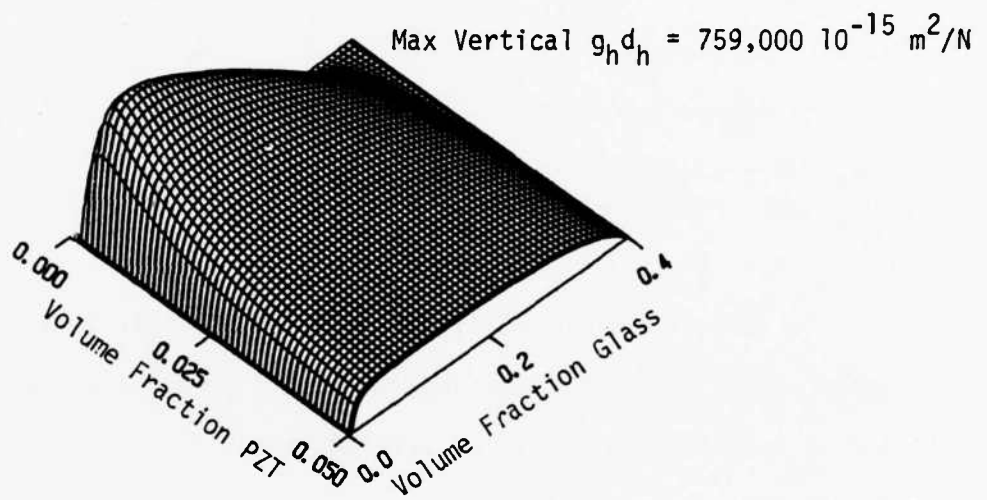


Figure 3.6. PZT:glass:polyurethane 1:2:3 composite.

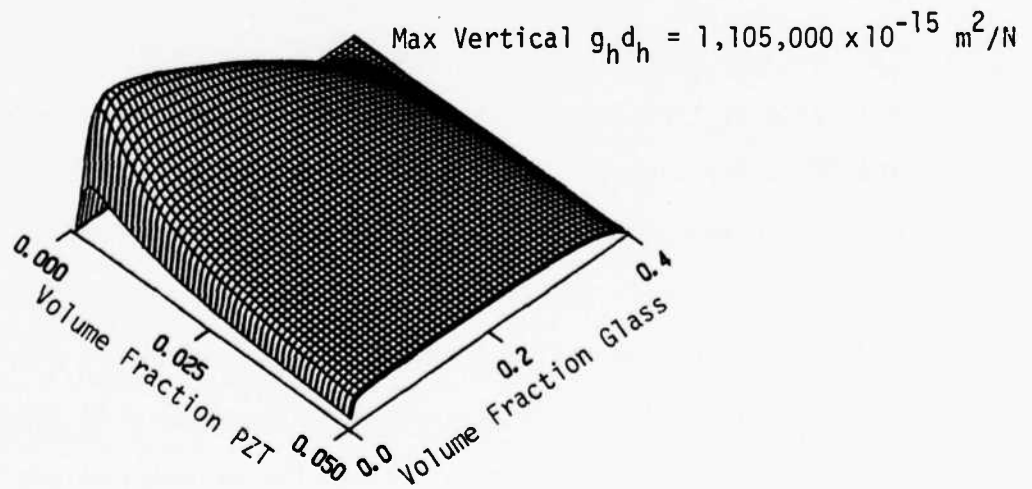


Figure 3.7. PZT:glass:polyurethane foam 1:2:3:0 composite 20 vol% foaming.

high Poisson ratio of the polymer, the zero volume fraction axis of glass reinforcement has almost no sensitivity irrespective of the PZT content while because of the very large compliance of the polymer only a small volume fraction of glass is needed to relieve the transverse stress. Theoretical maximum in $d_h g_h$ occurs at 0.45 vol% PZT and 4.7% volume fraction of glass with a values $759,000 \times 10^{-15} \text{ m}^2/\text{N}$.

Further softening the polymer and reducing Poissons ratio by foaming to 20 volume% air enhances the sensitivity, and produces significant sensitivity at 0 reinforcement ($P_s = 1 \times 10^{-8} \text{ m}^2/\text{N}$, $P_v = 0.48^\circ$, $\nu_v = 0.20$). Now a maximum sensitivity of $1,105,000 \times 10^{-15} \text{ m}^2/\text{N}$ occurs at 0.35 vol percent PZT and 3.5% glass fibers (Fig. 3.7).

3.4.4 Discussion

To compare more directly the measured and calculated performances, cuts of the three dimensional surfaces at the 5 vol% PZT are given in Figure 3.8, and an expanded scale for the unfoamed epoxy cut at the 5 volume% PZT in Figure 3.9.

In the PZT:epoxy composite, the trend of data is very well described by the theory, though the absolute values are only ~50% of the theoretical expectation.

For the polyurethane and foamed urethane samples, the much stronger influence of transverse reinforcement in the soft polymer is clearly evident though in the unencapsulated case the absolute values are much lower. Here, we believe the discrepancy is due to a fabrication problem which makes it very difficult to finish the samples for electroding without breaking some of the finer rods. Encapsulation not only permits additional transverse reinforcement, but also allows a reasonable surface finish without disastrous consequences for the internal structure. In this case, the measured values are given within a factor 2 of theoretical expectation and the trend is similar to theory.

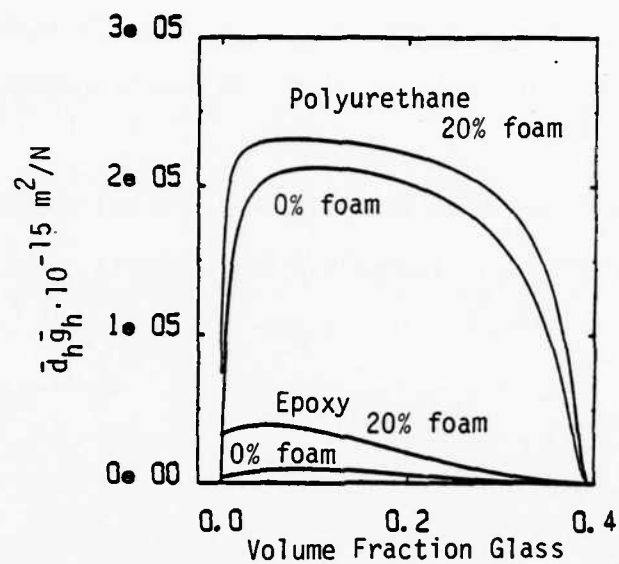
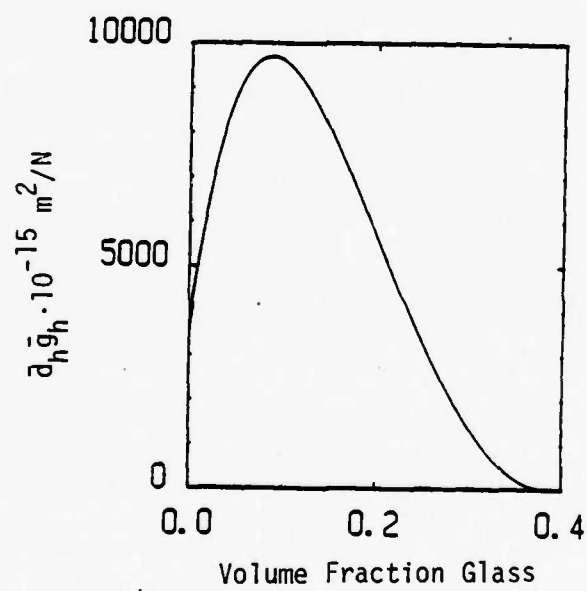


Figure 3.8. Theory for 5% PZT.

Figure 3.9. Theory for 5% PZT
(Expanded Scale).

Perhaps the major frailty of the analysis is now the assumption of common strain in polymer and PZT in the polar direction, which probably accounts for this discrepancy.

The more detailed theory does point up the cardinal advantage of transverse reinforcement in the 1:2:3 composites and supports the earlier contention of the importance of the Poisson ratio of the softer polymer phase.

3.5 Polar Glass Ceramics

3.5.1 Introduction

Bhalla and Halliyal^(3.3,3.4) have recently developed a completely new family of piezoelectric polycrystal materials which are polar but not ferroelectric. In their method, a glass of suitable composition is recrystallized in a very strong temperature gradient. The gradient of the scalar T produces a driving force which gives strong preference to crystal nuclei of a given polarity, so that a polar phase being crystallized from the glass is strongly oriented.

The polar texture in these oriented glass ceramics necessarily implies pyroelectric and piezoelectric properties.

3.5.2 Application of Piezoelectrics

In the fresnoite ($\text{Ba}_2\text{TiSi}_2\text{O}_8$) and its germanium analogue $\text{Ba}_2\text{TiGe}_2\text{O}_8$, both the silicate and germanate can be quenched from above the melting temperature to a glassy state. By careful control of temperature and temperature gradient, the glass can be recrystallized with a very strong polar texture. Measurements of the hydrostatic pressure sensitivity under AC pressure at 50 Hz give g_h values of ~ 100 to 120×10^{-3} Vm/N taken with the very low permittivity $K \sim 10$ gives $d_h \sim 16 \cdot 10^{-12}$ C/N and these figure of merit $d_h g_h \sim 1,800 \cdot 10^{-15}$ m²/N comparable to PVDF.

The very high stiffness of the glass, and the firm polar (non-ferroelectric) character of the polarization give an effective immunity to hydrostatic pressure

to much greater than 10 MPa. This very high stiffness in the glass ceramic ($s_{11} \sim 0.9 \cdot 10^{-11} \text{ m}^2/\text{N}$) taken together with the low permittivity suggest that the glass ceramic might be used as a piezoelectric stressing medium in combination with a glass fiber to generate a fiber optic electric field sensor. Preliminary calculations suggest that the stiff glass would be more than 20 times more effective than PVDF in this type of system.

3.6 Summary

A recent summary of the status of piezoelectric composites has been given by Newnham at the joint US:Japan Seminar on Electroceramics in Rappongi, Tokyo, May 1982. The abstract for this paper is included as Appendix 10.

4.0 PYROELECTRIC MATERIALS

4.1 Micro Composites

In the relaxor:ferroelectric lead scandium tantalate, the two B site cations Sc^{3+} and Ta^{5+} can be ordered by long thermal annealing^(4.1,4.2). In disordered states, the single crystal and ceramic show diffuse transition relaxor behavior. For the ordered state, the phase transition is sharp and first order.

Thermal depoling of the disordered ceramic occurs over a very wide temperature range and the slope of static $\partial P/\partial T$ would correspond to a very large pyroelectric coefficient. Clearly, however, most of this effect will be irreversible, however, under a DC bias field on the Smolenskii model for the disordered condition, there will be a competition between field ordering and thermal disordering of the polar micro regions. If at low frequency (~ 10 Hz) the thermal disordering of the smaller regions is fast enough, it should contribute an extrinsic (micro domain) enhancement of the reversible pyroelectric effect. To test for this possibility, it is necessary to use the Chynoweth method to separate reversible from irreversible components of the pyroelectric response; and since the Chynoweth response depends on the ratio p/ϵ , where p is the reversible pyroelectric effect and ϵ the dielectric permittivity, it is necessary to study also the effects of DC bias on the low frequency permittivity.

The results are reported in detail in the paper of Appendix 11 for the dielectric response, and in Appendix 12 for the pyroelectric effect.

In summary, disordered (relaxor) $\text{PbSc}_{1/2}\text{Ta}_{1/2}\text{O}_3$ shows a very strong enhancement of Chynoweth pyroelectric response under DC bias, the ordered crystal shows no such effect. The dielectric data indicates clearly that the level of enhancement in the relaxor cannot be accounted for by the DC bias dependence of the dielectric permittivity and thus we conclude that micro-polar regions do contribute an extrinsic component to the response.

It will be of real interest to experiment with partial ordering in the PST system as it is unlikely that we have the maximum possible extrinsic response in these preliminary studies.

4.2 'Doped' Tungsten Bronze and TGS Structure Single Crystals

From the earlier studies of Brezina^(4.1) and of Keve^(4.2), it is possible to modify the pyroelectric response in triglycine sulphate by doping with metal ions, or by substitution of a fraction of the glycine by alanine. Perhaps the most illustrative of the mechanism of change is the work of Keve on the alanine substitution. In his studies, Keve showed that if levo-alanine is substituted, the side group imparts a strong unidirectional bias to the hysteresis, just as if the crystal were subjected to a strong electrical bias, while if racemic alanine is incorporated into the TGS, the loop splits into oppositely biased segments.

In our studies, single crystals of strontium barium niobate at the $\text{Ba}_{0.5}\text{Sr}_{0.5}\text{Nb}_2\text{O}_6$ composition were modified by the incorporation of Nd^{3+} during the growth process. Comparison of doped and undoped crystals using the Byer-Roundy method show that an optimum composition improves the room temperature pyroelectric coefficient from 500 to 800 $\mu\text{C}/\text{m}^2\text{K}$.

For triglycine sulphate, we have been studying the possible substitution of $(\text{PO}_4)^{3-}$ and $(\text{AsO}_4)^{3-}$ for the sulphate group. To facilitate poling, the crystals were grown from a single domain alanine doped seed at temperatures below the Curie point. For a 12 mole% substitution of $\text{H}_3(\text{PO}_4)$ for H_2SO_4 , the crystal shows an enhancement of room temperature pyroelectric coefficient from $350 \cdot 10^{-6}$ MKS to $950 \cdot 10^{-6}$ MKS and a figure of merit P/K more than 2 x TGS. A more detailed account of this work will be presented at ISAF 83. The abstract for the paper is appended as Appendix 13.

5.0 FERROELECTRIC BICRYSTALS

5.1 Introduction

Work on the ferroelectric bicrystals formed by hot pressure bonding at LiNbO_3 single crystal plates at temperatures below the Curie temperature T_c has now been completed. Maintaining the temperature at 1100°C under a uniaxial pressure of 10^6 N/m^2 , excellent uniform bonding was achieved for 'c' cut plates with the polar axis in head-to-head (H-H), tail-to-tail (T-T) and head-to-tail (H-T) configurations, both with 'a' axes aligned and with 'a' axes twisted through 90° (H-H'), etc.

5.2 Summary of Work

Detailed etching studies reveal that using the thermal bonding under short circuited electrical condition, the domain structure of (H-T) bonded crystals is completely preserved. For (H-H) and (T-T) configuration, the major features are preserved, but a moving of the domain wall across the bonding plane is often observed. Details of the study are given in Appendix 14.

Dielectric properties show little change in the real part of the permittivity K' , but a significant change enhancing the transport dominated loss at higher temperature. Crystals bonded in the (H-H') twisted configuration show a new dielectric loss maximum. Details of the dielectric studies are given in Appendix 15, and a confirmation of the model for the proposed defect structure in the boundary region given from the analysis of thermally stimulated currents taken both parallel and perpendicular to the boundary (Appendix 15).

A most interesting spin off from the bicrystal work came from the realization that (H-H) and (T-T) bonded crystals preserved their individual piezoelectric thickness mode resonances, while (H-T) bonded bicrystals resonated as a whole. This suggested that LiNbO_3 might be used as a model ceramic to explore in a quantitative manner the way in which the damped resonances of

the individual grains would influence the frequency dependence of the impedance of the ceramic.

Model ceramics with a narrow distribution of grain sizes were made up, using both mixed oxide and liquid salt processed powders.

Dielectric impedance measurements gave a clear indication of damped resonant character in the massive dispersion of both real and imaginary parts of the permittivity for frequencies near the resonance point for the mean grain diameter.

Making use of the IBM ECAP computer analysis routine for complex circuits, and a special folding technique to multiply the number of nodes that the routine can handle, it was found to be possible to calculate directly from the known single crystal parameters, and the known grain size distribution impedance as a function of frequency.

Using only the damping factors as adjustable parameters, it was possible to match the measured impedance curve to better than $\pm 5\%$ over the whole measured frequency range from 100 Hz to 10^9 Hz (Appendix 17).

We believe that these calculations give the first clear proof of the importance of piezoelectric grain resonance for the dispersion at high frequencies which is found in all ferroelectric ceramics.

These studies were a part of the Ph.D. thesis for Dr. Yao Xi, and it is gratifying to report that this thesis was chosen as one of the two outstanding Ph.D. theses across the whole materials field at Penn State and that Dr. Yao Xi was a recipient of the Xerox Award for 1982.

6.0. CRYSTAL GROWTH

6.1 Introduction

The new Crystalox crystal growth system which was provided under this contract has been used to grow the following crystals by Czochralski pulling from the melt.

(1) Tungsten bronze crystals in the $\text{Pb}_{1-x}\text{Ba}_x\text{Nb}_2\text{O}_6$ solid solution family, with emphasis upon composition close to, but on the tetragonal side of the morphotropic boundary near $\text{Pb}_{0.6}\text{Ba}_{0.4}\text{Nb}_2\text{O}_6$.

(2) Single crystals of Fesnoite $\text{Ba}_2\text{TiSi}_2\text{O}_8$ and of the germanium analogue $\text{Ba}_2\text{TiGe}_2\text{O}_8$. These crystals have been needed to complement studies of the glass ceramics in these compositions.

(3) Perovskite type fluorides including KMgF_3 , KZnF_3 , KMnF_3 and KCaF_3 . These fluoride crystals have been the subject of study in the program to measure fundamental electrostriction constants.

6.2 Lead Barium Niobate

In the crystal growth experiments the material used were Specpure grade PbO , BaCO_3 and Nb_2O_5 . These were weighed out in stoichiometric proportions for $\text{Pb}_{1-x}\text{Ba}_x\text{Nb}_2\text{O}_6$ with x slightly larger than 0.4, then wet milled in ethanol for 12 hours. The slurry was air dried then fired in alumina at 650°C for 4 hours, to ensure the lead was fully oxidized before loading into the platinum growth crucible. The growth crucible was 40 mm diameter and height with parallel sides, and was supported in a fibrous alumina collar. A radiation shield of similar alumina was used to even the temperature above the crucible. The furnace was RF heated at 370 kHz.

Growth conditions included a pulling rate of 2 mm/hour, with rotation at 10 rpm. As grown crystals were annealed by slow programming the system to room temperature over 12 hours. The crystals grown were transparent, yellowish in color with dimensions up to 10x5x8 mm.

More details of growth and characterization are given in Appendix 18.

6.3 Fresnoite and Analogues

$\text{Ba}_2\text{TiSi}_2\text{O}_8$ and the germanium analogue $\text{Ba}_2\text{TiGe}_2\text{O}_8$ have been grown by pulling from the stoichiometric melt. In each case specpure grade chemicals were weighed in the required proportions using BaCO_3 , TiO_2 and SiO_2 as starting powders. The charges were first calcined at 1080°C in an oxidizing atmosphere before transfer to the pulling crucible.

For the silicate, the pulling speed was 1 mm/hr with shaft rotation at 30 rpm and the crucible not rotating. The high viscosity of the melt at the melting temperatures requires very low pulling rate but is, of course, essential for the glassy form which is of interest in the composite. Crystals up to 5 mm in diameter 1 cm long were pulled for initial study.

In the $\text{Ba}_2\text{TiGe}_2\text{O}_8$, the melting temperature is significantly lower markedly assisting in the growth process. Runs to date used a pulling rate of 0.5 mm/hr and seed rotation at 25 rpm.

In both germanate and silicate, only the c axis seeds have so far been used.

6.4 Perovskite Halides

Crystals which have been grown on this program from the mixed halide components include KMgF_3 (KF, MgF_2), KZnF_3 (KF, ZnF_2) and KCaF_3 (KF, CaF_2). For these materials, the problems are much different from those of the more familiar oxides. A major difficulty is the exclusion of water (OH) from the growth chamber and from the initial compositions without the complication and expense of reactive atmosphere processing.

Conditions for growth are briefly summarized in Table 6.1.

TABLE 6.1. Single Crystal Growth

	Calcining Temp (°C)	R.F. Power Indication	Pulling Shaft Rotation (rpm)	Crucible Rotation (rpm)	Pulling Speed (mm/hr)	Size of Crystal		Date
						Diameter (cm) or Cross Section (cm ²)	Length (cm)	
KMgF ₃	350		25	-5	4	d-1.2	2	81
KZnF ₃	350	4.50	20	0	4	c.s.-.7x.8	1	11/81, 12/82
KCaF ₃	350	6.9	20	-5	4	3-1.1	1.5	1-3/82, 11/82
RbCaF ₃								2/83

Too much evaporation, could hardly see the surface of the melt

7.0 THERMODYNAMIC PHENOMENOLOGY

7.1 Dielectric Measurements

Several interesting new developments in the evolution of the thermodynamic phenomenology have taken place due to our extension of dielectric and piezoelectric measurements over a much wider temperature and frequency range in PZTs and PLZTs.

The very soft commercial donor doped PZT 501 is a remarkably electrical insulator, and we have been able to take weak field permittivity data up to 700°C to obtain reliable stiffness measurements.

For a PLZT composition 8.6:80:20 with very small manganese doping, we find a most interesting well developed relaxation in the paraelectric permittivity before the normal grain:grain boundary dispersion. In two sets of measurements to low temperature, it is clear that $\text{PbZrO}_3\text{:PbTiO}_3$ compositions of differing Zr:Ti ratio freeze out to different values in intrinsic dielectric and piezoelectric response, while doped compositions with the same Zr:Ti ratio, which show strongly dissimilar room temperature piezoelectric and dielectric responses show almost identical intrinsic low temperature values.

7.2 Dielectric Measurements on 'Soft' PZT

In the course of studies of a new possible poling method for soft PZTs (Appendix 19), it became desirable to better characterize the dielectric and transport properties. We were surprised to find very high values of resistivity which permitted poling by cooling through T_c under field and also enable weak field permittivity measurement at 100 kHz to temperatures above 700°C.

Data for a PZT 501 formulation is given in Figure 7.1, with the reciprocal susceptibility in Figure 7.2. It is immediately apparent that the high temperature Curie Weiss behavior ($C \sim 1.5 \cdot 10^5$) breaks down completely in the vicinity of T_c and the transition is quite diffuse. Attempts to fit the data to a

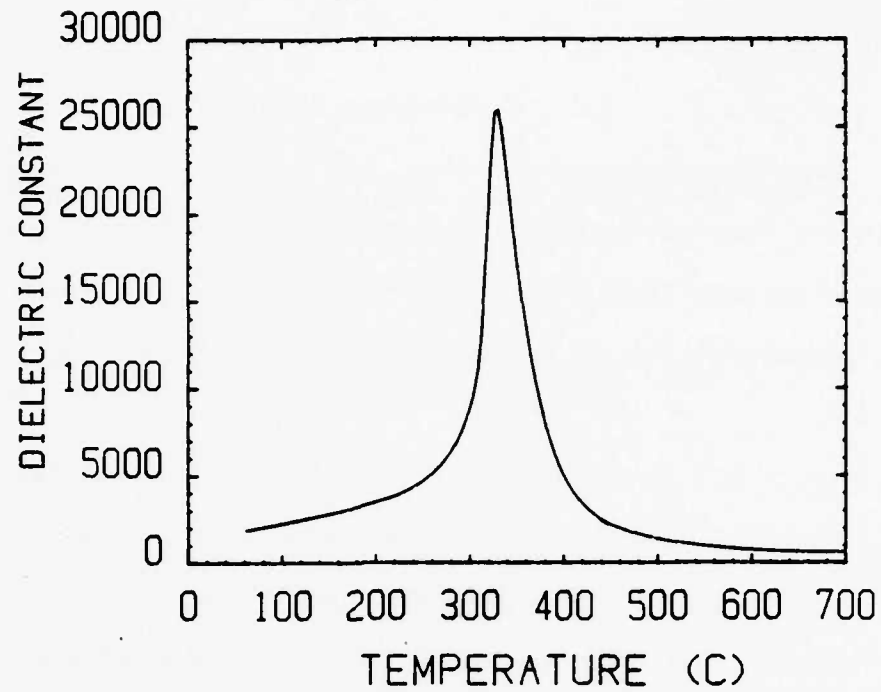


Figure 7.1. Dielectric permittivity vs T in PZT 501 (10 kHz).

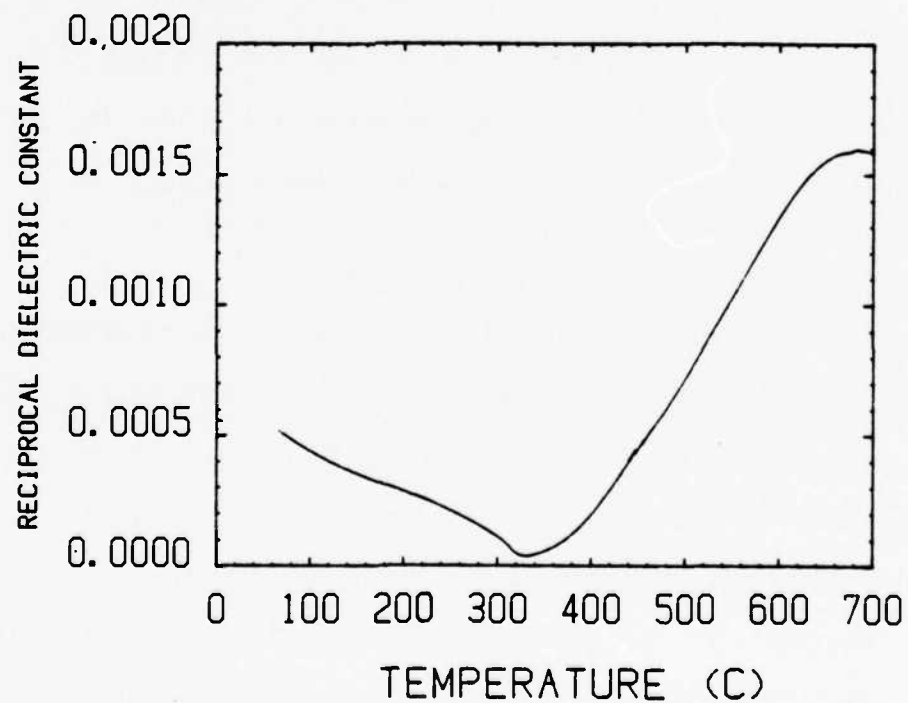


Figure 7.2. Dielectric stiffness vs T in PZT 501 (10 kHz).

Gaussian distribution of Curie temperatures T_c were not successful, and we have been unable to deconvolute the curve to find the effective Curie constant for the Devonshire function.

7.3 PLZT Relaxations

Dielectric measurements on ceramics of the composition 8.6:80:20 PLZT modified with 0.05 mole% MnO_2 show a most unusual high temperature relaxation. Weak field permittivity as a function of frequency and temperature is shown in Figure 7.3, and the associated loss curves in Figure 7.4. It would appear from the loss curves that the relaxation is thermally activated, and is of a form

$$\nu = \nu_0 e^{-E/kT}$$

where ν is the measured relaxation frequency, ν_0 a basic lattice frequency and E the activation energy. Then analysis of the data gives

$$E \sim 0.84 \text{ eV} \quad \nu_0 \sim 2.7 \cdot 10^{10} \text{ Hz}$$

For the steeply ascending loss at higher temperature, however, $E \sim 3.2 \text{ eV}$.

The pre-exponential ν_0 looks very low for a lattice frequency, suggesting that the loss maximum is of the Maxwell Wagner type, but the second up turn in $\tan \delta$ probably indicates that this is not the normal grain:grain boundary heterogeneity. It will be interesting to look more closely at the nanostructure of these samples to see if defect ordering, order disorder in Zr:Ti or heterogeneity dictate this Maxwell Wagner component.

7.4 Dielectric Properties of PZTs at Low Temperature

Dielectric and piezoelectric properties of pure $\text{PbZr}_{0.3}\text{PbTi}_{0.7}$ ceramics with compositions spaced about the 50:50 'morphotropic' boundary, have been measured over the temperature range from 300 to 4 K. The freeze out of extrinsic contributions is particularly evident in the dielectric loss data, and a 'knee'

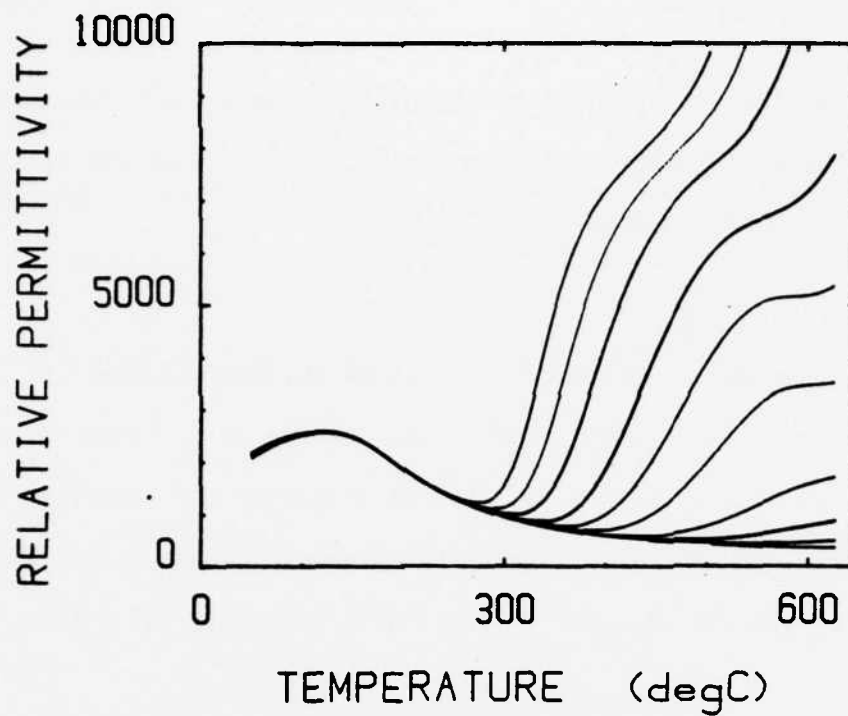


Figure 7.3. Dielectric permittivity in PLZT 8.6:80:20 + 0.05% Mn.

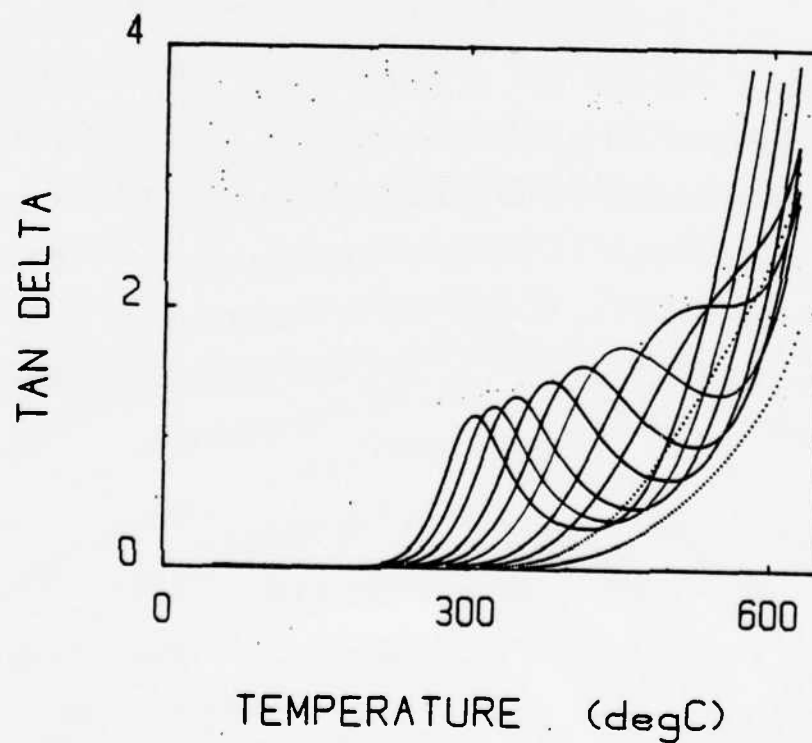


Figure 7.4. Tangents delta in PLZT 8.6:30:20 + 0.05% Mn.

in the permittivity appears to mark the morphotropic phase boundary and point up a weak temperature dependence. Values at freeze out (4°K) are difficult for different Zr:ti ratios. A complete description is given in the paper of Appendix 20.

For a range of commercial doped PZTs, measurements over a similar temperature range show freeze out to consistent values at 4°K independent of the dopant type. We believe that the values at 4°K are essentially averages of the intrinsic single domain values and this argument is taken up in Section II. Details of the experiments are given in the paper of Appendix 21.

8.0 GRAIN ORIENTED CERAMICS AND OTHER PREPARATIVE STUDIES

8.1 Introduction

Work on grain orientation has concentrated upon efforts to exploit shape anisotropy in single crystals grown from liquid salt to provide grain orientation mostly during processing in the green state of the ceramic. Two families of compounds have been explored, the bismuth oxide layer structures in which the growth anisotropy is platey, and the tungsten bronze families which give rise to acicular rod like crystallites.

Other preparative work has been concerned with the need to generate pure $\text{PbMg}_{1/3}\text{Nb}_{2/3}\text{O}_3$ and PbTiO_3 containing solid solutions free from the low permittivity pyrochlore modification. A small effort was given over to producing phase pure pyrochlore modification of PMN, so as to be better able to characterize its properties.

8.2 Grain Oriented Bismuth Oxide Layer Structures

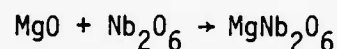
Earlier work to produce grain oriented Bi_2WO_6 ceramics by the molten salt process is discussed in Appendix 22, however, attempts to pole this composition proved difficult. More recently, effort has shifted to $\text{PbBi}_2\text{Nb}_2\text{O}_9$ (Appendix 23) where a high degree of shape anisotropy was achieved. In this system, simple hot pressing was used to produce samples of excellent orientation factor with densities greater than 96% theoretical. Poling was quite effective in these samples using a special oxidation step to reduce conductivity, and piezoelectric properties slightly better than the poled single crystal were obtained.

8.3 Grain Oriented Tungsten Bronze Materials

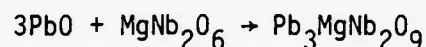
Initial work was carried out on PbNb_2O_6 again using liquid salt processing, tape casting to produce orientation, and final uniaxial or isostatic hot pressing to achieve densities up to 95% theoretical. Properties superior to randomly axed PbN samples were obtained. This work is discussed in Appendix 24.

8.4 Fabrication of $\text{PbMg}_{1/3}\text{Nb}_{2/3}\text{O}_3$

From a study of the kinetics of formation of the pyrochlore and perovskite modifications of $\text{PbMg}_{1/3}\text{Nb}_{2/3}\text{O}_3$ (PMN) during calcining from mixed oxides, it becomes evident that the pyrochlore forms early in the reaction sequence and is difficult to eradicate by later heat treatment. It appeared probable that early reaction of PbO with Nb_2O_5 forms the defect pyrochlore leaving some of the MgO unreacted. Pre-forming MgNb_2O_6 from the reaction

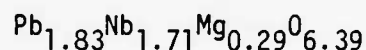


to tie in the magnesium, then reacting with PbO through



to give the perovskite form, proved a highly successful method to eliminate the pyrochlore phase (Appendix 25).

The pyrochlore phase was traced to have a defect composition



an anion deficient pyrochlore in space group $\text{Fd}\bar{3}\text{m}$ with lattice parameter $a = 10.599\text{\AA}$, a low dielectric constant of $\epsilon = 130$ with a weak relaxation maximum at a temperature near 20°K (Appendix 26).

9.0 RECENT STUDIES NEARING COMPLETION

Abstract of a number of topics which have been completed but are not yet fully written up have been included. These are mostly for papers to be presented at ISAF 83 and at EMF 5, so that written versions of these papers will be published shortly in the issues of Ferroelectrics covering these meetings.

The Papers are:

- Appendix 27 - "Electrostriction" by L.E. Cross.
- Appendix 28 - "Electrostriction and Its Relationship to Other Properties in Perovskite-Type Crystals" by K. Rittenmyer, A.S. Bhalla, Z.P. Chang and L.E. Cross.
- Appendix 29 - "Direct Measurement of Electrostriction in Perovskite Type Ferroelectrics" by M. Shishineh, C. Sundius, T. Shrout and L.E. Cross.
- Appendix 30 - "The Effects of Various B-Site Modifications on the Dielectric and Electrostrictive Properties of Lead Magnesium Niobate Ceramics" by D.J. Voss, S.L. Swartz and T.R. Shrout.
- Appendix 31 - "Perforated PZT Composites for Hydrophone Applications" by A. Safari, S. DaVanzo and R.E. Newnham.
- Appendix 32 - "Transversely Reinforced 1-3 Piezoelectric Composites" by M.J. Haun, T.R. Gururaja, W.A. Schulze and R.E. Newnham.
- Appendix 33 - "PZT-Polymer Composite Transducers for Ultrasonic Medical Applications" by T.R. Gururaga, W.A. Schulze, L.E. Cross, B.A. Auld, June Wang and Y.A. Shui.
- Appendix 34 - "Glass-Ceramics: New Materials for Hydrophone Applications" by A. Halliyal, A. Safari and A.S. Bhalla.
- Appendix 35 - "Pyroelectric Property of $\text{Pb}(\text{Sc}_{1/2}\text{Ta}_{1/2})\text{O}_3$ Ceramics Under DC Bias" by Chen Zhili, Yao Xi and L.E. Cross.

- Appendix 36 - "Electrical Poling and Depoling Studies on the Relaxor-Ferroelectric 8:65:35 PLZT" by Zhili Chen, Yao Xi and L.E. Cross.
- Appendix 37 - "Pyroelectric Properties of the Modified Triglycine Sulphate (TGS)" by A.S. Bhalla, C.S. Fang, L.E. Cross and Yao Xi.
- Appendix 38 - "Pyroelectric and Piezoelectric Properties of SbSI:Composites" by A.S. Bhalla and R.E. Newnham.
- Appendix 39 - "A New Family of Grain Oriented Glass-Ceramics for Piezoelectric and Pyroelectric Devices by A. Halliyal and A.S. Bhalla.
- Appendix 40 - "Low Temperature Pyroelectric Properties" by A.S. Bhalla and R.E. Newnham.
- Appendix 41 - "The Growth and Properties of a New Alanine and Phosphate Substituted Triglycine Sulphate (ATGSP) Crystal" by C.S. Fang, Yao Xi, Z.X. Chen, A.S. Bhalla and L.E. Cross.
- Appendix 42 - "Some Interesting Properties of Dislocation Free Single Crystals of Pure and Modified $\text{Sr}_{0.5}\text{Ba}_{0.5}\text{Nb}_2\text{O}_6$ " by S.T. Liu and A.S. Bhalla.
- Appendix 43 - "The Ferroic Phase Transition Behavior of $\text{Pb}(\text{Zr}_{0.6}\text{Ti}_{0.4})\text{O}_3$ " by A. Amin and L.E. Cross.
- Appendix 44 - "Dielectric and Piezoelectric Properties of Tungsten Bronze Lead Barium Niobate ($\text{Pb}_x\text{Ba}_{1-x}\text{Nb}_2\text{O}_6$) Single Crystals" by T.R. Shrout, H.C. Chen and L.E. Cross.
- Appendix 45 - "Relationship of Crystallographic Polarity to Piezoelectric, Pyroelectric and Chemical Etching Effects in Li_2GeO_3 and LiGaO_2 Single Crystals" by A.S. Bhalla, L.L. Tongson and R.E. Newnham.
- Appendix 46 - "Specific Heat of SbSI" by M.E. Rosar, W.A. Smith and A. Bhalla.
- Appendix 47 - "Magnetic-Field Dependence of the Soft-Mode Frequency in KTaO_3 at 20K" by W.N. Lawless, C.F. Clark and S.L. Swartz.

REFERENCES

- 1.1 A.D. Bruce and R.A. Cowley, J. Phys. C Solid State Phys. 6, 2422 (1973).
- 2.1 K. Uchino and L.E. Cross, Proc. 33rd Annual Frequency Control Symposium, Atlantic City, NJ, June, 1979, pp. 110-118.
- 2.2 K. Uchino and L.E. Cross, Ferroelectrics, 27, 35 (1980).
- 2.3 K. Rittenmyer and L.E. Cross, ONR Review, October 1982.
- 2.4 L. Bohaty and S. Haussühl, Acta Cryst. A33, 114-118 (1977).
- 2.5 B.J. Luymes, Ph.D. Thesis, Eindhoven University of Technology (1982).
- 2.6 J.S. Zheludev and A.A. Fatchenkov, Soviet Physics Crystallogr. 3, 312-318 (1958).
- 2.7 K. Uchino, S. Nomura, L.E. Cross, R.E. Newnham and S.J. Jang, J. Mat. Sci. 16, 569-578 (1981).
- 2.8 V.J. Minkiewicz and G. Shirane, J. Phys. Soc. Japan 26, 674 (1969).
- 2.9 K. Gesi, J.D. Axe and G. Shirane, Phys. Rev. B5, 1933 (1972).
- 2.10 P.A. Fleury, J.F. Scott and J.M. Warlock, Phys. Rev. Letters 21, 16 (1968).
- 2.11 B.N.N. Achar and G.R. Barsch, J. Phys. Chem. Solids (to be submitted).
(See abstract).
- 2.12 B.N.N. Achar, G.R. Barsch and L.E. Cross, Phys. Rev. B24, 1209 (1981).
- 2.13 B.N.N. Achar, G.R. Barsch and L.E. Cross, Ferroelectrics 37, 495 (1981).
- 2.14 A.D. Bruce and R.A. Cowley, J. Phys. C Solid State Phys. 6, 2422 (1973).
- 2.15 B.N.N. Achar and G.R. Barsch, Ferroelectrics (to be published) (See Abstract).
- 2.16 R.A. Toupin, J. Rat. Mech. Anal. 5, 849 (1956); Int. J. Engn. Sci. 1, 101 (1963).
- 2.17 G.R. Barsch, B.N.N. Achar and L.E. Cross, Phys. Rev. (to be published)
(See abstract).
- 2.18 G.R. Barsch, B.N.N. Achar and L.E. Cross Ferroelectrics 35, 187 (1981).

- 2.19 G.R. Barsch, B.N.N. Achar and L.E. Cross, Phys. Rev. B (to be published)
(See Abstract).
- 2.20 J.F. Nye, Physical Properties of Crystals (Clarendon Press, Oxford, 1957).
- 3.1 K. Rittenmyer, T. Shrout, W.A. Schulze and R.E. Newnham, Ferroelectrics 42,
189 (1982).
- 3.2 A. Safari, R.E. Newnham, L.E. Cross and W.A. Schulze, Ferroelectrics 42,
197 (1982).
- 3.3 A. Halliyal, A.S. Bhalla, R.E. Newnham and L.E. Cross, Ferroelctrics 28,
781 (1981).
- 3.4 A. Halliyal, A.S. Bhalla, R.E. Newnham, L.E. Cross and T. Gururaja, J.
Mat. Sci. 17(1):295 (1982).
- 4.1 N. Setter and L.E. Cross, J. Mat. Sci. 15, 2473 (1980).
- 4.2 N. Setter and L.E. Cross, J. Appl. Phys. 51, 4356 (1980).
- 4.3 B. Brezina, Private communication.
- 4.4 K.L. Bye and E.T. Keve, Ferroelectrics 4, 87 (1972).

APPENDIX 1

93. ELECTROSTRICTION IN FLUORIDE PEROVSKITES

Journal of Applied Physics (Submitted)

ELECTROSTRICTION IN FLUORIDE PEROVSKITES

K. Rittenmyer, Z.P. Chang, A.S. Bhalla and L.E. Cross

Abstract

Values of the hydrostatic electrostriction constant $Q_h = Q_{11} + 2Q_{12}$ have been measured for the perovskite structure fluorides KCaF_3 , KMnF_3 , KMgF_3 and KZnF_3 , by measuring the hydrostatic pressure dependence of the dielectric stiffness. The measured Q_h values range from 0.28 to 0.85 m^4/c^2 and, as expected from theory, are more than one order of magnitude larger than corresponding Q_h values in the oxide perovskites. Nonlinearity in the pressure dependence of the stiffness is too large to be explained by elastic nonlinearity and a sixth order electrostriction is invoked to explain the observed behavior.

APPENDIX 2

94. TEMPERATURE DEPENDENCE OF THE DIELECTRIC CONSTANT OF KMnF_3

Materials Research Bulletin (Submitted)

TEMPERATURE DEPENDENCE OF THE DIELECTRIC CONSTANT OF KMnF_3

K. Rittenmyer, A.S. Bhalla and L.E. Cross

Abstract

Dielectric measurements on single crystals of KMnF_3 show a clear dielectric maximum at the phase transition at 186°K. This phase change between $\text{Pm}3\text{m}$ and I4/mcm symmetry has been shown by Gesi¹ to be due to the condensation of a soft phonon mode at the R point of the Brillouin zone, and to be analogous to the 105°K transition in SrTiO_3 . In the absence of mechanical stress, the lower temperature state is twinned, however, the dielectric properties are reproducible upon cycling through the transition so that the twinning must be on a fine enough scale to effectively average out the tetragonal anisotropy.

¹K. Gesi, J.D. Axe, and G. Shirane, Phys. Rev., B5, 1933 (1972).

APPENDIX 3

95. THERMODYNAMIC DEFINITION OF HIGHER ORDER
ELASTIC, PIEZOELECTRIC AND DIELECTRIC COEFFICIENTS

Physical Review B (to be published)

THERMODYNAMIC DEFINITION OF HIGHER ORDER
ELASTIC, PIEZOELECTRIC AND DIELECTRIC COEFFICIENTS

G.R. Barsch, B.N.N. Achar and L.E. Cross

Abstract

The thermodynamic definition of the higher order elastic coefficients according to Brugger¹ is generalized to the nonlinear elastic dielectric. The electrostriction coefficients and the higher order elastic and dielectric coefficients are defined as derivatives of the pertinent thermodynamic potentials w.r.t. the proper electric and elastic field variables.

Two sets of material coefficients are introduced: one in terms of the deformation gradient and the dielectric polarization (or their conjugate variables: Piola-Kirchhoff stress tensor and electric field), and the second in terms of the Lagrangian strain tensor and the material measure of polarization² (or their conjugate variables: thermodynamic tension and material measure of field). Since the thermodynamic potentials of the first set are not automatically rotationally invariant, their associated material coefficients do not have the full tensor symmetry of those of the second set, which are derived from automatically rotationally invariant potentials. As a consequence, the number of independent material coefficients in the first set is higher than in the second.

General relations for converting the various material coefficients within each of the two sets and from one set to another are derived and explicitly given for O_h symmetry.

¹K. Brugger, Phys. Rev. 133, A1611 (1964).

²R.A. Toupin, J. Rat. Mech. Anal. 5, 849 (1956).

APPENDIX 4

96. PROPAGATION OF SMALL AMPLITUDE ELASTIC WAVES IN A
HOMOGENEOUSLY STRESSED AND POLARIZED DIELECTRIC MEDIUM

Journal of Applied Physics (to be published)

PROPAGATION OF SMALL AMPLITUDE ELASTIC WAVES IN A
HOMOGENEOUSLY STRESSED AND POLARIZED DIELECTRIC MEDIUM

G.R. Barsch, B.N.N. Achar and L.E. Cross

Abstract

Based on Toupin's theory of the nonlinear elastic dielectric¹, the electro-elastic constitutive relations and the equations of motion pertaining to the propagation of small-amplitude elastic waves in a non-polar nonlinear elastic dielectric medium subjected to a finite initial elastic deformation and dielectric polarization are derived. All magnetic effects, including retardation, are neglected. In addition, the difference between isothermal and isentropic quantities is ignored.

The equations so derived provide the basis for the experimental determination of the strain and field derivatives of the elastic and piezoelectric constants (including electrostriction constants) from ultrasonic velocity or mechanical resonance frequency measurements on homogeneously polarized and strained dielectric crystals. In addition, these equations are required to derive lattice theoretical expressions for the above quantities (see Abstract No. 5).

¹R.A. Toupin, Int. J. Engng. Sci. 1, 101 (1963).

APPENDIX 5

97. LATTICE THEORY OF THE NONPOLAR NONLINEAR ELASTIC
DIELECTRIC IN THE SHELL MODEL

Physical Review B (to be published)

LATTICE THEORY OF THE NONPOLAR NONLINEAR ELASTIC
DIELECTRIC IN THE SHELL MODEL

B.N.N. Achar and G.R. Barsch

Abstract

Expressions for the first order anharmonic coefficients in the effective constitutive relations of the nonpolar nonlinear elastic dielectric pertaining to a small deformation and electric field superimposed on a finite initial deformation and electric field have been derived for the static shell model by means of the method of long waves. They comprise the electrostriction, nonlinear dielectric, elasto-optic and electro-optic coefficients and the strain and electric-field derivatives of the piezoelectric and second order elastic constants and may easily be generalized for any anharmonic shell model in which both inter-ionic and intra-ionic anharmonicity is included.

APPENDIX 6

98. SHELL MODEL CALCULATION OF ELECTROSTRICTION
COEFFICIENTS OF ROCKSALT-TYPE ALKALI HALIDES

Physical Review B (to be published)

SHELL MODEL CALCULATION OF ELECTROSTRICTION
COEFFICIENTS OF ROCKSALT-TYPE ALKALI HALIDES

B.N.N. Achar and G.R. Barsch

Abstract

The electrostriction constants and the photoelastic constants of rocksalt-type alkali halides have been calculated for a variety of rigid ion models and shell models, with and without many-body interactions, and with and without intra-ionic anharmonicity included. For the electrostriction constants none of the models considered can account satisfactorily for the experimental data of Bohaty and Haussühl, especially for f_{12} and f_{44} . Moreover, in spite of the inclusion of intra-ionic anharmonicity the calculated electrostriction constants do not differ drastically from values calculated on the basis of a rigid-shell model with many-body forces included, although a perfect fit of the photo-elastic constants can be obtained in this case. One may therefore conclude (a) that inclusion of intra-ionic anharmonicity, while essential for the photoelastic constants, is only of minor importance for the electrostriction constants, (b) that the effect of many-body forces, while apparent in the second and third order elastic constants, is only small for the electrostriction constants, at least in alkali halides, and/or (c) that the experimental electrostriction data for the alkali halides could be seriously in error.

To substantiate conclusion (b), we have applied Keating's model of angle bending forces up to third order in the four anion-cation-anion angles of the rocksalt structure. The results indicate that as a result of the crystal symmetry these angle bending forces do not contribute to the anharmonic potential energy in the rocksalt structure. Thus the many-body forces present in the rocksalt structure must be of a more general nature. Furthermore, the role of thermal effects on the electrostriction constants in alkali halides is unknown.

APPENDIX 7

99. TEMPERATURE VARIATION OF ELECTROSTRICTION OF SrTiO_3

Ferroelectrics (to be published)

TEMPERATURE VARIATION OF ELECTROSTRICTION OF SrTiO_3

B.N.N. Achar and G.R. Barsch

Abstract

The hydrostatic electrostriction coefficient of SrTiO_3 has been calculated as a function of temperature on the basis of anharmonic many-body perturbation theory in the quasiharmonic approximation (QHA) of Bruce and Cowley¹. Although the anharmonic shell model employed properly includes Coulomb anharmonicity (and thus is an improvement over the model of these authors¹) it does not accurately reproduce the temperature dependence of the Γ_{15} and R_{25} phonon frequencies. Using, therefore, experimental temperature dependent phonon frequencies as input gives very good agreement with experiment for the R.T. value of the electrostriction coefficient, but not for its temperature derivative. This discrepancy seems to arise mostly from the limitations of the QHA, rather than those of the model employed.

¹A.D. Bruce and R.A. Cowley, J. Phys. C: Solid State Phys. 6, 2422 (1973).

APPENDIX 8

100. POLARIZATION AND DEPOLARIZATION BEHAVIOR OF HOT PRESSED
LEAD LANTHANUM ZIRCONATE TITANATE CERAMICS

Journal of Applied Physics (accepted)

POLARIZATION AND DEPOLARIZATION BEHAVIOR OF HOT PRESSED
LEAD LANTHANUM ZIRCONATE TITANATE CERAMICS

Yao Xi, Chen Zhili and L.E. Cross

Abstract

A detailed study of the polarization and depolarization behavior of 7:65:35 and 8:65:35 lead lanthanum zirconate titanate (PLZT) transparent ceramics under DC bias and constant heating rates has been carried out. The dielectric permittivity exhibits a new anomaly near 0°C in freshly thermally depoled samples which is associated with a build up of macrodomains and the development of a remanent polarization. From continuity of the dispersive behaviors it is suggested that the dielectric change at the so-called α - β transition T_d is not a conventional phase change, but rather is a loss of macro-ordering and a decay back to a disordered microdomain texture.

APPENDIX 9

101. NEW DEVELOPMENTS IN PIEZOELECTRIC AND ELECTROSTRICTIVE MATERIALS

Joint US:Japan Seminar on Electroceramics
Rappongi, June 1982

NEW DEVELOPMENTS IN PIEZOELECTRIC AND ELECTROSTRICTIVE MATERIALS

L.E. Cross

Abstract

Electrostriction is the basic electromechanical coupling in all centric crystals and in glasses, and is responsible for the 'morphic' piezoelectric parameters in all ferroelectric ceramics. Recent work to correct the definition of electrostriction, to improve the measurement of electrostriction in simple solids, to correlate electrostriction with other anharmonic properties of insulators and to develop an adequate theoretical model for electrostriction in the perovskites will be briefly reviewed.

Work on a thermodynamic Gibbs function to describe the $\text{PbZrO}_3\text{:PbTiO}_3$ solid solution system will be discussed, and new low temperature measurements of dielectric and piezoelectric parameters to 4.2°K presented.

Practical application of piezoelectrics and electrostrictive materials to high strain micro-positioners and multi-position mirrors will be described.

APPENDIX 10

102. PIEZOELECTRIC COMPOSITES

Joint US:Japan Seminar on Electroceramics
Rappongi, June 1982

PIEZOELECTRIC COMPOSITES

R.E. Newnham

Abstract

The concepts of Curie group symmetry, and interphase connectivity have been used to explore macrostructures of possible interest as piezoelectric composites. Based on these design considerations, polymer-ceramic composites have been fabricated with 3-3 phase connectivity by the replication of natural template structures such as coral, and by a simplified fabrication technique based on the mixing of volatilizable plastic spheres and PZT powder. Perforated 1-3 and 2-3 composites were made by drilling holes in solid PZT and back-filling with polymer. Alternatively, they can be made as extruded honeycomb structures. Polymer-ceramic composites with 1-3 phase connectivity were made by embedding PZT rods or PZT spheres in various polymers. A modified connectivity model with 1-3-0 phase connectivity was introduced to reduce the Poisson contraction problem found in 1-3 composites. In 1-3-0 composites, voids were introduced into the polymer matrix by a foaming process or by mixing in hollow glass microspheres. Lateral stiffening with glass fibers is another useful approach, resulting in 1-2-3 or 1-2-3-0 composites. Many of these composites are superior to single-phase piezoelectric for hydrophone applications. Compared to solid PZT, they have higher hydrostatic piezoelectric coefficients, lower permittivities, and lower densities which can sometimes be adjusted to neutral buoyancy in seawater.

More complex composites are required for high-frequency applications. A continuous poling technique has been developed to pole thin PZT fibers and ribbons. These are assembled to form multiply-poled piezoelectric transducers (MUPPETs) or d_{15} ultrasonic shear sensor (DOFUSS) devices with a wide variety of geometries and applications.

APPENDIX 11

103. THE DIELECTRIC PROPERTIES OF $\text{Pb}(\text{Sc}_{1/2}\text{Ta}_{1/2})\text{O}_3$ AND $\text{Pb}(\text{Sc}_{1/2}\text{Ta}_{1/4}\text{Nb}_{1/4})\text{O}_3$
CERAMICS UNDER DC BIAS

Journal of the American Ceramic Society (accepted)

THE DIELECTRIC PROPERTIES OF $\text{Pb}(\text{Sc}_{1/2}\text{Ta}_{1/2})\text{O}_3$ AND $\text{Pb}(\text{Sc}_{1/2}\text{Ta}_{1/4}\text{Nb}_{1/4})\text{O}_3$
CERAMICS UNDER DC BIAS

Chen Zhili, Yao Xi and L.E. Cross

Abstract

Earlier studies have shown that in lead scandium tantalate $\text{Pb}(\text{Sc}_{1/2}\text{Ta}_{1/2})\text{O}_3$ (PST) and in the solid solution lead scandium niobate tantalate at the composition $\text{Pb}(\text{Sc}_{1/2}\text{Ta}_{1/4}\text{Nb}_{1/4})\text{O}_3$ (PSNT) which form in the cubic perovskite structure, the degree of ordering of the different B site cations of the ABO_3 structure can be controlled thermally.

In this study the weak field dielectric permittivity has been explored as a function of DC bias fields up to 20 KV/cm over a temperature range of the order of 100°C about the dielectric permittivity maximum in both ordered and disordered samples of PST and PSNT. Distinction in properties between disordered and ordered cation structures are clearest in pure PST, but persist in the PSNT solid solution and are explained by the ordering of polar micro regions under bias in the disordered samples.

APPENDIX 12

104. REVERSIBLE PYROELECTRIC EFFECT IN $\text{Pb}(\text{Sc}_{1/2}\text{Ta}_{1/2})\text{O}_3$ CERAMICS UNDER DC BIAS

Ferroelectrics Letters 44, 271-276 (1983)

REVERSIBLE PYROELECTRIC EFFECT IN $\text{Pb}(\text{Sc}_{1/2}\text{Ta}_{1/2})\text{O}_3$ CERAMICS UNDER DC BIAS

Chen Zhili, Yao Xi and L.E. Cross

Abstract

It has been shown that quenched $\text{Pb}(\text{Sc}_{1/2}\text{Ta}_{1/2})\text{O}_3$ (PST) disordered ceramics and crystals show diffuse dispersive dielectric properties, while well annealed ordered materials exhibit normal sharp first order transition. The pyroelectric depolarization measurements taken using a Hewlett Packard Model 4140B picoammeter/DC Source under computer controlled heating cycle also have shown different behaviors between disordered and ordered materials.

In this work pyroelectric measurements by Chynoweth method under DC bias up to 1.8 KV/mm within a temperature range of 70°C around the temperature of maximum dielectric constant have been studied. A very significant enhancement of the pyroelectric signal under DC bias is observed in thermally quenched disordered samples. The largest enhancement of the signal appears at temperatures some degrees below the temperature of maximum dielectric constant.

The existence of microdomains in disordered materials is believed to be responsible for this new extrinsic component of reversible pyroelectricity.

The large reversible pyroelectric effect is a promising phenomenon for developing new pyroelectric devices.

APPENDIX 13

105. THE GROWTH AND PROPERTIES OF A NEW ALANINE AND PHOSPHATE
SUBSTITUTED TRIGLYCINE SULPHATE (ATGSP) CRYSTAL

Ferroelectrics (to be published)

THE GROWTH AND PROPERTIES OF A NEW ALANINE AND PHOSPHATE SUBSTITUTED
TRIGLYCINE SULPHATE (ATGSP) CRYSTAL

C.S. Fang*, Yao Xi**, Z.X. Chen† and L.E. Cross

Materials Research Laboratory, The Pennsylvania State University,
University Park, PA 16802

ABSTRACT

A modified alanine doped triglycine sulphate (ATGS) crystal has been grown with partial substitution of H_2SO_4 with H_3PO_4 . Growth of the ATGSP crystal from a unipolar ATGS seed in the temperature range 30-40°C gives a unipolar bulk crystal with lower permittivity ($\epsilon_r \sim 30$) and higher pyroelectric coefficient ($6.5 \cdot 10^{-4} \text{ C/K} \cdot \text{m}^2$) than pure TGS. In the doping range used, the higher pyroelectric coefficient is traced to a significantly larger spontaneous polarization P_s ($\sim 5 \text{ } \mu\text{C/cm}^2$ at room temperature). Tangent δ is below 0.01 over the whole frequency range from 100 Hz to 100 KHz.

APPENDIX 14

106. DOMAIN CONFIGURATION AND PIEZOELECTRIC BEHAVIOR
OF LITHIUM NIOBATE BICRYSTALS .

Ferroelectrics (submitted)

DOMAIN CONFIGURATION AND PIEZOELECTRIC BEHAVIOR OF LITHIUM NIOBATE BICRYSTALS

YAO XI^{*}, R.E. NEWNHAM and L.E. CROSS

Materials Research Laboratory, The Pennsylvania State University, University Park, PA 16802

Abstract—Domain configurations in lithium niobate bicrystals have been studied by chemical etching. The single domain status of linking-type bicrystals is completely preserved, while in encountering-type bicrystals, a complicated adjustment always takes place with domains shifting, domains splitting and the creation of new needle-like microdomains. The effects of the bicrystal boundary on the piezoelectric behavior is also described. The bicrystal boundary does not terminate the in-phase piezoelectric vibrations in linking type bicrystals, but it does isolate the out-of-phase vibrations in encountering type bicrystals.

APPENDIX 15

107. DIELECTRIC BEHAVIOR OF LITHIUM NIOBATE BICRYSTALS

Materials Research Bulletin (submitted)

DIELECTRIC BEHAVIOR OF LITHIUM NIOBATE BICRYSTALS

Yao Xi, R.E. Newnham, and L.E. Cross
Materials Research Laboratory
The Pennsylvania State University
University Park, PA 16802

ABSTRACT

The temperature and frequency dependence of dielectric properties of lithium niobate bicrystals are compared to those of the single crystal. A sharp increase of loss tangent of bicrystal at low frequency and high temperature dominated by electrical conduction has been observed, while the loss tangent spectra of the single crystal are featureless. Dielectric relaxation has been observed in twisted encountering bicrystals. The activation energies of electrical conduction and dielectric relaxation have been estimated.

APPENDIX 16

108. THERMALLY STIMULATED CURRENT IN LITHIUM NIOBATE BICRYSTALS

Journal of Applied Physics (submitted)

THERMALLY STIMULATED CURRENT IN LITHIUM NIOBATE BICRYSTALS

Yao Xi* and L.E. Cross
Materials Research Laboratory
The Pennsylvania State University
University Park, PA 16802

Abstract

Thermally stimulated current both perpendicular and parallel to the boundary surface of lithium niobate bicrystal have been measured. The TS currents are related to the trapped charge carriers at lattice defects in the boundary region of enocuntering type bicrystals. Three kinds of traps with single, double and a continuous distribution of depth have been observed. The trap depths are in the range of 0.9-1.1 eV. A potential barrier structure is discussed in terms of an atomistic model for the disturbed boundary region.

*Visiting scientist from Xian Jiaotong University, Xian, China.

APPENDIX 17

109. THE INFLUENCE OF PIEZOELECTRIC GRAIN RESONANCE ON
THE DIELECTRIC SPECTRA OF LiNbO_3 CERAMICS

Journal of the American Ceramic Society (accepted)

The Influence of Piezoelectric Grain Resonance on
the Dielectric Spectra of LiNbO_3 Ceramics

Yao Xi, H. McKinstry and L.E. Cross

Materials Research Laboratory
The Pennsylvania State University
University Park, PA 16802

Abstract

It has often been suggested that the higher frequency dispersion ($f \sim 10^7 \sim 10^8$ Hz) evident in the dielectric response of high permittivity ferroelectric ceramics might be associated with piezoelectrically driven resonant mechanical motion of individual grains. The hypothesis certainly appears reasonable, but so far no direct verification appears to have been attempted. Our discovery that the individual crystallite resonances are well preserved in poled LiNbO_3 bicrystals suggested that we explore the dispersion of LiNbO_3 ceramics. In both conventionally sintered and uniaxially hot pressed ceramics, the dielectric dispersion around 10^8 Hz has obvious resonant character. Using a modified ECAP computer program we are able to demonstrate that both the real and imaginary components of the impedance can be quantitatively described using the equivalent circuit models for the coupled individual grain resonances.

APPENDIX 18

110. FERROELECTRIC PROPERTIES OF TUNGSTEN BRONZE LEAD
BARIUM NIOBATE (PBN) SINGLE CRYSTALS

Ferroelectrics (accepted)

FERROELECTRIC PROPERTIES OF TUNGSTEN BRONZE LEAD BARIUM NIOBATE (PBN) SINGLE CRYSTALS

T.R. SHROUT and L.E. CROSS

Materials Research Laboratory, The Pennsylvania State University, University Park, PA 16802

D.A. HUKIN

Clarendon Laboratory, Oxford University, Oxford, England OX1 3PU

Abstract—A ferroelectric tungsten bronze single crystal of $\text{Pb}_{0.33}\text{Ba}_{0.70}\text{Nb}_2\text{O}_6$ was grown from a melt using the Czochralski technique. The crystal belongs to the tetragonal point group $4mm$ with the spontaneous polarization parallel to the 'c' axis. The room temperature lattice parameters were $a = 12.50 \text{ \AA}$ and $c = 3.995 \text{ \AA}$. The spontaneous polarization was found to be $0.40 \text{ C/m}^2\text{°C}$. The Curie transition was 350°C as determined from the temperature dependence of the dielectric constants. The pyroelectric properties were found to be typical of other tetragonal ferroelectric bronzes. Dielectric constant ϵ_{11} and piezoelectric constant d_{15} show a strong enhancement from the approach of the tetragonal:orthorhombic morphotropic phase boundary and it is clear that crystals with composition in the tetragonal phase field closer to this boundary will be of major interest for piezoelectric and electro-optic applications.

APPENDIX 19

111. LOW FIELD POLING OF SOFT PZTs

Ferroelectrics (submitted)

LOW FIELD POLING OF SOFT PZTs

T.R. Shrout, A. Safari and W.A. Schulze

Abstract

The inherent high electrical resistivity of donor doped or "soft" PZT's enables them to be poled using the field cooling method. The electric fields required for poling were reduced by a factor of five as compared to fields used in conventional poling. Dielectric and piezoelectric properties are reported.

APPENDIX 20

112. DIELECTRIC AND PIEZOELECTRIC PROPERTIES OF PURE
LEAD TITANATE ZIRCONATE CERAMICS FROM 4.2 TO 300°K

Journal of Phase Transitions (accepted)

Dielectric and Piezoelectric Properties of Pure
Lead Titanate Zirconate Ceramics from 4.2 to 300°K

X.L. Zhang, Z.X. Chen, L.E. Cross and W.A. Schulze

Materials Research Laboratory
The Pennsylvania State University
University Park, PA 16802, USA

Abstract: The dielectric and piezoelectric properties (D-P properties) of pure lead titanate zirconate piezoelectric ceramics (PZTs) with compositions close to the morphotropic phase boundary (MPB) have been measured from 4.2 to 300°K. The results are shown, as expected, that the dielectric and piezoelectric activity are sharply peaked at the composition of the MPB, and it is evident that both intrinsic single domain and extrinsic domain motion contribute to this enhancement which does not 'freeze out' altogether even at 4°K. The 50/50 composition has anomalous temperature responses of the D-P properties with a knee in the curve near 150°K, suggesting that the MPB may in fact be shifting position slightly towards PT richer composition at low temperature.

APPENDIX 21

113. DIELECTRIC AND PIEZOELECTRIC PROPERTIES OF MODIFIED
LEAD TITANATE ZIRCONATE CERAMICS FROM 4.2 TO 300°K

Journal of Materials Science (accepted)

AD-A132 136

TARGETED BASIC STUDIES OF FERROELECTRIC AND
FERROELASTIC MATERIALS FOR PI. (U) PENNSYLVANIA STATE
UNIV UNIVERSITY PARK MATERIALS RESEARCH LA.

2/4

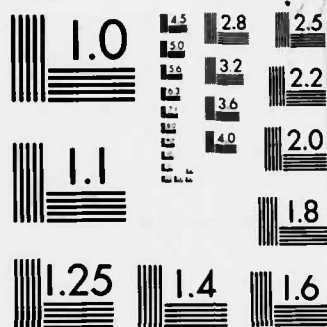
UNCLASSIFIED

L E CROSS ET AL. MAR 83 N00014-78-C-0291

F/G 9/1

NL





MICROCOPY RESOLUTION TEST CHART
NATIONAL BUREAU OF STANDARDS-1963-A

Dielectric and Piezoelectric Properties of
Modified Lead Titanate Zirconate Ceramics from 4.2 to 300°K

X.L. Zhang, Z.X. Chen, L.E. Cross and W.A. Schulze
Materials Research Laboratory
The Pennsylvania State University
University Park, PA 16802, USA

Abstract: The dielectric and piezoelectric properties (d-p properties) of four kinds of doped lead titanate zirconate piezoelectric ceramics (PZTs) have been measured from 4.2 to 300°K. The d-p properties of the materials converge with decreasing temperature down to liquid helium temperature, even though the properties have large differences at room temperature. The values of mechanical and electrical quality factors Q_e , Q_m and of the frequency constant N of the materials increased at low temperature. It is evident from the freeze out in K' and the associate temperature:frequency dependent maxima in $\tan \delta$ that the relaxation processes including ferroelectric domain wall motion and thermal defect motion contribute to the d-p properties. The Navy type-III composition has a minimum temperature coefficient of d-p parameters and it is evident that PZT ceramics modified with Fe_2O_3 can provide good stability and also give the strongest piezoelectric response at liquid helium temperature.

APPENDIX 22

114. FABRICATION OF GRAIN-ORIENTED Bi_2WO_6 CERAMICS

Journal of the American Ceramic Society (submitted)

FABRICATION OF GRAIN-ORIENTED Bi_2WO_6 CERAMICS

T. Kimura, M.H. Holmes and R.E. Newnham

Abstract

Grain-oriented Bi_2WO_6 ceramics were fabricated by normal sintering techniques. Platelike crystallites were initially synthesized by a fused salt process using an NaCl-KCl melt. When calcined at $<800^\circ\text{C}$, the Bi_2WO_6 crystallites are $325\text{ }\mu\text{m}$ in size and, at $>850^\circ\text{C}$, $\sim 100\text{ }\mu\text{m}$. After dissolving away the salt matrix, the Bi_2WO_6 particles were mixed with an organic binder and tapecast to align the platelike crystallites. Large particles were easily oriented by tapecasting but the sinterability of the tape was poor. Preferred orientation of small particles was increased by tapecasting and grain growth during sintering further improves the degree of orientation. Sintering above the 950°C phase transition, however, results in discontinuous grain growth and low densities. Optimum conditions for obtaining highly oriented ceramics with high density occur at sintering temperatures of 900°C using fine-grained powders which yield orientation factors of ~ 0.88 and densities of 94% theoretical.

APPENDIX 23

115. FABRICATION OF GRAIN ORIENTED $\text{PbBi}_2\text{Nb}_2\text{O}_9$ CERAMICS

Journal of the American Ceramic Society (submitted)

FABRICATION OF GRAIN ORIENTED $\text{PbBi}_2\text{Nb}_2\text{O}_9$ CERAMICS

Sheng-He Lin, S.L. Swartz, W.A. Schulze and J.V. Biggers

Abstract

This paper describes a process for the fabrication of grain oriented $\text{PbBi}_2\text{Nb}_2\text{O}_9$ ceramics. A molten salt technique was used to synthesize crystallites of $\text{PbBi}_2\text{Nb}_2\text{O}_9$ with a high degree of shape anisotropy. Tape casting and subsequent uniaxial hot pressing resulted in ceramics with grain orientation of greater than 90% with densities greater than 96% theoretical.

APPENDIX 24

116. GRAIN ORIENTED PIEZOELECTRIC CERAMICS AT PENN STATE

Joint US:Japan Seminar on Electroceramics
Rappongi, June 1982

GRAIN ORIENTED PIEZOELECTRIC CERAMICS AT PENN STATE

W.A. Schulze

Abstract

Ferroelectrics with high transition temperatures are typically those which have a large crystalline anisotropy and in some cases a symmetry limited number of polar axes. These materials have found little use for piezoelectric devices, due to the limited number of possible domain orientations in conventional polycrystalline ceramics, making them difficult to pole. An intensive effort is being made here at the Materials Research Laboratory of Penn State University to fabricate ferroelectric ceramics with a large degree of grain orientation. This technology might lead to applications for anisotropic ferroelectrics.

Two families of anisotropic ferroelectrics are presently being investigated: the bismuth oxide layer structures such as $\text{Bi}_4\text{Ti}_3\text{O}_{12}$ and $\text{PbBi}_2\text{Nb}_2\text{O}_9$, and the tungsten bronzes such as PbNb_2O_6 and $\text{Pb}_{1-x}\text{Ba}_x\text{Nb}_2\text{O}_6$. Our fabrication process utilizes the techniques of molten salt synthesis and tape casting and to develop grain orientations of greater than 95% and densities in the range of 80-95% theoretical.

APPENDIX 25

117. FABRICATION OF PEROVSKITE LEAD MAGNESIUM NIOBATE

Materials Research Bulletin, Vol. 17, pp. 1245-1250 (1982)

FABRICATION OF PEROVSKITE LEAD MAGNESIUM NIOBATE

S.L. Swartz and T.R. Shrout

Abstract

The perovskite relaxor ferroelectric lead magnesium niobate ($\text{PbMg}_{1/3}\text{Nb}_{2/3}\text{O}_3$) is an important material because of its high dielectric constant and correspondingly large electrostrictive strains. However, it is difficult to prepare a polycrystalline ceramic form because of the formation of a stable pyrochlore phase. The reaction kinetics during calcining were investigated and an improved fabrication scheme was developed.

APPENDIX 26

118. DIELECTRIC PROPERTIES OF PYROCHLORE LEAD MAGNESIUM NIOBATE

Materials Research Bulletin, Vol. 18 (1983)

DIELECTRIC PROPERTIES OF PYROCHLORE LEAD MAGNESIUM NIOBATE

T.R. Shrout and S.L. Swartz

Abstract

A pyrochlore with the composition $\text{Pb}_{1.83}\text{Nb}_{1.71}\text{Mg}_{0.29}\text{O}_{6.39}$ was fabricated and found to belong to the anion deficient structural family of pyrochlores having space group $\text{Fd}\bar{3}\text{m}$ with a lattice parameter $a = 10.5988\text{\AA}$. A room temperature dielectric constant of 130 with an anomalous peak near 20 K due to a relaxation phenomenon were as observed.

APPENDIX 27

119. ELECTROSTRICTION

Electrostriction

L.E. Cross

Materials Research Laboratory
The Pennsylvania State University
University Park, PA 16802

Electrostriction is the basic electromechanical coupling in all centric crystals and glasses, and the origin of the strong piezoelectric effects in all poled ferroelectric perovskite ceramics, yet reliable values of electrostriction constants are only available for a few crystals, the true temperature dependence of the constants is largely unknown, and a convincing atomistic theory for their origin has not been given.

This talk will focus upon electrostriction in oxygen octahedron type crystals where strain levels of practical interest can be achieved at realizable fields. The special features of behavior in a wide range of relaxor ferroelectric systems will be compared and contrasted with the response in simple ordered structures.

The separation of intrinsic, polarization biased electrostriction and extrinsic domain related phenomena will be considered in the piezoelectric effects in PZT, PLZT and other perovskites of complex composition.

Higher order electrostriction will be briefly touched upon and its possible effects upon elastic behavior considered.

APPENDIX 28

120. ELECTROSTRICTION AND ITS RELATIONSHIP TO OTHER
PROPERTIES IN PEROVSKITE-TYPE CRYSTALS

Electrostriction and Its Relationship to Other Properties in Perovskite-Type Crystals

K. Rittenmyer, A.S. Bhalla, Z.P. Chang and L.E. Cross

Materials Research Laboratory
The Pennsylvania State University
University Park, PA 16802

Electrostriction is the basic electromechanical coupling effect present in all solids. The direct quadratic electrostrictive effect represented in tensor notation by the coefficient, Q_{ijkl} , relates the strain induced in a solid, (ϵ_{ij}) , to the square of the polarization, $(P_k P_l)$, in the equation,

$$\epsilon_{ij} = Q_{ijkl} P_k P_l \quad (1)$$

Sixth and higher order terms can be added to this equation if the strain versus polarization-squared relationship is not linear. Alternatively, the electrostriction coefficients can be obtained through the converse electrostrictive effect,

$$\Delta\chi_{ij} = 2Q_{ijkl}\sigma_{kl} \quad (2)$$

by measuring the change in inverse dielectric susceptibility, $\Delta\chi_{ij}$, produced by the application of a stress, σ_{kl} . Again, higher order terms can be added phenomenologically to account for nonlinear behavior. A sixth-order term is adequate for our case. The complete converse effect can then be written as

$$\Delta\chi_{ij} = 2Q_{ijkl}\sigma_{kl} + 2\phi_{ijklmn}\sigma_{kl}\sigma_{mn} \quad (3)$$

where ϕ_{ijklmn} is a sixth order electrostriction constant. We have performed experiments of this type on several fluoride perovskite single crystals (e.g., KMgF_3 , KMnF_3 , KZnF_3 , KCaF_3 , etc.) and have evaluated both fourth and sixth order electrostriction coefficients.

The dielectric constant, which is inversely proportional to the inverse dielectric susceptibility, is related to the amplitude and frequency of optical phonons at long wavelengths. The pressure as well as temperature dependence of this vibrational mode gives information on the anharmonicity present in the crystals lattice. It is therefore possible, as shown by Uchino¹, to relate these effects to each other and other similar anharmonic effects such as thermal expansion and higher order elastic constants, and to other properties such as compressibility and dielectric constant. These observations are discussed with respect to our measurements on the fluoride perovskites.

¹K. Uchino, L.E. Cross, Jpn. J. Appl. Phys.

APPENDIX 29

121. DIRECT MEASUREMENT OF ELECTROSTRICTION
IN PEROVSKITE TYPE FERROELECTRICS

Direct Measurement of Electrostriction
in Perovskite Type Ferroelectrics

M. Shishineh, C. Sundius, T. Shrout and L.E. Cross

Materials Research Laboratory
The Pennsylvania State University
University Park, PA 16802

A simplified AC capacitance dilatometer based on the design of Uchino and Cross⁽¹⁾ has been constructed to measure directly the temperature dependence of electrostrictive strain in perovskite type ferroelectric crystals and ceramics. A mechanical bridge circuit is used to compensate for thermal expansion of the mechanical components eliminating the need for DC servo stabilization. The instrument has been used in the temperature range from 20°C to 200°C. In the AC method, the electrostrictive strain under AC driving field is compared to the known strain induced in a quartz reference crystal under phase locked conditions. The method has been checked with the known piezoelectric behavior of quartz and of selected PZT disk samples. Measurements of Q constants will be reported for lead magnesium niobate (PMN), lead magnesium niobate:lead titanate solid solutions (PMN:PT), lead iron niobate:lead iron tungstate (PFN:PFW) and related relaxor ferroelectrics. Temperature dependence of the electrostrictive Q constants in single crystals BaTiO_3 in the paraelectric phase above T_c will be reported and the results discussed and compared to earlier studies^(2,3).

1. K. Uchino, L.E. Cross, *Ferroelectrics* 27, 35 (1980).
2. H. Beige, G. Schmidt, *Exp. Technix. der Phys.* 22, 393 (1974).
3. E. Huibregtse, W.H. Bessey and M.E. Drougard, *J. Appl. Phys.* 30, 899 (1959).

APPENDIX 30

122. THE EFFECTS OF VARIOUS B-SITE MODIFICATIONS ON THE DIELECTRIC
AND ELECTROSTRICTIVE PROPERTIES OF LEAD MAGNESIUM NIOBATE CERAMICS

The Effects of Various B-site Modifications on the Dielectric and Electrostrictive Properties of Lead Magnesium Niobate Ceramics

D.J. Voss, S.L. Swartz and T.R. Shrout

Materials Research Laboratory
The Pennsylvania State University
University Park, PA 16802

Abstract

The perovskite relaxor ferroelectric lead magnesium niobate ($\text{PbMg}_{1/3}\text{Nb}_{2/3}\text{O}_3$, hereafter designated PMN) was first synthesized in the late 1950's and has since been widely investigated for both dielectric and electrostrictive strain applications. The dielectric properties of PMN are characterized by a broad, frequency dependent maximum of the dielectric constant just below room temperature. The magnitude of this maximum (at 1 KHz, $\sim 15,000$ for ceramic PMN) decreases and the temperature of this maximum increases with increasing frequency. Due to the large dielectric constant of PMN, electrostrictive strains are comparable to the piezoelectric strains of PZT ceramics¹.

Recent publications, out of this laboratory, have described an improved fabrication technique for ceramic PMN², and demonstrated that the dielectric properties of PMN are quite dependent on fabrication parameters (stoichiometry, sintering temperature, etc.)³. The purpose of this investigation is to study the effects of various B-site substitutions (Ni^{2+} , Co^{2+} , Zn^{2+} , Cd^{2+} , Fe^{3+} , Ti^{4+} , Ta^{5+} , W^{6+} , etc.) and fabrication parameters on the dielectric and electrostrictive properties of PMN. The effects of substitutional cation size and valence on the maximum dielectric constant, transition temperature range, and diffuseness of transition will be determined and correlated with electrostrictive measurements.

1. S. Nomura and K. Uchino, *Ferroelectrics* **41**, 117-132 (1982).

2. S.L. Swartz and T.R. Shrout, *Mat. Res. Bull.* **17**, 1245-1250 (1982)

3. S.L. Swartz, T.R. Shrout, W.A. Schulze and L.E. Cross, submitted for publication.

APPENDIX 31

123. PERFORATED PZT COMPOSITES FOR HYDROPHONE APPLICATIONS

PERFORATED PZT COMPOSITES FOR HYDROPHONE APPLICATIONS

A. Safari, S. DaVanzo and R.E. Newnham
 Materials Research Laboratory
 The Pennsylvania State University
 University Park, PA 16802

Macroscopy and interphase connectivity have been used to explore the possible macrostructures of interest for piezoelectric composites. Based on these design considerations, PZT-polymer composites with 3-1 and 3-2 connectivity patterns have been fabricated. These composites were prepared by drilling circular and square holes perpendicular to the poling direction in prepoled PZT blocks and filling the holes with epoxy. The influence of hole size, separation between the holes and thickness on the piezoelectric properties of the composites was studied. An enhancement in the piezoelectric \bar{d}_h coefficient was observed due to the decoupling of the piezoelectric \bar{d}_{33} and \bar{d}_{31} coefficients in the composites. The dielectric constant of PZT is lowered considerably because of the polymer phase. The combination of high \bar{d}_h and low dielectric constant results in greatly enhanced \bar{g}_h . For hydrophone applications, these composites give good acoustic matching with water because of their low density.

A theoretical analysis was made to calculate internal stress distribution and local polarization in order to understand the enhancement of \bar{d}_h and \bar{g}_h . The finite element method (FEM) was used to calculate the internal stress distribution inside the composites under hydrostatic loading. The local and remanant polarization and piezoelectric matrix were calculated. From these data the macroscopic piezoelectric coefficients \bar{d}_h and \bar{g}_h of the composites were calculated.

APPENDIX 32

124. TRANSVERSELY REINFORCED 1-3 PIEZOELECTRIC COMPOSITES

Transversely Reinforced 1-3 Piezoelectric Composites

M.J. Haun, T.R. Gururaja, W.A. Schulze and R.E. Newnham

Materials Research Laboratory
The Pennsylvania State University
University Park, PA 16802

Piezoelectric PZT-polymer 1-3 composites were transversely reinforced to increase the hydrostatic piezoelectric coefficients for possible use in hydrophone applications. These composites were made of a polymer matrix with PZT rods aligned in the poling direction (x_3) and reinforcement in the transverse directions. The reinforcement consisted of aligned glass fibers and/or a rigid encapsulation. Both types of reinforcement act to greatly decrease the piezoelectric \bar{d}_{31} coefficient by carrying most of the lateral stresses. The \bar{d}_{33} coefficient is relatively unaffected, because PZT rods carry most of the stress in the poling direction. This decoupling of the \bar{d}_{31} and \bar{d}_{33} coefficients enhances the hydrostatic piezoelectric \bar{d}_h coefficient. The effect of the glass fibers is dependent on the polymer matrix used. Because of the stiffness of many epoxies, no significant increase in \bar{d}_h results, but more compliant polyurethanes are significantly reinforced giving improved \bar{d}_h coefficients. Due to the differences in poisson's ratios and compliances of PZT and the polymer matrix, adverse internal stresses develop which can contribute to the \bar{d}_{31} coefficient. To lower the \bar{d}_{31} coefficient the polyurethane is foamed, in addition to adding glass fibers, which lowers the poisson's ratio, and reduces the internal stresses. Greater hydrostatic sensitivity is achieved by foaming polyurethane, but only at low pressures. At higher pressures the pores begin to collapse and the polymer stiffens, lowering the sensitivity of the composite. This pressure dependence can be greatly reduced by encapsulating the composite in epoxy. The epoxy encapsulation also prevents penetration of the liquid medium into the porous composite, as well as providing additional transverse reinforcement. Due to the small percentage of PZT used, these composites have densities near that of water, and much lower dielectric constants than solid PZT, resulting in large increases in the piezoelectric \bar{g}_h coefficient. By increasing \bar{d}_h and \bar{g}_h , the $\bar{d}_h \bar{g}_h$ product used as the figure of merit, is greatly enhanced.

APPENDIX 33

125. PZT-POLYMER COMPOSITE TRANSDUCERS FOR ULTRASONIC MEDICAL APPLICATIONS

PZT-Polymer Composite Transducers for Ultrasonic Medical Applications

T.R. Gururaja, W.A. Schulze and L.E. Cross
Materials Research Laboratory
The Pennsylvania State University
University Park, PA 16802, USA

B.A. Auld, June Wang and Y.A. Shui
Edward L. Ginston Laboratory
W.W. Hansen Laboratories of Physics
Stanford University
Stanford, CA 94305, USA

ABSTRACT

Composites of piezoelectric ceramic (lead zirconate titanate) rods aligned in an epoxy resin matrix have been evaluated for ultrasonic medical diagnostic application. The two main advantages of the composite materials over single phase lead zirconate titanate ceramics are: 1) acoustic impedance can be tailored to minimize reflection losses at the transducer-load interface; 2) composites have lower mechanical Q and lead to better pulse reproduction.

High frequency dynamic behavior of the composite materials in resonant configurations are very complex. The complex resonant modes are characterized by the following techniques: 1) IEEE standards for piezoelectric measurements; 2) complex admittance plots as a function of frequency for electroded samples in ambients of air and water; 3) laser probe dilatometry of the dynamic displacement as a function of frequency and of position in the composite lattice. A model for elastic wave propagation in a spatially periodic medium has been developed to predict the vibrational modes of the composites. Some predictions of the theory have been found in accord with experimental results.

The transducer performance of the composite was evaluated by the pulse echo response of air back composite transducers in the frequency range for 100 kHz to 3 MHz by the tone-burst pulse-echo technique. Transmitting and receiving voltage response of the composite was also measured separately for a better understanding of performance. Characteristic acoustic impedance of the composite materials is shown to be a function of probing frequency and composite design.

APPENDIX 34

126. GLASS-CERAMICS: NEW MATERIALS FOR HYDROPHONE APPLICATIONS

Glass-Ceramics: New Materials for Hydrophone Applications

A. Halliyal, A. Safari and A.S. Bhalla

Materials Research Laboratory
The Pennsylvania State University
University Park, PA 16802

Single crystals of fresnoite ($\text{Ba}_2\text{TiSi}_2\text{O}_8$) and its germanium analogue ($\text{Ba}_2\text{TiGe}_2\text{O}_8$) have been reported to have interesting piezoelectric properties. Glass-ceramics of these materials with oriented crystallites have been prepared for hydrophone applications. Samples were prepared by recrystallizing the glasses in a strong temperature gradient. Various modified compositions in the above system were tried to optimize the physical properties. These glass-ceramics showed high piezoelectric voltage coefficient g_h ($100\text{--}120 \times 10^{-3} \text{ Vm/N}$), low dielectric constant (10-15) and densities less than 4000 kg/m^3 . There was no variation of g_h with pressure up to 10 MPa for all the compositions. The g_h coefficients and the product $d_h g_h$ of these glass-ceramics were comparable to PVF_2 and much higher than solid PZT.

APPENDIX 35

127. PYROELECTRIC PROPERTY OF $\text{Pb}(\text{Sc}_{1/2}\text{Ta}_{1/2})\text{O}_3$ CERAMICS UNDER DC BIAS

Pyroelectric Property of $\text{Pb}(\text{Sc}_{1/2}\text{Ta}_{1/2})\text{O}_3$ Ceramics Under DC Bias

Chen Zhili, Yao Xi and L.E. Cross

Materials Research Laboratory
The Pennsylvania State University
University Park, PA 16802

It has been shown that quenched $\text{Pb}(\text{Sc}_{1/2}\text{Ta}_{1/2})\text{O}_3$ (PST) disordered ceramics and crystals show diffuse dispersive dielectric properties, while well annealed ordered materials exhibit normal sharp first order ferroelectric transitions.

In this work, pyroelectric measurements by Byer-Roundy technique under DC biases up to 6 KV/cm within a temperature range from -80°C to 60°C have been studied. The results show that for both disordered and ordered materials, DC biases shift the peak of the pyroelectric coefficient towards higher temperature. However, for disordered samples the temperature shifts under DC bias are much larger than that for ordered ones. DC biases also sharpen the peak of the pyroelectric coefficient curve of the disordered samples. Clearly the depolarization curve shows a more abrupt phase transition behavior under DC biases.

Delay by the ordering electric field of the break-up of macro-domains into polar micro-regions under thermal motion is believed to be responsible for the extensive shifting and steepening observed in the depoling process under DC bias for the disordered samples.

Measurements by Chynoweth method under DC bias have confirmed that order-disorder of the polar micro-regions in them diffuse transition compositions is partly reversible and contributes a new extrinsic component to the pyroelectric response.

APPENDIX 36

128. ELECTRICAL POLING AND DEPOLING STUDIES ON
THE RELAXOR-FERROELECTRIC 8:65:35 PLZT

Electrical Poling and Depoling Studies on
the Relaxor-Ferroelectric 8:65:35 PLZT

Zhili Chen, Yao Xi and L.E. Cross

Materials Research Laboratory
The Pennsylvania State University
University Park, PA 16802

ABSTRACT

Detailed poling and depoling studies of 8:65:35 PLZT transparent ceramics reveal a new dielectric anomaly, which occurs in the weak field permittivity on heating a freshly thermally depoled sample to which a low (less than 8 kv/cm) DC bias has been applied at low temperature. On heating through the anomaly region under weak bias, the dispersive character of the dielectric response is lost. Examination of the pyroelectric current under constant heating reveals that the anomaly in ϵ is associated with the build up of a remanent electric polarization. This build up is a slow process and the kinetics have been explored both as a function of bias field and heating rate. Depoling occurs on further heating at a temperature well below the dielectric maximum in weak field permittivity which is itself weakly frequency dependent as in other relaxor ferroelectrics.

The dielectric data is interpreted on the basis of the build up under field, and the decay with increasing temperature of macro polar domains built up from reorientable polar micro regions.

APPENDIX 37

129. PYROELECTRIC PROPERTIES OF THE MODIFIED TRIGLYCINE SULPHATE (TGS)

Pyroelectric Properties of the Modified Triglycine Sulphate (TGS)

A.S. Bhalla, C.S. Fang, L.E. Cross and Yao Xi
Materials Research Laboratory
The Pennsylvania State University
University Park, PA 16802

ABSTRACT

TGS in its pure single crystal form has one of the highest pyroelectric figure of merit $p/K \approx 1 \times 10^{-5} \text{ cm}^{-2} \text{ K}^{-1}$. In recent years several modified TGS compositions have been prepared and the pyroelectric properties are measured. So far, a maximum enhancement of the figure of merit ($\sim 1.5 \times \text{TGS}$) has been reported in the case of DTGFB.

In our present studies we have examined various doping substitutions in the TGS compositions and measured the pyroelectric, dielectric and the related properties. Higher pyroelectric coefficients and an enhancement of the pyroelectric figures of merit ($> 2 \times \text{TGS}$) have been observed in some of the modified TGS compositions.

Results of the pyroelectric measurements on these compositions will be discussed in this paper.

APPENDIX 38

130. PYROELECTRIC AND PIEZOELECTRIC PROPERTIES OF SbSI:COMPOSITES

Pyroelectric and Piezoelectric Properties of SbSI:Composites

A.S. Bhalla and R.E. Newnham
Materials Research Laboratory
The Pennsylvania State University
University Park, PA 16802

ABSTRACT

Antimony sulphur iodide (SbSI), in the ferroelectric phase below 20°C belongs to the orthorhombic point group symmetry $mm2$ and has very large pyroelectric coefficient, piezoelectric strain coefficients (d_{33}) and dielectric constant along the polar c-axis.

Composites of SbSI:polymer in (1:3) and (3:3) and SbSI:glass fibers in 3:1 connectivity modes have been prepared and electrical properties are measured. Pyroelectric and piezoelectric voltage sensitivities have substantially increased compared to those of pure SbSI single crystals.

Effects of doping in SbSI and the pyroelectric properties of the off c-axis cut composites will also be discussed.

APPENDIX 39

131. A NEW FAMILY OF GRAIN ORIENTED GLASS-CERAMICS
FOR PIEZOELECTRIC AND PYROELECTRIC DEVICES

A New Family of Grain Oriented Glass-Ceramics
for Piezoelectric and Pyroelectric Devices

A. Halliyal and A.S. Bhalla

Materials Research Laboratory
The Pennsylvania State University
University Park, PA 16802

ABSTRACT

Grain oriented polar glass-ceramics have been evaluated for application in piezoelectric and pyroelectric devices. The main advantage of the method is the possibility of preparing large area elements in a simple way at a relative low cost.

Samples for the present study were prepared by recrystallizing the glasses in a strong temperature gradient or in a uniform isothermal temperature environment. Samples crystallized in a temperature gradient had better crystallographic orientation and also showed better properties than the isothermally crystallized samples. The compositions of glasses selected for the present study were from the systems $\text{Li}_2\text{O-SiO}_2\text{-B}_2\text{O}_3$, $\text{BaO-TiO}_2\text{-SiO}_2$ and $\text{BaO-TiO}_2\text{-GeO}_2$. The crystalline phases identified in the glass-ceramics after recrystallization were $\text{Li}_2\text{Si}_2\text{O}_5$, $\text{Li}_2\text{B}_4\text{O}_7$, $\text{Ba}_2\text{TiSi}_2\text{O}_8$ or $\text{Ba}_2\text{TiGe}_2\text{O}_8$.

Pyroelectric coefficients and electromechanical properties of above glass-ceramics were measured over the temperature range -20 to 200°C . Many compositions showed a high pyroelectric figure of merit (p/k), because of low dielectric constants of these glass-ceramics. Fresnoite ($\text{Ba}_2\text{TiSi}_2\text{O}_8$) glass-ceramics showed high values of piezoelectric voltage coefficient g_h , comparable to the hydrostatic properties of PVF_2 . Both the piezoelectric and pyroelectric properties of glass-ceramics were comparable in magnitude to the single crystal values of corresponding crystalline phases.

APPENDIX 40

132. LOW TEMPERATURE PYROELECTRIC PROPERTIES

Low Temperature Pyroelectric Properties

by

A.S. Bhalla and R.E. Newnham

Materials Research Laboratory
The Pennsylvania State University
University Park, PA 16802

In the past, the major interest has been in the room temperature operating pyroelectric materials and relatively few pyroelectric measurements have been made at low temperatures. The low temperature pyroelectrics could be more efficient IR detectors as (i) ferroelectrics with low curie temperatures tend to show near second order behavior with large pyroelectric coefficients over wide temperature range. (ii) At low temperatures the secondary pyroelectric contribution which is often large and opposite in sign to the primary effect at room temperature, decreases rapidly and there can be unexpectedly large pyroelectric coefficients. (iii) Specific heat and electrical losses decrease at low temperature. (iv) Signal to noise ratio increases as temperature decreases. All these factors generally raise the figure of merit of the pyroelectric devices. In this paper we report the low temperature measurements of the pyroelectric and dielectric properties of several ferroelectric and non-ferroelectric materials and discuss the suitability of the pyroelectric material for device operation in the ambient conditions in the outer space.

APPENDIX 41

133. THE GROWTH AND PROPERTIES OF A NEW ALANINE AND PHOSPHATE
SUBSTITUTED TRIGLYCINE SULPHATE (ATGSP) CRYSTAL

THE GROWTH AND PROPERTIES OF A NEW ALANINE AND PHOSPHATE SUBSTITUTED
TRIGLYCINE SULPHATE (ATGSP) CRYSTAL

C.S. Fang, Yao Xi, Z.X. Chen, A.S. Bhalla and L.E. Cross

Materials Research Laboratory, The Pennsylvania State University,
University Park, PA 16802

ABSTRACT

A modified alanine doped triglycine sulphate (ATGS) crystal has been grown with partial substitution of H_2SO_4 with H_3PO_4 . Growth of the ATGSP crystal from a unipolar ATGS seed in the temperature range 30-40°C gives a unipolar bulk crystal with lower permittivity ($\epsilon_r \sim 30$) and higher pyroelectric coefficient ($6.5 \cdot 10^{-4} \text{ C/k.m}^2$) than pure TGS. In the doping range used, the higher pyroelectric coefficient is traced to a significantly larger spontaneous polarization P_s ($\sim 5 \text{ } \mu\text{C/cm}^2$ at room temperature). Tangent δ is below 0.01 over the whole frequency range from 100 Hz to 100 KHz.

APPENDIX 42

134. SOME INTERESTING PROPERTIES OF DISLOCATION FREE SINGLE CRYSTALS
OF PURE AND MODIFIED $\text{Sr}_{0.5}\text{Ba}_{0.5}\text{Nb}_2\text{O}_6$

Some Interesting Properties of Dislocation Free Single Crystals
of Pure and Modified $\text{Sr}_{0.5}\text{Ba}_{0.5}\text{Nb}_2\text{O}_6$

by

S.T. Liu¹ and A.S. Bhalla²

¹Honeywell Corporate Technology Center,
Bloomington, MN 55420

²Materials Research Laboratory
The Pennsylvania State University
University Park, PA 16802

High quality dislocation free single crystals of $\text{Sr}_{0.5}\text{Ba}_{0.5}\text{Nb}_2\text{O}_6$ (SBN) and rare earths doped SBN are grown for infrared pyroelectric detector and electro-optic applications. Pyroelectric and dielectric properties on these crystals are measured over a temperature range from liquid nitrogen to 150°C. The dislocation free crystals have higher pyroelectric coefficients and retain the total pyroelectricity in successive heating cycles through the phase transition. Electro-optic measurements are also made on these crystals. Both pyroelectric and electro-optic coefficients increase with an increase in rare earth doping concentration in SBN crystals. Pyroelectric coefficients lie in the range from 400 to 2500 $\mu\text{C}/\text{m}^2\text{K}$ and linear electro-optic r_{33} coefficients increase from 2.3 to 7×10^{-10} cm/V. The relationship between pyroelectric and electro-optic coefficient (r_{33}) is examined and discussed.

APPENDIX 43

135. THE FERROIC PHASE TRANSITION BEHAVIOR OF $\text{Pb}(\text{Zr}_{0.6}\text{Ti}_{0.4})\text{O}_3$

The Ferroic Phase Transition Behavior of $\text{Pb}(\text{Zr}_{0.6}\text{Ti}_{0.4})\text{O}_3$

A. Amin

Advanced Development Lab.
Texas Instruments, Inc.
Attleboro, MA 02703

and

L.E. Cross

Materials Research Laboratory
The Pennsylvania State University
University Park, PA 16802

Recent low temperature neutron diffraction and diffuse neutron scattering experiments on $\text{Pb}(\text{Zr}_{0.6}\text{Ti}_{0.4})\text{O}_3$ [1] revealed some interesting and unusual features: (i) the rhombohedral (R3c) rhombohedral (R3m) phase transition is rather broad, and the transition temperature is not well defined (somewhere between 250 and 300 K) as determined from the temperature dependence of the strongest pseudocubic 311 reflection.

(ii) The diffuse neutron scattering data show some structure in the Q range $0.9 - 3.0 \text{ \AA}^{-1}$ ($Q = \frac{4\pi \sin \theta}{\lambda}$). This type of background modulation most likely arises from static displacements in preferred directions since random displacements would simply lead to a monotonically increasing background, as is characteristic of thermal diffuse scattering. These may reflect a short range order which is a precursor of the tetragonal phase or perhaps a tendency towards ordering of Zr and Ti atoms.

The Landau-Ginzburg-Devonshire phenomenological theory for simple proper ferroelectrics has been successfully applied to the PbZrO_3 - PbTiO_3 (PZT) solid solution system. The theory correctly predicts the relative stability points of the different phases in the solid state portion of PZT phase diagram. It also permits the calculation of the observed physical properties (e.g., dielectric, piezoelectric, and other coupling coefficients) as function of temperature, pressure, and applied electric fields over the entire range of single cell compositions.

We have calculated the temperature dependence of the free energy function G for the rhombohedral (R3m), tetragonal (P4mm) and orthorhombic Bmm2) modification of the prototypic (Pm3m) symmetry of $(\text{Pb}_{0.6}\text{Ti}_{0.4})\text{O}_3$ using the PbZrO_3 - PbTiO_3 phenomenological theory. In this work we will present our results and correlate the neutron scattering results and those obtained from phenomenological theory.

1. A. Amin, R.E. Newnham, L.E. Cross and D.E. Cox, J. Solid State Chemistry 37, 248 (1981).

APPENDIX 44

136. DIELECTRIC AND PIEZOELECTRIC PROPERTIES OF TUNGSTEN BRONZE
LEAD BARIUM NIOBATE ($\text{Pb}_x\text{Ba}_{1-x}\text{Nb}_2\text{O}_6$) SINGLE CRYSTALS

Dielectric and Piezoelectric Properties of Tungsten Bronze
Lead Barium Niobate ($\text{Pb}_x\text{Ba}_{1-x}\text{Nb}_2\text{O}_6$) Single Crystals

Thomas R. Shrout, Huan Chu Chen and L.E. Cross
Materials Research Laboratory
The Pennsylvania State University
University Park, PA 16802, USA

ABSTRACT

Ferroelectric tungsten bronze crystals of $\text{Pb}_x\text{Ba}_{1-x}\text{Nb}_2\text{O}_6$ ($0.8 \geq x \geq 0.25$) were grown from a melt using the Czochralski technique. Crystals with compositions $x \leq 0.6$ belonged to the tetragonal point group $4mm$ with the spontaneous polarization parallel to the "c" axis. Crystals with compositions $x \geq 0.6$ belonged to the orthorhombic point group $mm2$ with the spontaneous polarization along the $\langle 110 \rangle$ axes of the paraelectric prototypic point group having symmetry $4/mmm$. The dielectric and piezoelectric constants, particularly ϵ_{11} and d_{15} , showed a strong enhancement from the approach of the tetragonal:orthorhombic morphotropic phase boundary and thus are of major interest for piezoelectric and electro-optic applications.

APPENDIX 45

137. RELATIONSHIP OF CRYSTALLOGRAPHIC POLARITY TO PIEZOELECTRIC,
PYROELECTRIC AND CHEMICAL ETCHING EFFECTS IN
 Li_2GeO_3 AND LiGaO_2 SINGLE CRYSTALS

RELATIONSHIP OF CRYSTALLOGRAPHIC POLARITY TO PIEZOELECTRIC,
PYROELECTRIC AND CHEMICAL ETCHING EFFECTS IN
 Li_2GeO_3 AND LiGaO_2 SINGLE CRYSTALS

A.S. Bhalla, L.L. Tongson and R.E. Newnham

Abstract

Absolute assignment of the atomic planes of Li_2GeO_3 and LiGaO_2 is made by ion surface scattering (ISS) and the crystallographic polarity is defined. Pyroelectric coefficients p_3 and the piezoelectric constants d_{33} of lithium metagermanate and lithium gallate are determined. Pyroelectric and piezoelectric coefficient signs when defined on the crystallographic sign convention of the axes are negative and positive, respectively. The results are correlated with chemical etching studies.

APPENDIX 46

138. SPECIFIC HEAT OF SbSI

SPECIFIC HEAT OF SbSI

M.E. Rosar, W.A. Smith and A. Bhalla

Abstract

The temperature dependence of the specific heat of vapor and flux grown single crystal samples of ferroelectric antimony sulfur iodide (SbSI) was measured over a temperature range from 230K to 400K. C_p^E at T_c of the electrical flux and vapor grown samples are 0.078 cal/gmK and 0.076 cal/gmK respectively. ΔS and ΔQ at T_c are evaluated. The samples measured were grown by two different methods^{1,2}. Differences are observed between the measurements made on the samples, both in the magnitude of the specific heat and the temperature at which the ferroelectric transition takes place. These differences are caused by the different levels of oxygen impurities in the samples.

APPENDIX 47

139. MAGNETIC-FIELD DEPENDENCE OF THE SOFT-MODE
FREQUENCY IN KTaO_3 AT 20K

MAGNETIC-FIELD DEPENDENCE OF THE SOFT-MODE
FREQUENCY IN KTaO_3 AT 20K

W.N. Lawless, C.F. Clark and S.L. Swartz

Abstract

The change in the soft-mode frequency in single-crystal KTaO_3 with magnetic field was measured at 20.1 K via dielectric measurements using the Lyddane-Sachs-Teller relation. At 10 T, the change in the soft-mode frequency is $\sim 0.2\%$. Converted to shift in the Curie temperature with magnetic field, the data indicate that $T_0(H) - T_0(0) \sim 5 \times 10^{-4} H^2 + 7.5 \times 10^{-6} H^4$ (H in Tesla). These data are consistent with recent neutron measurements on SrTiO_3 and dielectric measurements on BaTiO_3 .

SECTION II

SUMMARY OF WORK OVER THE FIVE YEAR CONTRACT PERIOD

1.0 SUMMARY OF WORK OVER THE FIVE YEAR CONTRACT PERIOD

1.1 Introduction

In a contract effort of the size and scope of that which we have been privileged to perform over the past five years, it is not possible to give a very detailed accounting of all aspects of the program at this time. This level of detail is, anyway, already available in the four earlier yearly reports. It is our intention in this section to highlight what we believe have been the most important major advances accomplished during the whole contract period.

The primary topic areas, ferroelectric and ferroelastic materials, cover the active materials in all ultrasonic transducer structures which are of vital interest to the Navy. The program mandate was to carry out basic studies which would be highly relevant to Navy needs in these transducer systems. In this summary, the primary advances in basic understanding will be first delineated, then their relevance to practical transducers discussed.

That the general program over the five year period has been highly productive is already well documented. Including the current year, participants in this ONR program have:

- 1) Published 130 technical papers in refereed journals.
- 2) Presented 23 invited and 99 contributed papers at National and International Meetings.
- 3) Submitted 12 invention disclosures.

During the contract period in 1981, Penn State was selected as the site for the 5th International Meeting on Ferroelectrics (IMF 5). This was the first time in 20 years that this prestigious IUPAP sponsored program was held in the USA, and it was indeed a signal honor to have the meeting at Penn State.

In 1982, Professor L.E. Cross and Dr. K. Okazaki co-chaired a joint US:JAPAN study seminar which took 20 US participants to Japan under ONR

sponsorship, for a closely knit technical seminar program and a week of individually scheduled visits to major companies and universities in Japan.

Over the period of the contract, 7 Ph.D. students employed on contract funds have achieved their degrees, and 3 M.S. students have graduated. Three more Ph.D. and one M.S. student have finished all their practical work on contract funds, and will probably graduate in June 1983. We are proud that two students, Dr. S.J. Jang and Dr. Yao Xi, achieved Xerox awards for the best Ph.D. work in Materials at Penn State in 1980 and 1982 respectively. In 1982, Professor L.E. Cross was also awarded the Penn State University Scholars Medal in Science and Engineering in recognition of work upon Electrostriction carried out largely upon this program.

2.0 IMPORTANT CONTRIBUTIONS IN BASIC SCIENCE

2.1 Composite Piezoelectrics

At the outset of this program, piezoelectric materials for transducer application had long been on a plateau in development with the highly successful PZT family dominating the field for the last 20 years. That dramatic improvement for certain types of application might be possible was, however, just becoming apparent through the pioneer efforts of Skinner^(2.1) at Penn State, using the replamine process to produce 3 dimensionally interconnected porous PZTs which could be back filled with a flexible polymer phase.

A key basic advance accomplished on the current program was the clear formulation of the critically important role of PHASE CONNECTIVITY in determining the distribution of fluxes and fields in a composite and thus controlling the performance^(2.2). Early simple formulations using 2 dimensional series and parallel models pointed up the dramatic improvements which could be expected for such applications as hydrophones, where the d_{hg} figure of merit could be improved by orders of magnitude. Early results in PZT:Epoxy 1:3 composites supported the simple models, but studies with softer elastomer polymers were terribly disappointing^(2.3). Realization of the important degradation of stress enhancement which could occur through the POISSON RATIO of the polymer was the second important step, and the control of the poisson ratio effects by foaming and by transverse reinforcement have lead to small "research type" samples which can achieve the 3 orders of magnitude improvement in d_{hg} figure of merit which the early studies promised^(2.4).

A third step in the evolution of the piezoelectric ceramic polymer composites was the development of alternative strategies for stress enhancement leading to the 3:1 and 3:2 composites developed by Newnham and Safari^(2.5) and the alternative simplified fabrication techniques for 3:3 composites by direct ceramic processes.

Early work on the composites was well summarized in the paper by Newnham, Bowen, Klicker and Cross^(2.6) included as Appendix 2.1. More recent studies by Safari and Newnham^(2.5) are given in Appendix 2.2. A very detailed analysis of the effects of porosity and transverse reinforcement has been presented by Haun in his M.S. thesis. This work will be reported in ISAF 83 and published in the proceedings. Some results of this work as also given in Section I.

2.2 Electrostriction

2.2.1 Introduction

Electrostriction is the basic coupling mechanism between polarization and strain in all ceramic transducer materials, yet, up to the time of this contract there was no convincing atomistic theory for the origin, and almost no reliable measures of electrostriction in simple low permittivity cubic crystals.

2.2.2 Theoretical Work

A basic weakness in the current phenomenological theory of electrostriction was pointed out by Toupin^(2.7), and again by Gindlay^(2.8) in that if the conventional infinitesimal strain and polarization are related, the tensor Q_{ijkl} is not strictly invariant under simple rotation. Using the Toupin material measure of polarization and the Lagrangian strain, a rotationally invariant formulation has been developed and applied to simple crystals to ascertain the magnitude of the difference between correct and earlier formulations^(2.9) (Appendix 2.3).

In the microscopic theory, using a realistic model for the interatomic forces, the quasi-harmonic theory of Bruce and Cowley^(1.1) has been used to calculate Q values in SrTiO_3 and other simple perovskites. Unfortunately, though the theory is adequate for fixed temperature, it is completely unable to account for the observed temperature variation of electrostriction in SrTiO_3 .

2.2.3 Experimental Observation

(a) Low Level Electrostriction

Much effort has been expended to develop capacitance ultra-dilatometry to the level required for direct measurement of electrostriction in alkali halides and perovskites fluorides. The development of an instrument capable of resolving displacement of 10^{-3} Å^(2.10) was clearly a major achievement (Appendix 2.4).

This instrument has been of major use in measuring piezoelectricity at low levels and in thin samples^(2.11), but the original intention to measure low level electrostriction has proven much more difficult than was originally anticipated. Early data gave values more than two orders too large, but scaling perfectly as quadratic with field. Some of these problems were traced to the mode of mounting, and it was not until we adapted a technique to glue the sample in place that data comparable to Bohaty and Haussühl^(2.12) and Luymes^(2.13) studies were obtained. Our data, however, suggest (see Section I) a strong extrinsic frequency dependence for M_{1111} .

Very recently the picture has been further complicated by Preu and Haussühl^(2.14) with measurement of the converse effect using uniaxial stress which show values of M_{1111} of opposite sign (positive). Thus in spite of the extreme difficulty of experimentation in this area, there is urgent need for additional studies.

2.2.4 Electrostriction in Perovskites

Early work on the contract by Uchino and Cross^(2.15) established some most useful empirical relations for the Q_{ijk} constants and demonstrated the clear advantage of the relaxor ferroelectrics for high level electrostriction.

Measurements by Jang indicated the signal advantage of multilayer monolithic systems for electrostriction and lead to a major advance in the development of the lead magnesium niobate:lead titanate family^(2.16) of high response - low

thermal expansion electrostrictors for practical application Appendix (2.5 and 2.6). A major forward step in the basic understanding of relaxor ferroelectric was catalyzed by Setter^(2.17,2.18) with the discovery of order:disorder in $\text{Pb}(\text{Sc}_{1/2}\text{Ta}_{1/2})\text{O}_3$ single crystals and ceramics. Her clear evidence that the Sc:Ta ordered structure had a sharp first order ferroelectric phase change, while the disordered crystals was a relaxor, gave immediate proof of the importance of microheterogeneity and the first clear scaling of the heterogeneity in a relaxor material (Appendix 2.7).

Recent work on PLZT relaxors at the 8:65:35 composition permit a detailed evaluation of the build up and decay of macro-domain polarization in these compositions and what appears to be the first clear evidence of superparaelectric disordering of the polar micro-regions at a temperature below the dielectric maximum. This study correlates well with the observation of shape-memory observed in the PLZTs and discussed later.

3.0 FERROELECTRIC BICRYSTALS

3.1 Introduction

In the study of mechanical properties of ceramics, significant progress was made through the study of bicrystals which can mimic in a simpler geometric form the characteristics of a single grain boundary. The present study was initiated using water soluble triglycine sulphate crystals, but early in the program it was found that LiNbO_3 could be hot pressure bonded at temperatures below T_c so that the domain configuration of the bicrystal halves could be largely preserved.

3.2 Bicrystal Studies

For LiNbO_3 , anisotropy in the thermal expansion limits the bonding surfaces which can be used and in this work planes normal to the rhombohedral c axis were bonded with the polar axis head-to-head (H:H), tail-to-tail (T:T) and head-to-tail (H:T). Studies were carried through of the effect of the bicrystal boundary upon dielectric properties, domain structure, defect structure, charge transport and piezoelectric resonance.

From the resonance and domain studies, it became apparent that H:H and T:T bonded crystals resonate as separate thickness mode resonators, while H:T bonded samples resonate as a whole almost as if the boundary were not present.

3.3 Lithium Niobate Ceramics

The very simple domain structures and resonant behavior in the bicrystals of LiNbO_3 suggested that the material might be used as a model ceramic in which it should be relatively simple to model the frequency dependence of the impedance. Model ceramics were made up using both liquid salt produced powders, and mixed oxide techniques so as to develop a narrow distribution of grain sizes.

Dielectric impedance measurements suggested at once a weak resonant character for the response, with massive dispersion in both real and imaginary parts of

the apparent permittivity for frequencies near the mean grain resonance. Using the ECAP computer analysis routine for complex circuits, and a specially devised folding technique to multiply the accessible number of elements which can be handled by ECAP it was shown that the full frequency dependence of the ceramic impedance could be calculated from the known dielectric and piezoelectric parameters of the single crystal, the grain size, and the size distribution.

We believe that these calculations are the first clear proof of the importance of damped piezoelectric grain resonance upon the dispersion character of high permittivity ferroelectric dielectric ceramics (Appendix 2.8).

4.0 FERROELASTIC SHAPE MEMORY

4.1 Introduction

Shape memory is an interesting elastic phenomenon which has been well documented for a number of metal alloy systems which show a martensitic type phase change. NiTiNOL, a nickel titanium alloy, first developed by the Naval Research Laboratory is perhaps the best known example. If a wire or rod of NiTiNOL is heated through the martensitic temperature T_m then cooled, it becomes very soft and plastic, so that even quite stout rods can be bent in the fingers. Now on re-heating through T_m the rod straightens without any applied force, remembering its original shape (hence the name shape memory). Since ferroelectric displacive transitions are martensitic, it appeared interesting to explore possible shape memory in these materials.

4.2 Shape Memory in PLZT Compositions

Using a very simple loading jig to apply a bending moment to thin rods of PLZTs in the x:65:35 composition field, Kimura was able to demonstrate that when $x < 4$ mole% in the sharp transition materials shape memory occurs for all temperatures below the Curie temperature, in exact analogue to the metal martensites. In compositions with higher lanthanum concentrations which show clear ferroelectric relaxor character, the recovery process does not take place at the temperature of the dielectric maximum, but at the so called α - β transition where the macro-remanent polarization is lost (Appendix 2.9).

These studies correlate very well with the polarization:depolarization studies on relaxor PLZTs giving additional support for the super-paraelectric model for these ceramics.

5.0 DEVELOPMENT OF A FULL ELASTIC GIBBS FUNCTION FOR PZT

5.1 Introduction

The ADAGE computer graphics system at Penn State has been used to develop a modified Devonshire thermodynamic function to describe phase stability and intrinsic properties in the simple solid solutions between PbZrO_3 and PbTiO_3 . For the Devonshire function which only describes a proper ferroelectric, the range must be limited to include only single cell parts of the structure field. Since, however, these encompass the interesting morphotropic region, the constraint is not penal. In the computer fitting, higher order coefficients were permitted to vary as linear functions of composition, and it was assumed that the Devonshire constraint imposed by the necessity to balance free energies at the first order cubic:tetragonal phase change persisted for a limited range into the rhombohedral field. The condition of morphotropy turns out to be a strong constraint upon the permitted coefficients.

Choosing the simplest combination in the families of constants which give good fitting to the phase diagram, more exact coefficients were evaluated using measured Curie temperatures. Polarization data for polycrystal PZTs cannot be used, so to fit the single domain P_s values, spontaneous strain was evaluated. With composition independent electrostriction Q constants, the fitting to measured strain was excellent.

To evaluate single domain permittivities, piezoelectric constants and thermal effects at T_c , it is necessary to have values of the Curie-Weiss constant C which appears in the Devonshire function as a scale parameter. Unfortunately, values of C in the literature range from $1.5 \cdot 10^5$ to $\sim 1.2 \cdot 10^6$, so that for the original fitting, a constant (composition independent) value of $3.0 \cdot 10^5$ was selected. At this value of C , fitting to measured dielectric response for the PbTiO_3 end of the phase diagram is excellent, however, at compositions

close to morphotropy $\bar{\epsilon}$ and \bar{d} values are very low even compared to those of hard PZTs.

5.2 New Data for PZT Family Compositions

5.2.1 Thermal Changes

Early measurements of the thermal changes in PZT by Setiveau and Troccaz^{5.1} show a steep drop in the heat of transition from PbTiO_3 to the $\text{Pb}(\text{Ti}_{0.5}\text{Zr}_{0.5})\text{O}_3$ composition near morphotropy. Since these were early measurements on mixed oxide prepared samples which could have large compositional heterogeneity it was decided to repeat the data using samples carefully prepared from organic precursors so as to minimize such effects.

Surprisingly, the new results^{2.} agree closely with the early French work, suggesting that if the PZT maintains 'sharp' transition character, C must climb from $\sim 1.5 \cdot 10^5$ in PbTiO_3 to $\sim 7.7 \cdot 10^5$ in the $\text{PbZr}_{0.5}\text{Ti}_{0.5}\text{O}_3$ composition.

5.2.2 Low Temperature Measurements

It is a defensible thesis that the major differences between differently doped soft and hard PZTs at compositions close to morphotropy are extrinsic in nature.

Powerful additional evidence that this is in fact the case has been given by our recent measurements of the properties of hard, intermediate and soft commercial PZTs down to 4°K where all extrinsic domain related phenomena in the response will be frozen out (see Section I for details). Very briefly the commercial PZTs which are of similar Zr:Ti ratio but with different dopants all come together in dielectric, piezoelectric response, and coupling coefficients^{5.3}, while pure PZTs of different Zr:Ti ratio remain distinct in properties down to 4K^{5.4}.

From the data in 5.3 the mean value $\bar{K} \simeq 360$ at 4K. From the phenomenological analysis \bar{K} at 4K using Amin's calculation with $C = 3 \cdot 10^5$ gives $\bar{K} = 142$.

If, however, the Curie constant is taken to be $7.7 \cdot 10^5$ as required for the thermal data, the calculated \bar{K} at 4°K is 365 in excellent agreement with the measured intrinsic average. Based on the large 'effective' Curie constant, the value of \bar{K} vs T can be re-calculated and is compared with the temperature dependence of \bar{K} for commercial PZTs in Figure 5.1

Clearly the indication from this phenomenology is that even in the hard PZT, some 30% of the dielectric and piezoelectric activity is extrinsic, while in the soft PZT the major part is certainly extrinsic.

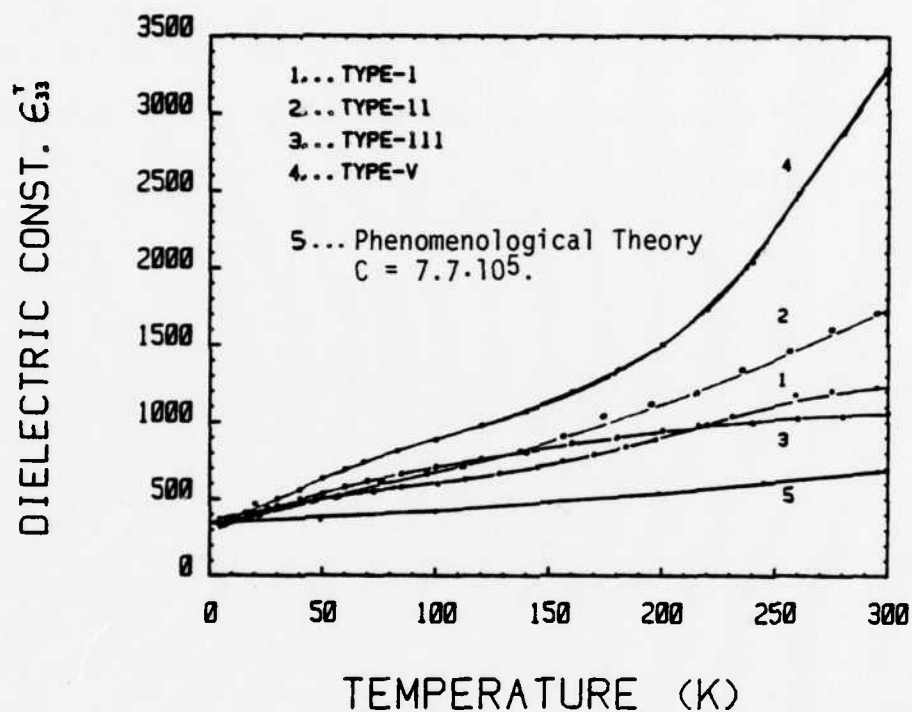


Figure 5.1. Permittivity ϵ_{33} vs T for doped PZTs compared to calculated intrinsic permittivity.

6.0 PYROELECTRICS

Work on this family of topics was not begun until late in the contract but has been exceedingly productive. A major break through has been the development of a completely new family of pyroelectric:piezoelectric glass ceramics, in which a polar crystalline phase which is not ferroelectric is grown into the glass under steep temperature gradient to form an ensemble with strong polar texture and therefore, pyroelectric and piezoelectric properties.

Piezoelectric effects are summarized in Appendix 2.10 and pyroelectrics in 2.11. This work also shared support from the U.S. Army under contract DAAG-29-78-003.

7.0 PREPARATIVE STUDIES

Much detailed work on the preparation and characterization of both ceramic and single crystal materials has been required to cover the practical needs of composites and relaxor ferroelectrics and other material systems required for study.

Of major importance are the detailed studies of the calcining reactions in the $\text{PbZrO}_3\text{:PbTiO}_3$ system (Appendix 2.12) and the development of reliable synthesis techniques for the relaxor ferroelectric $\text{PbMg}_{1/3}\text{Nb}_{2/3}\text{O}_3$, and its solid solutions with PbTiO_3 .

REFERENCES

- 2.1 D.P. Skinner, R.E. Newnham and L.E. Cross, Mat. Res. Bull. 13, 599 (1978).
- 2.2 R.E. Newnham, D.P. Skinner and L.E. Cross, Mat. Res. Bull. 13, 525 (1978).
- 2.3 K.A. Klicker, Ph.D. Thesis, Solid State Science, The Pennsylvania State University (1980).
- 2.4 M. Haun, M.S. Thesis, Solid State Science, The Pennsylvania State University (1983).
- 2.5 A. Safari, R.E. Newnham, L.E. Cross and W.A. Schulze, Ferroelectrics 42, 197 (1982).
- 2.6 R.E. Newnham, L.J. Bowen, K.A. Klicker and L.E. Cross, Materials in Engineering II 2, 93 (1980).
- 2.7 R.A. Toupin, J. Rat. Mech. Anal. 5, 849 (1956).
- 2.8 J. Grindlay, Phys. Rev. 149, 637 (1966).
- 2.9 G.R. Barsch, B.N.N. Achar and L.E. Cross, Ferroelectrics 35, 187 (1981).
- 2.10 K. Uchino and L.E. Cross, Ferroelectrics 27, 35 (1980).
- 2.11 K. Uchino and L.E. Cross, Proc. 33rd Ann. Freq. Control Symp., Atlantic City, NJ, 110 (1979).
- 2.12 L. Bohaty and S. Haussühl, Acta Cryst. A33, 114 (1977).
- 2.13 B.J. Luymes, Ph.D. Thesis, Eindhoven University of Technology (1982).
- 2.14 P. Prev and S. Haussühl, Solid State Comm. 45, 619 (1983).
- 2.15 K. Uchino, S. Nomura, L.E. Cross, R.E. Newnham and S.J. Jang, J. Mat. Sci. 16, 569 (1981).
- 2.16 S.J. Jang, K. Uchino, S. Nomura and L.E. Cross, Ferroelectrics 27, 31 (1980).
- 2.17 N. Setter and L.E. Cross, J. Mat. Sci. 15, 2478 (1980).
- 2.18 N. Setter and L.E. Cross, J. Appl. Phys. 51, 4356 (1980).
- 5.1 Y. Setiveau and M. Troccaz, C.R. Acad. Sci., Ser. B, T266 (1968).
- 5.2 A. Amin, L.E. Cross and R.E. Newnham, Ferroelectrics 37, 647 (1981).

- 5.3 X.L. Zhang, Z.X. Chen, L.E. Cross and W.A. Schulze, J. Mat. Sci. (to be published).
- 5.4 X.L. Zhang, Z.X. Chen, L.E. Cross and W.A. Schulze, J. Phase Transitions (accepted).

APPENDIX 2.1
COMPOSITE PIEZOELECTRIC TRANSDUCERS

Composite Piezoelectric Transducers.

R.E. NEWNHAM, L.J. BOWEN, K.A. KLICHER and L.E. CROSS

Materials Research Laboratory, Pennsylvania State University, University Park, Pa., U.S.A. 16802

Considerations of the influence of crystal symmetry, macrosymmetry, and interphase connectivity have been used to explore possible macrostructures of interest as piezoelectric composites. Based on these design considerations, ceramic-plastic composites have been fabricated with 3-3 phase connectivity by the replication of natural template structures such as coral. Composites prepared in this way have piezo-electric g_{33} and g_{31} coefficients more than an order of magnitude higher than the coefficients of the homogeneously poled ferroelectric ceramic. A simplified fabrication technique has been developed by mixing volatilizable plastic spheres and PZT powder. When sintered and back-filled with epoxy, and poled, these composites give excellent piezoelectric voltage coefficients. Large voltage coefficients were also obtained from 3-1 piezoelectric composites made by embedding PZT fiber arrays in epoxy cement. A continuous poling method has been developed for these fibers which makes it possible to assemble complex composites from pre-poled PZT fibers in epoxy matrices. Multilayer composites with 2-2 connectivity have been produced for filters and other high-frequency applications. Processing methods for producing 3-1 and 2-2 connected composites are described.

1. Introduction

Progress in materials science - like progress in most fields - follows an S-shaped curve of history (Figure 1). When a new effect such as ferroelectricity is discovered, scientific development is rather slow at first, until its importance is recognized. Then follows

a period of rapid growth when practical applications and new materials are discovered. During this period, rapid changes take place in selecting the "best" material for each application. Eventually the field matures as the choices are made, and the curve of history saturates.

We see this saturation effect in many branches of solid state research. In electroceramics, lead zirconate-titanate (PZT) has been the best transducer material, and barium titanate the best high-permittivity capacitor material for the past twenty years. Similar situations prevail in magnetic materials, semiconductors, ceramics, and metallurgy. Despite intensive search for new compounds, relatively few major changes have been made in the past decade.

Led by the semiconductor industry, materials science now appears to have entered a new era, the age of carefully patterned inhomogeneous solids designed to perform specific functions. Examples of heterogeneous systems optimized for particular applications include semiconductor integrated circuits, fiber-reinforced metals, and barrier-layer ferroelectric capacitors. No longer as much concerned with the properties of the best single-phase materials, many investigators now search for the best combination of materials and ways to process them. In a very real sense, the field has matured from materials science to materials engineering just as electrical science changed to electrical engineering many years ago.

In most electronic devices there are several phases involved and a number of material parameters to be optimized. An electromechanical transducer, for

example, might require a combination of properties such as a large piezoelectric coefficient (d or g), low density, and high mechanical flexibility. A pyroelectric detector might require a large pyroelectric coefficient, low thermal capacity, and low dielectric constant. In general, the task of materials design may be considerably simplified if it is possible to devise a figure of merit which combines the most sensitive parameters in a form allowing simple intercomparison of the possible "trade offs" in property coefficients. In certain pyroelectric systems, for example, a useful figure of merit is p/e where p is the pyroelectric coefficient and e the electric permittivity.

Unfortunately, the figure of merit often involves property coefficients which are conflicting in nature. To make a flexible electromechanical transducer it would be desirable to have the large piezoelectric effects found in poled piezoelectric ceramics, but ceramics are brittle and stiff lacking the required flexibility, while polymers with the desired mechanical properties are at best very weak piezoelectrics. Thus, for such an application a composite material combining the desirable properties of two different phases might be vastly superior. The main problem is to effect the combination in such a manner as to exploit the desirable features of both components and thereby maximize the figure of merit.

During the past few years we have been experimenting with piezoelectric and pyroelectric composites made from plastics and ferroelectric ceramics, hoping to improve on some of the properties of homogeneous materials^{1, 2, 3}. Some of the results are

summarized in this paper, along with a few design principles and potential applications.

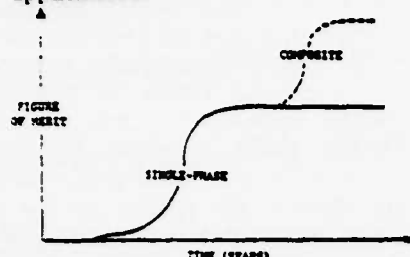


Fig. 1 Curve of history for materials. Discovery is followed by a period of rapid development, and then a leveling off. The use of composites sometimes leads to further progress.

2. Design Principles

Combining materials means not only choosing component phases with the right properties, but also coupling them in the best manner. Connectivity of the individual phases is of utmost importance, because this controls the electric flux pattern as well as the mechanical properties. Symmetry is a second important consideration, since symmetry and properties are inter-related through tensor coefficients. In this regard there are several levels of symmetry to be considered: the crystallographic symmetry of each phase, the symmetry after processing, the combined symmetry of the composite, and the environmental influence on the total symmetry including electrodes and clamps.

The points of interest are schematically formalized in Figure 2 for a simple two-phase system. It is interesting to note that in some composites, not only are the properties of the separate phases modified (sum properties), but the composite may exhibit completely new couplings (product properties) not found in the separate phases.

2.1 Sum Properties and Product Properties

A physical property relates an input physical quantity X to an output physical quantity Y . The X - Y effect may be a linear relationship specified by a property coefficient $C = \partial Y / \partial X$, or it may be a more complicated effect. As pointed out by van Suchtelen⁴, two classes of X - Y effects can be distinguished in composites.

Sum properties are those in which the X - Y effect of the composite is determined by the X - Y effects in phases 1 and 2. As an example, consider the stiffening of a matrix by

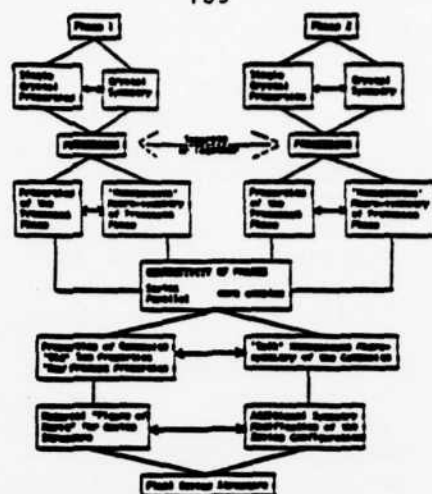


Fig. 2 Flow chart illustrating design considerations for optimizing the performance of solid state devices. The task of the materials engineer is to find the materials, processing methods, and connectivity patterns which maximize the figure of merit.

strong parallel fibers. Young's modulus of the composite (\bar{E}) depends on the moduli of the matrix phase (1E) and the embedded fiber phase (2E). In the direction of the fibers, \bar{E} is given by $^1E_v + ^2E(1-v)$, where v is the volume fraction⁵. When measured in various directions, such properties often vary between the geometric and arithmetic mean of the properties associated with the constituent phases.

Product properties are less expected and somewhat more complicated: An X - Y effect in the composite results

from an X - Z effect in phase 1 and a Z - Y effect in phase 2. In other words, applying X to the composite causes Z to change in phase 1; the change in Z in phase 1 causes Z to change in phase 2, which then results in a change in Y in phase 2. The transfer of the quantity Z from 1 to 2 can be accomplished by several different kinds of coupling.

As an example of a product property, consider a magnetoelectric composite made from a ferroelectric (phase 1) and a ferromagnetic (phase 2). Crystallites of the two phases are assumed to be in good mechanical contact. The ferroelectric grains are poled near the ferroelectric Curie temperature in a strong electric field to make the composite piezoelectric. Magnetic poling of the ferromagnetic phase is accomplished in a similar way, by annealing the composite in a magnetic field.

When an electric field is applied to a magnetoelectric composite of this type the ferroelectric grains elongate parallel to the electric field. The change in shape of the ferroelectric grains causes the ferromagnetic grains to deform, resulting in a change in magnetization. Magnetoelectric measurements on $\text{BaTiO}_3\text{-CoFe}_2\text{O}_4$ composites prepared by unidirectional solidification at the eutectic composition show magnetoelectric coefficients two orders of magnitude larger than

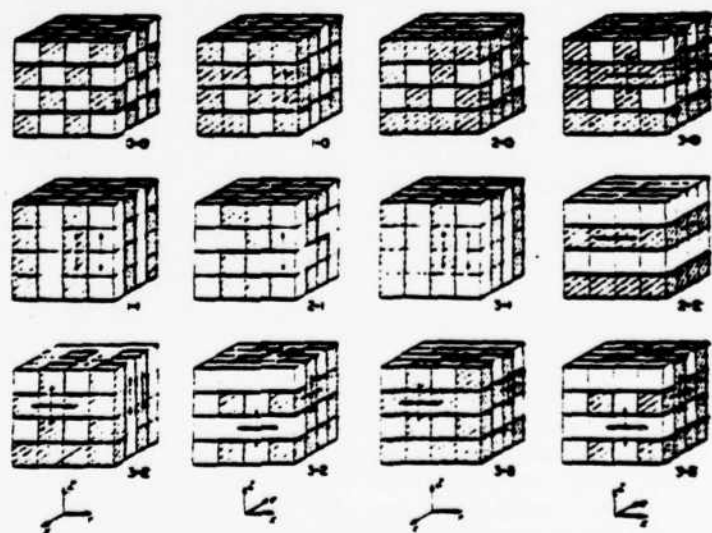


Fig. 3 Ten connectivity patterns for a diphasic solid. Each phase has zero-, one-, two- or three-dimensional connectivity to itself. In the 3-1 composite, for instance, the shaded phase is three-dimensionally connected and the unshaded phase is one-dimensionally connected. Arrows are used to indicate the connected directions. Two views of the 3-3 and 3-2 patterns are given because the two interpenetrating networks are difficult to visualize on paper. The views are related by 90° counterclockwise rotation about Z .

the best single phase material^{6,7}.

2.2 Connectivity

Connectivity is a key feature in property development in multiphase solids since physical properties can change by many orders of magnitude depending on the manner in which connections are made. Imagine, for instance, an electric wire in which the metallic conductor and its rubber insulation were connected in series rather than in parallel!

Each phase in a composite may be self-connected in zero, one, two, or three dimensions. It is natural to confine attention to three perpendicular axes because piezoelectricity and other property tensors are referred to such systems⁸. If we limit the discussion to diphasic composites, there are ten connectivities designated as 0-0, 1-0, 2-0, 3-0, 1-1, 2-1, 3-1, 2-2, 3-2, and 3-3. The ten different connectivities are illustrated in Figure 3 using a cube as the basic building block. A 2-1 connectivity pattern, for example, has one phase self-connected in two-dimensional layers, the other self-connected in one-dimensional chains or fibers. The connectivity patterns are not geometrically unique. In the case of a 2-1 pattern the fibers of the second phase might be perpendicular to the layers of the first phase, as in Figure 3, or they might be parallel to the layers.

In passing we note that connectivity patterns for more than two phases are basically similar to the diphasic patterns, but far more numerous. There are 20 three-phase patterns and 35 four-phase patterns compared to the 10 two-phase patterns in Figure 3. For n phases the number of connectivity patterns is $(n+3)!/3!n!$. Triphasic connectivity patterns are important when electrode patterns are incorporated in the diphasic ceramic structures.

2.3 Processing Methods

During the past few years we have been developing processing techniques for making diphasic ceramic composites with different connectivities. Extrusion, tape-casting and replamine methods have been especially successful. The 3-1 connectivity pattern in Figure 3 is ideally suited to extrusion processing. A ceramic slip is extruded through a die giving a three-dimensionally connected pattern with one-dimensional holes, which can later

be filled with a second phase.

Another type of connectivity well suited to processing is the 2-2 pattern made up of alternating layers of the two phases. The tape-casting of multilayer capacitors with alternating layers of metal and ceramic is a way of producing 2-2 connectivity. In this arrangement both phases are self-connected in the lateral X and Y directions but not connected perpendicular to the layers along Z.

In 3-2 connectivity, one phase is three-dimensionally connected, the other in two. This pattern can be considered a modified multilayer pattern with 2-2 connectivity. If holes are left in the layers of one phase, layers of the second phase can connect through the holes giving three-dimensional connectivity.

The most complicated and in many ways the most interesting pattern is 3-3 connectivity (Figure 2) in which the two phases form interpenetrating three-dimensional networks. Patterns

can also be used to duplicate the connectivity patterns found in foam, wood, and other porous materials.

Four examples of electroceramics with different connectivity patterns are shown in Figure 4. Diphasic ceramic capacitors have been made of BaTiO_3 grains separated by thin layers of NaNbO_3 in the grain boundary regions. The sodium niobate is three-dimensionally connected while the barium titanate grains are not in contact, making it a 3-0 connectivity pattern. The ceramic is manufactured by liquid phase sintering at temperatures above the melting point of NaNbO_3 , but below that of BaTiO_3 . At these temperatures, sodium niobate melts and coats the BaTiO_3 grains but rapid cooling prevents reaction between the two phases. High dielectric constant capacitors made with these microstructures show excellent high-voltage characteristics. Normally, the polarization of barium titanate capacitors saturates at high voltages, with the

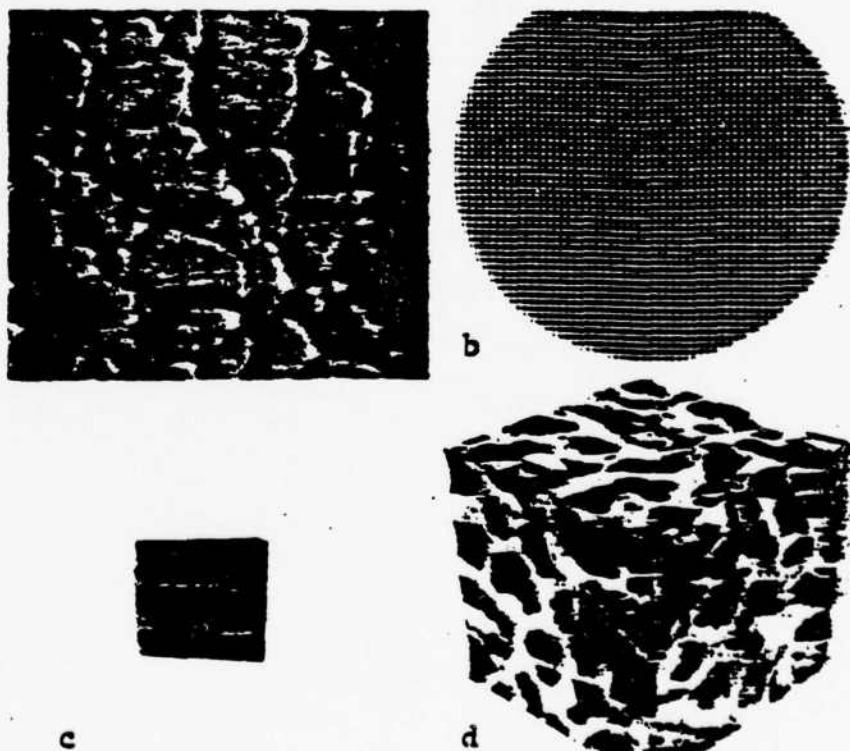


Fig. 4 Four types of connectivity: (1) 3-0, (b) 3-1, (c) 2-2 and (d) 3-3 (replamine).

of this type often occur in living systems such as coral where organic tissue and an inorganic skeleton interpenetrate one another. These structures can be replicated in other materials using the lost-wax method⁹. The replamine process, as it is called,

dielectric constant decreasing by as much as a factor of two; but separating the grains of ferroelectric BaTiO_3 with a thin layer of antiferroelectric NaNbO_3 compensates the saturation effect to give a flat voltage response¹⁰.

PZT-plastic composites with 3-0

connectivity have been examined by Furukawa, Fujino and Fukada¹¹. Samples containing 10 to 30% PZT were made by embedding fine-grained powder in an epoxy resin then sliced into thin wafers, and electroded with silver. Limited poling was possible because of the conductivity of the epoxy, but the piezoelectric coefficients were small. Mixing rules were developed for spherical piezoelectric inclusions in a non-piezoelectric matrix. The calculated d_{31} values gave reasonable agreement with experiment.

Connectivity patterns can be synthesized as macrostructures, as microstructures, or even as crystal structures. The BaTiO_3 - NaNbO_3 composite just considered had a 3-0 microstructure. The next three examples involve macrostructures with 3-1, 2-2, and 3-3 connectivities. Figure 4b shows an extruded BaTiO_3 honeycomb ceramic made by Dr. Irwin Lachman of the Corning Research Center. The ceramic is three-dimensionally connected with empty channels in one direction to provide the desired 3-1 connectivity. When the channels are filled with metal electrodes, sizeable electric fields can be applied across the thin ceramic walls. The device is intended for use as an electrostrictive micropositioner for adaptive optic systems.

Two composite piezoelectric transducers are illustrated in Figures 4c and 4d. The multilayer composite of "hard" and "soft" PZT has 2-2 connectivity and properties superior to a single-phase piezoelectric. The soft PZT has a large piezoelectric response and is kept in a poled state by the hard PZT. Figure 3d shows a silicone rubber-PZT composite made by the replamine process². The 3-3 connectivity provides mechanical strength and flexibility from the high polymer, and electric continuity and a large piezoelectric effect from PZT. The last two materials will be discussed in more detail later.

3. Piezoelectricity

A number of materials with acentric structure develop an electric polarization in response to mechanical stress. The magnitude of the charge is linearly proportional to the applied stress through the piezoelectric coefficient d , and the sign of the charge can be changed by reversing the direction of the stress.

Piezoelectric materials can be either

single crystals or polycrystalline. Quartz is the most widely used single crystal piezoelectric and finds applications primarily in electronic frequency control as resonators and filters. Polycrystalline materials are generally isotropic after densification, but can be made piezoelectric if the material is ferroelectric. A polar axis is introduced by electroding the ceramic and applying a high electric field (typically about 3MVm^{-1}) at temperatures just below the Curie temperature. Polycrystalline ceramic piezoelectrics are easily fabricated in complex shapes and are considerably less expensive than single crystals. PZT ($\text{PbZr}_{1-x}\text{Ti}_x\text{O}_3$) is the most widely used piezoelectric ceramic.

The polarization (P_i) developed in a piezoelectric under applied stress T_j is

$$P_i = d_{ij}T_j \quad (1)$$

The converse piezoelectric effect is given by

$$S_i = d_{ji}E_j \quad (2)$$

where S_i is a strain component, E_j the applied electric field, and d_{ij} the piezoelectric coefficient expressed in coulombs per newton, or meters per volt. Subscripts i and j refer to orthogonal directions within the specimen⁸.

In ceramics, the poling direction is taken as X_3 .

Large d_{ij} coefficients are desirable in piezoelectric driver applications such as ultrasonic cleaners and sonar. For gramophone pick-ups and hydrophones a useful figure of merit is the piezoelectric voltage coefficient, g , defined by:

$$g_{ij} = \frac{d_{ij}}{\epsilon_i} \quad (3)$$

where ϵ_i is the dielectric permittivity of the material.

Typical single crystal and polycrystalline piezoelectrics and some of their relevant electromechanical properties are listed in Table 1.

3.1 Flexible Transducers

There is considerable practical interest in developing low-density, compliant, flexible piezoelectric transducers. A low-density piezoelectric would have better acoustic coupling to water and have more easily adjusted buoyancy than the high-density PZT ceramics now used for hydrophones. A compliant material would have better resistance to mechanical shock than a conventional ceramic transducer and a large compliance would also mean high damping, which is desirable in a passive device. A flexible material could be deformed to any desired profile. The development of a piezoelectric material which exhibits this combination of seemingly conflicting

TABLE 1 Properties of Common Piezoelectric Materials (reference 12).

Piezoelectric Material	Property							
	Relative Permittivity		Elastic Compliance		Piezoelectric Coefficient		Piezoelectric Voltage Coefficient	
	T ϵ^1	T ϵ^2	E S_{11} pm^2/N^1	E S_{33} pm^2/N^1	d_{31} pC/N^1	d_{33} pC/N^1	g_{31} $\times 10^{-3} \text{Vm/N}^1$	g_{33} $\times 10^{-3} \text{Vm/N}^1$
α-Quartz Single Crystal (Trigonal, J2)	4.5	4.6	12.8	9.6	$2.3(d_{11})$	—	$57.0(g_{11})$	—
BaTiO_3 Single Crystal (Tetragonal, 4mm)	2920	168	8.05	15.7	-34.5	85.6	-23.0	57.6
BaTiO_3 Ceramic (4mm)	1620	1900	8.55	8.93	-79.0	191.0	-4.7	11.4
$\text{PbTi}_{0.98}\text{Zr}_{0.02}\text{O}_3$ Ceramic (4mm)	1180	730	13.8	17.1	-93.5	223.0	-14.5	34.5
PVP, ($\text{C}_2\text{H}_5\text{F}_2$) _n Polymer (4mm) (Biaxially stretched and poled)	—	3.1	—	—	0.5	-7.5	95	—
Collagen (α)	—	8	—	—	$-2.6(d_{11})$	—	—	—

properties may be carried out in basically two different ways. The traditional approach is to look for a single homogeneous material possessing all the required properties. A material of current interest in this category is poly (vinylidene fluoride), generally referred to as PVF₂.

Piezoelectricity was first reported in this material in 1969 by Kawai¹³. In order to make PVF₂ piezoelectrically active, a film of the material, usually about 25 to 75 μm thick, is electrode and polarized under very large electric fields (about 10 to 100 MVm^{-1}) at elevated temperatures ($>100^\circ\text{C}$) for times up to several hours. The films are then cooled to room temperature before the field is turned off¹⁴. PVF₂ has a dielectric constant of 15 which is high for normal organic materials but two orders of magnitude lower than a typical PZT ceramic. The longitudinal piezoelectric strain coefficients (d_{33}) of "poled" PVF₂ are quite high for polymers - on the order of 10 pCn^{-1} , but this is also significantly lower than the d_{33} values for PZT ceramics which range from about 100 to 600 pCn^{-1} . Although PVF₂ has a relatively small d_{33} , the permittivity of this material is low enough that a large figure of merit (g_{33}) is obtained ($140 \times 10^{-3} \text{ VmN}^{-1}$ compared to about $20 \times 10^{-3} \text{ VmN}^{-1}$ for a typical PZT ceramic)¹⁵. The compliance and flexibility of PVF₂ is high and its density is low compared to conventional ceramic piezoelectrics. Overall, this combination of properties appears quite attractive and, in fact, PVF₂ has gained the attention of a number of investigators whose efforts have been directed toward developing devices based on piezoelectricity in PVF₂^{15, 16}. There are, however, problems associated with the use of PVF₂. The low piezoelectric strain coefficient indicates that the material would not be of interest as an active device, and although its high voltage sensitivity means it may be good as a passive device, a problem arises here, too. When used as a hydrophone, the material must be fixed to a curved surface which can flex in response to pressure changes. The difficulty lies in designing a sealed flexible mount for the polymer which will function when exposed to the high pressures which exist deep in the ocean and still retain sensitivity when near the surface.

So we see, then, that the figure of merit g_{ij} is not the sole criterion, but the other aspects of the problem must be examined.

A second approach involves the design and use of a composite material. The composite should be designed to take maximal advantage of the useful properties of each phase. A logical choice is a composite made of a polymer and a PZT ceramic. The polymer phase would lower the density and permittivity and increase the elastic compliance. If an elastomer is used, the composite would be compliant and flexible. The properties of piezoelectric PZT are well known to electromechanical transducer designers, and these materials could impart large piezoelectric strain coefficients to the composite. A few attempts have been made at creating an elastomer/PZT composite for use as a flexible low-density transducer¹⁷. The approach used in these attempts was to load a polymer film with particles of a piezoelectric material. The degree of flexibility and the magnitude of the d and g coefficients are primarily controlled by the size of the piezoelectric particles in the heavily loaded elastomer film.

Earlier flexible composites made at Gould were fabricated using 5 to 10 μm particles bound in a polyurethane matrix. A similar material (T-flex) was developed by Harrison¹⁷ using 120 μm particles in a silicone rubber matrix. The longitudinal d values obtained in both cases were comparable to the piezoelectric PVF₂ material but the voltage sensitivities were lower because of the higher permittivities in the composites. The difficulty with this type of composite where the piezoelectric particles are smaller in diameter than the thickness of the polymer sheet (Figure 5a) is that low permittivity polymer layers interleave the piezoelectric particles preventing saturation poling after the composite is formed. After some poling has been achieved, the interleaved compliant polymer attenuates the piezoelectric response of the composite.

Composites are made at Honeywell¹⁷ which contain much larger particles (up to 2.4 mm in diameter). A material of this type is shown schematically in Figure 5b. Here the particle size approaches the thickness of the composite. Since the piezoelectric particles run from electrode to

electrode, near saturation poling can be achieved. The large rigid piezoelectric particles can transmit an applied stress well leading to high d values if d is measured across the particles. Permittivities in these materials are low compared to homogeneous PZT, resulting in high g coefficient. The problem here is that properties of the composite are extremely position sensitive.

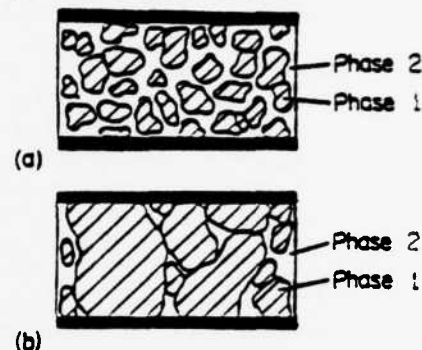


Fig. 5 Two types of piezoelectric/polymer composites: (a) represents small piezoelectric particles suspended in a polymer film; (b) represents bound piezoelectric particles of a size comparable to the thickness of the polymer sheet.

To make an effective composite transducer, it can be seen that one cannot merely mix two materials together - some other consideration is necessary. Designing a composite entails not only choosing component phases with the right properties but also coupling the materials in the optimal manner. The connectivity of each phase is of major importance since this controls the electric flux pattern and the mechanical stress distribution.

3.2 Composites: Series Connection

To illustrate the major modifications in ensemble properties which can be effected even in simple linear systems, one-dimensional solutions are presented for the piezoelectric and pyroelectric properties of heterogeneous two-phase structures^{1, 2}.

Consider first the piezoelectric properties of lamellar diphasic composites. Longitudinal piezoelectric coefficient d_{33} has been derived for a diphasic piezoelectric with the constituent phases arranged in alternating layers normal to the N_3 direction (Figure 6a). Designating phase 1 with a superscript 1, and phase 2 with superscript 2, phase 1 has volume fraction 1_v , piezoelectric coefficient d_{33}^1 , and permittivity ϵ_{33}^1 , and

phase 2 has 1v , $^2d_{33}$, and $^2\epsilon_{33}$, respectively. Solving for the piezoelectric coefficient of the composite gives

$$\bar{d}_{33} = \frac{^1v^1d_{33}^2\epsilon_{33} + ^2v^2d_{33}^1\epsilon_{33}}{^1v^2\epsilon_{33} + ^2v^1\epsilon_{33}} \quad (1)$$

Using the relation $g_{33} = d_{33}/\epsilon_{33}$ yields the piezoelectric voltage coefficient

$$\bar{g}_{33} = \frac{^1v^1d_{33}}{^1\epsilon_{33}} + \frac{^2v^2d_{33}}{^2\epsilon_{33}} = ^1v^1g_{33} + ^2v^2g_{33} \quad (2)$$

It is interesting to note that for series connection even a very thin low-permittivity layer rapidly lowers the d-coefficient but has little effect on the corresponding g-coefficient.

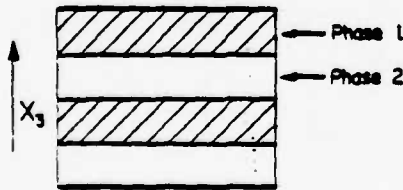
3.3 Composites: Parallel Connection

If the two phases lie in layers perpendicular to the electrode (Figure 6b), again for the one-dimensional case and neglecting transverse coupling, the composite piezoelectric coefficient is

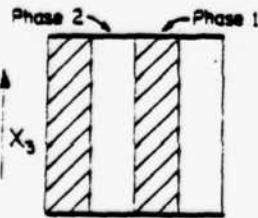
$$\bar{d}_{33} = \frac{^1v^1d_{33}^2s_{33} + ^2v^2d_{33}^1s_{33}}{^1v^2s_{33} + ^2v^1s_{33}} \quad (3)$$

where $^1s_{33}$ and $^2s_{33}$ are the elastic compliance for stresses normal to the electrodes. For the voltage coefficient,

$$\bar{g}_{33} = \frac{^1v^1d_{33}^2s_{33} + ^2v^2d_{33}^1s_{33}}{(^1v^2s_{33} + ^2v^1s_{33})(^1v^1\epsilon_{33} + ^2v^2\epsilon_{33})} \quad (4)$$



(a)



(b)

Fig. 6 The series (a) and parallel (b) models used in estimating the piezoelectric and pyroelectric effects of diphasic solids.

A composite of interest here is that of an elastically compliant nonpiezoelectric in parallel with a stiff piezo-

electric. In this case $^1d_{33} > ^2d_{33}$, $^1s_{33} < ^2s_{33}$, $^1v = ^2v = 1/2$ then $\bar{d}_{33} \approx ^1d_{33}$, and if $^1\epsilon_{33} > ^2\epsilon_{33}$, $\bar{g}_{33} \approx ^1g_{33}$, and for smaller volume fractions of the piezoelectric phase, the g-coefficient is correspondingly amplified. It is this case which accounts for the highly successful performance of the replamineform transducer structure described in a later page. The structure also has considerable hydrostatic sensitivity.

3.4 Hydrostatic sensitivity

A problem arises when one attempts to use solid PZT as a hydrostatic sensor because d_{33} is approximately equal to $-2d_{31}$, resulting in a low piezoelectric response to hydrostatic pressure change. Since sizeable \bar{g}_{33} coefficients can be obtained for composites with parallel connection, it is interesting to inquire into the hydrostatic sensitivity of this type of connectivity².

To evaluate the effective hydrostatic sensitivity for parallel connection, it is necessary to evaluate the transverse piezoelectric coefficient \bar{d}_{31} since $P_3 = -p(\bar{d}_{33} + 2\bar{d}_{31})$ where p is the applied hydrostatic pressure. Since the PZT rods are connected in series in the lateral directions it can be shown that $\bar{d}_{31} \approx ^1v^1d_{31} + ^2v^2d_{31}$. This leads to a hydrostatic piezoelectric coefficient

$$\bar{d}_h = \bar{d}_{31} + \bar{d}_{33} = \frac{^1v^1d_{31}^2s_{33} + ^2v^2d_{31}^1s_{33}}{^1v^2s_{33} + ^2v^1s_{33}} + \frac{^1v^1d_{33}^2s_{33} + ^2v^2d_{33}^1s_{33}}{^1v^2s_{33} + ^2v^1s_{33}}$$

Suppose for the composite we choose equal volumes of piezoelectric PZT (phase 1) and a soft elastomer (phase 2) such that $^1v = ^2v = 1/2$, $^1s_{33} < ^2s_{33}$, $^1d_{33} > ^2d_{33}$, and $^1d_{33} \approx -2^1d_{31}$. For the composite $\bar{d}_{31} \approx 1/2^1d_{31}$ and $\bar{d}_{33} \approx ^1d_{33}$, giving $\bar{d}_h \approx 1/2^1d_{33}$.

This is a considerable improvement over single phase performance. Since the hydrophones used under hydrostatic conditions are normally voltage generators, the further favourable enhancement of the voltage coefficient \bar{g}_h can also be exploited: $\bar{g}_h = \bar{d}_h/\epsilon_{33}$. Lowering the permittivity ϵ_{33} increases the sensitivity to small pressure changes by raising \bar{g}_h .

4. Piezoelectric Composites with 3-1 Connectivity

Considering the parallel connectivity described above, the ideal three

dimensional case is one of PZT rods embedded in a continuous polymer phase, that is, 3-1 connectivity (section 2.2). According to this equal strain composite theory, \bar{d}_{33} should not be a function of the volume fraction of PZT in the composite. This assumes an idealized situation in which the polymer phase is far more compliant than PZT, causing all the stress on the polymer to be transferred to the PZT rods. That is, as the volume fraction of PZT decreases, the stress on the rods increases proportionally, so that the charge per unit area of the composite is constant. For pressure sensors, it is not necessary that \bar{d}_{33} be large in order to enhance the \bar{d}_h coefficient of the composite. If, as the volume fraction of PZT is decreased, d_{31} decreases more rapidly than d_{33} , then \bar{d}_h will be increased. Likewise, if ϵ_{33} decreases more rapidly than \bar{d}_h , as the volume fraction PZT decreases, then \bar{g}_h will be enhanced.

4.1 Fabrication Method

The thin PZT rods required for 3-1 composites must be sintered to near theoretical density (7900 kgm^{-3}) before they can be poled. For the composite transducers described here, the rods are formed by extrusion of a PZT-organic binder slip^{1,8}.

Ninety weight percent of PZT is mixed with a solution of 2% polyvinyl alcohol and 8% water, and the mixture ball milled for 16 hours to homogenize the slip. Further homogenization is achieved by repeatedly extruding the slip through a one mm diameter die. The PZT rods are then extruded onto a moving glass plate, dried for ten hours at 120°C , cut into 3 cm lengths and heated at 550°C for 30 minutes to burn out the binder. Sintering is carried out at 1300°C for 30 minutes in the presence of a PbO vapor source composed of 97 mole % PZT and 3 mole % PbO to compensate for lead loss. To reduce porosity and improve their dielectric breakdown strength, the sintered rods are refired in a hot isostatic press (HIP) for one hour at 1300°C under 20 MPa argon pressure. Use of the HIP unit increases the relative density of the rods from 0.94 to about 0.98. PZT rods ranging between 200 and 840 μm in diameter have been used in the composites.

A fixture consisting of two brass discs, each with an array of holes, is used to align the rods (Figure 7).

Several hole patterns have been drilled for each of the rod sizes so that composites of 50, 40, 30, 20 and 10 volume % PZT can be prepared. When a rack has been filled with rods it is placed in a plastic tube and the tube filled under vacuum with the appropriate epoxy resin, thus ensuring complete investment of the rods by the polymer. The epoxy is cured at 70°C for sixteen hours, and segments 1.2, 3 and 4 mm in thickness are cut from the slug (Figure 7) with a diamond saw. The excess epoxy around the composite is trimmed off so that a uniform composite remains.



Fig. 7 Fabrication of 3-1 composites with PZT rods and an epoxy.

Air-dry silver electrodes were applied and the samples poled in a 75°C oil bath for five minutes using a field of 2.2 MVm⁻¹. Permittivity was measured at 1 kHz using a capacitance bridge, and the piezoelectric coefficient determined with a d_{33} -meter using two rounded rams. The hydrostatic piezoelectric coefficient (d_{h1}) was measured by altering pressure in an oil chamber at a rate of 3.5 MPas⁻¹ and collecting the charge with an electrometer connected in a feedback integration mode which maintained constant electric field conditions.

4.2 Piezoelectric Coefficients

To providing a better understanding of piezoelectric composites, the following factors have been varied: volume fraction PZT, rod diameter, and sample thickness. Specifying the rod diameter and volume fraction PZT automatically fixes a fourth factor: the distance between rods. Obviously, if the stress on the polymer is to be transferred to the PZT rods, the distance from a particular point in the polymer to the nearest rod is important. For a given volume fraction of PZT, the rods are much closer together in composites with small rod diameters, and with closely-spaced rods, the composite becomes more

piezoelectrically homogeneous.

Figure 8 shows that for PZT volume percentages down to 40% the \bar{d}_{33} coefficients are comparable to the value of d_{33} for solid PZT, about 400 pC/N. Below 40% PZT, the d_{33} values decrease, but even at 10% are still greater than half the value for pure PZT.

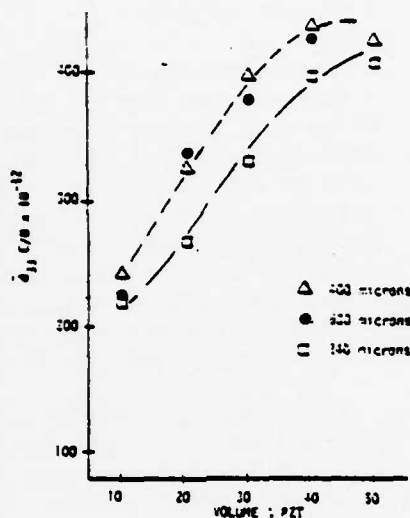


Fig. 8 \bar{d}_{33} vs volume % PZT.

The data shown in Figure 8 were measured on composites 4 mm thick. \bar{d}_{33} values for composites of 3.2 and 1 mm thickness were also measured, and a thickness effect was observed. For all composites the d_{33} coefficients decreased with increasing thickness. The magnitude of the thickness effect was a function of rod diameter, volume fraction PZT and separation between the rods.

4.3 Permittivity and Voltage Coefficient

The dielectric constant of a 3-1 composite can be estimated from a model based on two capacitors connected in parallel. The value of $\bar{\epsilon}_{33}$ varies linearly with volume fraction, and since the dielectric constant of PZT is about 1600, and that of the epoxy is about 7, the value of $\bar{\epsilon}_{33}$ may be approximated as 1600 v , where v is the volume fraction of PZT. Experimental values of $\bar{\epsilon}_{33}$ agree well with the theoretical values, as shown in Figure 9.

The piezoelectric voltage coefficient under uniaxial loading is defined as $g_{33} = d_{33}/\epsilon_{33}$. The g_{33} coefficient of solid PZT is approximately 29×10^{-3} VmN⁻¹. Figure 10 shows the dependence of \bar{g}_{33} on volume fraction of

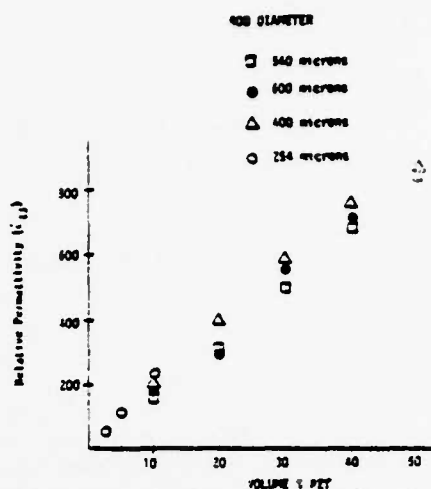


Fig. 9 Relative permittivity as a function of volume % PZT.

PZT and on rod diameter for composite samples 4 mm thick. While there is little dependence on rod diameter, the magnitude of \bar{g}_{33} is greatly affected by volume fraction. A composite of 254 μ m diameter rods with a volume fraction of 0.025 PZT has a piezoelectric voltage coefficient nearly nine times greater than that of pure PZT. All the 3-1 composites have larger g_{33} coefficients than solid PZT.

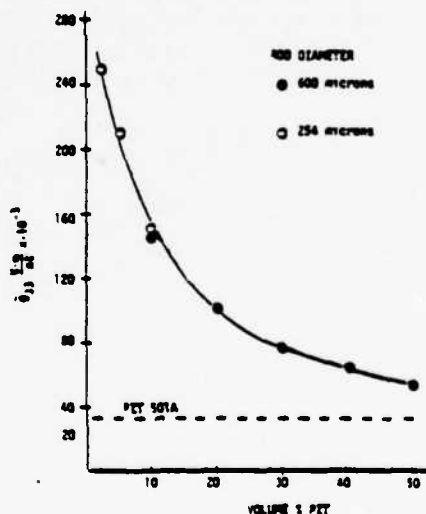


Fig. 10 \bar{g}_{33} as a function of volume % PZT.

4.4 Hydrostatic Piezoelectric Effects

In figures 11-13, d_{h1} is plotted as a function of composite thickness, rod diameter and volume % PZT. As observed in the d_{33} measurements, the hydrostatic piezoelectric coefficient is a function of sample thickness. For most of the composites, the d_{h1} values are substantially larger than that of pure PZT. Solid ceramic pellets identical in composition with the PZT rods have an average d_{h1} of 31 pC/N.

As predicted, composites with

lower volume fractions of PZT have higher values of d_h . Theory² indicates that d_{31} should decrease linearly with the volume fraction of PZT while d_{33} remains constant. If this were true, d_h should increase linearly as the volume fraction of PZT decreases. However, the measurements indicate that d_{33} decreases when the volume fraction of PZT drops below 40% PZT. If both d_{31} and d_{33} decreased with PZT content, then d_h might decrease, or increase, or remain constant as the volume % PZT decreased. As shown in Figure 12 all of these occur. In composites made with 840 micron diameter rods, d_h decreases with volume fraction PZT. For composites containing 600 micron rods, d_h is nearly constant from 50% to 20% PZT, while the composites made with 400 micron rods show an increase in d_h over the same range. Although the 10% composites have the lowest d_h coefficients for all the rod sizes, these samples show the largest increases in d_h with each reduction in rod diameter. From the data it appears that if the rod diameter could be further reduced, the 10% composites would have the largest hydrostatic piezoelectric coefficient. The fact that the composites with the lowest volume fraction of PZT have the highest d_h is consistent with theory, but the magnitude of the experimental d_h values are less than one third the theoretical values. It must be remembered that the theory called for a second phase which was much more compliant than the piezoelectric phase, and since epoxy is a stiff polymer, better agreement with

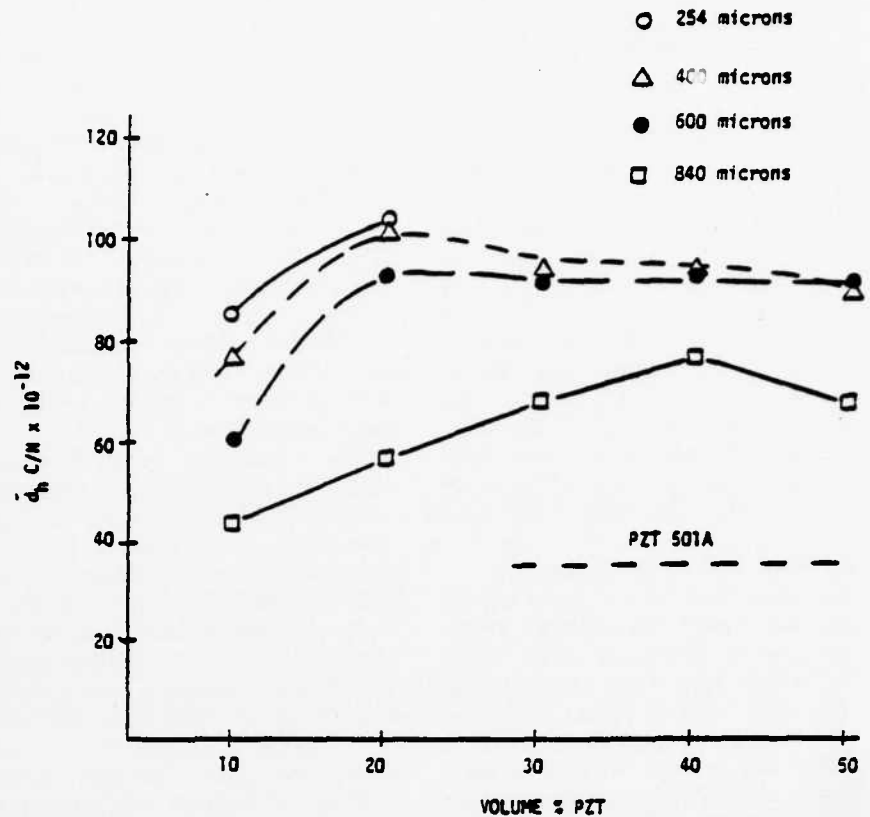


Fig. 12 d_h as a function of volume % PZT and rod diameter (sample thickness 4 mm).

the theory is expected when an elastomer is used as the second phase.

The hydrostatic voltage coefficient g_h is equal to d_h divided by ϵ_{33} , the composite permittivity measured in the poling direction. Composites with substantial values of d_h and small volume fractions of PZT, have extremely large hydrostatic voltage coefficients. Figure 13 shows a plot of g_h for the data shown in Figures 9 and 12. The dotted line in Figure 13 is the value of

g_h for solid PZT. A 10% PZT composite made from 254 micron rods has a voltage coefficient more than twenty-five times that of the solid PZT. Although use of a more compliant matrix would not appreciably affect ϵ_{33} , the resulting enhancement of d_h would cause a corresponding increase in g_h .

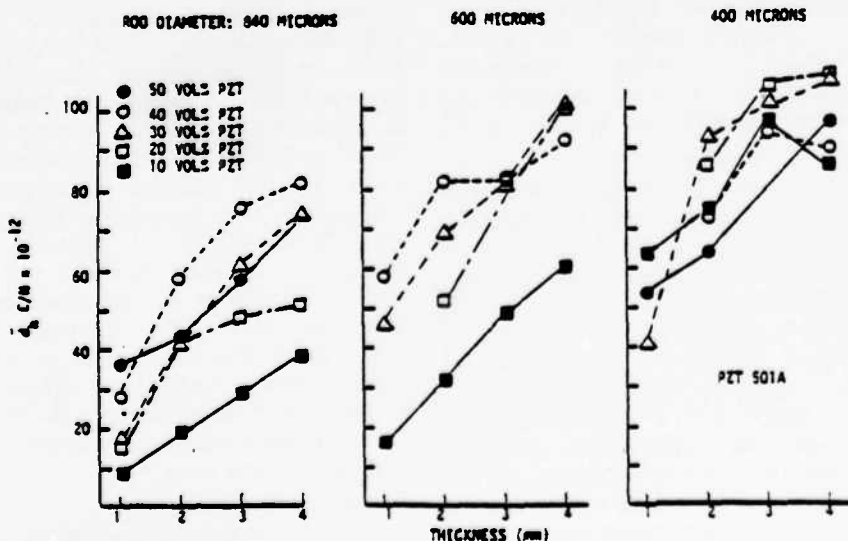


Fig. 11 d_h as a function of volume % PZT, rod diameter and composite thickness.

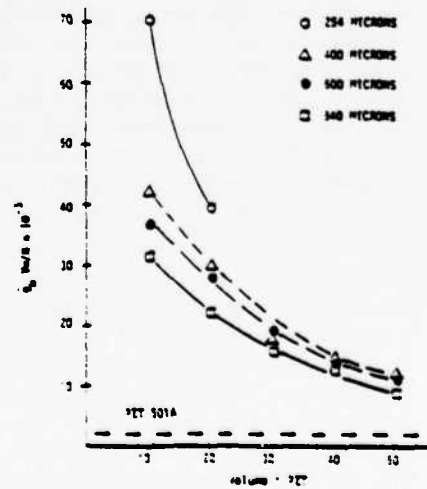


Fig. 13 g_h as a function of volume % PZT

4.5 Specific Gravity

The density of a composite transducer is important because of weight considerations and acoustic impedance matching to the load. Density and

acoustic velocity differences between the transducer and the surrounding medium cause reflection losses due to mismatch in acoustic impedances. Reducing the density of the transducer to a value near that of water may help to minimize these losses, at least in the quasi-static case.

The density of the composite can be adjusted between the density of PZT ($7,900 \text{ kgm}^{-3}$) and that of the epoxy (about 1000 kgm^{-3}). It is important to note that the greatest values of \bar{d}_{31} , \bar{g}_{31} , and \bar{g}_{33} are all found in the composites with low volume fractions of PZT. Therefore the desired properties of low density and large piezoelectric coefficients are obtained with the same composites.

4.6 Other Fabrication Methods

The production of 3-1 composites is not limited to the use of extruded rods. Rods, bars, fibers, or other small PZT elements may be made by other techniques such as dicing a sintered PZT ceramic, dipping cloth thread in a PZT slip or solution, or spraying a thread with PZT slip and then burning out the thread and sintering the PZT. A sintered PZT slug might be cut in a criss-cross manner with a diamond saw to produce an array of PZT columns of desired dimension and spacing. The manner in which the rods are produced is not important. Neither is the technique in which the rods are aligned. We have aligned rods by moving the discs of the alignment rack close together so that rods aligned in the rack protrude several millimeters beyond the end of the rack. By positioning the array upright in a shallow dish, a single composite may be made by pouring epoxy into the dish to the depth of the desired composite thickness. This technique is especially useful when making composites with an elastomer matrix.

Composites may be made with a matrix other than epoxy. A matrix of a polyester resin results in \bar{d}_{31} , \bar{g}_{31} , \bar{d}_{33} , and \bar{g}_{33} coefficients comparable to those obtained with epoxy composites. Composites have been made with elastomers such as silicone rubber and polyurethane. Transducers made with these elastomers are mechanically flexible. Because of the difficulty of cutting or sawing elastomer composites without breaking the PZT rods, such composites must be cast to size as just described.

4.7 Continuous Poling of PZT Fibers

With normal fabrication procedures, the composite thickness is limited by the size of the electric field required to pole the piezoelectric component. At 2.2 MVm^{-1} poling field, 10kV power supply restricts the thickness of PZT-polymer composites to about 5 mm. The continuous poling technique developed by Gururaja¹⁹ eliminates this problem by using pre-poled PZT rods of any length. The pre-poled rods can also be used to fabricate composites in which rods are aligned in many different patterns, making new transducer designs feasible.

The continuous poling technique utilizes the idea of gradually advancing a rod between two electrical contacts maintained at the required potential difference. Electrical contact to the PZT rods is achieved in two ways.

In the first method, the wetting behaviour of a low-melting solder with copper is utilized to form a molten film of solder over a circular hole (2.4 mm in diameter) in a copper plate (2 mm thick). The entire system is immersed in an oil bath maintained at 150°C . The surface tension and the upward thrust of the heated oil keep the molten film stable. A second copper plate is positioned 2.4 mm away from the first plate to provide the second electrical contact.

In the second method, conductive carbon foam is attached to both the top and bottom copper plates using a conductive epoxy. The PZT rods are pulled through the foam attached to the copper plates, in an oil bath maintained at 80°C . The separation between the two electrodes and the pulling rate are the same as in the molten-solder method. An electric field of $1.6\text{--}1.8 \text{ MVm}^{-1}$ is required to pole the rods to saturation because the poling temperature is only 80°C .

4.8 PZT Spheres

Initial work on PZT-polymer composites undertaken by Harrison and co-workers¹⁷ utilized coarse granules of sintered PZT rather than PZT rods. A schematic drawing of this PZT-loaded polymer film is shown in Figure 5b. Silicone rubber was used as the matrix material because of its flexibility over a wide temperature range. The piezoelectric properties were optimized by adjusting the size of the granules and the volume fraction of PZT. Typical values were given in Table 2.

PZT granules of irregular shape assume a variety of orientations with respect to the parallel surface of the composite and thus grinding does not expose every granule to the electroded surface. For poling of the PZT elements to occur, these elements must be in electrical contact with both electroded surfaces. Therefore, composites fabricated from irregular granules are The inactive PZT fragments not only detract from piezoelectric response of the composite but also increase the density and decrease the flexibility unnecessarily.

Similar composites have been fabricated by Safari and Bowen²⁰ using PZT spheres instead of irregular granules. Spheres offer several potential advantages over irregularly shaped particles. Composites are easily fabricated by pouring the spheres into a pan to form a mono-layer, and then covering them with the polymer phase. A light sanding exposes the PZT, allowing contact to both electrodes. This results in excellent poling and piezoelectric activity.

There is the possibility of stress modification in the PZT sphere composites since the compressive stress is born primarily by the small regions at the top and bottom exposed to the electroded surface, resulting in a tensile orthogonal stress. The sign of \bar{d}_{31} is thus reversed near the perimeter of the spheres, where the ceramic is under tension, and \bar{d}_{33} may be enhanced (section 3.4). Piezoelectric voltage coefficients \bar{g}_{33} and \bar{g}_{31} may also be enhanced because of the low permittivity.

5. Piezoelectric Composites with 3-3 Connectivity

As shown in the previous section, a composite with 3-1 connectivity makes an effective piezoelectric transducer. Since, however, in firing the ceramic fibers one must maintain this orientation, some interconnections between the rods are helpful; i.e. partial 3-3 character is required. In a 3-3 template, both phases are continuously connected in all three dimensions. This type of structure is exhibited by certain polymer foams, some diphasic glasses, three-dimensionally woven materials, and by biological substances such as wood and coral.

5.1 Replamine Process

Coral skeletons are characterized by a structure with the following features:



Fig. 14 The replamine "lost-wax" fabrication process.

(i) a narrow pore size distribution; (ii) a pore volume approximately equal to the solid phase volume, and (iii) complete pore interconnectivity making every pore accessible from all other pores. The dimensions of the pores vary from species to species, but within one species the size range is quite narrow. Different species of coral have various degrees of anisotropy in their structure ranging from a 3-1 connectivity of nearly parallel tubes to highly isotropic 3-3 structures. Figure 4 shows a micrograph cube of the calcium carbonate skeleton of the coral species *goniopora* which we have used as a structural template for making composite transducers. The replicating technique, known as the replamineform process, was developed at the Materials Research Laboratory at Penn State for producing prosthetic materials⁹. We chose the replamineform process for reproducing the 3-3 connectivity type because of past experience with this procedure, although other preparation techniques may be more practical.

The first step of the replamine process (Figure 14) is to shape the coral, which is easily machinable, to the desired geometry. The coral template is then vacuum-impregnated with a casting wax and the wax allowed to harden, after which the calcium carbonate coral skeleton is leached away in hydrochloric acid leaving a wax negative of the original coral template. The negative is re-

invested with a PZT slip (average grain size $\sim 2 \mu\text{m}$) containing PZT, water, and poly(vinyl alcohol). Investment is carried out by vacuum impregnation with vibratory action to render the thixotropic PZT slip fluid. The wax negative is burned off leaving a coral-type structure of PZT which is then sintered for one hour at 1300°C . A 13% linear shrinkage is observed in the replicas, but the replicated pore structure is maintained. The PZT replica is back-filled with a suitable polymer such as a high purity silicone

rubber, and, after the surface has been cleaned, a silver-loaded silicone rubber electrode is applied. The composite is then poled at a field strength of 1.4 MVm^{-1} for 5 minutes at 100°C . Relative permittivity of the unbroken composite, as determined with a capacitance bridge, is about 100. The



Fig. 15 Flexibility in a PZT/silicone rubber composite fabricated using the Replamine process.

average longitudinal piezoelectric coefficient \bar{d}_{33} obtained for the unbroken composite is approximately 160 pCm^{-1} . As poled, the replamine replica is still a rigid structure because of the three-dimensional connectivity of the ceramic phase. If, however, the body is now crushed to break the ceramic connectivity, an extremely flexible piezoelectric composite results (Figure 15). Crushing is carried out by reducing the sample height to about 80% of its original value and simultaneously shearing the sample 20% of the sample

TABLE 2 Hydrostatic Mode Materials

	K_{33}	d_h pCm^{-1}	g_h 10^{-3}VmN^{-1}	$d_h g_h$ $10^{-15} \text{M}^2 \text{N}^{-1}$
Ceramics				
PZT Type I	1300	45.9	4	180
PZT Type II	1700	30.0	2	60
PbNb_2O_6	225	67.6	34	2300
Flexible Composites				
PZT Particles in a Silicone Rubber Matrix	100	28.3	32	900
PZT Replamine in a Silicone Rubber Matrix	50	35.8	80	2800
PZT Cubes in a Silicone Rubber Matrix	715	25.2	4	100
PZT Rods in an Epoxy Matrix (3-1 Connectivity)	200	77.6	40.4	3138
Polymer				
PVF ₂	12	11.5	108	1246

height about an axis perpendicular to the crushing force direction.

By breaking the poled ceramic the easy electric flux path through the poled piezoelectric is interrupted, thus lowering the permittivity. The pieces of poled piezoelectric are still held in position by the polymer matrix and will therefore still transmit stress. As a result, the \bar{d}_{33} coefficient remains high while the permittivity is reduced and thus the longitudinal piezoelectric voltage coefficient, \bar{g}_{33} ($= \bar{d}_{33}/\bar{\epsilon}_{33}$), is greatly enhanced with respect to the g value of a homogeneous ceramic piezoelectric.

After disrupting the connectivity of the PZT phase by crushing the sample, the relative permittivity is reduced to about 40, while \bar{d}_{33} is only reduced to about 100 pC/N. Hence, the \bar{g}_{33} values of these flexible composites are approximately 300×10^{-3} VmN⁻¹, which is fifteen times better than a homogeneous PZT transducer. Table 2 contains a comparison of transducer characteristics, from which it is obvious that the replamine composite of PZT and silicone rubber compares very favourably with homogeneous transducer materials for passive device applications. The compliance of the composite is large compared to solid PZT, imparting mechanical shock resistance.

5.2 Alternative Fabrication Methods

Several alternative methods of making 3-3 transducer composites have been suggested^{1,2,3}, utilizing simpler fabrication techniques than the coral replamine process.

The method proposed by Shrout²¹, involves the use of a volatile phase in the fabrication procedure. Commercially available PZT powder is mixed with polymethyl methacrylate (PMM) spheres (50 to 150 μ m diameter) in a 30/70 volume ratio. The mixture is die-pressed using poly(vinyl alcohol) as a binder and the binder and PMM spheres volatilized out by very slowly heating the pressed pellet to 400°C. After sintering at 1300°C for 0.5 hours the cold highly porous pellets are vacuum impregnated with a suitable polymer: either a flexible silicone rubber elastomer or a stiff epoxy resin.

SEM micrographs of the PZT-epoxy composites are shown in Figure 16. A similar microstructure is observed in the PZT/silicone rubber compo-

sites. It is clearly seen that the two phases are randomly interconnected. The size of the PZT phase regions ranges from a few microns to 100 microns, whereas the polymer regions range from 20 to 120 μ m and are quite spherical in nature. The replamine microstructure is somewhat more open with polymer regions in the order of 500 μ m in diameter interspersed with PZT regions of about 200 μ m diameter. Piezoelectric properties are similar to the replamine materials. When filled with silicone rubber, \bar{d}_{33} is about 200 pC/N⁻¹ and \bar{g}_{33} about 170×10^{-3} VmN⁻¹. The piezoelectric coefficients are somewhat lower with an epoxy filling: $\bar{d}_{33} \sim 90$ pC/N⁻¹, $\bar{g}_{33} \sim 90 \times 10^{-3}$ VmN⁻¹. The principal advantage of this method is that it is readily adapted to mass production.

Interconnected PZT-polymer composites have also been made by Nagata and co-workers²². Using an undisclosed powder preparation technique, porous Pb (Zr_{0.53}Ti_{0.47})O₃ ceramics were conventionally sintered to a volume fraction of 48%. Silicone rubber was injected to fill the pore channels giving 3-3 connectivity. Volume fractions are about 50% for the two phases, and skeletal diameters about 20 μ m. Poled specimens exhibit \bar{g}_{33} coefficients of 130×10^{-3} VmN⁻¹, increasing the hydrophone sensitivity to nearly four times that of solid PZT ceramics.

Miyashita, Takano and Toda (1979) have synthesized a more regular PZT-polymer composite resembling a ladder structure made from thin strips of PZT. Specimens with porosity levels in the 40 to 60% range have good \bar{g}_{33} coefficients of 90×10^{-3} VmN⁻¹.



Fig. 16 PZT-epoxy composite fabricated by mixing organic spheres with the PZT prior to sintering (Light grey phase is PZT).

6. Piezoelectric Composites with 2-2

Connectivity

Piezoelectric composites with multilayer structures (2-2 connectivity) have been fabricated to give (i) enhanced electromechanical coupling under high driving fields, (ii) high

stability electrical filters and (iii) improved impedance matching.

6.1 Tape-cast Composites

Tape-casting provides a convenient way of making thin ceramic layers, approximately 250 μ m thick²⁴. In the tape-casting process, a ceramic powder is mixed with a liquid organic binder to form a homogeneous slurry, which is then spread in a thin continuous layer onto a moving glass substrate. The thickness and uniformity of the sheet are controlled by a series of knife edges set parallel to the surface of the glass plate and a fixed distance above it. After drying, the organic binder hardens to give a flexible plastic tape impregnated with ceramic powder. The tape can be cut to size and sintered in the normal way. Green density and sintering characteristics can be modified by a post casting pressing operation so that materials which normally would sinter at different rates can be fired together without problems arising from uneven shrinkage. To fabricate multilayer composites, the component layers are stacked alternately and pressed together at about 50°C to obtain a firm bond before firing²⁵.

Using this technique, lamellar heterogeneous devices comprised of layers of a commercial soft ferroelectric (modified PZT) and an antiferroelectric (modified PZSnT) have been produced²⁶. The purpose of the antiferroelectric layers is to prevent depoling of the soft ferroelectric phase under high electric fields, since the antiferroelectric has a large coercive field. Series model calculations show that a high piezoelectric coefficient can be obtained if a high permittivity antiferroelectric phase is employed. By selecting a temperature (90°C) at which the antiferroelectric had maximum coercive field, it was shown that antiferroelectric-ferroelectric composites were dielectrically more stable (harder) under high field cycling than a typical commercially used hard PZT.

In another 2-2 connected composite, layers of lead magnesium niobate Pb₃MgNb₂O₉ alternated with layers of 0.8Pb₃MgNb₂O₉-0.2PbTiO₃ have been used to form a temperature-stable resonator for electrical filter applications²⁷. These two materials have compensating positive and negative temperature coefficients of elastic compliance. As a result, changes of

less than 60 ppm/°C in the radial resonant frequency over a temperature range between -10°C and 80°C have been obtained.

In a third application, multilayered composites of poled PZT incorporating platinum metal internal electrodes have been developed for applications where electrical impedance matching is important²⁸. The basic electrode configuration used in the piezoelectric devices is similar to that employed in multilayer capacitors. In such a device the poling of alternate layers is of opposite direction but the responses are additive in either a driven or driver mode. Thus, the voltage required to produce a given displacement is found to be greatly reduced compared to homogeneous devices of the same PZT composition, and the measured direct \bar{d}_{33} is increased by a factor approximately equal to the number of internal electrodes employed. Resonant properties are unaffected by the presence of the internal electrodes²⁸.

Consequently, internal electrodes can be incorporated into piezoelectric transformers in order to increase their step-up ratio. Here the transformer ratio is multiplied by the number of layers introduced into the primary end of a conventional bar-shaped transformer²⁹. A second advantage is that the ends of the internal electrodes, which act as the low side of the secondary circuit allow a more uniform poling and larger electrode area, thereby increasing the current capacity and hence the power of the secondary. If DC isolation of the primary and secondary

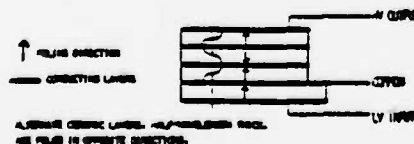


Fig. 17(a) Series resonant device for bandwidth reduction, composed of half-wave-length thick piezoelectric layers separated by electrically-conducting epoxy.

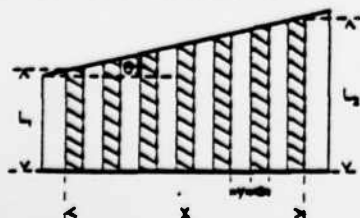


Fig. 17(b) Parallel resonant device for broadband applications. Piezoelectric layers (shaded) are decoupled mechanically by an inactive, low Q polymer.

is required, a thin section of strip electrodes may be included as the low side of the secondary circuit.

6.2 High Frequency Applications

Piezoelectric composites are not limited to low frequency applications. A 2-2 connected temperature-compensated resonator material composed of lead magnesium niobate and lead titanate has already been described (Section 6.1). Another high frequency application involves bandwidth modification in electrical filters.

Electrical circuits operating at high frequency often require some form of frequency control to limit the pass band of frequencies. This control can take the form of piezoelectric crystal or ceramic component shaped so that the frequency range of interest coincides with a resonance frequency of the piezoelectric element. At resonance the piezoelectric filter has

minimum impedance, several orders of magnitude lower than its nonresonant impedance. Consequently, the element readily passes signals at frequencies close to its resonant frequency, the width of the pass band usually being defined by the mechanical Q of the device as $Q =$

$\frac{f}{\Delta f_{3dB}}$ for $Q > 10.0$. Here f is the center frequency and Δf_{3dB} is the (power) 3 decibel pass band. For ceramic piezoelectrics the mechanical Q is typically in the range of 50 - 1000, giving 3dB bandwidths in the range 0.1 - 2% of the center frequency. Using composite devices, it is possible to reduce or widen the bandwidth of a piezoelectric material by combining several active piezoelectric elements mechanically in series or in parallel respectively.

A reduction in bandwidth can be obtained by carefully grinding several piezoelectric discs to the same thickness and bonding them together in a series configuration using an electrically conducting epoxy resin, as shown in Figure 17(a). For the fundamental thickness mode of a single disc, the resonant frequency is governed by the equation:

$$f_L = \frac{1}{2L} \sqrt{\frac{1}{\rho s}}$$

where ρ is the density and s the elastic compliance. The disc thickness L is equal to half the acoustic wavelength. Therefore, since the sign of the stress changes every half wavelength, in order to resonate in phase the polarity of adjacent discs must be reversed.

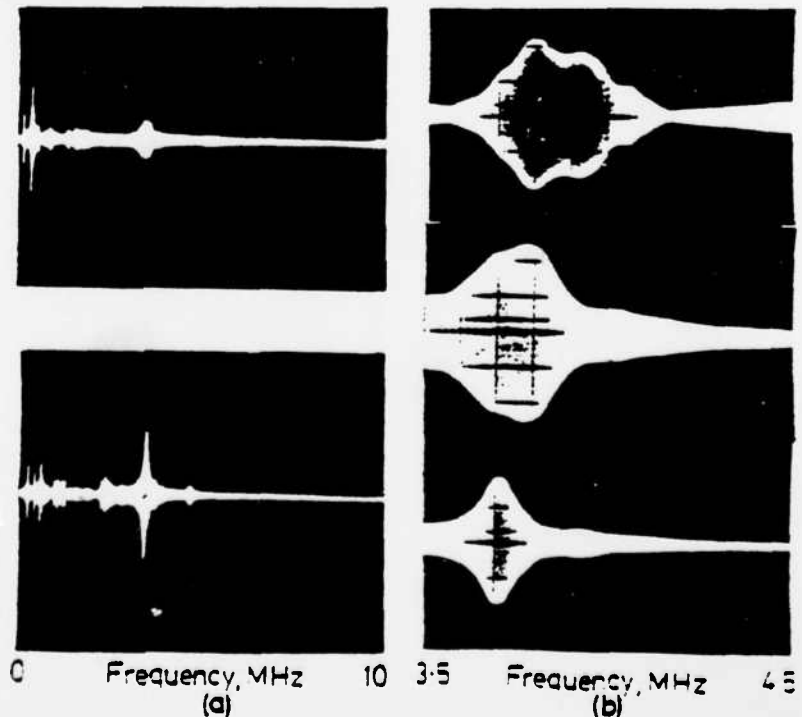


Fig. 18(a) Increase in amplitude of thickness mode resonance for series, connected resonant composites (3 layers thick).

Fig. 18(b) Decrease in bandwidth of thickness mode. From Top: single layer, 2 layer, 3 layer case.

Acoustic wave transmission occurs only at frequencies very close to f_L and consequently the bandwidth is reduced. Using one PZT disc as a driver or "primary" Figure 17(a), the output from the "secondary" (Figures 18(a) and 18(b)) is reduced in bandwidth and increased in amplitude compared to a single disc of the same material. The increase in amplitude arises because the device also acts as a piezoelectric transformer²⁹.

A similar composite device, capable of operation at microwave frequencies, has been developed³⁰ using cadmium sulfide as the active piezoelectric element. The CdS layers are separated by inactive half-wavelength-thick films of silicon monoxide so that polarity reversal is unnecessary.

One problem associated with series multilayer transducer designs is the extremely accurate dimensional tolerances which must be achieved if constructive interference is to be achieved³¹. Moreover in many applications, the reduction in bandwidth and increase in amplitude are simply trade-offs, and do not result in an overall increase in conversion efficiency³². Since narrow bandwidth materials are abundant ($Q > 10^4$ for quartz), it seems likely that series-connected multilayer filters will find only limited applications.

Although narrow band pass filters are readily available for most frequency ranges of interest, broadband filters, in which bandwidths up to 50% of the center frequency are required, are more difficult to produce. Apart from electrical filters, broadband devices are being employed in acoustic imaging, especially for noninvasive medical uses, and nondestructive flaw detection³³⁻³⁶. Ultrasonic imaging has an advantage over its optical counterpart of improved contrast, since it relies for contrast on elastic discontinuities which are generally of greater magnitude than changes in refractive index, particularly in biological tissue. In acoustic imaging the piezoelectric element acts as both source and detector in a "pulse-echo" operational mode^{37,38}. At present the image is built up by mechanically scanning a single transducer over the area of interest, and integrating its output to form a coherent picture³⁹. Typical commercial broadband transducers for biomedical applications are shown in Figure 19.



Fig. 19 Ultrasonic transducers for medical diagnostic applications in echocardiography and two-dimensional imaging. (Photographs courtesy of KB-Aerotech, Lewiswood, Pa.)

Previously, bandwidth has been increased^{39,40} by: (i) electrically connecting narrow bandwidth filters with slightly different resonance frequencies in parallel, (ii) damping the resonance of a low Q piezoelectric element in order to spread the resonance peak over a wider frequency range, or (iii) impedance matching piezoelectric transducers to the load with quarter-wave acoustic transformers. Methods (i) and (iii) have the disadvantages of extreme complexity, and in method (ii) much of the input energy is wasted by damping.

Based on the equation for f_L , it is possible to fabricate a broad bandwidth electromechanical transducer from a single piezoelectric element by forming the element into a wedge shape of varying thickness and driving it at frequencies corresponding to resonance of the thickness dimensions. In this case the thickness mode resonance encompasses a range of frequencies governed by its maximum and minimum dimensions. However, since the element is strongly mechanically coupled at all points, destructive mechanical interference occurs between regions of different thickness resonating at different frequencies, and low efficiency results.

Connecting piezoelectric ceramic elements in parallel with a mechanically lossy polymer can overcome the shortcomings of the wedge configuration,

and produce an efficient broadband device. In this application many piezoelectric elements with different dimensions are used to provide a wide pass band, but the elements are combined into a single array using an inactive, low Q polymer which decouples the elements mechanically and prevents interference. The device consists of sheets of piezoelectric material, e.g. PZT, laminated with sheets of polymer so that the active elements are separated by sufficient polymer that most of the mechanical coupling between the elements is removed (see Figure 17(b)). The slope of the device, $\tan \theta$, defines its bandwidth according to the relationship:

$$\Delta f = \frac{x \tan \theta f_1 f_2}{N}$$

where Δf is the bandwidth in Hz, x is the width of the device, and f_1 and f_2 are the resonance frequencies of elements of length L_1 and L_2 , respectively, and N is the longitudinal mode frequency constant of the piezoelectric material used. The bandwidth can be increased by increasing θ as far as the natural mechanical Q of the PZT will allow.

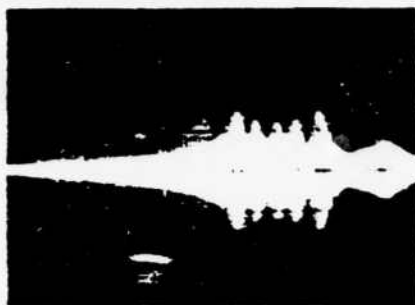
The above concept has been verified experimentally by substituting for the 2-2 connected lamellar composite a composite of soft PZT ceramic fibers embedded in epoxy, similar to those described in Section 4.1. This material has the advantage of accepting any surface profile, thus providing a greater versatility in applications. In principle, the pass band of this composite can be tailored to provide a frequency spectrum of any shape.

Figures 20(a) and 20(b) compare the frequency spectra from 0 to 1 MHz for 30 volume % PZT fibre composites with their opposite faces inclined at



Fig. 20(a) Bandwidth broadening in parallel connected resonant composites. (a) $Q=2^2$.

2° and 10° respectively. The 6dB bandwidth has been increased from 7% for a composite with faces ground parallel, to 11% for the 2° composite, and to 45% for the device with faces inclined at 10°.



0 FREQUENCY, MHz 1.0

Fig. 20(b) $Q=10^3$.

Vertical scale = amplitude

Horizontal scale = frequency.

Summary and Conclusions

Composite piezoelectric elements form an interesting family of materials which highlight the major advantages composite structures afford in improving coupled properties in solids for transduction applications. By careful consideration of the crystal symmetry, macrosymmetry, and possible modes of phase interconnection (connectivity) which can be realised by modern processing technologies, it is possible to design new composite transducers with property combinations tailored for specific device requirements.

For electromechanical applications at low frequencies where the acoustic signal has a wavelength λ much larger than the scale of the macrostructure, it is shown that ceramic:plastic composites can be designed which have mean piezoelectric voltage coefficients \bar{g}_{33} and \bar{g}_h which are orders of magnitude larger than those of the active ceramic phase. Such materials have obvious application in hydrophones and other listening devices.

Composites in other geometries can be designed so as to modify the poling and depoling characteristics of the active ceramic PZT phase, and thus to effectively stiffen the electrical characteristics against depoling under high stresses.

By prepoling ceramic PZT fibers before the composite is assembled, it is possible to construct new types of polar solid with interpenetrating polar axes and property combinations which would be impossible in the single phase solid.

For high frequency applications where λ is comparable to the scale of the composite macrostructure, the full potential of composite structures begins to become apparent. In such systems impedance, bandwidth, and radiation pattern can be controlled in a sophisticated manner which is impossible in single phase systems. For transducer arrays which could be used in focusing and scanning modes, the potential for composite structures is clear.

We believe that the composite materials offer a new versatility in property combinations, and it will be most interesting to observe how this is taken up and exploited in subsequent generations of piezoelectric devices.

References

1. R.E. Newnham, D.P. Skinner, and L.E. Cross, *Mat. Res. Bull.* 13 525 (1978).
2. D.P. Skinner, R.E. Newnham, and L.E. Cross, *Mat. Res. Bull.* 13 599 (1978).
3. R.E. Newnham, D.P. Skinner, K.A. Klinker, A.S. Bhalla, B. Hardiman and T.R. Gururaja, *Ferroelectrics*, vol. 3, p. 49 (1980).
4. J. van Suchtelen, *Philips Res. Rpts.* 27, 28 (1972).
5. J.L. Broutman and R.H. Krock, *Modern Composite Materials*, Addison-Wesley Publ. Co., Reading, Mass. (1967).
6. J. van den Boomgaard, D.R. Terrell, R.A.J. Born and H.F.J.J. Giller, *J. Mat. Sci.* 9, 1705 (1974).
7. A.M.J.G. van Run, D.R. Terrell and J. H. Scholing, *J. Mat. Sci.* 9, 1710 (1974).
8. J.F. Nye, *Physical Properties of Crystals*, Oxford University Press, London (1957).
9. R.A. White, J.N. Weber and E.W. White, *Science* 176, 922 (1972).
10. D.A. Payne, "The Role of Internal Boundaries Upon the Dielectric Properties of Polycrystalline Ferroelectric Materials," Ph.D. Dissertation in Solid State Science, The Pennsylvania State University, March 1973.
11. T. Furukawa, K. Fugino and E. Fukada, *Japan. J. Appl. Phys.* 15, 2119 (1976).
12. Landolt-Bornstein Tables on Elastic, Piezoelectric, Piezoelectric and Electro-optic Constants of Crystals, Vols II, 1 (1966) and II, 2 (1969). Springer Verlag, Berlin.
13. H. Kawai, *Japan. J. Appl. Phys.* 8, 975 (1969).
14. H. Burkard and G. Pfister, *J. Appl. Phys.* 45, 3360 (1974).
15. S. Edelman, *Proceedings of the Workshop on Sonar Transducer Materials*, Naval Research Laboratory (Feb. 1976).
16. Y. Wada and R. Hayakawa, *Japan. J. Appl. Phys.* 15, 2041 (1976).
17. W.B. Harrison, *Proceedings of the Workshop on Sonar Transducer Materials*, Naval Research Laboratory (Feb. 1976).
18. K.A. Klinker, J.V. Biggers and R.E. Newnham, *J. Amer. Ceram. Soc.* (accepted).
19. T.R. Gururaja, R.E. Newnham and L. E. Cross, *Amer. Ceram. Soc. Bulletin*, (accepted).
20. A. Safari and L. Bowen, *Private Comm.*
21. T.R. Shrout, W.A. Schulze, and J.V. Biggers, *J. Amer. Ceram. Soc.* (in press).
22. K. Nagata, H. Igarashi, K. Okazaki, and R.C. Bradt, *Japan. J. Appl. Phys.* 19, L37-40 (1980).
23. M. Miyashita, K. Takano, and T. Toda, *Proc. Int. I.E.E.E. Symp. on Appl. of Ferroelectrics*, Minneapolis, June 13-15 (1979) (to be published in *Ferroelectrics*).
24. J.C. Williams, "Doctor-Blade Process," *Treatise on Materials Science and Technology*, vol. 9 (Ceramic Fabrication Processes), F.Y. Wang, editor: p. 173, Academic Press, 1976.
25. J.V. Biggers, T.R. Shrout and W.A. Schulze, *Bull. Amer. Ceram. Soc.* 58, 516 (1979).
26. T.R. Shrout, W.A. Schulze and J.V. Biggers, *Ferroelectrics* (to be published).
27. T.R. Shrout, W.A. Schulze and J.V. Biggers, *Ferroelectrics* (to be published).
28. L.J. Bowen, T.R. Shrout, W.A. Schulze and J.V. Biggers, *Ferroelectrics* (to be published).
29. H.W. Katz, "Solid State Magnetic and Dielectric Devices", Wiley, 1959, Chapter 5.
30. J. de Klerk, P.A. Klemens and E.F. Kelly, *Appl. Phys. Lett.*, 7 265 (1965).
31. R. Holland and E.P. EerNisse, "Design of Resonant Piezoelectric Devices", *Research Monograph No. 50*, MIT Press, 1969, p.89.
32. E.K. Sittig, *IEEE Transactions on Sonics and Ultrasonics*, Su-14, (4), 167 (1967).
33. A. Wade, *IEEE Transactions on Sonics and Ultrasonics*, Su-22, 385 (1975).
34. K.R. Erikson, F.J. Pry and J.P. Jones, *IEEE Transactions on Sonics and Ultrasonics*, Su-21, 144 (1974).
35. A. Nemet, *Phil. Trans. R. Soc. Lond.* A292, 137 (1979).
36. R.S. Sharpe, *Phil. Trans. R. Soc. Lond.* A292, 163 (1979).
37. B.T. Khuri - Yakub and G.S. Kino, *Appl. Phys. Lett.*, 30, (1977).
38. K.R. Erikson, *IEEE Transactions on Sonics and Ultrasonics*, Vol SU-28, 7 (1979).
39. A. de Sterke, "Advances in the Technology of Mechanized Ultrasonic Testing", *Phil. Trans. R. Soc. Lond.* A292, 207-221, 1979.
40. W.P. Mason, "Physical Acoustics", Vol 1A, Academic Press, 1964.
41. J.H. Goll, "The Design of Broad-Band Fluid-Loaded Ultrasonic Transducers", *IEEE Transactions on Sonics and Ultrasonics*, Su-28, (6) 385-393, 1979.

APPENDIX 2.2

PERFORATED PZT-POLYMER COMPOSITES FOR
PIEZOELECTRIC TRANSDUCER APPLICATIONS

PERFORATED PZT-POLYMER COMPOSITES FOR PIEZOELECTRIC TRANSDUCER APPLICATIONS

A. SAFARI, R. E. NEWNHAM, L. E. CROSS† and W. A. SCHULZE

*Materials Research Laboratory, The Pennsylvania State University, University Park,
Pennsylvania 16802, USA*

(Received April 3, 1981)

Composites of PZT and polymer with 3-1 and 3-2 connectivity patterns have been fabricated by drilling holes in sintered PZT blocks and filling the holes with epoxy. The influence of hole size and volume fraction PZT on the hydrostatic properties of the composites was evaluated. By decoupling the piezoelectric d_{33} and d_{31} coefficients in the composite, the hydrostatic coefficients are greatly enhanced. On samples optimized for hydrophone performance, the dielectric constants of 3-1 and 3-2 composites are 600 and 300 respectively. The piezoelectric coefficients d_3 , \bar{g}_3 , and $\bar{g}_3 d_3$ for 3-1 composites are 230 (pC/N⁻¹), $34 (\times 10^{-3} \text{ VmN}^{-1})$, and $7800 (10^{-12} \text{ m}^2 \text{N}^{-1})$ respectively, and the corresponding values for 3-2 composites are 372 (pC/N⁻¹), $123 (10^{-3} \text{ VmN}^{-1})$, and $45000 (10^{-12} \text{ m}^2 \text{N}^{-1})$.

1. INTRODUCTION

In recent years several types of PZT-polymer composites have been fabricated to improve the piezoelectric properties of poled PZT (lead zirconate titanate) ceramics. Different types of macro-symmetry and interphase connectivity were utilized in the design of the PZT-polymer composites listed in Table I.¹⁻⁴ Here connectivity 1-3 means that the PZT phase is self-connected in one direction, and the polymer phase is self-connected in all three directions. In all composites, the dielectric constant \bar{K}_{33} of solid PZT is lowered by the introduction of a polymer phase, and in all cases the hydrostatic piezoelectric charge coefficient d_3 is also enhanced. The hydrostatic piezoelectric voltage coefficient \bar{g}_3 and the $\bar{g}_3 d_3$ product used as a figure of merit for hydrophone application are therefore considerably enhanced in all the composite designs.

Klicker *et al.*⁵ have fabricated 1-3 composites of PZT rods embedded in an epoxy matrix. As shown in Table I, these composites have better piezoelectric properties than solid PZT. The hydrostatic coefficients d_3 and \bar{g}_3 are a function of the dimension of PZT rods, the spacing between the PZT rods, and the thickness of the composite. Based on the previous work with PZT-polymer

composites and on simple series and parallel models,¹ it is clear that the difference in the elastic compliances of the PZT and epoxy has a favorable influence on piezoelectric properties by altering the stress pattern inside the composites.

Rittenmyer *et al.*³ have fabricated 3-3 composites of PZT and polymer (polymethyl methacrylate) with PZT powder in an organic binder and firing the mixture to give a ceramic skeleton. After cooling, the ceramic skeletons were back-filled with polymer (Burps composites). As shown in Table I, these composites have better piezoelectric and mechanical properties compared to 1-3 composites of PZT rods with epoxy. In addition, the Burps composites are much easier to prepare.

The present study focuses on composites with 3-1 and 3-2 connectivity patterns, in which the PZT phase is self-connected in three dimensions and the polymer phase is self-connected in either one or two dimensions. Samples were prepared by drilling holes in sintered PZT blocks either in one direction (3-1 connectivity) or in two directions (3-2 connectivity) and backfilling the perforated PZT blocks with a suitable polymer. Enhancement of d_3 was anticipated in these composites because of the modified stress distribution within the composite.

2. SAMPLE PREPARATION

PZT-polymer composites were prepared by drilling holes in sintered PZT blocks and filling the

† Also affiliated with the Department of Electrical Engineering.

TABLE I
Piezoelectric Properties of PZT-Polymer Composites

	\bar{K}_{11}	\bar{d}_3 (PCN ⁻¹)	\bar{g}_3 (10 ⁻³ VmN ⁻¹)	$\bar{d}_3\bar{g}_3$ (10 ⁻¹⁵ m ² N ⁻¹)	Reference
PZT	1600	50	4	200	Present work
PZT particles in silicone rubber matrix (0-3 connectivity)	100	28.3	32	900	4
PZT replamine in a silicone rubber matrix (3-3 connectivity)	50	35.8	80	2800	2
PZT rods in an epoxy matrix (1-3 connectivity)	200	77.6	40.4	3138	5
PZT rods in a polyurethane matrix (1-3 connectivity)	83	176.2	239	42100	5
Burps composite (epoxy matrix) (3-3 connectivity)	500	120	27	3200	3
Burps composite (silicone rubber matrix (3-3 connectivity)	300	260	100	26000	3

perforated block with a polymer. To prepare the ceramic, 95 wt% of PZT 501A† was mixed with 5 wt% of 15% PVA solution. After mixing and drying the powder, square pellets measuring 2 cm on edge and 4 to 8 mm thick, were pressed at 20,000 psi (140 MPa). The pellets were placed on a platinum sheet and the binder was burned out at 550°C for one hour. Sintering was carried out in a sealed alumina crucible using a silicon carbide resistance furnace at a heating rate of 200°C per hour, with a soak period of one hour at 1285°C. A PbO-rich atmosphere was maintained with sacrificial ceramic pellets of composition 97 mole% PZT and 3 mole% PbO inside the crucible.‡ After firing, the samples were polished and cut into smaller pieces of various dimensions. Air-dried silver paste electrodes§ were applied to the pellets. Poling was done in a stirred oil bath at 140°C at a field of 25 KV/cm for three minutes. After poling, three or four holes were drilled perpendicular to the poling direction using an ultrasonic cutter.¶ Samples were prepared with different hole sizes and hole separation X (Figure 8a). The drilled samples were then placed in a small plastic tube and a commercial polymer (vinylcyclohexene dioxide-epoxy||) was poured into the tube. The epoxy was cured

at 70°C for eight hours. Finally, the composites were polished on silicon carbide paper to expose the PZT and to ensure that the faces of the disk were smooth and parallel. Electrodes of air-dried silver paste were applied and the composites were aged for at least 24 hours prior to any measurement. Some of the 3-1 and 3-2 composites are shown in Figure 1.

3. MEASUREMENTS

The dielectric constants and loss factors of all the samples were measured at a frequency of 1 KHz using an automated capacitance bridge.¶ The piezoelectric coefficient \bar{d}_{31} along the poling direction was measured using a d_{31} meter.†† The hydrostatic piezoelectric \bar{d}_h was measured by a pseudo-static method.‡ Samples were immersed in an oil-filled cylinder, and pressure was applied at a rate of 3.5 MPa/sec. The resulting charge was collected with a Keithley electrometer‡‡ operated in a feedback charge integration mode. The piezoelectric voltage coefficients $\bar{g}_{31} = \bar{d}_{31}/\epsilon_0\bar{K}_{11}$ and $\bar{g}_h = \bar{d}_h/\epsilon_0\bar{K}_{11}$ were calculated from the measured values of \bar{d}_{31} , \bar{d}_h and \bar{K}_{11} .

† Ultrasonic Powders, Inc., South Plainfield, NJ (PZT 501A).

‡ Materials for Electronics, Inc., Jamaica, NY, Demetron 200.

§ Sheffield Ultrasonic Machine Tool, Dayton OH.

¶ Spurr's low viscosity embedding media, No. 5135, Poly-science Inc., Warrington, PA, 18976.

¶ Hewlett Packard (Model 4270A) Automated Capacitance Bridge, Hewlett Packard, 1-59-1 Yoyogi, Tokyo, Japan 151.

†† Bertlinecourt (Model 333) d_{31} meter, Channel Product, Inc., 16722 Park Circle Drive, Chagrin Falls, OH, 44020.

‡‡ Keithley (Model 616) Digital Electrometer, Keithley Instruments, Inc., Cleveland, OH.

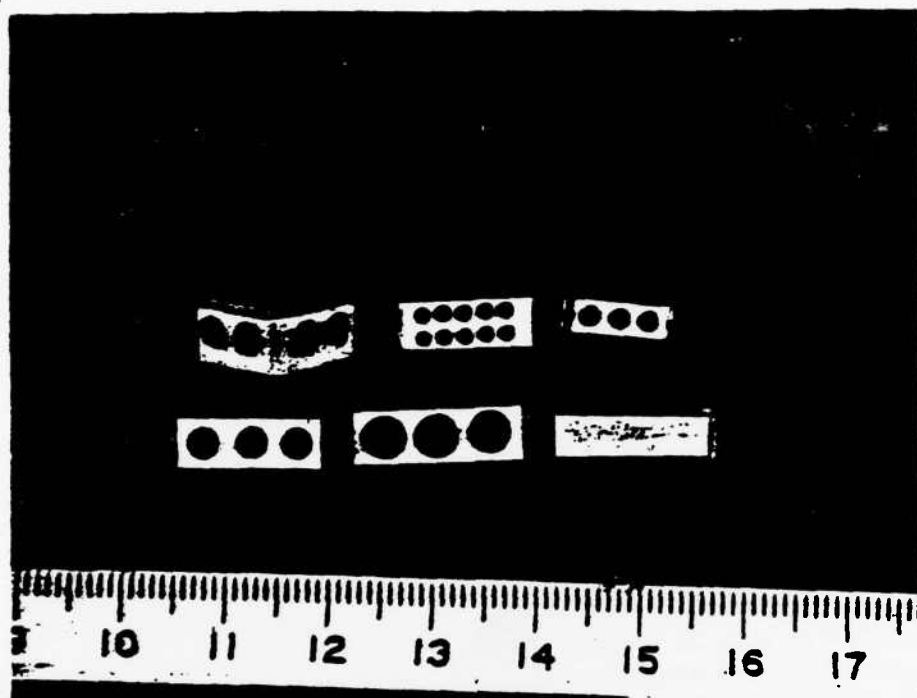


FIGURE 1.

4. RESULTS AND DISCUSSION

Unless otherwise stated, the results refer to composites with 3-1 connectivity. The dielectric constants for 3-1 composites are plotted in Figures 2 and 3 as a function of X (the center-to-center distance for adjacent holes) for two different hole sizes. The dielectric constant increases linearly with X at lower values of X , but reaches a saturation value for higher values. Composites with smaller thicknesses have lower dielectric constants. Also, it is observed that for the same D/t (diameter to thickness ratio), composites with smaller diameter holes have higher dielectric constants than composites with larger holes (see Figures 2 and 3). Dielectric constants of 3-2 composites were much lower than the 3-1 composites for samples with identical hole sizes (Table II). Calculated values of dielectric constants are also plotted in Figures 2 and 3 for comparison.

The values of d_{33} were used as a measure of the degree of poling. Measured values of d_{33} for 3-1 composites are plotted as a function of X in Figure 4. It is observed that d_{33} increases linearly with X at lower values of X , but approaches a saturation value at higher values of X . Each of the data points represents the average of at least twelve

value measurements at different places on the electroded surface of the composites. The measured values of d_{33} in the regions over the holes were about 10% lower than the d_{33} values in solid regions (Figure 8a). It is significant that the d_{33} values for most of the composites exceed 300 pC/N, which is close to the d_{33} coefficients of solid PZT (400 pC/N). It is found that in all composites d_{33} decreases slightly with thickness. Also, composites with smaller hole sizes had larger d_{33} coefficients than composites with larger hole sizes. In all 3-2 composites the measured d_{33} values were also higher than 300 pC/N (Table I).

In Figure 5 the hydrostatic piezoelectric coefficient (\bar{d}_h) of 3-1 composites is plotted as a function of X for different thicknesses. A broad maximum is observed for X values between 4 and 4.5 mm for composites containing 60% to 70% PZT by volume. Figure 6 shows \bar{d}_h plotted as a function of thickness for composites with different X . Again it is found that \bar{d}_h increases with thickness, up to certain thickness, and then decreases. Figure 7 shows the effect of poling on the values of \bar{d}_h , when poling is carried out at several different stages in the process:

1. Poling PZT block before drilling the holes.

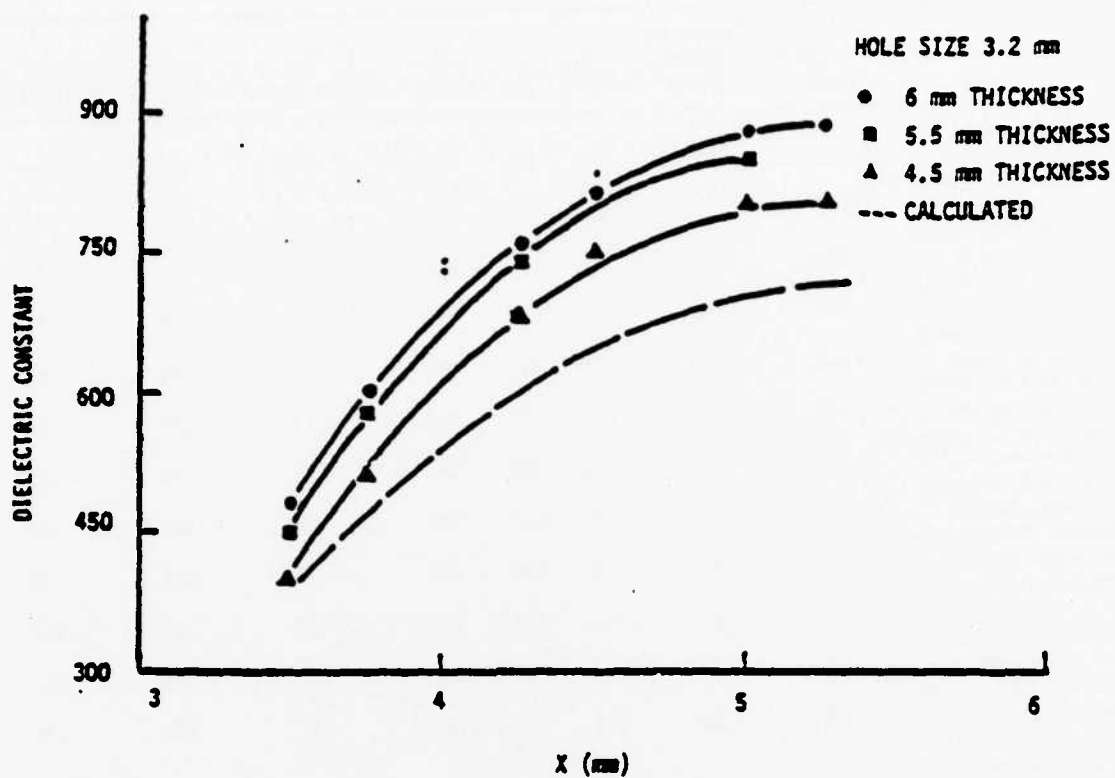


FIGURE 2.

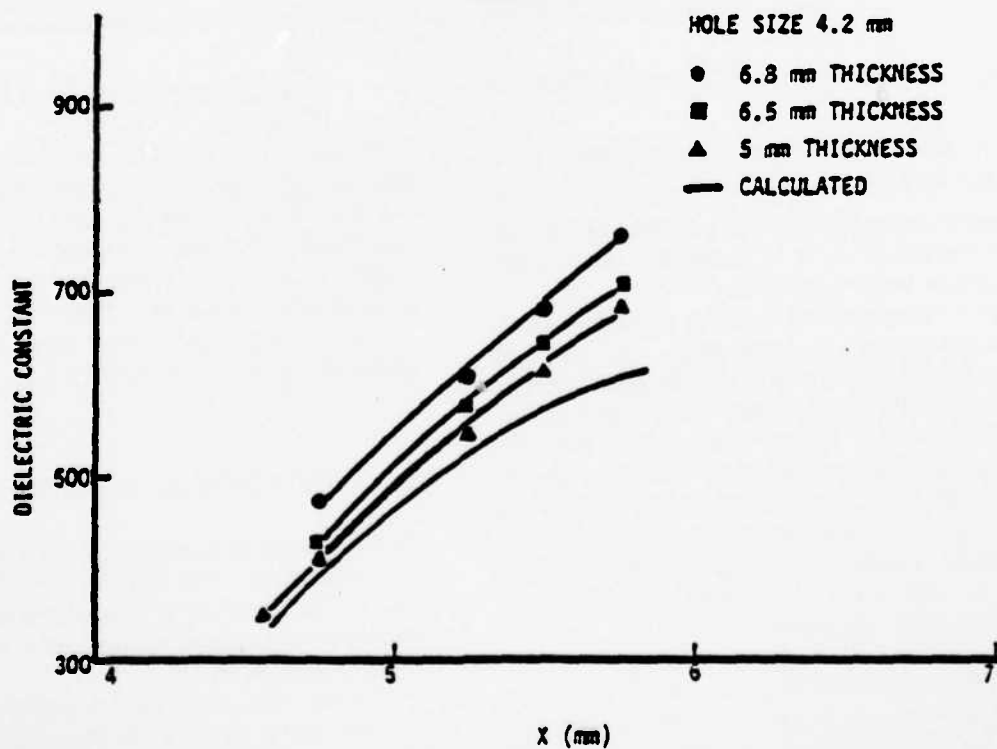


FIGURE 3.

TABLE II

	Hole Size (mm)	Composite Thickness (mm)	X (mm)	\bar{K}_{11}	\bar{d}_{11} (PCN ⁻¹)	\bar{g}_{11} (10 ⁻³ VmN ⁻¹)	\bar{d}_h (PCN ⁻¹)	\bar{g}_h (10 ⁻³ VmN ⁻¹)	$\bar{d}_h \bar{g}_h$ (10 ⁻¹² M ² N ⁻¹)
Perforated PZT/epoxy (3-1 connectivity)	3.2	6.5	4.25	810	340	47	210	29	6000
Perforated PZT/epoxy (3-1 connectivity)	3.2	6	4.25	760	350	52	230	34	7800
Perforated PZT/epoxy (3-1 connectivity)	3.2	5.5	4.25	740	330	50	200	30	6000
Perforated PZT/epoxy (3-1 connectivity)	3.2	4.5	4.25	680	320	53	190	31	5900
Perforated PZT/epoxy (3-1 connectivity)	4.2	6.8	4.75	470	290	70	190	46	8600
Perforated PZT/epoxy (3-1 connectivity)	4.2	6.5	4.75	450	290	73	222	56	12300
Perforated PZT/epoxy (3-1 connectivity)	4.2	6	4.75	425	280	74	170	45	7600
Perforated PZT/epoxy (3-1 connectivity)	4.2	5.5	4.75	410	275	76	120	33	3950
Perforated PZT/epoxy (3-2 connectivity)	3.2	6.7	4.5	360	290	90	238	74	17600
Perforated PZT/epoxy (3-2 connectivity)	3.2	6.2	4.5	330	290	99	294	100	29000
Perforated PZT/epoxy (3-2 connectivity)	3.2	6	4.5	320	300	105	322	113	36300
Perforated PZT/epoxy (3-2 connectivity)	3.2	5.8	4.5	290	290	114	329	128	42000
Perforated hollow PZT sealed with polymer (3-2 connectivity)	3.2	6.2	4.5	340	340	112	372	123	45700

2. Poling the perforated PZT before filling it with epoxy.

3. Poling after embedding the perforated PZT block with epoxy.

From these experiments it was concluded that to get higher values of \bar{d}_h it is necessary to prepole the PZT blocks before drilling.

It should be emphasized that for all composites, the \bar{d}_h coefficients are at least twice that of solid PZT (50 pC/N). Hydrostatic coefficients for the 3-2 composites are much larger than those of 3-1 composites. An even higher value of \bar{d}_h was observed when measurements were made on perforated blocks of PZT in which the open sides were enclosed with a thin polymer sheet, thereby keeping the inside region completely empty. When measured in this way a \bar{d}_h value of nine times greater than that of solid PZT was observed (Table II).

Some typical values of \bar{K}_{11} , \bar{d}_{11} , and \bar{d}_h are given in Table II. It is important to note that \bar{d}_h depends markedly on the thickness of the PZT region above and below the holes (see Figure 8a). There

is a critical thickness for which \bar{d}_h becomes a maximum (Table II).

Piezoelectric voltage coefficients \bar{g}_{11} and \bar{g}_h are also substantially larger than those of solid PZT. As shown in Table II, the piezoelectric voltage coefficients \bar{g}_{11} and the hydrostatic voltage coefficients \bar{g}_h are very large for 3-2 composites. The $\bar{d}_h \bar{g}_h$ product used as a figure of merit for hydrostatic applications is more than 200 times the corresponding value for solid PZT.

5. THEORETICAL MODEL

The physical properties of 3-1 composites can be approximated with the model illustrated in Figure 8. For simplicity, consider a square of length l whose area is equal to that of a circle with radius r . Then $l = r\sqrt{\pi}$.

We can visualize the 3-1 composite as made up of two parts A and B connected in parallel as shown in Figure 8b. Part B is composed of two phases connected in series, PZT and polymer. The

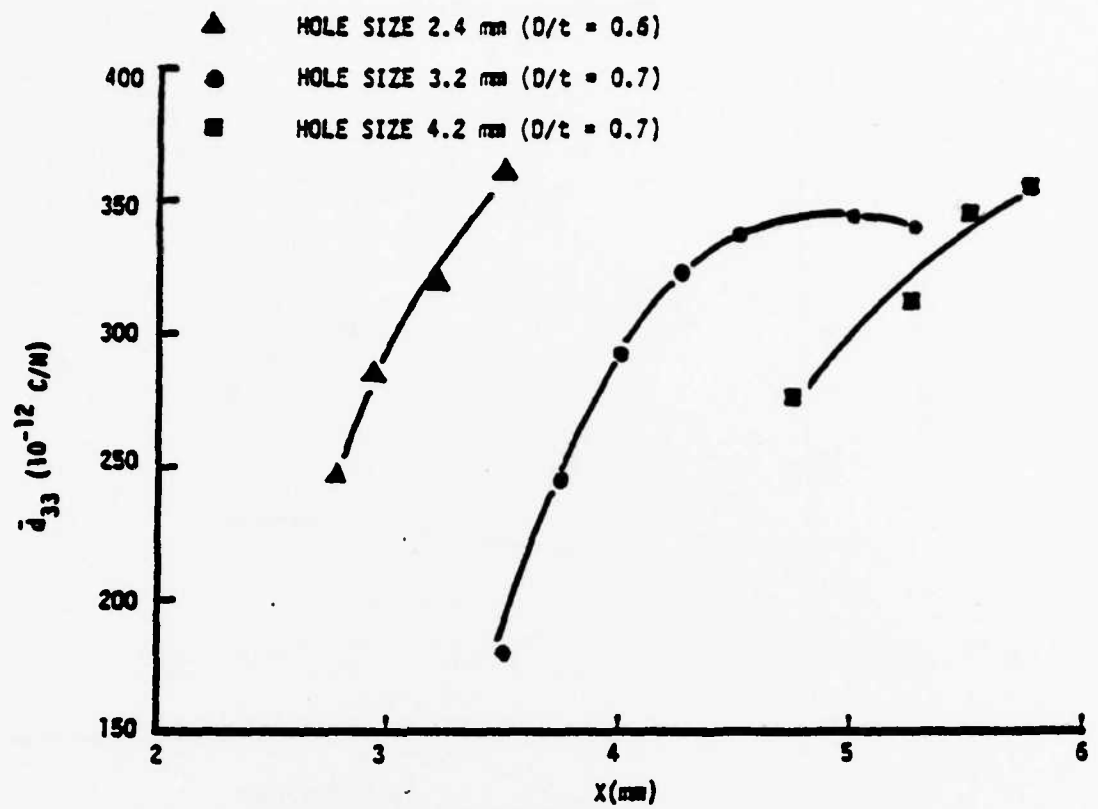


FIGURE 4.

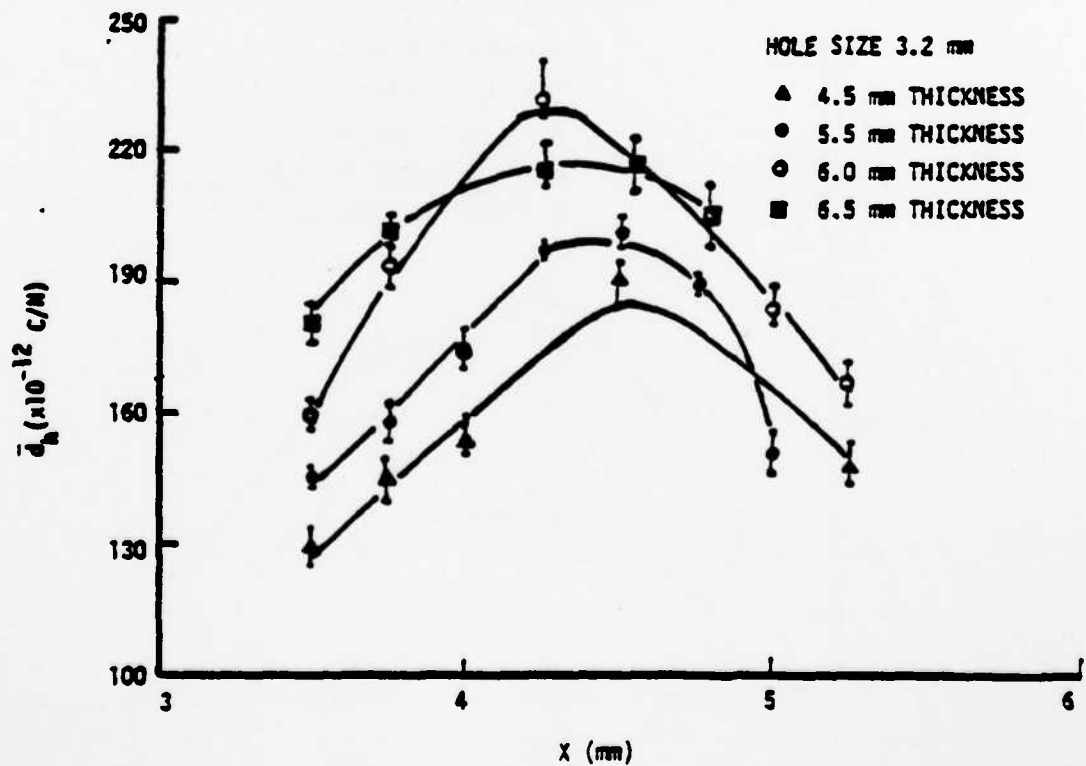


FIGURE 5.

PERFORATED PZT POLYMER COMPOSITES

[337]/203

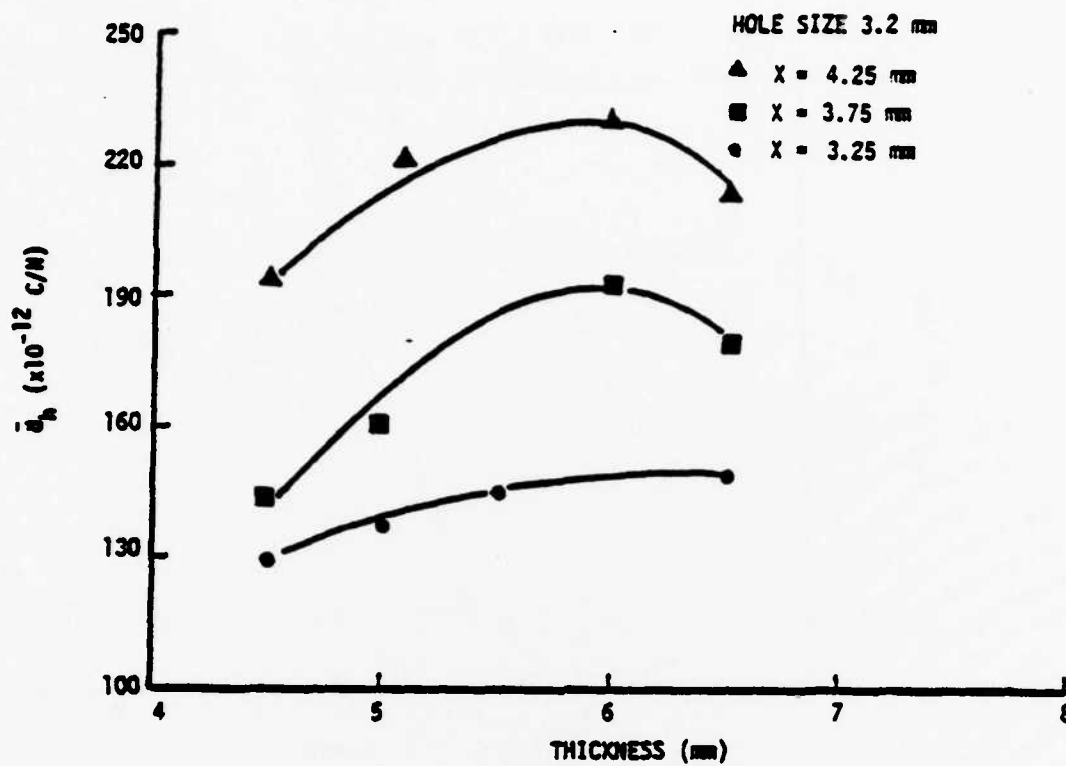


FIGURE 6.

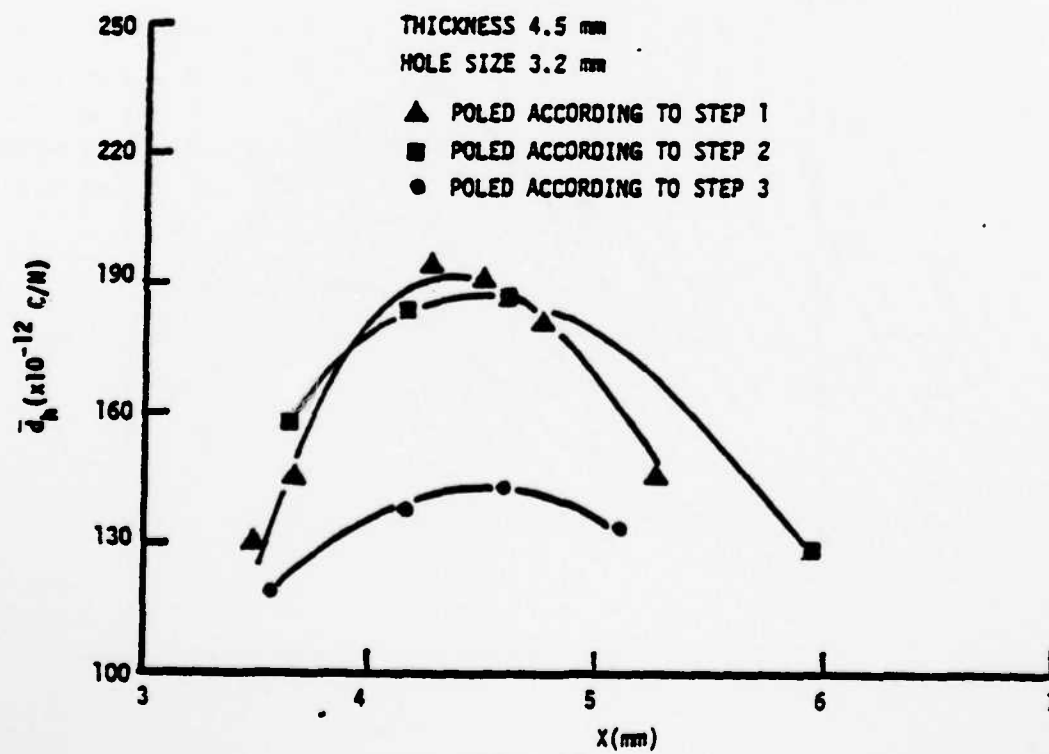


FIGURE 7.

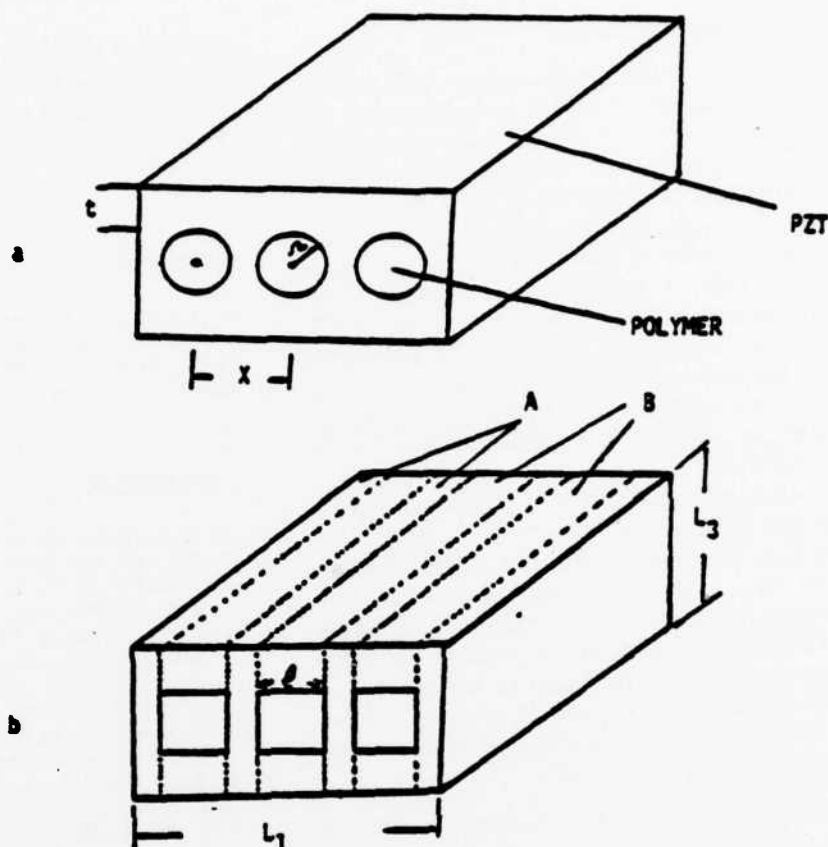


FIGURE 2.

following quantities can be defined with respect to the dimensions of the composites.

$${}^A V \text{ (volume fraction of PZT of part A)} = (L_1 - \pi t)/L_1$$

$${}^B V \text{ (volume fraction of part B)} = \pi/L_1$$

$${}^{1B} V \text{ (volume fraction of PZT in part B)} = (L_1 - t)/L_1$$

$${}^{2B} V \text{ (volume fraction of polymer in part B)} = t/L_1$$

where L_1 and L_3 are length and thickness of composite and π is the number of holes.

5.1 Dielectric Constant

The component of the dielectric constant of interest is \bar{K}_{11} , since the electrode surfaces are perpendicular to the poling direction. In the notation used here, \bar{K}_{11} is the dielectric constant of the composite, ${}^A K_{11}$ the dielectric constant of PZT, ${}^{1B} K_{11}$ that

of the polymer, and ${}^{2B} K_{11}$ is the dielectric constant of part B. Since part A and part B are in parallel connection,

$$\bar{K}_{11} = {}^A V {}^A K_{11} + {}^B V {}^B \bar{K}_{11}$$

Because PZT and polymer in part B are in series connection we can apply series model:

$${}^B \bar{K}_{11} = {}^{1B} V {}^{1B} K_{11} + {}^{2B} V {}^{2B} K_{11}$$

Using these relations we can calculate \bar{K}_{11} of composites. Since ${}^A K_{11} = 1600$ and ${}^{2B} K_{11} = 5$, most of the contribution to \bar{K}_{11} comes from part A, which is PZT. Calculated values are plotted in Figures 1 and 3. In general, the measured dielectric constants are somewhat higher than the predicted values. This may be due to the approximation involved in the above calculations. The contribution to the dielectric constant from part B may be much higher than that assumed above because of the bending of the flux lines around the holes containing the polymer.

5.2 Piezoelectric Coefficients

The longitudinal coefficient \bar{d}_{33} relates the polarization component P_3 to stress component σ_3 by the following relation: $P_3 = \bar{d}_{33}\sigma_3$. As stated earlier, the \bar{d}_{33} values of 3-1 composites are slightly smaller than that of solid PZT. In a composite most of the stresses are borne by the ceramic, and if the stress transfer to the vertical columns (section A, Figure 8b) is complete, the \bar{d}_{33} of the composite should be equal to the value of \bar{d}_{33} for PZT. But because of the curved shapes around the perforations, the stress distribution in the composite is not as simple as the model predicts. Horizontal components of stress are produced which lower the \bar{d}_{33} coefficient.

The hydrostatic coefficient of the composite is given by the relation $\bar{d}_h = \bar{d}_{33} + 2\bar{d}_{31}$. In a solid PZT ceramic, the value of \bar{d}_h is low due to the fact that $\bar{d}_{31} = -2\bar{d}_{33}$. In the 3-1 composites the arc-like geometry of the composite results in mechanically stiffened electrodes which transfer the horizontal stress pattern, significantly lowering \bar{d}_{31} , and enhancing \bar{d}_h . The fact that in some of the 3-1 and 3-2 composites $\bar{d}_h \approx \bar{d}_{33}$ clearly indicates that \bar{d}_{31} is almost zero in some cases.

SUMMARY

A simple technique for fabricating PZT polymer composites with 3-1 and 3-2 connectivity patterns has been proposed. These composites exhibit better piezoelectric properties than the previously

studied PZT polymer composites with different types of connectivity patterns. For 3-2 composites the \bar{K}_{33} , \bar{d}_h , \bar{g}_h , and $\bar{d}_h\bar{g}_h$ values are $300, 370 \times 10^{-12}$ C/N, 123×10^{-3} Vm/N and $45,000 \times 10^{-15}$ m²/N respectively.

ACKNOWLEDGEMENT

This work was sponsored by the Office of Naval Research through Contract No. N00014-78-C-0291. We also wish to thank Mr. Arvind Halliyal and our other colleagues at the Materials Research Laboratory.

REFERENCES

1. R. E. Newnham, D. P. Skinner and L. E. Cross, *Mat. Res. Bull.*, 1B, 525 (1978).
2. D. P. Skinner, R. E. Newnham and L. E. Cross, *Mat. Res. Bull.*, 13, 599 (1978).
3. K. Rittenmyer, T. Shrout, W. A. Schulze and R. E. Newnham, *Ferroelectrics* (accepted).
4. W. B. Harrison, Proc. Workshop on Sonar Transducer Materials, Naval Research Laboratory (Feb. 1976).
5. K. A. Klinker, Ph.D. Thesis, Solid State Science, The Pennsylvania State University (1980).
6. T. R. Shrout, L. J. Bowen and W. A. Schulze, *Mat. Res. Bull.*, 15, 1371 (1980).
7. R. E. Newnham, L. J. Bowen, K. A. Klinker and L. E. Cross, *Int. J. Mat. in Eng.*, 2, 93 (1980).
8. K. A. Klinker, J. V. Biggers and R. E. Newnham, *J. Amer. Ceram. Soc.*, 64, 5 (1981).
9. K. A. Klinker, Control of PbO Partial Pressure During the Sintering of PZT Ceramic, M. S. Thesis, The Pennsylvania State University (1979).
10. J. F. Nye, *Physical Properties of Crystal*, Oxford University Press, London (1957).

AD-A132 136

TARGETED BASIC STUDIES OF FERROELECTRIC AND
FERROELASTIC MATERIALS FOR PI. (U) PENNSYLVANIA STATE
UNIV UNIVERSITY PARK MATERIALS RESEARCH LA..

3/4

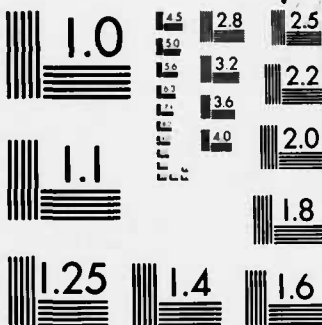
UNCLASSIFIED

L E CROSS ET AL. MAR 83 N00014-78-C-0291

F/G 9/1

NL





MICROCOPY RESOLUTION TEST CHART
NATIONAL BUREAU OF STANDARDS-1963-A

APPENDIX 2.3

LANDAU-DEVONSHIRE THEORY WITH ROTATIONALLY
INVARIANT EXPANSION COEFFICIENTS

LANDAU-DEVONSHIRE THEORY WITH ROTATIONALLY INVARIANT EXPANSION COEFFICIENTS*

G.R. BARSCH, B.N.N. ACHAR^a AND L.E. CROSS
The Pennsylvania State University, University Park, PA 16802, U.S.A.

Abstract--General expressions pertaining to a centrosymmetric prototype phase are given for the correction terms to the third and fourth order expansion coefficients of the Landau-Devonshire free energy with respect to the displacement gradient and the polarization, that arise as a consequence of the rotational invariance condition. Application to crystals of O_h symmetry shows that the correction terms may be numerically significant.

TOUPIN'S THEOREM

In the electrostatic approximation (i.e. without retardation of the electromagnetic field and in the absence of a magnetic field) the internal energy U (per unit mass) of a homogeneous infinite elastic dielectric medium isentropically subjected to a finite elastic deformation and a finite electric field (for isothermal conditions: the Helmholtz free energy F) is a function of the deformation gradient $(\partial \bar{x}/\partial \bar{a}) = \{\partial x_i/\partial a_j\}$ and the polarization vector $\bar{P} = \{P_r\}$ (electric dipole moment per unit volume in the deformed state), $U = \hat{U}(\partial \bar{x}/\partial \bar{a}, \bar{P})$. Here x_i and a_j ($i, j = 1, 2, 3$) denote the coordinates of a material point in the deformed state and in the undeformed and unpolarized reference state, respectively, referred to a common stationary cartesian frame. The rotational invariance condition requires that¹ $\hat{U}(\bar{R}(\partial \bar{x}/\partial \bar{a}), \bar{R}\bar{P}) = \hat{U}(\partial \bar{x}/\partial \bar{a}, \bar{P})$ for all rotation matrices $\bar{R} = \{R_{ij}\}$. As a consequence, the internal energy may be expressed in terms of the symmetric Lagrangian strain tensor (LST) $\bar{\epsilon} = \{\epsilon_{ij}\}$ defined by (tensor notation; summation convention!)

$$\epsilon_{ij} = \frac{1}{2}[(\partial x_k/\partial a_i)(\partial x_k/\partial a_j) - \delta_{ij}] \quad (1)$$

and in terms of Toupin's material measure of polarization (MMP) $\bar{\pi} = \{\pi_i\}$ defined by

$$\pi_i = J(\partial a_i/\partial x_r)P_r \quad (2)$$

where

$$J = (\rho_0/\rho) = \det(\partial x_i/\partial a_j) \quad (3)$$

denotes the Jacobian of the deformation, and ρ (ρ_0) the density in the deformed (undeformed) state, respectively¹. The resulting internal energy function $U(\bar{\epsilon}, \bar{\pi})$ is then automatically invariant under rigid rotations¹ (Toupin's Theorem).

An alternative formulation of the theory of the nonlinear elastic dielectric was given by Grindlay² in terms of the dielectric displacement instead of the polarization and has been shown to be equivalent to Toupin's theory³. Following Toupin, we prefer

*Work supported by ONR Contract No. N00014-78-C-0291.

^aAlso affiliated with Bucknell University, Lewisburg, PA 17832, USA.

to use the polarization, because in the Landau-Devonshire theory it contains the order parameter.

LANDAU-DEVONSHIRE FREE ENERGY

As a consequence of Toupin's Theorem the Taylor expansion of the Landau-Devonshire (LD) energy function with respect to elastic and electric variables must be expressed in terms of the LST and the MMP, or their proper thermodynamic conjugate variables, if the expansion coefficients are to have the symmetry of indices familiar from the linear theory of elasticity and piezoelectricity. The Taylor expansion of the LD free energy density per unit initial volume $\rho_0 F(\tilde{\eta}, \tilde{\Pi})$ pertaining to a centrosymmetric prototype phase has the form

$$\begin{aligned} \rho_0 F(\tilde{\eta}, \tilde{\Pi}) = & \frac{1}{2} c_{ijkl} \eta_{ij} \eta_{kl} + \frac{1}{2} b_{rs} \Pi_r \Pi_s + \frac{1}{6} c_{ijklmn} \eta_{ij} \eta_{kl} \eta_{mn} - \frac{1}{2} h_{rs,mn} \Pi_r \Pi_s \eta_{mn} \\ & + \frac{1}{24} c_{ijklmnpq} \eta_{ij} \eta_{kl} \eta_{mn} \eta_{pq} - \frac{1}{4} h_{rs,mnpq} \Pi_r \Pi_s \eta_{mn} \eta_{pq} + \frac{1}{24} b_{rstu} \Pi_r \Pi_s \Pi_t \Pi_u + \dots \end{aligned} \quad (4)$$

The coefficients $c_{ijkl} \dots$ are the isothermal second, third and fourth order elastic constants according to the definition of Brugger⁴, the $h_{rs,mn} \dots$ are the first and second order electrostriction coefficients, and the $b_{rs} \dots$ are the second and fourth order reciprocal dielectric susceptibilities. All coefficients pertain to the reference state of the medium, assumed to be stress free. The choice of the kernel letters and of the signs for the expansion coefficients follows the IEEE convention⁵ for the linear theory of piezoelectricity and extends it to the nonlinear elastic dielectric, except that the coefficients are referred to the MMP.

The coefficients are invariant under exchange of indices of the following kind:

- I. $c_{ijkl} \dots$ (a) Index pairs, e.g. $c_{ijklmn} = c_{klijnm}$; (b) Indices within a given pair, e.g. $c_{ijklmn} = c_{jiklmn}$.
- II. $h_{rs,mn} \dots$ (a) Indices preceding the comma (pertaining to the MMP), e.g. $h_{rs,mn} = h_{sr,mn}$; (b) Index pairs following the comma (pertaining to the LST), e.g. $h_{rs,mnpq} = h_{rs,pqmn}$; (c) Indices within a given pair following the comma (pertaining to the LST), e.g. $h_{rs,mnpq} = h_{rs,nmpq}$.
- III. $b_{rs} \dots$ Any two indices, e.g. $b_{rstu} = b_{srtu} = b_{tsru}$.

Alternatively, the LD free energy density may be expressed as a function of the displacement gradient (DG) $v_{ij} = [(\partial x_i / \partial a_j) - \delta_{ij}]$ and the polarization \bar{P} with the Taylor expansion:

$$\begin{aligned} \rho_0 \hat{F}(\tilde{v}, \bar{P}) = & \frac{1}{2} \hat{c}_{ijkl} v_{ij} v_{kl} + \frac{1}{2} \hat{b}_{rs} P_r P_s + \frac{1}{6} \hat{c}_{ijklmn} v_{ij} v_{kl} v_{mn} - \frac{1}{2} \hat{h}_{rs,mn} P_r P_s v_{mn} \\ & + \frac{1}{24} \hat{c}_{ijklmnpq} v_{ij} v_{kl} v_{mn} v_{pq} - \frac{1}{4} \hat{h}_{rs,mnpq} P_r P_s v_{mn} v_{pq} + \frac{1}{24} \hat{b}_{rstu} P_r P_s P_t P_u + \dots \end{aligned} \quad (5)$$

The coefficients $\hat{c}_{ijkl} \dots$, $\hat{h}_{rs,mn} \dots$ and $\hat{b}_{rs} \dots$ represent an alternative set of second through fourth order elastic constants, first and second order electrostriction constants, and second and fourth order reciprocal dielectric susceptibilities, respectively. Since the DG is not symmetric ($v_{ij} \neq v_{ji}$) the coefficients $\hat{c}_{ijkl} \dots$ and $\hat{h}_{rs,mn} \dots$ are not invariant under exchange of indices within a given pair pertaining to the DG. That is, the $\hat{c}_{ijkl} \dots$ only have the symmetry property I(a) but not I(b), and the $\hat{h}_{rs,mn}$ only have the symmetry properties II(a) and II(b), but not II(c). However, the $\hat{b}_{rs} \dots$ and the $b_{rs} \dots$ have the same symmetry III, so one expects $\hat{b}_{rs} \dots = b_{rs} \dots$. The free energy function $\rho_0 \hat{F}(\tilde{v}, \bar{P})$ is constrained by the rotational invariance condition, from which, following Leibfried and Ludwig⁶, it may be deduced that certain linear combinations of the coefficients $\hat{c}_{ijkl} \dots$, $\hat{h}_{rs,mn} \dots$, etc. obtained by index permutation must have the additional symmetries I(b) and II(c), and that these conditions are

equivalent to Eqs. (6a,b,c) to (8a,b) given below.

RELATION BETWEEN EXPANSION COEFFICIENTS OF $\alpha_0 F(\tilde{\eta}, \tilde{\pi})$ AND $\alpha_0 F(\tilde{v}, \tilde{p})$

The relations between the coefficients $\hat{c}_{ijkl}...$, etc. and the $c_{ijkl}...$, etc. are obtained by expanding $\tilde{\eta}$ and $\tilde{\pi}$ in Equ. (4) with respect to \tilde{v} and \tilde{p} , and equating equal powers of P_r and v_{kl} in Eqs. (4) and (5). The result is:

$$\hat{c}_{ijkl} = c_{ijkl} \quad (6a) \quad \hat{c}_{ijklmn} = c_{ijklmn} + c_{ijln}^{\delta km} + c_{kljn}^{\delta im} + c_{mnlj}^{\delta ik} \quad (6b)$$

$$\begin{aligned} \hat{c}_{ijklmnpq} = & c_{ijklmnpq} + c_{ijklnq}^{\delta mp} + c_{ijmnlq}^{\delta kp} + c_{ijpqln}^{\delta km} + c_{klmnlq}^{\delta ip} + c_{klpqjn}^{\delta im} \\ & + c_{mnpqjl}^{\delta ik} + c_{jlnq}^{\delta ik} c_{mp}^{\delta} + c_{jnql}^{\delta im} c_{kp}^{\delta} + c_{jqln}^{\delta ip} c_{km}^{\delta} \end{aligned} \quad (6c)$$

$$\hat{h}_{rs,mn} = h_{rs,mn} + b_{rm}^{\delta sn} + b_{sm}^{\delta rn} - 2b_{rs}^{\delta mn} \quad (7a)$$

$$\begin{aligned} \hat{h}_{rs,mnpq} = & h_{rs,mnpq} + 2(h_{rs,mn}^{\delta pq} + h_{rs,pq}^{\delta mn}) + h_{rs,nq}^{\delta mp} - (h_{rm,pq}^{\delta sn} + h_{sm,pq}^{\delta rn}) \\ & - (h_{rp,mn}^{\delta sq} + h_{sp,mn}^{\delta rq}) + 2b_{rs}^{\delta} (c_{mq}^{\delta np} - 2c_{mn}^{\delta pq}) + 2(b_{rp}^{\delta sq} + b_{sp}^{\delta rq}) c_{mn}^{\delta} \\ & + 2(b_{rm}^{\delta sn} + b_{sm}^{\delta rn}) c_{pq}^{\delta} - b_{mp}^{\delta} (c_{rn}^{\delta sq} + c_{rq}^{\delta sn}) - (b_{rm}^{\delta sq} + b_{sm}^{\delta rq}) c_{np}^{\delta} \\ & - (b_{rp}^{\delta sn} + b_{sp}^{\delta rn}) c_{mq}^{\delta} \end{aligned} \quad (7b)$$

$$\hat{b}_{rs} = b_{rs} \quad (8a) \quad \hat{b}_{rstu} = b_{rstu} \quad (8b)$$

Table I: Correction terms to third order elastic^a and first order electrostriction constants for O_h symmetry and their relative magnitude for $SrTiO_3$ and $NaCl$ at 300K, calculated from experimental data of Refs. 7 to 10.

ijklmn	ΔC_{ijklmn}	$\Delta C_{ijklmn}/C_{ijklmn}$	
		$SrTiO_3$	$NaCl$
11 11 11	$3C_{1111}$	-2.00	-0.18
11 11 22	C_{1122}	-0.13	-0.25
11 22 33	0	0	0
11 12 12	$C_{1122} + 2C_{1212}$	-1.16	-0.64
11 21 12	C_{1212}	-0.41	-0.21
11 21 21	C_{1111}	-1.10	-0.82
11 23 23; 11 32 32	C_{1122}	-0.12	0.44
11 32 23	0	0	0
12 23 31; 21 32 13	0	0	0
12 23 13; 12 32 13	C_{1212}	1.38	0.49
rs, mn	$\Delta h_{rs,mn}$	$\Delta h_{rs,mn}/h_{rs,mn}$	
		$SrTiO_3$	$NaCl$
11, 11	0	0	0
11, 22	-2b	0.27	-0.31
12, 12; 12, 21	b		-0.26

^aSecond order elastic constants are given in tensor notation.

DISCUSSION AND CONCLUSIONS

As shown elsewhere¹¹ it is possible to construct the usual thermodynamic potentials and the corresponding LD energy functions either with $\tilde{\eta}$ and $\tilde{\pi}$, and their conjugate

Equ. (6b) has been given before by Leibfried and Ludwig⁶. For the higher order elastic and electrostriction constants $\hat{c}_{ijklmn}...$ and $\hat{h}_{rs,mn}...$ the loss of symmetries Ib and IIc arises from correction terms of lower order and in general leads to an increase in the number of independent coefficients.

In Table I the correction terms for the third order elastic constants and for the first order electrostriction constants are listed for the cubic point group O_h , together with their numerical values for $SrTiO_3$ and $NaCl$. The correction terms increase the number of third order elastic constants, but not the number of electrostriction constants. The magnitude of the correction is in general quite substantial. However, because of the Curie-Weiss Law for ferroelectric materials the correction to the electrostriction coefficients should according to Eqs. (7a,b) vanish at the Curie temperature.

intensive variables $t_{ij} = \partial_0(\partial F/\partial n_{ij})_{T, \bar{n}}$ and $f_r = \partial_0(\partial F/\partial \bar{n}_r)_{T, \bar{n}}$, or with \bar{v} and \bar{p} , and their conjugate intensive variables $\tau_{ij} = \partial_0(\partial \bar{F}/\partial v_{ij})_{T, \bar{p}}$ and $\bar{E}_r = \partial_0(\partial \bar{F}/\partial p_r)_{T, \bar{p}}$. It should be noted, however, that the Cauchy stress tensor $\bar{\gamma} = \{\sigma_{ij}\}$ (force per unit area in the deformed state) is not the conjugate variable for any of the thermodynamic potentials so introduced, but is related to the Piola-Kirchhoff stress tensor $\hat{\gamma} = \{\tau_{ij}\}$ (force per unit area in the reference state) by¹ $\sigma_{ij} = (1/J)(\partial x_i/\partial a_k)\tau_{jk}$ where the Piola-Kirchhoff stress tensor is related to the thermodynamic tensions t_{kl} by¹ $\tau_{jk} = (\partial x_j/\partial a_n)t_{kn}$. The electric field E_r is related to the conjugate variable \bar{f}_r according to $\bar{E}_r = (\partial a_r/\partial x_s)\bar{f}_s$. Whereas the expansion coefficients of the thermodynamic potentials with respect to the thermodynamic tensions t_{ij} have the full symmetry I(a,b), II(a,b,c) and III as listed above, the higher than second order expansion coefficients with respect to the asymmetric Piola-Kirchhoff stress tensor have the same reduced symmetry as the $\hat{c}_{ijkl} \dots$, etc.

The choice of variables is a matter of convenience as suggested by the experimental situation. However, whenever the "physical" variables $\bar{\gamma}, \bar{E}$ (or \bar{v}, \bar{p}) rather than the "thermodynamic" variables $\hat{\gamma}, \bar{f}$ (or $\bar{n}, \bar{\pi}$) are used, the number of independent higher order elastic and electrostriction coefficients is increased, and the experimental data cannot be fitted to the coefficients pertaining to the thermodynamic variables, which possess the full symmetry I(a,b,c) to III listed above.

Furthermore, in spite of its widespread use, the linearized strain tensor $\epsilon_{ij} = (1/2)(v_{ij} + v_{ji})$ in general is not an appropriate strain variable in a LD free energy function, and its use amounts to replacing the correction terms in Eqs. (6b,c) and (7b,c) and in Table I by their average values.

The symmetry-reducing correction terms may be expected to be especially significant where the dependence of the ferroelectric or ferroelastic transition on stress or strain is involved. However, for zero stress or strain according to Equ. (2) the MMP $\bar{\pi}$ reduces to the polarization \bar{P} , and the familiar results of the LD theory are recovered.

REFERENCES

1. R.A. Toupin, (a) J. Rat. Mech. Anal. **5**, 849 (1956); (b) Int. J. Engng. Sci. **1**, 101 (1963).
2. J. Grindlay, (a) Phys. Rev. **149**, 637 (1966); (b) Phys. Rev. **160**, 698 (1967); (c) An Introduction to the Phenomenological Theory of Ferroelectricity (Pergamon, Oxford, 1970), Chapter 4.
3. P. Hájíček, Phys. Lett. **25A**, 36 (1967).
4. K. Brugger, Phys. Rev. **133**, A1611 (1964).
5. IEEE Standard on Piezoelectricity, IEEE Std. 176-1978 (The Institute of Electrical and Electronics Engineers, Inc., New York, 1978).
6. G. Leibfried and W. Ludwig, Z. Phys. **169**, 80 (1960).
7. A.G. Beattie and G.A. Samara, J. Appl. Phys. **42**, 2376 (1971).
8. J.R. Drabble and R.E.B. Strathen, Proc. Phys. Soc. **92**, 1090 (1967).
9. G. Schmidt and E. Hegenbarth, Phys. Status Solidi **3**, 329 (1963).
10. L. Bohatý and S. Haussühl, Acta Cryst. **A33**, 114 (1977).
11. G.R. Barsch, B.N.N. Achar, and L.E. Cross, Phys. Rev. B25 (to be published, 1982).

APPENDIX 2.4

A HIGH-SENSITIVITY AC DILATOMETER FOR THE DIRECT MEASUREMENT
OF PIEZOELECTRICITY AND ELECTROSTRICTION

A HIGH-SENSITIVITY AC DILATOMETER FOR THE DIRECT MEASUREMENT OF PIEZOELECTRICITY AND ELECTROSTRICTION

Kenji Uchino and Leslie E. Cross
Materials Research Laboratory, The Pennsylvania State University
University Park, Pennsylvania

Summary

A capacitance type dilatometer has been constructed which is capable of resolving low frequency AC linear displacements of 10^{-13} meters (0.001\AA) and can be used for the direct measurement of piezoelectric and electrostrictive deformations.

The sensing element of the dilatometer system is a parallel plate capacitor with sputtered platinum electrodes supported on fused silica optical flats. Changes of plate separation are sensed by the associated change in dielectric capacitance which is monitored by a capacitance bridge. Slow drift in the capacitance due to thermally induced changes in the plate separation are reduced to an equivalent plate separation change of less than $\pm 0.002\text{\AA}/\text{minute}$ by a DC servo actuated by the bridge unbalance signal which corrects the capacitor plate position through ceramic piezoelectric PZT pushers.

For AC measurement, one plate of the dilatometer is driven along the axis of the capacitor at a frequency of 14 Hz by a standard piezoelectric quartz crystal. The second plate of the sensing capacitor is driven in phase at the same frequency by the piezoelectric or electrostrictor of interest. A narrow band phase locked detector isolates and amplifies the 14 Hz signal detected in the unbalance output of the bridge detector. By adjusting the magnitude of the AC voltage applied to the standard and the unknown crystals to produce a null response at 14 Hz, the electromechanical constants of the two crystals can be compared with very high precision.

Some examples are given of piezoelectric and electrostrictive crystals and ceramics which have been measured on the instrument.

Introduction

Electrostriction which is the basic electro-mechanical coupling in all non-piezoelectric solids is at present very poorly understood. There are few reliable data for the separate components of the electrostriction tensor even in simple solids, and there is no theory which is adequate even for alkali halide crystals. Experimentally, the difficulty is clearly associated with the very small magnitude of the electrostrictive strains even at the highest possible field levels in simple low permittivity solids. Theoretically the absence of well authenticated experimental values has certainly

been a major disincentive to development and none of the present theories is viable.

The instrument described in this paper has been designed to resolve AC linear displacements of 10^{-13} meters (10^{-3}\AA) and to permit the precise measurement of the very small electrostrictive strains in low permittivity solids. (The work is a preliminary part of a larger program in the Materials Research Laboratory which focuses upon both the experimental measurement and the theoretical description of electrostriction.) The AC differential capacitance dilatometer which has been constructed is based upon an early design by Bohatý and Heussühl.¹

In this paper, the principle of the capacitance dilatometer is described first, the DC servo stabilization of the sensing capacitor which is the key to improved stability and sensitivity discussed, and the experimental arrangement detailed. The development of a unique new AC calibration capacitor is briefly described and finally some examples are given of piezoelectric and electrostrictive crystals and ceramics which have been measured on the instrument.

Design of the Capacitance Dilatometer

The scheme of the dilatometer is shown in Fig. 1. The strain sensing capacitor consists of two platinum sputtered fused silica plates (2" diameter). The electrostrictive (or piezoelectric) sample plated with sputtered platinum electrodes is rigidly mechanically connected through an insulating lucite support to the right plate of the sensing capacitor. If the sample crystal is driven electrically, the right plate will be excited mechanically through the electrostrictive (or piezoelectric) strain generated in the crystal. A standard piezoelectric crystal is mounted in a similar manner so that the piezoelectrically generated strain is communicated to the left plate. Since the sensing capacitance C is given by

$$C = \epsilon \frac{A}{l} \quad (1)$$

where ϵ is the permittivity of air at atmospheric pressure, A the plate area, and l the separation, the capacitance change ΔC associated with a small change in l (Δl) will be given by

$$\Delta C = \left(-\frac{\epsilon A}{l^2}\right) \Delta l = -K \Delta l \quad (2)$$

If the electrostrictive and the piezoelectric standard crystals are driven with AC voltages at frequencies of ω and 2ω , both capacitor plates will be excited mechanically at a frequency of 2ω . When the phase and amplitudes of the electric fields of both crystals are suitably chosen, the capacitor plates will vibrate in exact synchronism producing a net zero modulation of the separation and thus of the capacitance at 2ω . Figure 2 shows the crystal deformations in the piezoelectric standard and the electrostrictive sample at the null condition. Clearly, if this null condition can be precisely established, then from the AC voltages applied to both crystals, their known dimensions and the piezoelectric coefficient of the standard crystal (quartz) the unknown electrostrictive coefficient can be calculated. For the piezoelectric sample the situation is slightly different.

A simple block diagram of the full measuring system is given in Fig. 3. The components of the mechanical circuit (e,b,c,d) are identical in principle to those used by Bohaty and Haussühl.¹ However, to sense and control the capacitor (b,c) a General Radio 1620 capacitance measuring assembly is used (j,k,l). To obtain maximum sensitivity, the capacitance bridge is operated at a frequency of 5 kHz, the standard piezoelectric crystal is driven at 14 Hz and the electrostrictor under study at 7 Hz. The phase locked detector is locked to the 14 Hz driving oscillator.

DC Servo Stabilization

Obviously the sensitivity constant K in Eq (2) can be made very large if the separation l can be made very small. In a practical system, however, a limiting value of l is set by slow dimension changes due to thermal drift. Even though the mechanical support for the sensing capacitor is made from super invar with a very small thermal expansion coefficient ($\leq 0.3 \times 10^{-6} \text{ deg}^{-1}$), and the assembly is put into a chamber controlled to $\pm 0.04^\circ\text{C}$, thermal dimension changes are still very much larger than the electrostrictive displacements induced at tolerable fields, and would take the bridge detector well out of its linear range. To overcome this problem, a DC output from the phase locked bridge detector is used to operate a Burleigh RC42 servo amplifier which actuates three parallel piezoceramic mechanical actuators made of PZT controlling the static plate separation (bc).

Instrument Examinations

Servo-Positioner Check

After the system has stabilized for some four hours, the DC servo system is disabled and the intrinsic drift rate of the capacitance determined by measuring the bridge unbalance signal as a function of time (Fig. 4). By rebalancing the bridge periodically the capacitance increment for a given unbalance voltage can be determined, and from the ΔC a corresponding Δl can be calculated. It is evident from Fig. 4 that without compensation the drift rate corresponds to a plate separation change of $1 \text{ Å}/\text{minute}$. Maintaining the same conditions, the DC servo is now turned on, and at the same gain

setting no drift is discernible. Turning the gain up by a factor of 100, however, (Fig. 4, right-hand scale) it is evident that the drift rate now corresponds to a linear dimension change of $0.002 \text{ Å}/\text{minute}$.

Resolution Check

To check the AC sensitivity the standard quartz crystal was driven by a Wavetek Model 142 oscillator at 14 Hz. With 30 volts rms applied to the bridge, the lock-in output as a function of voltage applied to the quartz crystal is given in Fig. 5. The linear relation expected for a piezoelectric is clearly evident. Right-hand scale shows the actual deformation of the quartz crystal in Å rms , calculated by use of the absolute calibrator that will be discussed later. The experimental error is much smaller than the solid circles and is about $\pm 0.1 \text{ mV}$, which corresponds to $\pm 10^{-3} \text{ Å}$. This value is the smallest resolvable increment at present. Taking the quartz thickness value of $l = 5.45 \text{ mm}$, the resolvable increment corresponds to the resolvable strain $\Delta l/l = \pm 2 \cdot 10^{-11}$.

Further Checks

The lock-in output for a fixed value of drive voltage to the quartz standard (10.8 V rms) was recorded as a function of capacitor plate separation (Fig. 6) and of voltage applied to the capacitance bridge (Fig. 7). If the measured signal comes only from the capacitance bridge unbalance, this should scale linearly with the square of capacitance and with the bridge oscillator voltage as is evident in Figs. 6 and 7. A slight anomaly observed at 110 pF in Fig. 6 is caused by the sensitivity dial change of the capacitance bridge.

AC Calibration Capacitor

We have described, so far, a system in which the known piezoelectric coefficient of a standard quartz crystal has been used to calibrate the AC voltage output in terms of a calculated plate separation change. We propose a different way of deriving the sensitivity by using a very small 3-terminal variable air capacitor which can be driven at low AC. Figure 8 shows the principle of the absolute calibrator using an alternating capacitance. When the capacitor plate is driven mechanically by the electromechanically generated strain in the crystal (I), the capacitance bridge output (5 kHz) is modulated at 14 Hz as in the bottom figure. If we use the small alternating capacitance connected in parallel to the sensing capacitor instead of driving the sample (II), the same order of modulated output can be established. If we measure the lock-in output by driving this alternating capacitance, from the known alternating capacitance change and the capacitance of the sensing capacitor, we can calculate the equivalent AC linear deformation using Eq (2). The scheme of the alternating capacitance generator designed is shown in Fig. 9. The capacitance is made in a completely shielded aluminum box. When the central circular aluminum plate is in the vertical position, no electric flux can thread between the needles and the capacitance is almost equal to zero. In the horizontal position the capacitance shows a maximum. By rotating the

aluminum plate with a constant speed motor (Electro-Craft Motomatic System), a sinusoidal capacitance change (3-26 pF) can be obtained as shown in the bottom figure. The reference signal to the phase locked detector is produced by the photodiode and the rotating shutter fixed on the rotating axis.

If we obtain the lock-in output of V_{ACG} mV by driving the alternating capacitance generator under one instrument condition with the sensing capacitor of C pF, the sample crystal deformation in \AA rms corresponding to the unit lock-in output in mV can be calculated as follows when measured under the same condition:

$$\left(\frac{\Delta l}{V_{ACG}}\right) = \frac{1430}{V_{ACG} C^2} [\text{\AA}/\text{mV}] \quad (3)$$

Sample Measurements

To get the unknown piezoelectric or electrostrictive coefficient, there are three different ways of using the present instrument:

1. Absolute Calibration
(using alternating capacitance generator)
2. Relative Calibration
(using standard quartz driving)
 - A. Separate vibrating method
 - B. Null condition method
3. Sign Determination of Electrostrictive Coefficient
(using electrostrictive standard PMS driving)

Absolute Calibration

By using the output from the alternating capacitance generator, the deformation corresponding to the lock-in output can be calculated. The piezoelectric or electrostrictive coefficient will, therefore, be given as follows:

$$d = \left(\frac{\Delta l}{V_{ACG}}\right) \times 10^{-10} V_{P,OUT}/V_{P,IN} [\text{mV}^{-1}] \quad (4a)$$

or

$$M = \sqrt{2} \left(\frac{\Delta l}{V_{ACG}}\right) \times 10^{-10} l_E V_{E,OUT}/V_{E,IN}^2 [\text{m}^2\text{V}^{-2}] \quad (4b)$$

where V_{OUT} is the lock-in output voltage in mV, V_{IN} is the voltage applied to the sample in V rms and l the thickness of the sample in m. Figure 5 is a good example for the piezoelectric case. We obtained the piezoelectric coefficient of quartz as $d_{11} = 2.27 \pm 0.01 \times 10^{-12} \text{ mV}^{-1}$ from the data.

Separate Vibrating Method

The lock-in output was recorded separately for the piezoelectric wurtzite and quartz under the optimum condition (Fig. 10). By using the output ratio of wurtzite and quartz at the same applied voltage and the quartz piezoelectric coefficient,

the wurtzite piezoelectric coefficient can be calculated as follows:

$$d_S = \frac{V_{S,OUT}}{V_{Q,OUT}} d_Q \quad (5)$$

Null Condition Method

With a fixed value of drive voltage to the wurtzite sample, the lock-in output as a function of voltage applied to the standard quartz crystals was measured (Fig. 11). The null condition is established at the output minimum position. By using the ratio of the voltage applied to the wurtzite and the minimum position voltage and the quartz piezoelectric coefficient, the wurtzite coefficient can also be calculated as follows:

$$d_S = \frac{V_{Q,IN}}{V_{S,IN}} d_Q \quad (6)$$

where crystal driving voltages are treated as root mean square values. Both methods gave the same value of the wurtzite piezoelectric coefficient ($d_{33} = 3.20 \pm 0.02 \times 10^{-12} \text{ mV}^{-1}$).

Figures 12 and 13 show the data for the electrostrictive sample $\text{Pb}(\text{Mg}_{1/3}\text{Nb}_{2/3})\text{O}_3$ ceramic. Lock-in output was completely proportional to the square of applied voltage (Fig. 12). Very clear null condition can also be obtained at about 100 V rms to the standard quartz (Fig. 13). In this case the electrostrictive coefficient is calculated as follows:

$$M_S = \sqrt{2} l_S d_Q V_{Q,IN}/V_{S,IN}^2 \quad (7)$$

where $V_{S,IN}$ and $V_{Q,IN}$ are voltages applied to the sample and to quartz standard at the output minimum position, l_S the sample thickness.

It is worth mentioning here that in a practical case, however, the lock-in output minimum is not exactly equal to zero because of a slight phase difference between the vibrations of both crystals. The details are discussed in the appendix.

Sign Determination of Electrostrictive Coefficient

To determine the sign of the unknown electrostrictive coefficient is rather complicated in a system which consists of the piezoelectric standard and the unknown electrostrictor, not only because the electric field frequency applied to the sample is different from the frequency for the standard, but also because the vibrational phase of the piezoelectric has two possibilities (180° difference) due to the crystal setting. We propose to use a known electrostrictor as a standard instead of quartz crystal, since the electrostrictive strain is not affected by 180° setting difference.

$\text{Pb}(\text{Mg}_{1/3}\text{Nb}_{2/3})\text{O}_3$ ceramic with perovskite-type structure is one of the best examples, which has a positive electrostrictive coefficient ($M = 1.05 \pm 0.01 \times 10^{-16} \text{ m}^2\text{V}^{-2}$).²

Example Data and Discussion

Some example data of piezoelectric and electrostrictive crystals and ceramics measured by the established instrument are listed in Table I, compared with the previous data. Coincidence between the values determined by the present and previous works for quartz and wurtzite indicates the precision of the established instrument. It is worth mentioning that the error is ten times smaller than the ones in the previous works. We emphasize that the resolution of $\pm 0.001\text{A}$ is equal to the greatest one in the world and corresponds to the resolvable strain $\Delta l/l \approx 10^{-10}$, the order of which other measurements (e.g. x-ray diffractometer) cannot attain to.

Further measurements about many samples including alkali halide crystals will be made in the near future.

Acknowledgments

This work was sponsored by the Office of Naval Research through Contract N00014-78-C-0291. We also wish to thank our colleague Dr. Barsch at the Materials Research Laboratory for his many samples.

References

- 1) Bohatý, L. and Hausühl, S. (1977) Acta Cryst. **A33**, 114.
- 2) Cross, L.E., Jang, S.J., Newham, R.E., Nomura, S. and Uchino, K. Ferroelectrics (submitted).
- 3) Bottom, V.E. (1970) J. Appl. Phys. **41**, 3941.
- 4) Kobayakov, I.B. and Pado, G.S. (1968) Soviet Phys. Solid State **9**, 1707.
- 5) Chang, Z.P. and Barsch, G.R. (1976) IEEE Trans.-Sonics and Ultrasonics **3**, 127.

Appendix

Superposition of Two Waves with Different Phases

When e_1 and e_2 are the amplitudes of AC deformations of the sample and the standard crystals respectively and δ the phase difference, the change of the sensing capacitor separation Δl will be given as follows:

$$\begin{aligned}\Delta l &= a_1 \sin \omega t - a_2 \sin (\omega t + \delta) \\ &= (a_1 - a_2 \cos \delta) \sin \omega t - a_2 \sin \omega \cos \omega t \\ &= [a_1^2 - 2a_1 a_2 \cos \delta + a_2^2]^{1/2} \sin (\omega t - \psi) \quad (8)\end{aligned}$$

where $\tan \psi = a_2 \sin \delta / (a_1 - a_2 \cos \delta)$.

$[1 - 2r \cos \delta + r^2]^{1/2}$ term represents, therefore, the normalized shape of the dilatometer output curve as a function of driving voltage applied to the quartz standard. Figure 14 shows the theoretical calculation of the null condition method for various phase differences.

Table I. Some example data of electromechanical coefficients

Sample	Coefficient	Present	Previous
Quartz <100>	$d_{11} (\times 10^{-12} \text{ mV}^{-1})$	+2.27 (± 0.01)	+2.27 ³
Wurtzite <001>	$d_{33} (\times 10^{-12} \text{ mV}^{-1})$	+3.20 (± 0.02)	+3.2 (± 0.2) ⁴
Berlinite <100>	$d_{11} (\times 10^{-12} \text{ mV}^{-1})$	-3.98 (± 0.05)	-5.3 (± 1.6) ⁵
$\text{Pb}(\text{Mg}_{1/3}\text{Nb}_{2/3})\text{O}_3$ (ceramic)	$M'_{11} (\times 10^{-16} \text{ m}^2\text{V}^{-2})$	+1.05 (± 0.01)	+1.4 (± 0.2) ²

Sample Holder

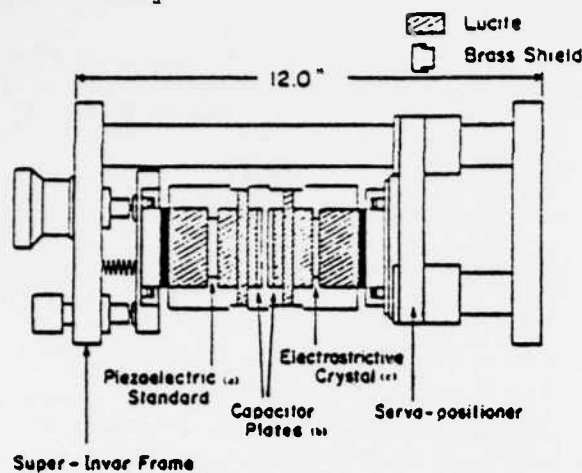


Fig. 1

Schematic of the dilatometer and support structure.

Block Diagram

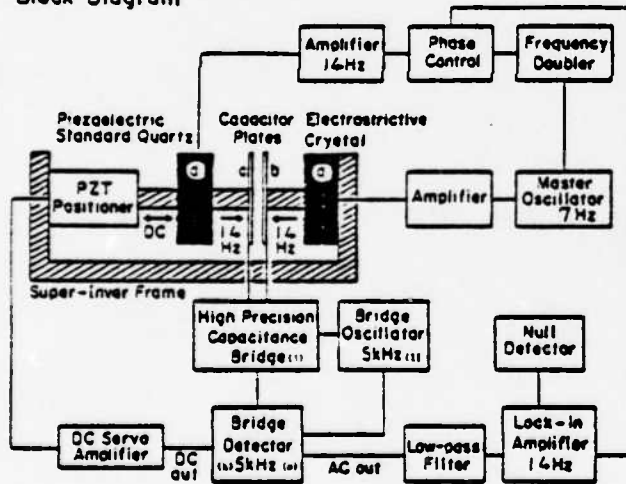


Fig. 3 Schematic diagram of the AC dilatometer.

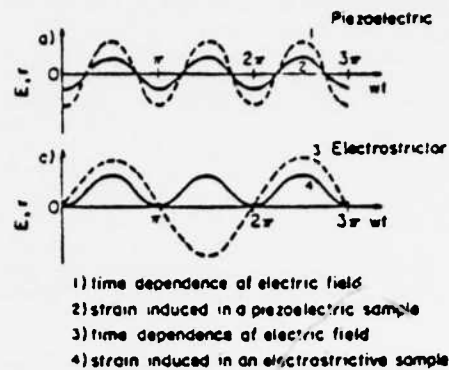
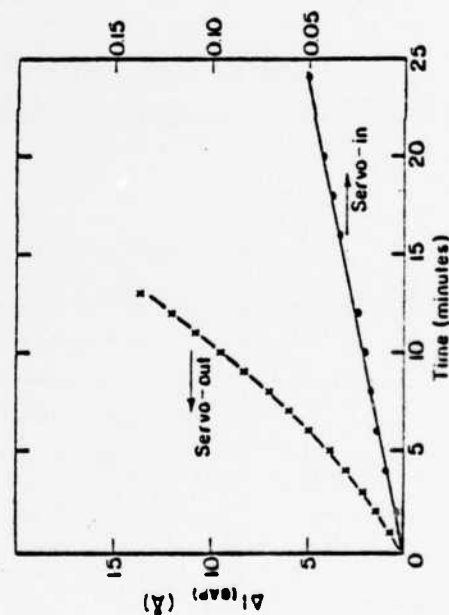


Fig. 2 Crystal deformations induced in the piezoelectric and the electro-strictor at null condition.

Fig. 4 DC plate separation change Δl as a function of time with and without the drift compensation Servo amplifier.

Quartz Driving Voltage Dependence

<100> longitudinal effect
Under the optimum condition
with $C = 79.6 \text{ pF}$

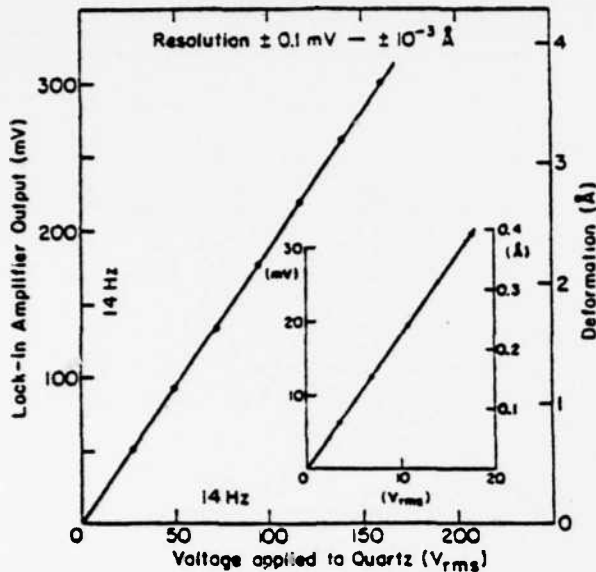


Fig. 5 Dilatometer output and the actual deformation as a function of driving voltage applied to the quartz standard crystal.

Bridge Oscillator Voltage Dependence

measured by Standard Quartz Driving

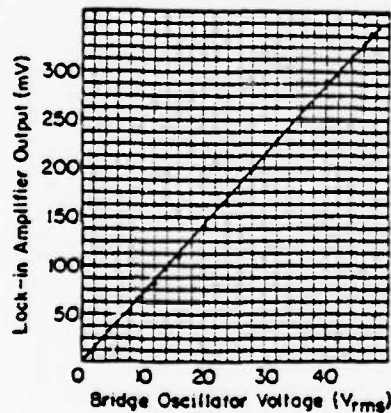


Fig. 7 Dilatometer output as a function of bridge oscillator voltage for fixed 10.8 V rms applied to the quartz crystal.

Capacitor Plates Gap Dependence

measured by Standard Quartz Driving

$$\text{Lock-in Amp. Output} \propto \Delta C = \left(-\frac{\Delta l}{\epsilon_0 A} \right) C^2$$

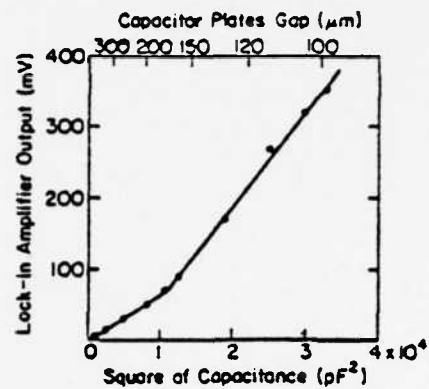
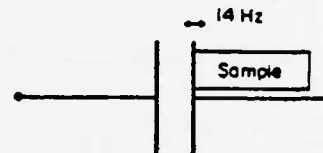


Fig. 6 Dilatometer output as a function of capacitor plate separation.

Principle of Absolute Standard using Alternating Capacitance

I) Sample Driving



II) Equivalent Alternating Capacitance

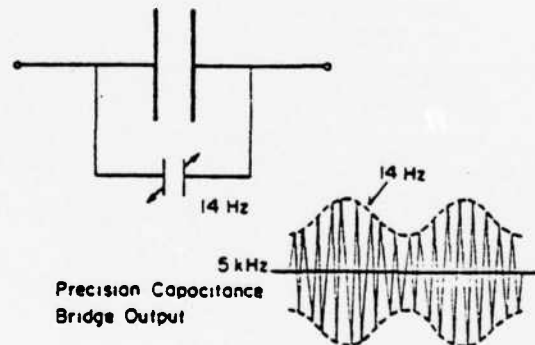


Fig. 8 Principle of the absolute calibrator. (I) sample driving; (II) equivalent alternating capacitance.

Alternating Capacitance Generator

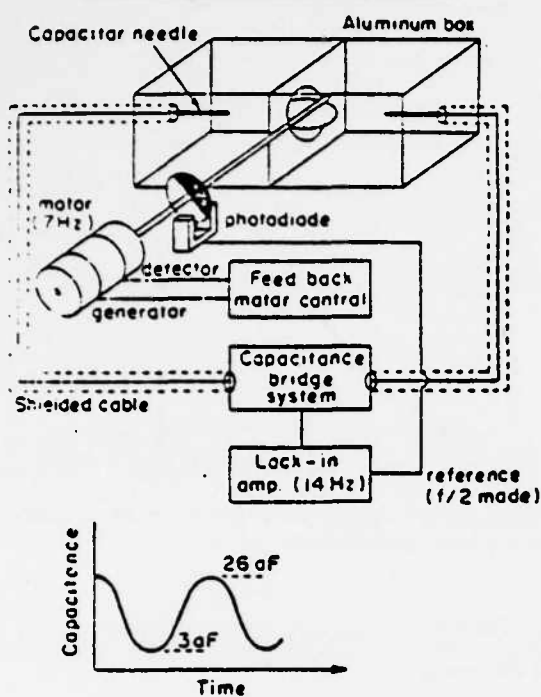


Fig. 9 Scheme of the alternating capacitance generator.

Null-condition Method

Quartz (100)
Wurtzite (001) $R = 1.41$
Under the optimum condition
with $C = 105.5 \text{ pF}$

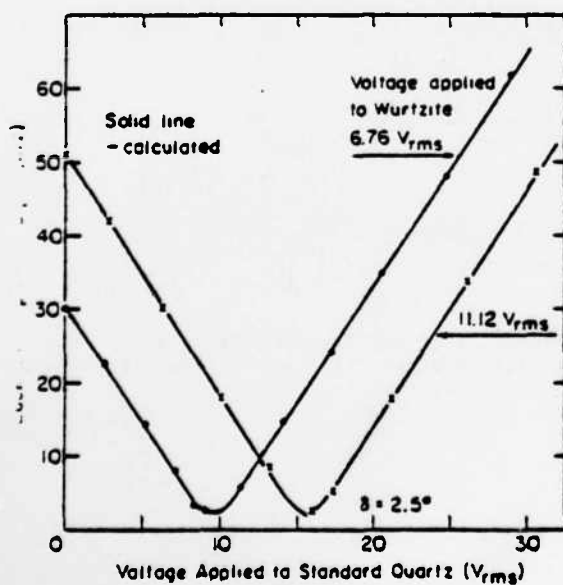


Fig. 11

Null condition method between wurtzite and quartz.

Separate - vibrating Method

Quartz (100)
Wurtzite (001) $R = 1.39$
Under the optimum condition
with $C = 105.5 \text{ pF}$

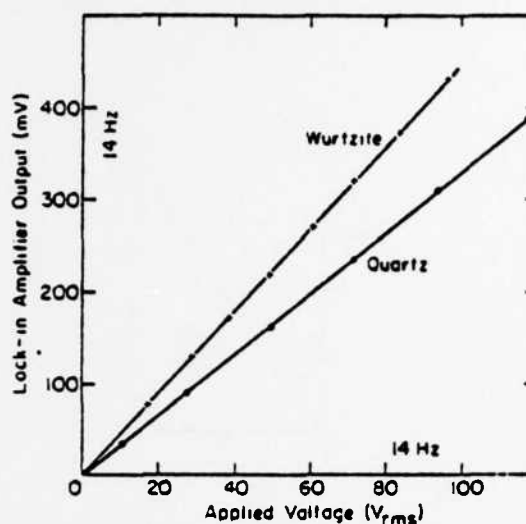


Fig. 10

Separate vibrating method for wurtzite and quartz.

Electrostriction of $\text{Pb}(\text{Mg}_{1/3}\text{Nb}_{2/3})\text{O}_3$ Ceramic

Sample thickness = 3.68 mm

Under the optimum condition
with $C = 74.1 \text{ pF}$

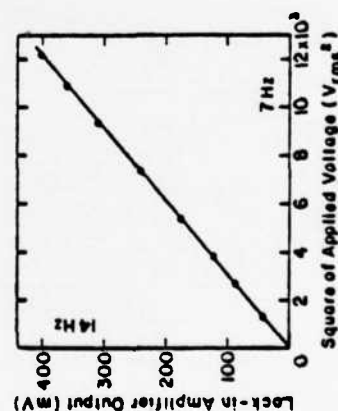


Fig. 12 Dilatometer output as a function of square of driving voltage applied to $\text{Pb}(\text{Mg}_{1/3}\text{Nb}_{2/3})\text{O}_3$ ceramic.

Null-condition between Quartz and
 $\text{Pb}(\text{Mg}_{1/3}\text{Nb}_{2/3})\text{O}_3$ Vibration
 Under the optimum condition
 with $C = 74.0 \text{ pF}$
 PMN Driving Voltage: $74.7 \text{ V}_{\text{rms}}$ (7Hz)

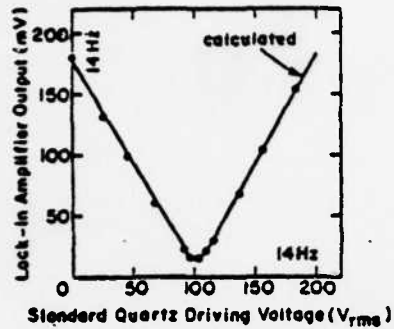


Fig. 13 Null condition method between PMN and quartz.

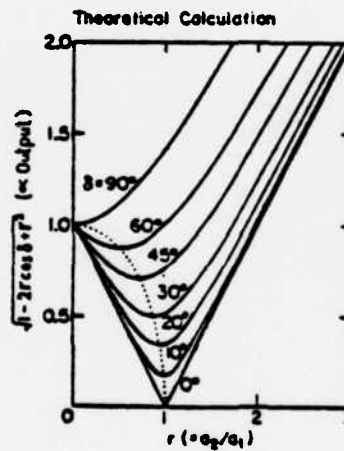


Fig. 14 Theoretical calculation of the null condition method for various phase differences between the sample and the standard vibrations.

APPENDIX 2.5

LARGE ELECTROSTRICTIVE EFFECTS IN RELAXOR FERROELECTRICS

LARGE ELECTROSTRICTIVE EFFECTS IN RELAXOR FERROELECTRICS†

L. E. CROSS, S. J. JANG and R. E. NEWNHAM

*Materials Research Laboratory, The Pennsylvania State University, University Park,
Pennsylvania 16802, USA*

and

S. NOMURA and K. UCHINO‡

*Department of Physical Electronics, Tokyo Institute of Technology, Ookayama, Meguro-ku,
Tokyo 152, Japan*

(Received April 14, 1979)

Lead magnesium niobate and other relaxor ferroelectrics are promising transducer materials for use as active elements in adaptive optic systems and similar applications. These ceramics are dominantly in the paraelectric phase, and dimension control is obtained through the high intrinsic quadratic electrostrictive effect. Since stable ferroelectric domain structures do not occur, the problems of dimensional creep and non-reproducibility (aging and de-aging effects) of the conventional poled piezoelectric ceramic are largely eliminated. Suitably chosen compositions in the $\text{Pb}_3\text{MgNb}_2\text{O}_9$ - PbTiO_3 family give electrostriction strains ten times larger than those of conventional BaTiO_3 -based ceramics. Low expansion coefficients are an added advantage for thermal stability.

Early in the evolution of piezoelectric ceramics, "soft" low-coercivity ferroelectric ceramics were often used under DC bias for piezoelectric applications. However, with the evolution of the $\text{Pb}(\text{Zr}, \text{Ti})\text{O}_3$, where the effective coercivity could be controlled by suitable dopants, the present generation of poled piezoceramics completely replaced these early electrostrictive devices. Over the past ten years, however, the rapid development of tape-cast multilayer technology, and the ensuing development of new high-permittivity low-saturation an hysteretic capacitor dielectrics has considerably changed the situation.

Foremost among these formulations are a large family of ferroelectrics which exhibit strong relaxation character in their dielectric response near the ferroelectric Curie temperature.¹⁻³ Lead-magnesium niobate ($\text{Pb}_3\text{MgNb}_2\text{O}_9$) is perhaps the best example for which a wide spectrum of properties has been measured in both single and poly-

crystal samples. In this crystal, the unusual response has been traced to a statistical inhomogeneity in the distribution of the Mg^{2+} and Nb^{5+} ions in the B-sites of the ABO_3 perovskite structure. This random arrangement leads to a distribution of microvolumes within the sample which have widely different Curie temperatures. Thus on cooling from high temperature, there is a Curie range rather than a distinct Curie point, and within this Curie range the crystal exhibits an intimate mixture of paraelectric and ferroelectric regions.

The point which is of major interest for potential electrostriction applications is that for temperatures within this Curie range, the crystal can be poled into a strongly ferroelectric form, but on removal of the poling field reverts back to a random arrangement of microdomain volumes with no net remanent moment. It is the growth, reorientation and subsequent decay of the microdomains which gives rise to the time-dependent dispersive dielectric response over the Curie region.

High field dielectric measurements at 60 Hz for temperatures just below the Curie range show an apparent normal hysteretic response with large levels of induced polarization.⁴ However, low-frequency pyroelectric studies indicate clearly that

† This work was supported by the Department of the Navy through the Office of Naval Research.

‡ Present address: Materials Research Laboratory, The Pennsylvania State University, University Park, PA 16802.

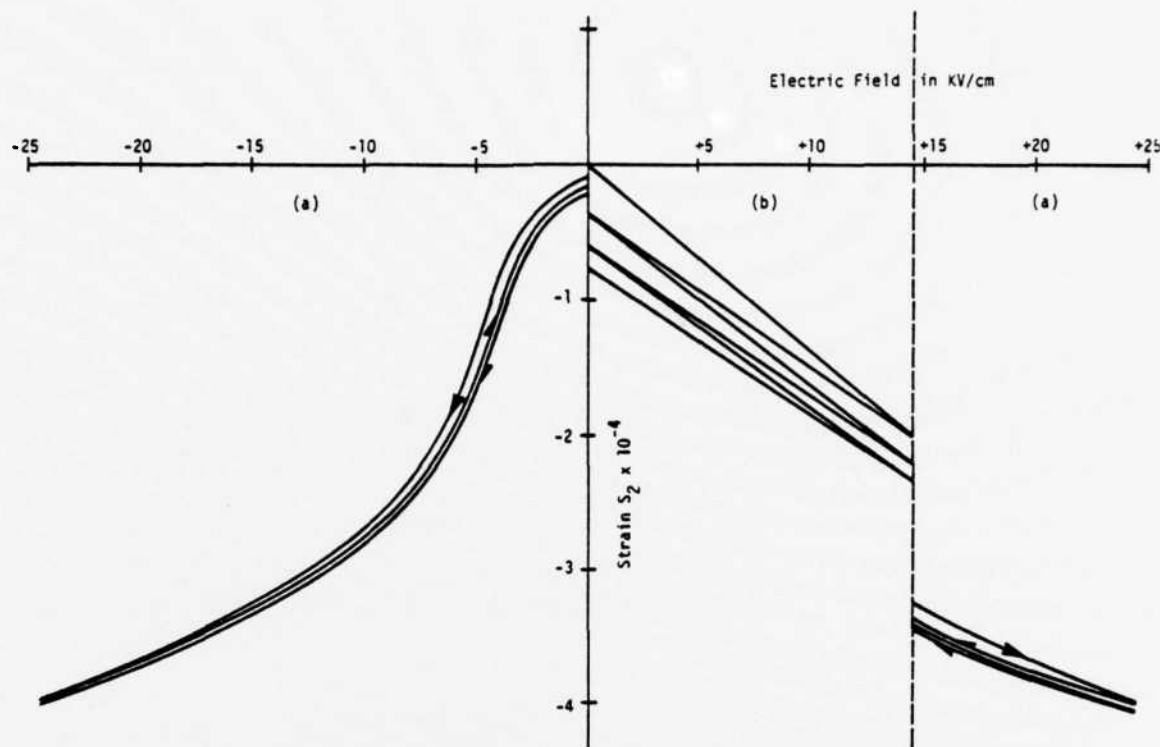


FIGURE 1 Transverse strain in ceramic specimens of 0.9 PMN-0.1 PT (a) and a typical hard PZT 8 piezoceramic (b) under slowly varying electric fields. Strains are comparable in the two materials but are far more reproducible in the electrostrictive relaxor because of de-aging effects in piezoelectric PZT.

the apparent remanence is spurious⁵ and is associated with the more slowly decaying domain component of the total polarization, thereby causing an S-shaped saturation curve without remanence.

Clearly, then, in the ferroelectric relaxors the possibility exists for utilizing the major poling strain for position control and for generating a high strain device which would be a close dielectric analog of the magnetostrictive systems. A critical initial datum required is a measure of the simple electrostriction in a relaxor ferroelectric for some temperature above the Curie range. If the magnitudes of the Q_{ij} constants are similar to those in more normal perovskites such as BaTiO_3 , then the high-induced polarizations in the Curie range will cause very high strain levels and these systems are obviously of practical interest for further study.

The thrust of our current studies is to develop materials with large electrostrictive response for static or low frequency position control and to

explore some of the materials systems in which an electric field-induced phase change may be used to generate and control a highly nonlinear strain response. Applications of current interest include optical interferometers, phase-correction mirrors, and other multiposition optical components.⁶

The relaxor ferroelectric chosen for study is $\text{Pb}_3\text{MgNb}_2\text{O}_9$, hereinafter abbreviated PMN. Early optical studies show that above -20°C PMN has no stable remanent polarization, even though large polarization levels can be field-induced with corresponding high stable quadratic electrooptic response. Clearly, if the quadratic electrostriction constants in this structure are "normal," high stable quadratic electrostriction should also occur. This was shown to be the case, and PMN itself is superior to modified BaTiO_3 in its electrostrictive response. The response can be further improved if the Curie range, which is below room temperature in PMN, could be shifted to slightly higher temperature, and our major effort has been focused on solid solution systems

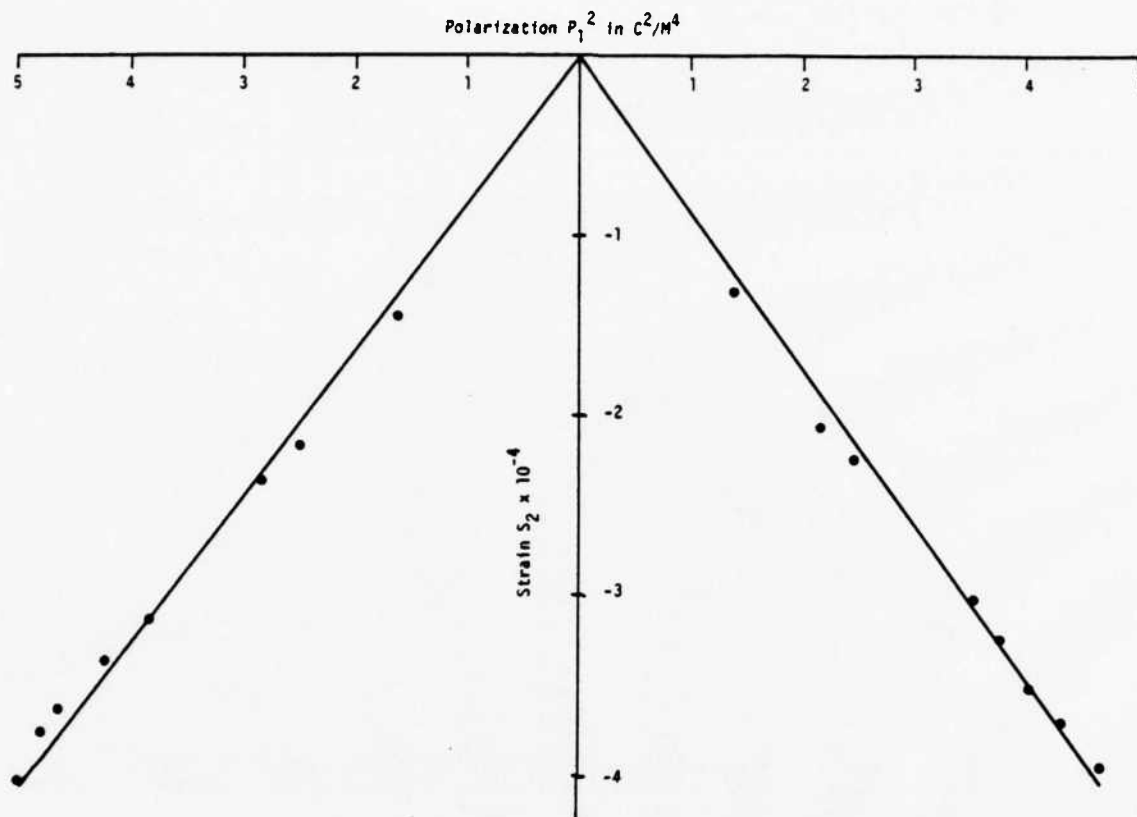


FIGURE 2. Field-induced transverse strain in polycrystalline 0.9 PMN-0.1 PT plotted against the square of the electric polarization. The linear relationship between these two quantities indicates that the strain is primarily electrostrictive in origin.

based on PMN which might accomplish this goal. In this paper, we report the results for a composition in the $Pb_3MgNb_2O_9$ - $PbTiO_3$ solid solution series, 0.9 PMN-0.1 PT.

Ceramic samples of 0.9 PMN-0.1 PT were prepared from reagent grade PbO , MgO , Nb_2O_5 , and TiO_2 . The constituent oxides were mixed in the appropriate proportions, ball-milled in alcohol, then dried and calcined at $950^\circ C$ for 15 hours. The calcine was reground and refired twice more under the same conditions to ensure complete reaction. After cold pressing to form disks of the required shape, samples were fired in a closed alumina crucible at $1320^\circ C$ for two hours, giving a specific gravity of 7.41. X-ray diffractometer patterns recorded at room temperature verified the cubic perovskite structure.

Weak-field dielectric measurements were recorded as a function of temperature using a

HP 427A automatic bridge and a model Delta Design 2300 environment control chamber. At 1 kHz, the dielectric constant of 0.9 PMN-0.1 PT is about 7000 at room temperature. The Curie range extends from about 0 to $40^\circ C$.

Electrostrictive strain was measured with a Model 24 DCDT-050 transducer manufactured by Hewlett Packard which operates as a differential transformer dilatometer. The transverse contraction S_2 was measured along a thin ceramic rod subject to DC bias fields (E_1) applied in a direction normal to the length of the rod. Figure 1 shows the transverse contraction of polycrystalline 0.9 PMN-0.1 PT plotted as a function of bias field. The relaxor ceramics are anhysteretic, and retrace the same curve with rising and falling fields.

For comparison the piezoelectric strain of a hard PZT 8 under cyclic fields is also plotted in Figure 1. This material has often been used in the

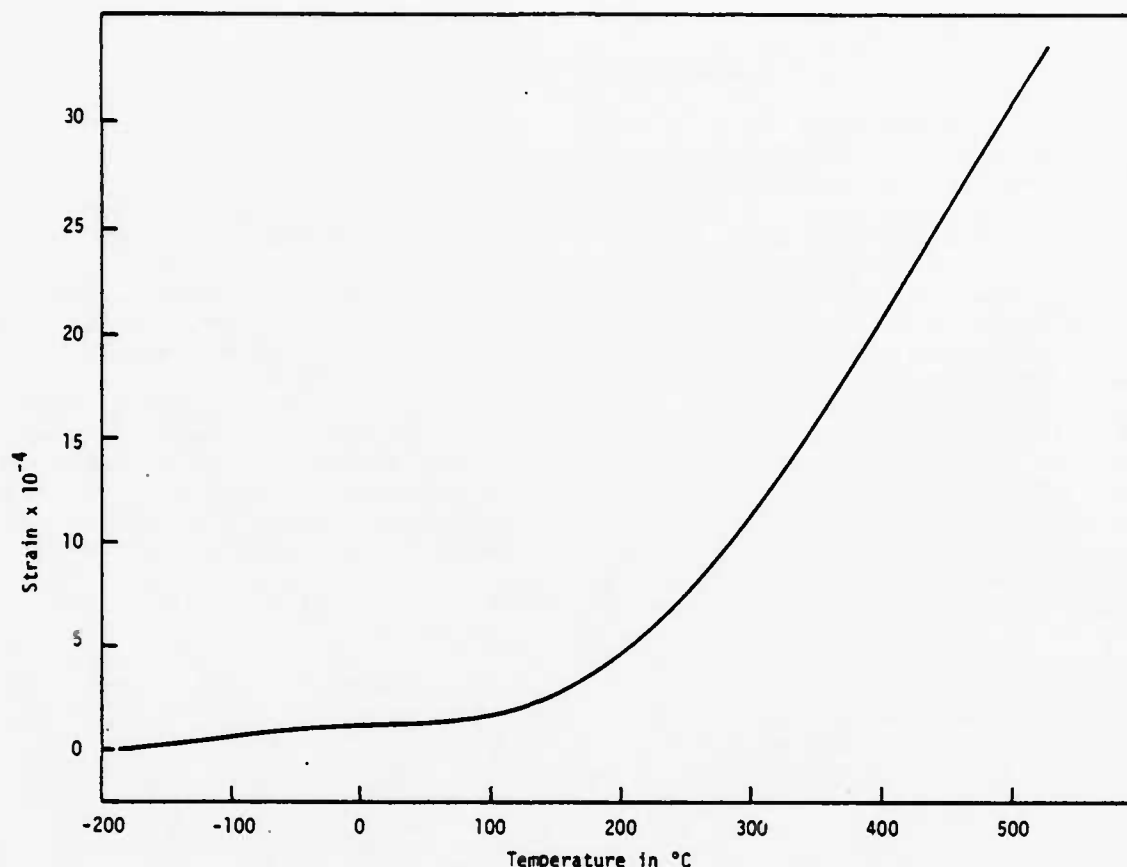


FIGURE 3 Thermal strain of polycrystalline 0.9 PMN-0.1 PT ceramic. The linear thermal expansion is about $10^{-5} \text{ }^{\circ}\text{C}^{-1}$ at 400°C and less than $10^{-6} \text{ }^{\circ}\text{C}^{-1}$ at room temperature.

fabrication of multi-dither mirrors and other active optical components.⁶ Of special interest in this comparison is the maximum strain and reproducibility under cyclic drive conditions.

It is in the area of dimensional stability and reproducibility where the relaxor material compares most favorably with PZT. Using a typical PZT 8 which has a piezoelectric coefficient $d_{31} = -128 \times 10^{-2} \text{ m/V}$, with a drive of 14 kV/cm which is required to produce a deformation comparable to the relaxor ceramics, initial deaging on the first cycles produces a considerable walk-off in the initial zero position. Field-induced strains in 0.9 PMN-0.1 PT are larger than those in PZT and far more reproducible.

Transverse electric strain is defined as $S_2 = Q_{12} P_1^2$ where Q_{12} is the polycrystalline (averaged) electrostriction constant and P_1 the electric polarization induced by an electric field E_1 . To confirm

the electrostrictive nature of the response in relaxor ferroelectrics, S_2 was plotted as a function of P_1^2 (Figure 2). The electric polarization was measured using the Sawyer and Tower method in which dielectric hysteresis loops were generated with a slow wave sweep of 1 Hz , and the maximum polarization read from the tip of the loop for each level of applied field. It is evident from Figure 2 that transverse strain S_2 is linearly related to P_1^2 for 0.9 PMN-0.1 PT ceramics. We have found the relation to be qualitatively satisfied for other high-permittivity materials as well.

The electrostriction coefficient Q_{12} calculated from the slope of the line in Figure 2 is $-0.9 \times 10^{-2} \text{ m}^4/\text{C}^2$, which is comparable to other perovskites. Ceramic BaTiO_3 , SrTiO_3 , $\text{Pb}(\text{Zr}, \text{Ti})\text{O}_3$ and KAlO_3 all have Q_{12} values of about $-1 \times 10^{-2} \text{ m}^4/\text{C}^2$. The large electrostrictive strains of PMN and other relaxor ferroelectrics

are not caused by unusually large electrostriction coefficients, but rather by unusually large induced polarizations. In other words, the strain can be attributed primarily to the large dielectric constant rather than a big coupling coefficient.

Another interesting property of relaxor ferroelectrics is the very small thermal expansion effect throughout the Curie range. Smolenskii and co-workers reported a linear expansion coefficient of $2 \times 10^{-6}/^{\circ}\text{C}$ for ceramic PMN near room temperature. Figure 3 shows the thermal strain of 0.9 PMN-0.1 PT plotted as a function of temperature. These measurements were made on a 93% dense ceramic prepared as a rectangular bar $3.5 \times 0.6 \times 0.6$ cm. The sample was mounted in a fused silica holder, and the strain measured with a displacement transducer, Hewlett-Packard Model 24 DCDT-250. After cooling down to liquid nitrogen temperature, the sample was heated at a rate of about $0.5^{\circ}\text{C}/\text{min}$ to 500°C . Calibration was carried out with a barium titanate standard, reproducing previous measurements to better than 5° .

In the temperature range -100 to $+100^{\circ}\text{C}$, the thermal expansion coefficient of 0.9 PMN-0.1 PT is less than $1 \times 10^{-6}/^{\circ}\text{C}$, comparable to the very best low-expansion ceramics. Thermal expansion coefficients of spodumene, petalite, and fused silica are in the range 0.2 to 0.9×10^{-6} . At higher temperatures above 300°C , the expansion coefficient of 0.9 PMN-0.1 PT increases to 10×10^{-6}

which is typical of perovskite oxides. By way of comparison, alumina, zirconia, and most oxide refractories also lie between 5 and 15×10^{-6} .

The thermal strains (Figure 3) are far smaller than the electrostrictive strains (Figure 1), which is extremely advantageous for micropositioner applications, since dimension changes caused by temperature variations can easily be compensated electrically. Near room temperature, a ten degree temperature shift produces a strain of about 5×10^{-6} , which could be eliminated by a field change of about 200 V/cm.

In summary, relaxor ferroelectrics offer several advantages over normal piezoelectric transducers: (1) large electrostrictive strains comparable to the best piezoelectric ceramics; (2) excellent positional reproducibility; (3) no poling is required, and (4) very low thermal expansion coefficients.

REFERENCES

1. G. A. Smolenskii, V. A. Isypov, A. I. Agranovskaya, and S. N. Popov, *Sov. Phys. Solid State*, **2**, 2584 (1961).
2. V. A. Bokov and I. E. Mylnikova, *Sov. Phys. Solid State*, **3**, 613 (1961).
3. G. A. Smolenskii, *Suppl. J. Phys. Soc. Japan*, **28**, 26 (1969).
4. R. Blinc, S. Detroni, I. Levstek, M. Pitas, S. Probesaj, and M. Schara, *J. Phys. Chem. Solids*, **20**, 187 (1961).
5. J. W. Smith, Ph.D. Thesis, The Pennsylvania State University (July 1967).
6. J. Feinleib, S. G. Lipson, and P. F. Cone, *Appl. Phys. Lett.*, **25**, 311 (1974).

APPENDIX 2.6

REVIEW: ELECTROSTRICTIVE EFFECT IN PEROVSKITES
AND ITS TRANSDUCER APPLICATIONS

Review

Electrostrictive effect in perovskites and its transducer applications

KENJI UCHINO, SHOICHIRO NOMURA

Department of Physical Electronics, Tokyo Institute of Technology, Ookayama, Meguro-ku, Tokyo 152, Japan

LESLIE E. CROSS, ROBERT E. NEWNHAM, SEI J. JANG

Materials Research Laboratory, The Pennsylvania State University, University Park, Pennsylvania 16802, USA

Properties of new electrostrictive materials for displacive transducers are reviewed including theoretical, material and design studies. Intensive investigation of the electrostrictive effects in ferroelectric and antiferroelectric perovskites have led to some empirical rules: the product of the electrostriction coefficient Q and the Curie-Weiss constant C is constant for all perovskite crystals and the Q value is proportional to the square of the thermal expansion coefficient, α . Consistent with the empirical rules, the relaxor ferroelectric ceramic $0.9 \text{ Pb}(\text{Mg}_{1/3}\text{Nb}_{2/3})\text{O}_3 - 0.1 \text{ PbTiO}_3$ possesses much larger strain with lower hysteresis, aging effects and thermal expansion than that obtained with piezoelectric lead zirconate titanate (PZT). Using a multilayer configuration similar to commercial capacitors, a new mirror control device capable of large strains with high reproducibility, up to $\Delta L/L \sim 10^{-3}$, with only 200 V applied has been developed.

1. Introduction

Electrostriction, the basic electromechanical coupling in all non-piezoelectric solids, is at present very poorly understood. There are few reliable measurements of the electrostriction tensor components, even in simple solids. The principal difficulty is associated with the small magnitude of the electrostrictive strains even at very high field levels. Theoretically, the absence of well authenticated experimental values has certainly been a major disincentive to development, and none of the present theories are viable.

The introduction of new displacive transducers to control optical beams in astronomy and communication have, however, prompted the development of a new family of electrostrictive ceramics. Properties which are important in materials for displacement transducers are as follows:

- (1) Sensitivity (strain/electric field);
- (2) Reproducibility (hysteresis);
- (3) Stability (temperature, aging);

- (4) Response time, resonances, damping;
- (5) Dielectric strength, resistivity;
- (6) Availability (size, weight).

The initial choices of materials were magnetostrictive or piezoelectric. Magnetostriction is not very useful because the strains ($\Delta L/L \sim 10^{-5} - 10^{-4}$) are much smaller than in piezoelectric materials ($\Delta L/L \sim 10^{-4} - 10^{-2}$) and because of the necessity of a large driving coil. The problems with piezoelectric ceramics are a large hysteresis and a substantial aging effect. On the other hand, the electrostriction in non-ferroic crystals is not associated with hysteresis or aging, and the response time is much faster than that of domain reorientations in ferroelectrics. An additional merit is that electric poling is not required. To take advantage of these characteristics new materials are needed with "enormous" electrostriction, contrary to the usual conception!

In this paper we review the properties of new electrostrictive transducers developed in

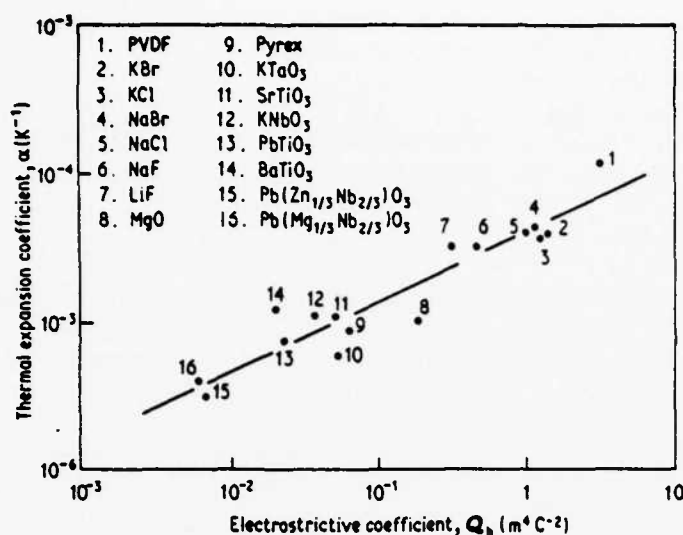


Figure 1 Thermal expansion coefficient α plotted as a function of hydrostatic electrostriction coefficient Q_h for various materials. The straight line has a slope of 0.5.

co-operative work at the Tokyo Institute of Technology and The Pennsylvania State University, including theoretical, material and design studies.

2. Electrostriction and its interrelation with thermal expansion

Electrostriction is a measure of the electric field (or polarization) induced shifts of the atoms or ions away from their natural equilibrium positions. Induced shifts of equivalent atoms or ions almost cancel each other in centric crystals, and only the shift difference due to potential anharmonicity causes strain. The electrostriction coefficients Q (or M) are defined as coefficients in the relationship between electric polarization, P , (or field E) and observed elastic strain x , expressed as $x = QP^2$ (or ME^2). Clearly, since the strain is a second rank polar tensor and E and P are polar vectors, then Q or M are fourth rank polar tensors. In a similar manner, the thermal expansion coefficient, α , can be regarded as a "compliance" coefficient defined by the relationship of strain with temperature T ($\Delta L/L = \alpha T$).

It is thus not unreasonable to expect that these anharmonicity related "compliance" coefficients will be interrelated. In Fig. 1, the thermal expansion coefficient α is plotted against the hydrostatic electrostriction coefficient $Q_h (= Q_{11} + 2Q_{12})$ for the materials of isotropic or cubic symmetry. Sources of the experimental data are listed in reference [1]. The power relation

$$\alpha = 4.2 \times 10^{-5} Q_h^{0.5} \quad (1)$$

was obtained for this graph.

3. Phenomenology of electrostriction

3.1. Case of ferroelectrics

First the thermodynamic phenomenology of electrostriction in ferroelectrics will be reviewed. Detailed treatments of this effect can be found in the papers of Devonshire [2], Kay [3] and Forsbergh [4]. For convenience, take the elastic Gibbs energy $G_1(X, P, T)$ ($dG_1 = x_{ij} dX_{ij} + E_m dP_m - SdT$) as the thermodynamical function where S is entropy. The free energy, G_1 , can be expressed as a polynomial in electric polarization P and stress X

$$\begin{aligned} G_1 = & \frac{1}{2} \alpha_{ij} P_i P_j + \frac{1}{6} \beta_{ijkl} P_i P_j P_k P_l \\ & + \frac{1}{6} \gamma_{ijklmn} P_i P_j P_k P_l P_m P_n \\ & - \frac{1}{2} s_{ijkl} X_{ij} X_{kl} \\ & - Q_{ijkl} P_i P_j X_{kl}. \end{aligned} \quad (2)$$

The subscripts denote directional tensor components.

Using the Voigt notation, the electrostriction coefficient tensor Q_{ij} is defined in a stress-free cubic crystal ($X = 0$) by the following equation

$$\begin{pmatrix} x_1 \\ x_2 \\ x_3 \\ x_4 \\ x_5 \\ x_6 \end{pmatrix} = \begin{pmatrix} Q_{11} & Q_{12} & Q_{12} & 0 & 0 & 0 \\ Q_{12} & Q_{11} & Q_{12} & 0 & 0 & 0 \\ Q_{12} & Q_{12} & Q_{11} & 0 & 0 & 0 \\ 0 & 0 & 0 & Q_{44} & 0 & 0 \\ 0 & 0 & 0 & 0 & Q_{44} & 0 \\ 0 & 0 & 0 & 0 & 0 & Q_{44} \end{pmatrix} \begin{pmatrix} P_1^2 \\ P_2^2 \\ P_3^2 \\ P_2 P_3 \\ P_3 P_1 \\ P_1 P_2 \end{pmatrix}. \quad (3)$$

These equations suggest one way of determining the electrostriction coefficients: by comparing the field or the polarization with the resulting strain. Note that the polarization can be either induced or spontaneous, corresponding to an induced or spontaneous strain, respectively. Therefore, the spontaneous volume change $(\Delta V/V)_s$ at the transition temperature can be written as

$$(\Delta V/V)_s = Q_h P_s^2, \quad (4)$$

where $Q_h = Q_{11} + 2Q_{12}$ and $P_s^2 (= P_1^2 + P_2^2 + P_3^2)$ is the spontaneous polarization at the Curie temperature.

Another way of determining the coefficients is obtained from the following argument. When a hydrostatic pressure, p , is applied to a centrosymmetric paraelectric crystal, the reciprocal dielectric susceptibility, χ_1 , is derived from the free energy G_1 as

$$\chi_1 = \alpha_1 + 2Q_h P, \quad (5)$$

where $\alpha_1 = (T - T_0)/C$ (Curie-Weiss law), T_0 is the Curie-Weiss temperature, and C the Curie-Weiss constant. The hydrostatic electrostriction coefficient Q_h is a measure of the rate of variation of the reciprocal susceptibility with pressure.

The values of the electrostriction coefficients can also be checked by using the shift of transition temperature, T_c , or Curie-Weiss temperature, T_0 , with hydrostatic pressure, derived from Equation 6

$$(\partial T_0/\partial p) = (\partial T_c/\partial p) = -2Q_h C. \quad (6)$$

3.2. Case of antiferroelectrics

Electrostrictive terms have been introduced into the Kittel free energy expression [5] for antiferroelectrics in reference [6] as follows

$$\begin{aligned} G_1 = & \frac{1}{2}\alpha(T)(P_a^2 + P_b^2) + \frac{1}{2}\beta(P_a^4 + P_b^4) \\ & + \frac{1}{6}\gamma(P_a^6 + P_b^6) + \eta P_a P_b - \frac{1}{2}\chi_T p^2 \\ & + Q_h(P_a^2 + P_b^2 + 2\Omega P_a P_b)p. \end{aligned} \quad (7)$$

This is a one-dimensional expression in which P_a and P_b denote the two sublattice polarizations, p is the hydrostatic pressure, χ_T the isothermal compressibility, and Q_h and Ω are electrostriction coefficients. An additional coefficient Ω is required to take account of the interaction between the sublattice polarizations. Introducing the Cross transformations [7] $P_F = (P_a + P_b)/2^{1/2}$ and $P_A = (P_a - P_b)/2^{1/2}$ leads to the following results.

Above the transition temperature the induced

volume change is related to the induced ferroelectric polarization by

$$(\Delta V/V)_i = Q_h(1 + \Omega)P_{F,i}^2, \quad (8)$$

while below the Néel temperature the spontaneous volume change is related to the spontaneous antiferroelectric polarization by

$$(\Delta V/V)_s = Q_h(1 - \Omega)P_{A,s}^2. \quad (9)$$

In the case of antiferroelectrics, the spontaneous volume change at the transition temperature can be either positive or negative, depending on the Ω values, which differs markedly from ferroelectrics.

The pressure derivatives of the Néel and Curie-Weiss temperature are

$$(\partial T_N/\partial p) = -2Q_h(1 - \Omega)C \quad (10)$$

and

$$(\partial T_0/\partial p) = -2Q_h(1 + \Omega)C, \quad (11)$$

where C is the Curie-Weiss constant. The variation of the reciprocal susceptibility, χ , with hydrostatic pressure in the paraelectric phase is

$$(\partial \chi/\partial p) = 2Q_h(1 + \Omega). \quad (12)$$

Good agreement between the experimental data [8, 9] and the predictions has been obtained for the antiferroelectric perovskites PbZrO_3 and $\text{Pb}(\text{Mg}_{1/2}\text{W}_{1/2})\text{O}_3$.

4. Experimental methods of measuring electrostriction

As suggested in the previous section, there are several experimental methods for determining the electrostriction coefficients. Direct measurements of strain include optical methods (interferometer and optical lever), X-ray methods, electrical methods (capacitance and differential transformer), and strain gauge methods. Pressure gauge methods and the pressure dependence of the dielectric permittivity are indirect measurements. Some experimental measurements on the relaxor ferroelectric perovskite $\text{Pb}(\text{Mg}_{1/3}\text{Nb}_{2/3})\text{O}_3$ are discussed in the following sections.

4.1. Strain gauge methods [10]

Fig. 2 shows a strain gauge determination of longitudinal electrostrictive strain σ_1 measured as a function of an applied electric field (0.002 Hz) at various temperatures between -10 and $+80^\circ\text{C}$. Experimental values of the electrostriction coefficients are plotted as a function of temperature in

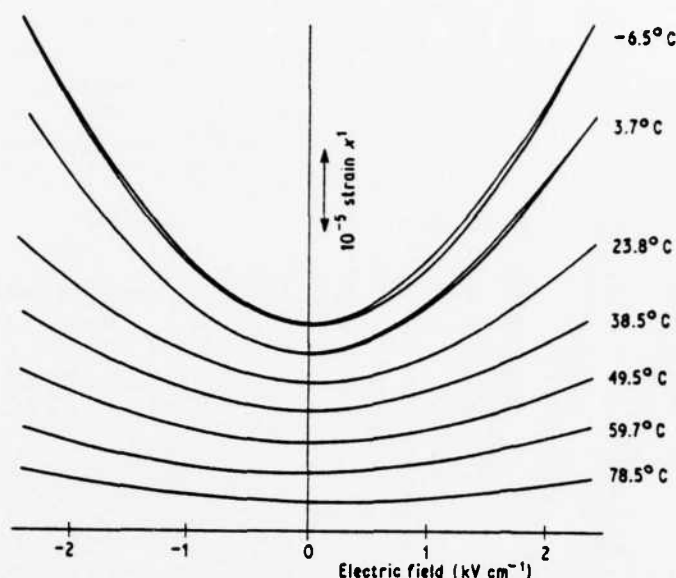


Figure 2 Electric field dependence of the longitudinal electrostriction in $\text{Pb}(\text{Mg}_{1/3}\text{Nb}_{2/3})\text{O}_3$ at various temperatures (Strain gauge methods).

Fig. 3. It is evident that the electrostriction coefficients do not change significantly through the relaxation temperature range

$$(Q_{11} = 2.50(\pm 0.14) \times 10^{-2} \text{ m}^4 \text{ C}^{-2},$$

$$Q_{12} = -0.96(\pm 0.02) \times 10^{-2} \text{ m}^4 \text{ C}^{-2}).$$

4.2. Pressure dependence of permittivity [10]

Fig. 4 shows the variation of the reciprocal susceptibility with hydrostatic pressure at various tem-

peratures. The gradual increase in slope observed for $\text{Pb}(\text{Mg}_{1/3}\text{Nb}_{2/3})\text{O}_3$ with increasing temperature, can be explained by the diffuse phase transition theory. Using Equation 6 the hydrostatic electrostriction coefficient Q_h can be calculated as $0.60(\pm 0.08) \times 10^{-2} \text{ m}^4 \text{ C}^{-2}$, in good agreement with the value calculated from the direct electro-

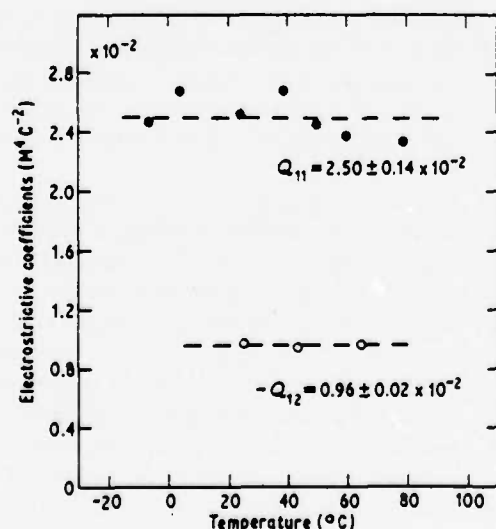


Figure 3 Temperature dependence of the electrostriction in $\text{Pb}(\text{Mg}_{1/3}\text{Nb}_{2/3})\text{O}_3$ single crystals.

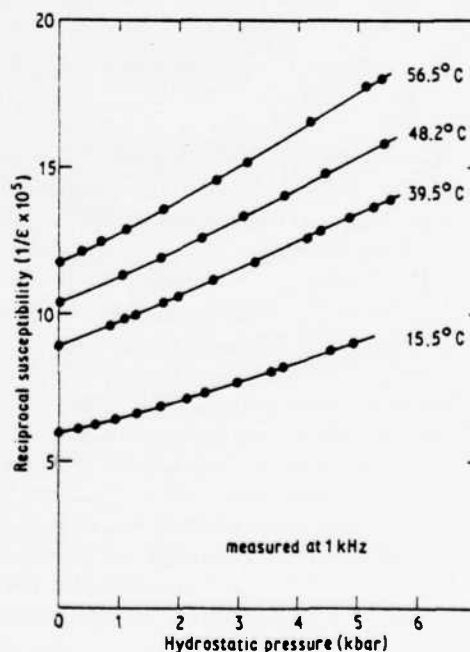


Figure 4 Hydrostatic pressure dependence of the reciprocal permittivity in $\text{Pb}(\text{Mg}_{1/3}\text{Nb}_{2/3})\text{O}_3$ at various temperatures.

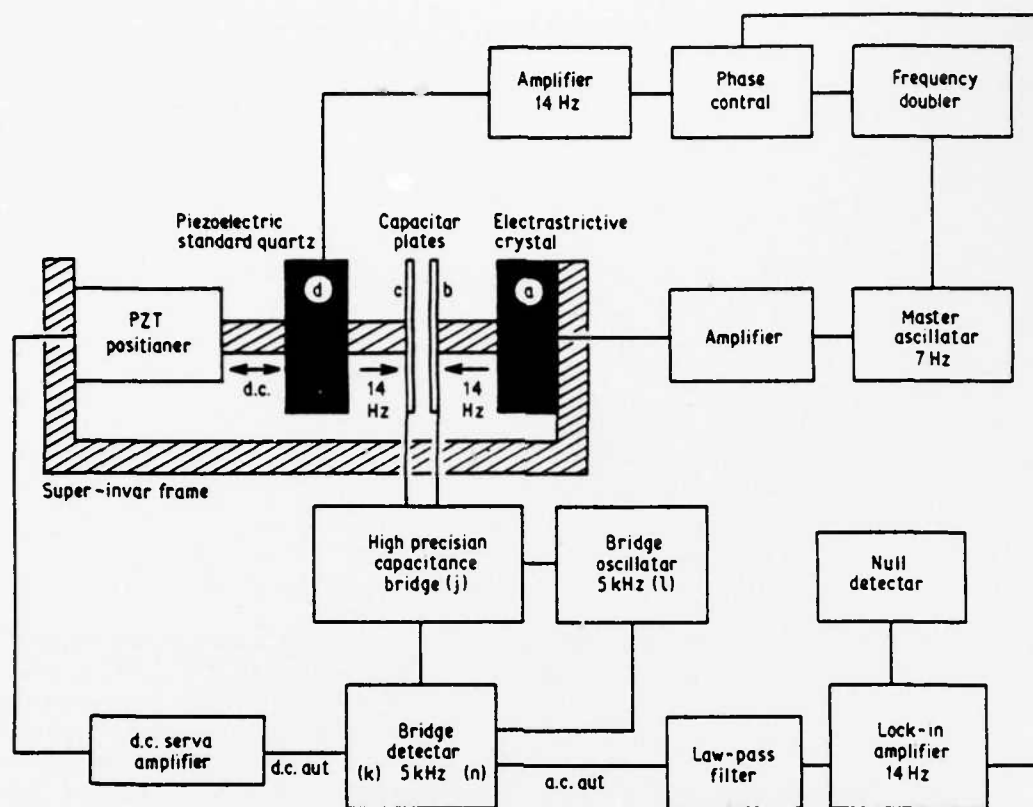


Figure 5 Schematic diagram of the a.c. capacitance dilatometer.

strictive strain measurements ($Q_{11} + 2Q_{12} = 0.58(\pm 0.18) \times 10^{-2} \text{ m}^4 \text{ C}^{-2}$).

4.3. A.c. capacitance dilatometer [11, 12]

A new type of ultrasensitive capacitance dilatometer especially suited to low permittivity solids has been constructed which is capable of resolving low frequency a.c. linear displacements of 10^{-13} m (10^{-3} \AA) (Fig. 5). To measure the electrostriction coefficient, an electric field at 7 Hz is applied to the sample crystal through an oscillator amplifier combination. This sets the sensing capacitor plate vibrating at 14 Hz. A phase locked signal at 14 Hz is then applied to the standard quartz crystal. The lock-in amplifier which is phase-locked to the 14 Hz driving frequency senses any component in the bridge output (capacitance) which is at 14 Hz and in phase with the driving oscillator. By manipulating voltages applied to the unknown and standard crystals, a null condition can be achieved. The unknown coefficient can then be derived from the voltage ratio and appropriate geometrical constants. Thermal drift causes

a change in the separation of the capacitor plates, resulting in a d.c. unbalance at the bridge. This signal is determined by the bridge detector, amplified, and applied to the lead zirconate titanate (PZT) piezoelectric pushers to return the capacitor plates to position. Because of this servo action, the bridge detector may be operated at maximum sensitivity without being driven beyond its linear range.

The $\text{Pb}(\text{Mg}_{1/3}\text{Nb}_{2/3})\text{O}_3$ ceramic sample was driven at 7 Hz without applying a voltage to the standard crystal (Fig. 6a). The expected quadratic relation between voltage and output is clearly evident. Fig. 6b shows an example of the null condition. After proper adjustment of phase with a certain voltage level applied to the sample, the output curve was obtained as a function of voltage applied to the quartz standard. Balance gave the electrostriction coefficient $\bar{M}_{11} = 8.46 \times 10^{-3} d_{11}$ (quartz) or $1.92(\pm 0.02) \times 10^{-16} \text{ m}^2 \text{ V}^{-2}$, in good agreement with the value determined by the strain gauge method [13].

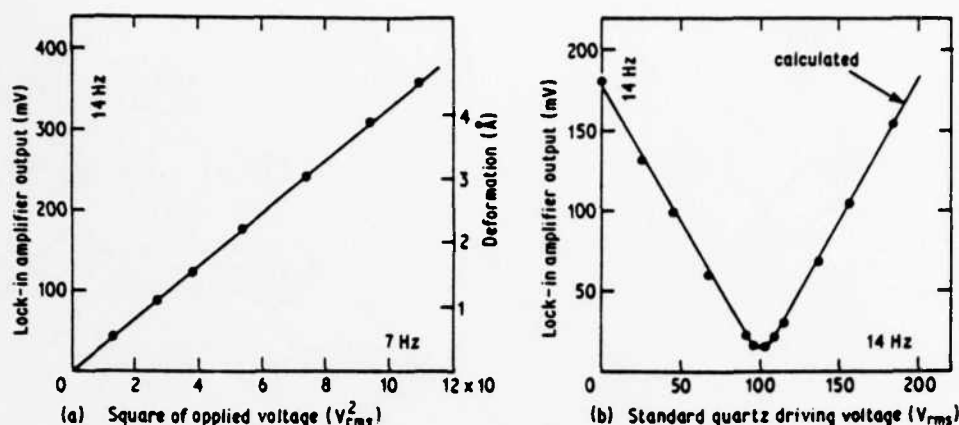


Figure 6 (a) Dilatometer output as a function of square of driving voltage applied to $\text{Pb}(\text{Mg}_{1/3}\text{Nb}_{2/3})\text{O}_3$ ceramic; sample thickness = 3.68 mm and $C = 74.1$ pF. (b) Null condition between $\text{Pb}(\text{Mg}_{1/3}\text{Nb}_{2/3})\text{O}_3$ and quartz; PMN driving voltage = $74.7 V_{rms}$ (7 Hz) and $C = 74.0$ pF.

5. Electrostriction in perovskite crystals

Hydrostatic electrostriction coefficients Q_h and Curie-Weiss constants C , for several kinds of perovskite type oxide crystals are summarized in Table I. Coefficients are listed for simple, disordered, partially-ordered and ordered ferroelectrics, antiferroelectrics, and non-polar dielectrics. Sources of the original experimental data are listed in references [6, 10, 14]. The magnitude of the electrostrictive coefficient is not effected strongly by ferroelectricity, antiferroelectricity, or non-polar behaviour, but is very dependent on the degree of order in the cation arrangement. It is proposed that "the electrostrictive coefficient Q increases with cation order from disordered, through partially-ordered, simple and then ordered perovskites", is used as an empirical rule i.e. Rule I. The decrease in the Curie-Weiss constant from its

highest values in disordered, through partially-ordered, and simple and ordered perovskites is also suggestive. This leads to experimental Rule II, that is, "the product of the electrostriction coefficient, Q , and the Curie-Weiss constant, C , is nearly constant for all ferroelectric and antiferroelectric perovskites ($Q_h C = 3.1(\pm 0.4) \times 10^3 \text{ m}^4 \text{ C}^{-2} \text{ K}$)."

The results of the electrostriction measurements on the solid solution systems are also very suggestive. In the $\text{SrTiO}_3\text{--Bi}_{2/3}\text{TiO}_3$ system [14], the substitution of Bi^{3+} for Sr^{2+} causes a remarkable decrease in the electrostriction coefficient from $Q_h = 5.0 \times 10^{-2} \text{ m}^4 \text{ C}^{-2}$ in SrTiO_3 to $Q_h = 1.3 \times 10^{-2} \text{ m}^4 \text{ C}^{-2}$ in $0.856 \text{ SrTiO}_3\text{--}0.144 \text{ Bi}_{2/3}\text{TiO}_3$. In the systems $\text{Pb}(\text{Mg}_{1/3}\text{Nb}_{2/3})\text{O}_3\text{--PbTiO}_3$ [13] and $\text{Pb}(\text{Mg}_{1/3}\text{Nb}_{2/3})\text{O}_3\text{--Pb}(\text{Mg}_{1/2}\text{W}_{1/2})\text{O}_3$ [15], the small Q_h value of $\text{Pb}(\text{Mg}_{1/3}\text{Nb}_{2/3})\text{O}_3$ increases

TABLE I Electrostrictive coefficients, Curie-Weiss constants and their product values for various perovskite-type crystals [6, 10, 14]

Polar-type	Order-type	Substance	Q_h ($\times 10^{-2} \text{ m}^4 \text{ C}^{-2}$)	C ($\times 10^4 \text{ K}$)	$Q_h C$ ($\times 10^3 \text{ m}^4 \text{ C}^{-2} \text{ K}$)
Ferroelectric	Disordered	$\text{Pb}(\text{Mg}_{1/3}\text{Nb}_{2/3})\text{O}_3$	0.60	4.7	2.8
		$\text{Pb}(\text{Zn}_{1/3}\text{Nb}_{2/3})\text{O}_3$	0.66	4.7	3.1
	Partially ordered	$\text{Pb}(\text{Sc}_{1/2}\text{Nb}_{1/2})\text{O}_3$	0.83	3.5	2.9
	Simple	BaTiO_3	2.0	1.5	3.0
		PbTiO_3	2.2	1.7	3.7
		SrTiO_3	4.7	0.77	3.6
		KTaO_3	5.2	0.5	2.6
Antiferroelectric	Partially ordered	$\text{Pb}(\text{Fe}_{2/3}\text{U}_{1/3})\text{O}_3$	—	2.3	—
	Simple	PbZrO_3	2.0	1.6	3.2
	Ordered	$\text{Pb}(\text{Co}_{1/2}\text{W}_{1/2})\text{O}_3$	—	1.2	—
		$\text{Pb}(\text{Mg}_{1/2}\text{W}_{1/2})\text{O}_3$	6.2	0.42	2.6
Non-polar	Disordered	$(\text{K}_{2/3}\text{Bi}_{1/3})(\text{Zn}_{1/3}\text{Nb}_{2/3})\text{O}_3$	0.55–1.15	—	—
	Simple	BaZrO_3	2.3	—	—

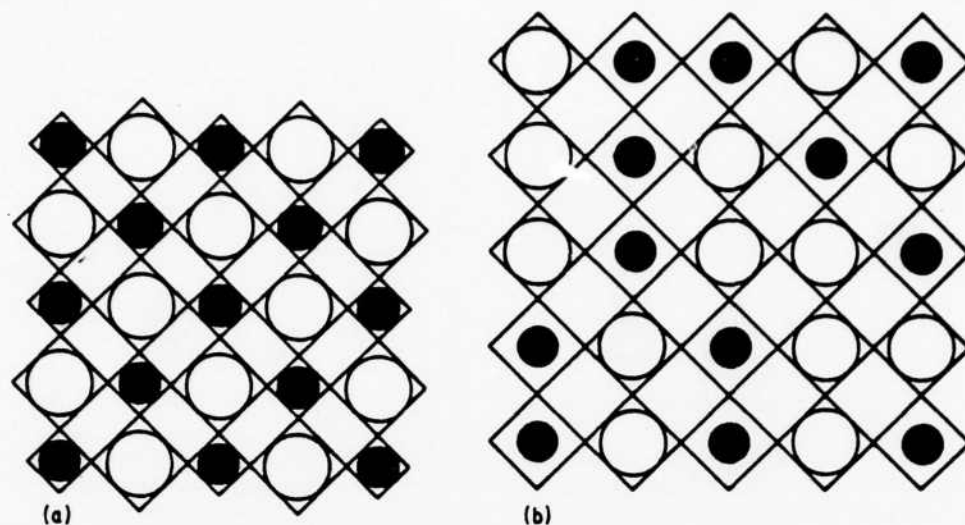


Figure 7 Crystal structure models of the $A(B_{I/2}B_{II/2})O_3$ type perovskite: (a) ordered structure with a small rattling space, and (b) disordered structure with a large rattling space. $\circ = B_I$ ion and $\bullet = B_{II}$ ion.

with increasing $PbTiO_3$ or $Pb(Mg_{1/2}W_{1/2})O_3$ content. A larger rate of increase was observed for the $Pb(Mg_{1/3}Nb_{2/3})O_3$ – $Pb(Mg_{1/2}W_{1/2})O_3$ system than for the $Pb(Mg_{1/3}Nb_{2/3})O_3$ – $PbTiO_3$ system because of the tendency of Mg and W ions to order.

An intuitive crystallographic model to explain the “constant QC rule” has been proposed. Fig. 7a and b show the ordered and disordered structures for an $A(B_{I/2}B_{II/2})O_3$ perovskite crystal. Assuming a rigid ion model, a large “rattling” space is expected for the smaller B ions in the disordered structure because the larger B ions prop open the lattice framework. Much less “rattling” space is expected in the ordered arrangement where neighbouring atoms collapse systematically around the small B ions. The densely-packed structure of B ions in the ordered perovskite illustrated in Fig. 7a has been observed for 0.9 $Pb(Mg_{1/2}W_{1/2})O_3$ –0.1 $Pb(Mg_{1/3}Nb_{2/3})O_3$ by Amin *et al.* [16]. When an electric field is applied to a disordered perovskite, the B ions with a large rattling space can shift easily without distorting the oxygen framework. Larger polarization can be expected for unit magnitude of electric field, in other words, larger dielectric constants and larger Curie–Weiss constants. Also smaller strains are expected per unit magnitude of polarization, resulting in lower electrostriction coefficients. On the other hand, in ordered perovskites with a very small rattling space, the B ions cannot move easily without distorting the octahedron. A smaller Curie–Weiss constant and a larger electrostriction coefficient are expected.

6. Giant electrostriction in relaxor ferroelectrics [13, 17]

Since the magnitude of electrostrictive displacement under electric field may be estimated from the value of $Q\epsilon^2$ (ϵ = permittivity) or QC^2 (eliminating the temperature dependence), and the product QC is nearly constant for all ferroelectric perovskites, relaxor (disordered) ferroelectrics with small electrostrictive Q coefficient but very large permittivity (or Curie–Weiss constant), are preferred to the usual perovskites (e.g. $Pb(Zr, Ti)O_3$ or $BaTiO_3$ based ceramics) for practical applications.

The relaxor ferroelectric chosen for study is $Pb(Mg_{1/3}Nb_{2/3})O_3$, which itself is superior to conventional modified $BaTiO_3$ ceramics in its electrostrictive response. The response can be further improved if the Curie range, which is below room temperature in $Pb(Mg_{1/3}Nb_{2/3})O_3$, could be shifted to a slightly higher temperature. In this section the results for a composition in the $Pb(Mg_{1/3}Nb_{2/3})O_3$ – $PbTiO_3$ solid solution series, 0.9 $Pb(Mg_{1/3}Nb_{2/3})O_3$ –0.1 $PbTiO_3$ are described.

The Curie range of this sample extends from about 0 to 40°C, and the room temperature dielectric constant is about 7000 at 1 kHz. Using a differential transformer dilatometer, the transverse electrostrictive strain x_2 was measured along the length of a thin ceramic rod, subject to d.c. bias fields (E_1) applied in a perpendicular direction (Fig. 8). The relaxor ceramics are anhysteretic, and

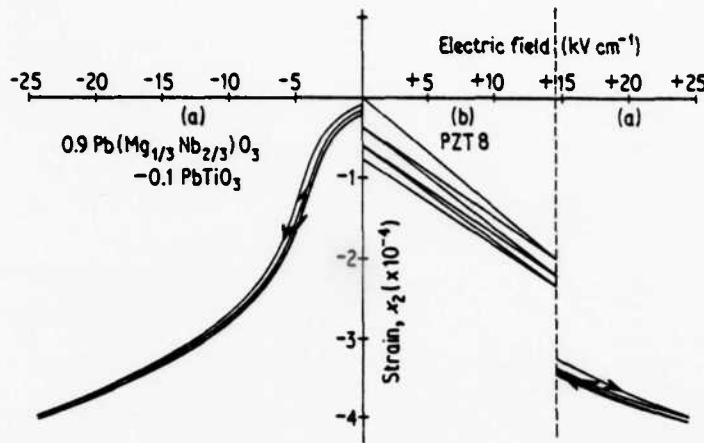


Figure 8 Transverse strain in ceramic specimens of (a) $0.9 \text{ Pb}(\text{Mg}_{1/3}\text{Nb}_{2/3})\text{O}_3 - 0.1 \text{ PbTiO}_3$, and (b) a typical hard PZT 8 piezoceramic under slowly varying electric fields.

retrace the same curve with rising and falling fields. For comparison the piezoelectric strain of a hard PZT 8 under cyclic fields is also plotted in Fig. 8. This material has often been used in the fabrication of multi-dither mirrors and other active optical components [18]. Field-induced strains in $0.9 \text{ Pb}(\text{Mg}_{1/3}\text{Nb}_{2/3})\text{O}_3 - 0.1 \text{ PbTiO}_3$ are larger than those in PZT and far more reproducible under cyclic drive conditions. Transverse electrostrictive strain is defined as $x_2 = \bar{Q}_{12}P_1^2$ where \bar{Q}_{12} is the polycrystalline (averaged) electrostriction coefficient and P_1 the electric polarization induced by an electric field E_1 . The strain x_2 is plotted as a function of P_1^2 in Fig. 9. It is evident that the linear relation between x_2 and P_1^2 is substantiated even for high-permittivity materials such as $0.9 \text{ Pb}(\text{Mg}_{1/3}\text{Nb}_{2/3})\text{O}_3 - 0.1 \text{ PbTiO}_3$. The electrostriction coefficient \bar{Q}_{12} calculated from the slope of the line is $-0.9 \times 10^{-2} \text{ m}^4 \text{ C}^{-2}$, which is slightly smaller than other simple perovskites. The

large electrostrictive strains of relaxor ferroelectrics can be attributed primarily to the large dielectric constant rather than to a big (electrostrictive) coupling coefficient.

Another interesting property of relaxor ferroelectrics is the very small thermal expansion effect throughout the Curie range, as expected from the empirical rule $\alpha^2 \propto Q$ as discussed in Section 2. Fig. 10 shows the thermal strain of $0.9 \text{ Pb}(\text{Mg}_{1/3}\text{Nb}_{2/3})\text{O}_3 - 0.1 \text{ PbTiO}_3$ plotted as a function of temperature. In the temperature range -100 to $+100^\circ \text{C}$, the thermal expansion coefficient is less than $1 \times 10^{-6} \text{ K}^{-1}$, comparable to the best low-expansion ceramics or fused silica. The thermal strains (Fig. 10) are far smaller than the electrostrictive strains (Fig. 8), which is extremely advantageous for micropositioner applications, since dimension changes caused by temperature variations ($\Delta L/L \sim \pm 5 \times 10^{-6}$ for $\Delta T \sim \pm 10 \text{ K}$) can easily be compensated electrically ($\pm 200 \text{ V cm}^{-1}$ feedback).

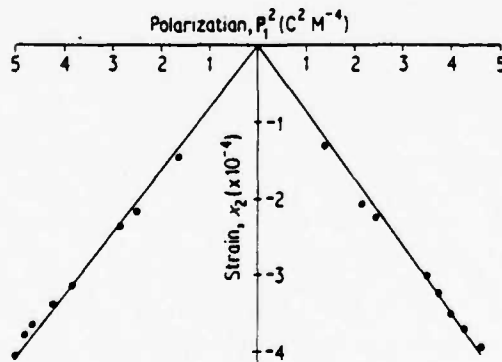


Figure 9 Field-induced transverse strain in ceramic $0.9 \text{ Pb}(\text{Mg}_{1/3}\text{Nb}_{2/3})\text{O}_3 - 0.1 \text{ PbTiO}_3$ plotted against the square of the electric polarization.

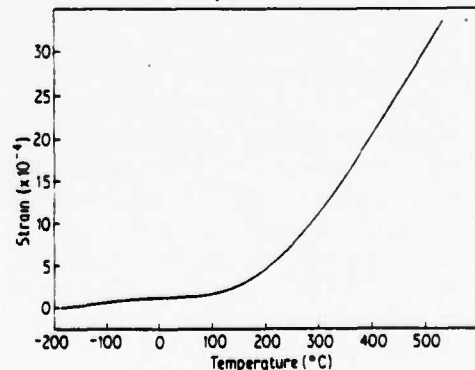


Figure 10 Thermal expansion in polycrystalline $0.9 \text{ Pb}(\text{Mg}_{1/3}\text{Nb}_{2/3})\text{O}_3 - 0.1 \text{ PbTiO}_3$.

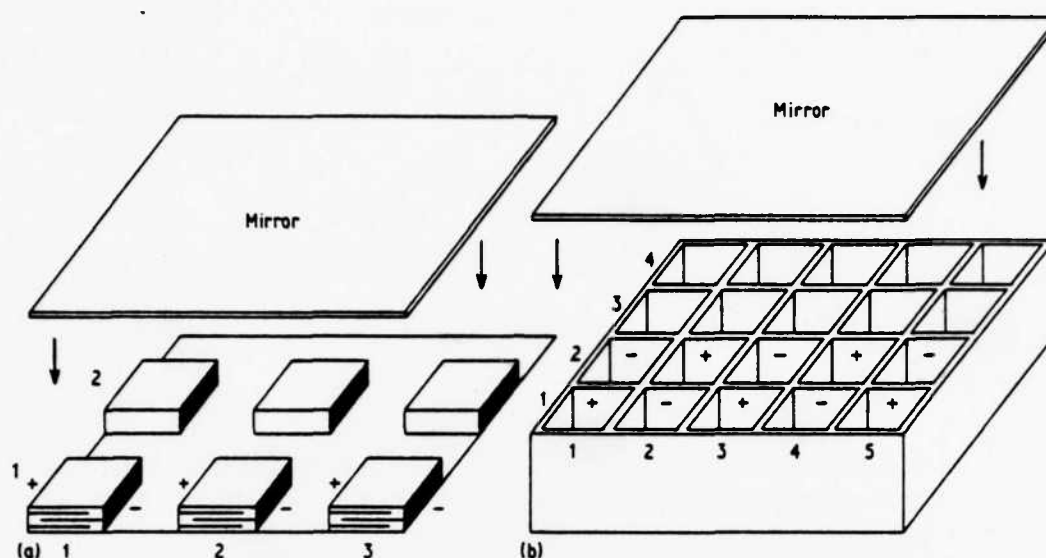


Figure 11 Device arrangements for mirror control application: (a) a multilayer type (longitudinal effect device) and (b) a honeycomb-type (transverse effect device).

7. New mirror-control devices [19]

The multilayer technology used in the capacitor industry is one of the important factors prompting the development of new electrostrictive devices. Fig. 11a shows the basic internal-electrode configuration used in displacement transducers. The electric field across alternate layers is of opposite direction, but the displacive responses are additive. In a piezoelectric device of fixed total thickness, the total displacement for a given voltage is proportional to the number of layers. On the other hand, in an electrostrictive device the total displacement is proportional to the *square* of the number of layers, more effective than in a piezoelectric material.

Internally-electroded multilayer samples were prepared by standard tape-casting techniques using calcined $0.9\text{Pb}(\text{Mg}_{1/3}\text{Nb}_{2/3})\text{O}_3-0.1\text{PbTiO}_3$ powder and a commercial doctor blade media (Cladan Inc., San Diego, CA, type B42). Internal electrodes were applied by screen printing platinum ink (Englehard industries, East Newark, NJ, type E-305-A) onto the dried cast tape. Detailed procedures are described in the paper of Bowen *et al.* [20]. Ten-layer devices with a total thickness of 2.5 mm were prepared by firing on platinum setters in air at 1000°C for 2 h.

Compared with the electrostriction data for simple plate devices in Section 6, the strain of the multilayer devices was smaller than expected, which can be attributed to the effect of the multi-

layer configuration. Two separate electrode systems and the insulated electrode edges reduce the measured displacement [20].

Notwithstanding this clamping effect, a mirror control device has been constructed from *ten* ten-layer ceramics bonded together. With only 200 V applied, the device develops large displacements up to $\Delta L \sim 25\text{ }\mu\text{m}$ ($\Delta L/L \sim 10^{-3}$) with very high reproducibility under cyclic fields. The dimension change associated with a temperature variation of 10 K was less than $0.4\text{ }\mu\text{m}$. With further refinement of the tape casting process, it is probable that the driving voltage can be further reduced to less than 40 V. The total displacement of about $25\text{ }\mu\text{m}$ is an order of magnitude larger than that of the commercial piezoelectric transducers [21] (e.g. PZT-5H, 25 mm plate using d_{31}); and may introduce a new class of micropositioner devices.

Fig. 11a and b show the device arrangements for practical mirror-control applications. Fig. 11a is an example using the multilayer devices (longitudinal effect device) and Fig. 11b is a honeycomb-type displacement device which is manufactured by an extrusion technique, and electroded inside the tubes (transverse effect device). Voltages applied to each address (element) leads to localized mirror control.

8. Summary

From intensive studies on the electrostrictive effects in ferroelectric, antiferroelectric and non-

polar perovskites, several empirical rules have been found:

(a) The magnitude of the electrostrictive coefficient Q is not effected strongly by ferroelectricity, antiferroelectricity or non-polar behaviour, but is very dependent on the degree of order in the cation arrangement. The Q value increases with cation order from disordered, though partially-ordered to simple and then ordered perovskites.

(b) The product of the electrostriction coefficient Q and the Curie-Weiss constant C is nearly constant for all ferroelectric and antiferroelectric perovskites ($Q_b C = 3.1 (\pm 0.4) \times 10^3 \text{ m}^4 \text{ C}^{-2} \text{ K}$).

(c) The value of the electrostriction coefficient Q is approximately proportional to the square of the thermal expansion coefficient α ($\alpha = 4.2 \times 10^{-5} Q_b^{0.5}$).

Relaxor ferroelectrics offer several advantages over normal piezoelectric transducers:

(1) Large electrostrictive strains comparable to the best piezoelectric ceramics.

(2) Excellent positional reproducibility.

(3) No poling is required.

(4) Very low thermal expansion coefficients.

Using the multilayer configuration of existing capacitor technology with the ceramic $0.9 \text{ Pb}(\text{Mg}_{1/3}\text{Nb}_{2/3})\text{O}_3 - 0.1 \text{ PbTiO}_3$, a mirror control device which can develop a large strain with high reproducibility, up to $\Delta L/L \sim 10^{-3}$ when only 200 V is applied has been developed.

In the inverse electrostrictive effect, that is, the pressure dependence of dielectric constant, a sensitive pressure characteristic has also been observed in the same material. Applications of this electrostrictive material for pressure gauges, water-depth meters and heavy-weight detectors are also very promising [22].

References

1. K. UCHINO and L. E. CROSS, *Japan. J. Appl. Lett.* 19 (1980) L171.
2. A. F. DEVONSHIRE, *Phil. Mag. Suppl.* 3 (1954) 85.
3. H. F. KAY, *Rep. Prog. Phys.* 43 (1955) 230.
4. P. W. FORSBERGH, Jr. "Handbuch der Physik", Vol. 17, (Springer-Verlag, Berlin, 1956) p. 264.
5. C. KITTEL, *Phys. Rev.* 82 (1951) 729.
6. K. UCHINO, L. E. CROSS, R. E. NEWNHAM and S. NOMURA, *J. Appl. Phys.* 8 (1980) 4356.
7. L. E. CROSS, *J. Phys. Soc. Japan* 23 (1967) 77.
8. G. A. SAMARA, *Phys. Rev. B1* (1970) 3777.
9. I. N. POLANDOV, *Sov. Phys.-Sol. Stat.* 5 (1963) 838.
10. K. UCHINO, S. NOMURA, L. E. CROSS, S. J. JANG and R. E. NEWNHAM, *J. Appl. Phys.* 51 (1980) 1142.
11. K. UCHINO and L. E. CROSS, *Proceedings 33rd Annual Symposium on Frequency Control*, US Army Electronics Command, Fort Monmouth, NJ (1979) 110.
12. *Idem*, *Ferroelectrics* 27 (1980) 35.
13. S. J. JANG, K. UCHINO, S. NOMURA and L. E. CROSS, *ibid.* 27 (1980) 31.
14. K. UCHINO, L. E. CROSS, R. E. NEWNHAM and S. NOMURA, *J. Phase Transitions* 1 (1980) 333.
15. S. NOMURA, J. KUWATA, K. UCHINO, S. J. JANG, L. E. CROSS and R. E. NEWNHAM, *Phys. Stat. Sol. (a)* 57 (1980) 317.
16. A. AMIN, R. E. NEWNHAM, L. E. CROSS, S. NOMURA and D. E. COX, *J. Sol. State. Chem.* 35 (1980) in press.
17. L. E. CROSS, S. J. JANG, R. E. NEWNHAM, S. NOMURA and K. UCHINO, *Ferroelectrics* 23 (1980) 187.
18. J. FEINLEIB, S. G. LIPSON and P. F. CONE, *Appl. Phys. Lett.* 25 (1974) 311.
19. K. UCHINO, L. E. CROSS and S. NOMURA, *J. Mater. Sci.* 15 (1980) 2643.
20. L. J. BOWEN, T. SHROUT, W. A. SCHULZE and J. V. BIGGERS, *Ferroelectrics* 27 (1980) 59.
21. R. A. LEMONS and L. A. COLDREN, *Rev. Sci. Instrum.* 49 (1978) 1650.
22. K. UCHINO, S. J. JANG, L. E. CROSS and R. E. NEWNHAM, USA Patent disclosure 80-461. Pressure gauge using relaxor ferroelectric.

Received 24 July and accepted 8 October 1980.

APPENDIX 2.7

THE ROLE OF B-SITE CATION DISORDER IN DIFFUSE PHASE
TRANSITION BEHAVIOR OF PEROVSKITE FERROELECTRICS

The role of B-site cation disorder in diffuse phase transition behavior of perovskite ferroelectrics

N. Setter and L. E. Cross

Materials Research Laboratory, The Pennsylvania State University, University Park, Pennsylvania 16802

(Received 24 March 1980; accepted for publication 9 May 1980)

In $\text{Pb}(\text{Sc}_{0.5}\text{Ta}_{0.5})\text{O}_3$, it has been shown that the degree of order in the B-site Sc^{3+} , Ta^{5+} cations can be controlled by suitable thermal annealing. For samples which have been well-ordered by long annealing, dielectric measurements on single crystals show a normal first-order ferroelectric phase change at 13 °C and a maximum low-temperature spontaneous polarization of $23.0 \mu\text{C}/\text{cm}^2$. With increasing disorder, the crystals begin to exhibit the classical diffuse phase transition of a ferroelectric relaxor, with a broad Curie range and strong low-frequency dielectric dispersion in the transition range. X-ray diffraction measurements of the size of the ordered microregions suggest that ordering proceeds by different mechanisms in single-crystal versus ceramic samples, though the resulting effects upon the dielectric behavior are very similar.

PACS numbers: 77.80.-e, 71.55.Jv

I. INTRODUCTION

Structural disorder upon certain crystallographic sites has long been believed to be responsible for the diffuse phase transition (DPT) in a large group of ferroelectric oxides of complex composition with structures in the perovskite and tungsten bronze families. The diffuse phase transition is evidenced in many properties associated with the ferroelectric transition: slow change in dielectric permittivity, and very slow temperature dependence of the spontaneous electric polarization in the relaxation range are examples of the dielectric characteristics.

It is suggested that crystals exhibiting DPT can be viewed as having composition fluctuations on a microscopic scale and so of consisting of microvolumes each with slightly

different Curie temperature for the onset of ferroelectric polarization.¹ The overall properties result from the distribution of the Curie temperatures of these individual microvolumes. Expressions for the dielectric properties have been derived in a statistical treatment by Rolov,² and Clarke and Burfoot³ have expanded the model to include a composition dependent parameter. The model of Rolov predicts successfully the observed dielectric properties of ferroelectric relaxors such as lead magnesium niobate (PMN) and lead zinc niobate (PZN), but no verification appears yet to have been given for the direct role of composition fluctuations.

In solid solutions it has been observed that as the composition becomes close to that favoring a homogeneous distribution, the phase transition sharpens^{4,5} and an increase in structural ordering could explain the observed behavior but has not been verified. A difficulty in the interpretation of all earlier observations has been the changing chemical composition accompanying the changes observed in the solid solutions, which makes unequivocal interpretation impossible.

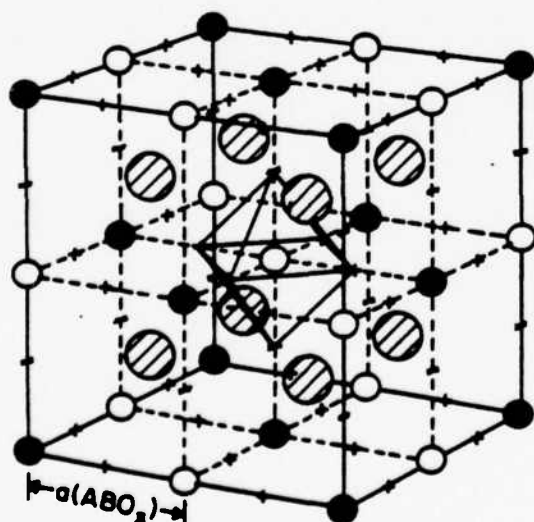


FIG. 1. Structure of ordered perovskite $\text{Pb}(\text{Sc}_{0.5}\text{Ta}_{0.5})\text{O}_3$ [after Galasso (7)].

TABLE I. Degree of ordering and size of ordered domains for PST of various annealing treatments.

Material	Heat treatment	Degree of order (<i>S</i>)	Approximate size of ordered domains
Ceramic PST	No annealing	0.37	100 Å
	15 min at 1000 °C	0.46	200 Å
	40 min at 1000 °C	0.51	300 Å
	65 min at 1000 °C	0.59	750 Å
	2 h at 1000 °C	0.72	900 Å
	4 h at 1000 °C	0.80	> 1000 Å
	6 h at 1000 °C	0.81	> 1000 Å
	9 h at 1000 °C	0.83	> 1000 Å
	24 h at 1000 °C	0.86	> 1000 Å
	103 h at 1000 °C	0.86	> 1000 Å
Single-crystal PST	As grown	0.80	100 Å
	1 h at 1400 °C	0.35	< 100 Å

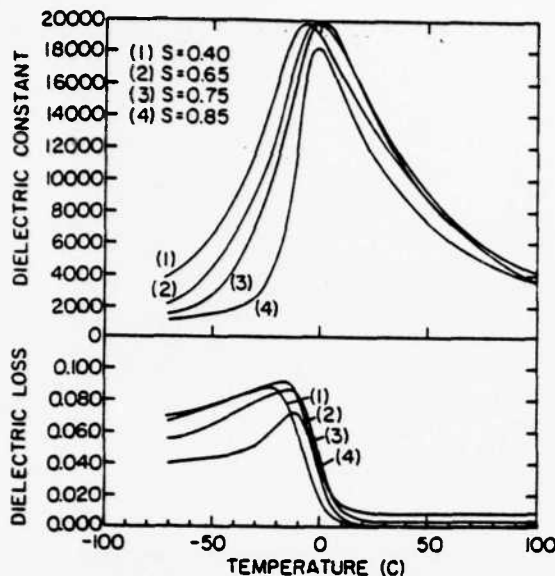


FIG. 2. Temperature dependence of dielectric permittivity and dielectric loss at 1 kHz of PST ceramics with different degree of order.

It has been shown⁶ that $\text{Pb}(\text{Sc}_{0.5}\text{Ta}_{0.5})\text{O}_3$ (PST) is close to the limit of stability between order and disorder for the B-site cations, and that the compound can exist at room temperature with different degrees of order. The influence of changing order upon the ferroelectric phase change can therefore be demonstrated very clearly in PST without any need to change the chemistry. The results of experiments upon both single crystal and ceramic samples with controlled degrees of ordering are presented in this paper.

II. EXPERIMENTS

Samples of the compound PST were prepared by reacting stoichiometric proportions of the mixed PbO , Sc_2O_3 , and

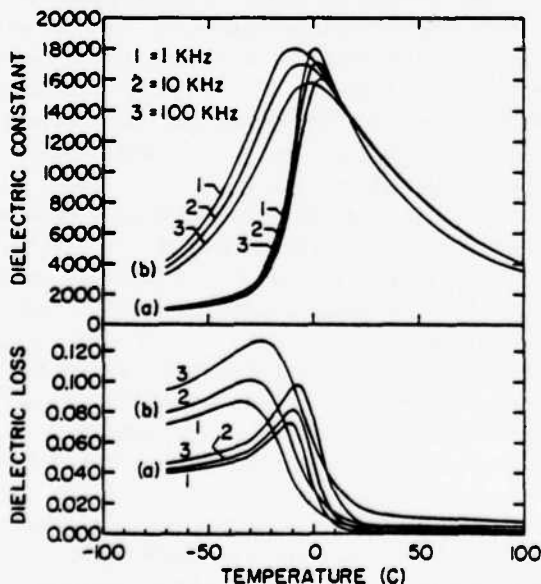


FIG. 3. Frequency dispersion of dielectric permittivity and dielectric loss of (a) mostly ordered ($S = 0.85$) ceramic and (b) disordered ($S = 0.40$) ceramic.

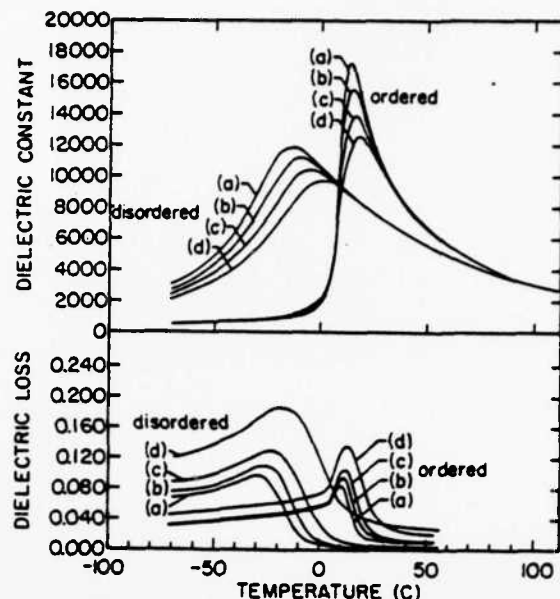


FIG. 4. Temperature dependence of dielectric constant and dielectric loss or ordered ($S = 0.80$) and disordered ($S = 0.35$) single crystals at (a) 1 kHz, (b) 10 kHz, (c) 100 kHz, (d) 1000 kHz.

Nb_2O_5 . The mixture was ball milled under alcohol to achieve intimate mixing, then fired for 2 h at 800 °C. The resulting cake was reground, pressed into pellets, and refired at 1300 °C for 1 h. Powder x-ray diffraction of this reacted powder showed a simple cubic perovskite structure with very small traces of a pyrochlore phase present.

To prepare ceramic disks for dielectric studies, the reacted powder was ground again to pass No. 400 mesh and pressed into 3/8-in.-diam pellets, using a small amount of polyvinyl alcohol as a binder. The pellets were then sintered at 1560 °C in a closed alumina crucible using extra PST pellets with 20 wt. % added PbO to maintain a PbO -rich atmo-

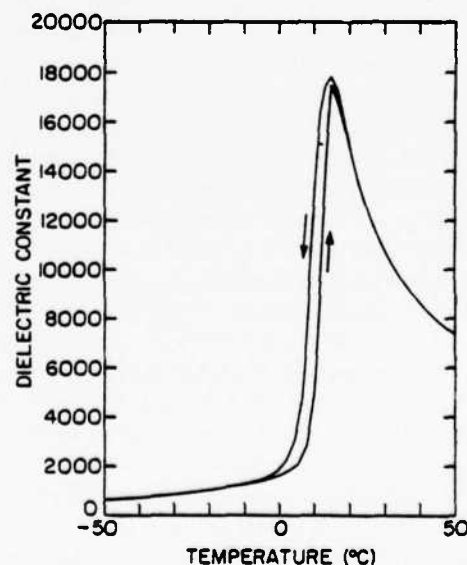


FIG. 5. Thermal hysteresis of an ordered crystal (1 kHz).

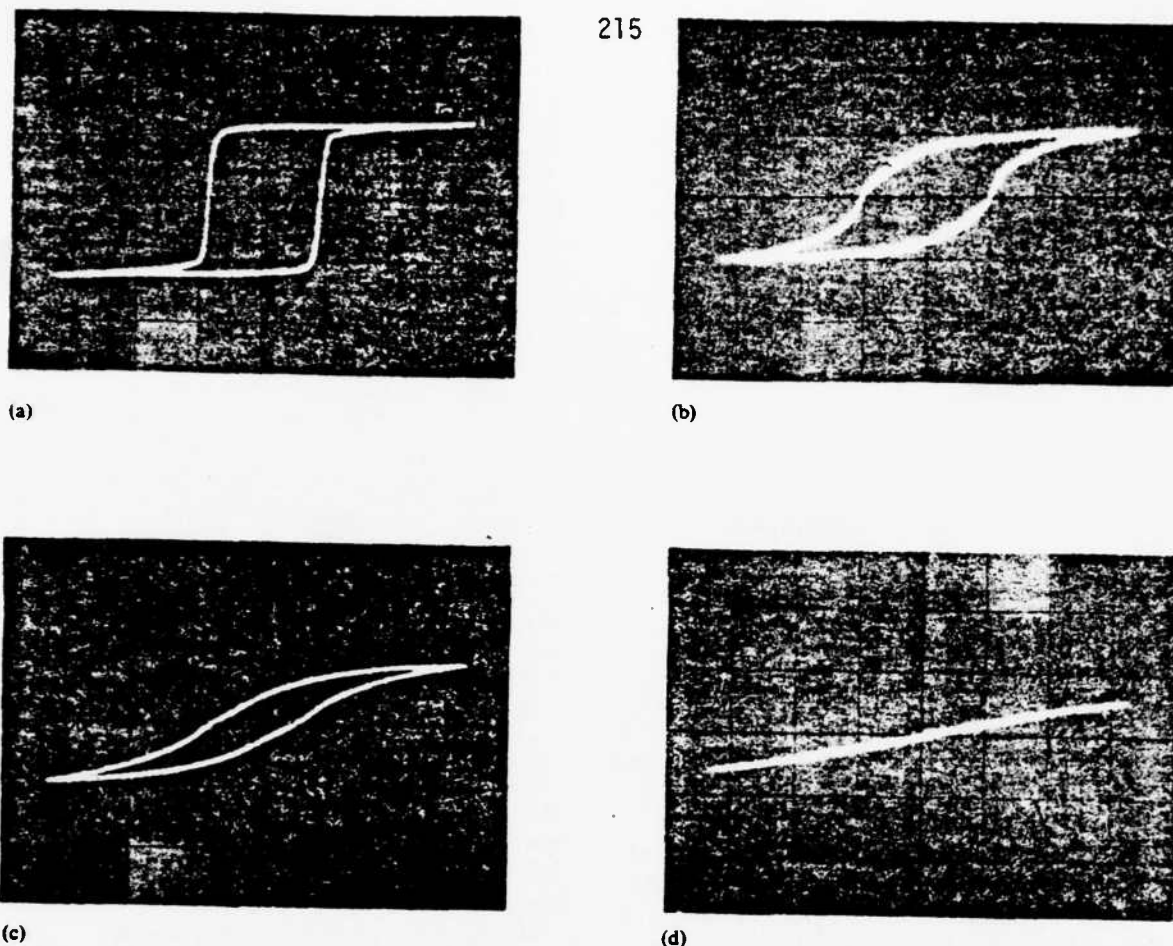


FIG. 6. Dielectric hysteresis of disordered PST single crystal. (a) -58°C , (b) -48°C , (c) -40°C , (d) -20°C .

sphere during firing. By this technique, weight loss during firing was kept to less than 2.5%, and final densities in the range 94–97% theoretical were achieved.

To establish the required degree of ordering, pellets were sliced and annealed at 1000°C for different lengths of time in the range from 10 min to 100 h. The degree of ordering and the size of the ordered domains were established by x-ray diffraction. In PST, ordering places Sc^{3+} and Ta^{5+} ions on adjacent B sites in a three-dimensional array, leads to an effective doubling of the a parameter of the original perovskite cell (Fig. 1), and thus to the appearance of superlattice lines in the x-ray diffractograms. The degree of ordering was determined by calculation from the ratio of the integrated intensities of pairs of base and superlattice reflections, and the ordered domain size determined by the broadening of the superlattice reflections with respect to the base lattice peaks. These data are summarized in Table I. It should be noted that the degree of ordering achieved is not just a function of the annealing time from the initial high-temperature quenched state, but does depend in a complex manner upon the previous thermal history of the individual sample. In these annealing studies no change was detected in the lattice spacing between ordered and disordered states.

Single crystals for dielectric study were grown by a flux technique which has been described elsewhere.⁸ In the as-grown condition, the B-site cations are well ordered. To establish a disordered condition, crystals were heated to 1400°C and air quenched. Stoichiometry of the single crystals was checked both before and after heat treatments using energy dispersive x-ray spectroscopy, and no stoichiometry change was detected.

Dielectric permittivity and loss tangent under weak ac fields were measured at frequencies of 1, 10, 100, and 1,000 kHz using a Hewlett Packard 4270 A automatic capacitance bridge under full program control in a HP9825 bus-controlled system. The sharpening of the permittivity versus temperature curves measured at 1 kHz as a function of increasing order of B-site cations is clearly evident in Fig. 2. The strong control of the degree of ordering upon the dielectric dispersion in the transition region is evident in Fig. 3, which contrasts the behaviors of disordered and highly ordered ceramics. Weak-field permittivity data for single-crystal PST, measured with the E field applied along (001) is shown in Fig. 4. Again the highly dispersive character of the broadened transition in a 35% ordered sample is contrasted with the sharp transition in a crystal with 80% ordering. The

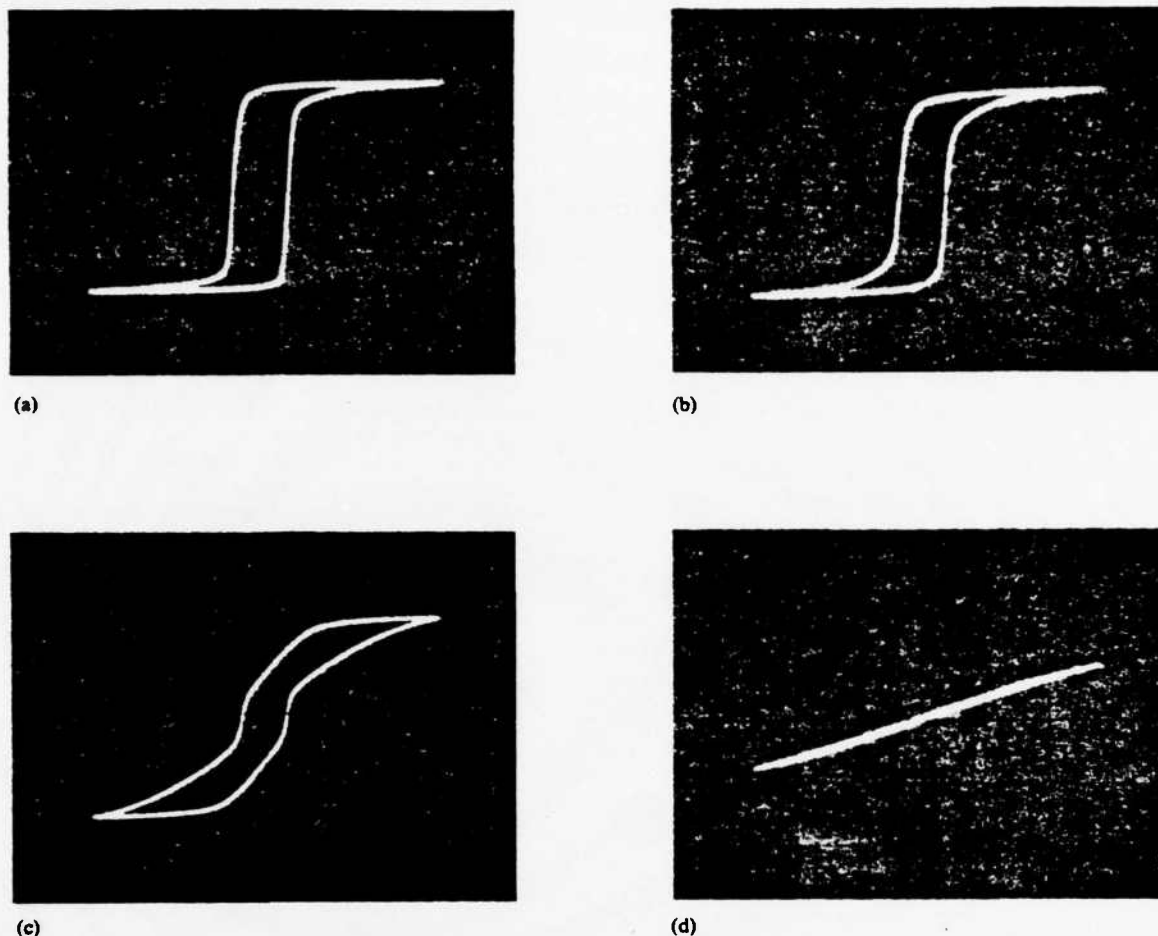


FIG. 7. Dielectric hysteresis of ordered PST single crystal. (a) 0 °C, (b) 7 °C, (c) 8 °C, (d) 14 °C.

first-order nature of the transition in the well-ordered crystal is further suggested by the obvious thermal hysteresis between heating and cooling curves (Fig. 5).

High-field behavior was explored using a balanced Sawyer-Tower Bridge. The dielectric hysteresis in the disordered single crystal shows the characteristic rounded curves and slow saturation for temperatures in the transition range [Figs. 6(a)–6(d)] in contrast to the sharp square lower coercivity behavior of the highly ordered crystals [Figs. 7(a)–7(d)]. The P_r values obtained by extrapolation of the saturation arms of the loops are shown in Fig. 8, where the major shift in Curie temperatures which accompanies ordering in the monocrystal is clearly evident, as is the sharper transition in the ordered sample.

III. DISCUSSION

The dielectric properties of the disordered crystals and ceramics of PST show all the characteristic features of a ferroelectric with DPT: (i) The dielectric peaks are rounded in the ϵ versus T curves; (ii) the temperature of peak permittivity shifts up with increasing frequency; (iii) strong dispersion in the radio frequency range occurs over the transition region; (iv) rounded dielectric hysteresis curves exhibit slow saturation and large effective coercivity.

With enhanced B-site cation ordering, however, crystals of the same composition show classical sharp transition behavior: (1) very sharp dielectric peaks, (2) almost no shift of T_m with frequency, (3) thermal hysteresis, and (4) square loops with low coercivity.

The dielectric behavior is qualitatively similar between ceramic and single crystals, and it is clear that the disorder

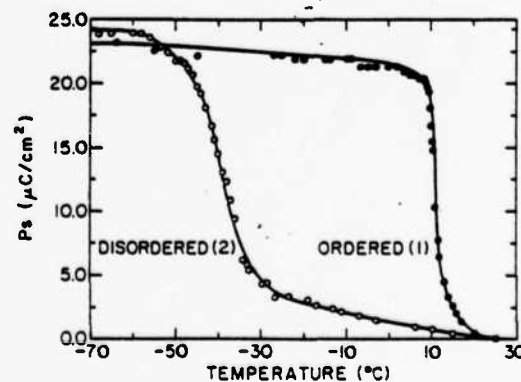


FIG. 8. Spontaneous polarization for ordered (1) and disordered (2) single crystals.

which contributes the local composition fluctuations responsible for the dispersion behavior is on a scale which is much below the ceramic grain size. The maximum P_r value $\sim 20 \mu\text{C}/\text{cm}^2$ is reasonable for a ferroelectric perovskite oxide with $T_c \sim 13^\circ\text{C}$.

A major difference between the ceramic and single-crystal samples appears to exist in the mode by which the Sc:Ta-cation ordering occurs under thermal annealing. In the ceramic it is evident from Table I that the ordered domains expand continuously in size up to macroscopic dimensions with continuous heat treatment. In the single crystal, however, the domain sizes are always small even in the highly ordered crystal.

Altogether, the dependence of DPT on positional disorder has been demonstrated unequivocally for perovskite ferroelectric relaxors, using PST as a suitable example. Indeed, the effect of other parameters such as thermal fluctuations,

defects, and internal stresses cannot be inferred from the above experimental results. However, the results strongly support the model of compositional fluctuation as correctly describing the diffused phase transition in ferroelectric relaxors.

This work was supported by the Office of Naval Research, Contract No. N00014-78-C-0291.

¹G. A. Smolenskii, J. Phys. Soc. Jpn. 28, 26 (1970).

²B. N. Rolov, Fiz. Tverd. Tela. (Leningrad) 6, 2128 (1964) [Sov. Phys. Solid State 6, 1676 (1965)].

³R. Clark and J. C. Burfoot, Ferroelectrics 8, 505 (1974).

⁴A. M. Glass, J. Appl. Phys. 40, 4699 (1969).

⁵L. Benguigi, K. Bethe, J. Appl. Phys. 47, 2787 (1976).

⁶N. Setter, L. E. Cross, J. Mater. Sci. (in press).

⁷F. S. Galasso, *Structure, Properties and Preparation of Perovskite-Type Compounds*, (Pergamon, New York, 1969).

⁸N. Setter, L. E. Cross, J. Cryst. Growth (in press).

APPENDIX 2.8

THE INFLUENCE OF PIEZOELECTRIC GRAIN RESONANCE ON
THE DIELECTRIC SPECTRA OF LiNbO_3 CERAMIC

The Influence of Piezoelectric Grain Resonance on
the Dielectric Spectra of LiNbO_3 Ceramics

Yao Xi, H. McKinstry and L.E. Cross

Materials Research Laboratory
The Pennsylvania State University
University Park, PA 16802

Abstract

It has often been suggested that the higher frequency dispersion ($f \sim 10^7 \sim 10^8$ Hz) evident in the dielectric response of high permittivity ferroelectric ceramics might be associated with piezoelectrically driven resonant mechanical motion of individual grains. The hypothesis certainly appears reasonable, but so far no direct verification appears to have been attempted. Our discovery that the individual crystallite resonances are well preserved in poled LiNbO_3 bicrystals suggested that we explore the dispersion of LiNbO_3 ceramics. In both conventionally sintered and uniaxially hot pressed ceramics, the dielectric dispersion around 10^8 Hz has obvious resonant character. Using a modified ECAP computer program we are able to demonstrate that both the real and imaginary components of the impedance can be quantitatively described using the equivalent circuit models for the coupled individual grain resonances.

I. Introduction

The nature of the high frequency dispersion around 10^7 - 10^{10} Hz in the dielectric response of ferroelectric ceramics has been studied since late 1940 and early 1950s. Powles and Jackson¹ observed a decrease in the real part of the permittivity ϵ' in the region below 10^{10} Hz in BaTiO_3 ceramics. This was later confirmed by Von Hippel² and other authors. Frequency dependence of ϵ' and the dielectric loss tangent were also found in polydomain single crystals of barium titanate^{3,4}. The presence of high frequency dielectric dispersions in solid solutions of $(\text{Ba},\text{Sr})\text{TiO}_3$, $\text{Pb}(\text{Zr},\text{Ti})\text{O}_3$ and other commercial ferroelectric ceramics was also presented⁵.

Several theoretical attempts have been made to explain the high frequency dispersion of ferroelectrics.

Von Hippel expressed the opinion⁶ that the decrease in ϵ' was not given by an internal polarization mechanism. He explained it by a piezoelectric resonance of the crystal grains in the ceramic. Mason and Matthias⁷ related the dielectric dispersion to the relaxation of titanium ions between different potential minima in the cell of the crystal based on their model of potential minima of the Ti ion. Ginzburg⁸ explained the decrease of permittivity by the dispersion of ionic polarization corresponding to the Ba ions. Kittel⁹ believed that the resonance of domain walls led to a decrease in ϵ' of substances. The early efforts in explaining of the high frequency dispersion were summarized by Fousek^{4,10}. His analysis showed that neither the concept of piezoelectric resonance of the crystal grain in a ceramic nor the theory of ionic dispersion led to agreement with experiment.

The discussion of the high frequency dielectric dispersion of ferroelectric ceramics and crystals is extending to recent years. Turik et al. published several papers on this subject^{5,11,12}. They related the dispersion in the 10^8 range for polycrystalline materials to the relaxations of loosely-coupled charges screening the spontaneous polarization⁵. But in recent papers they found that the high frequency dielectric spectra around 10^7 - 10^8 Hz of poly-domain single crystals was dominated by the piezoelectric resonance of individual domains. They believed that in polycrystalline ceramics the piezoelectric domain oscillations also should contribute to the dielectric dispersion in the higher frequency band.

The hypothesis of piezoelectrically driven resonant mechanical motion of individual grains in ferroelectric ceramics suggested by Von Hippel certainly appears reasonable, but so far no direct verification appears to have been attempted.

Lithium niobate ceramics present an unique chance to examine the piezoelectric grain resonance phenomenon. LiNbO_3 can be thermally bonded below its Curie temperature. Only 180° domains exist in LiNbO_3 . There are no 90° domains. Therefore the frequency of domain resonance can be related directly to the grain size. In early studies¹³, we discovered that in LiNbO_3 bicrystals linked-type bicrystal resonate as a whole, while the individual wafers of encountering-type bicrystal resonate separately. This suggests that in LiNbO_3 ceramics grains resonate either separately or cooperatively. The resonant frequency depends on both grain size and grain orientation. It is evident that the grain resonance should influence the dielectric spectra of the LiNbO_3 ceramic sample. We do find a marked dielectric dispersion around 10^8 Hz, which exhibits obvious resonant characters in both conventionally sintered and uniaxially hot pressed ceramics. Using a modified ECAP computer program, we are able to demonstrate that both real and imaginary components of the impedance can be quantitatively described using the equivalent circuit models for the coupled individual piezoelectric grain resonances.

II. Sample Preparation

Lithium niobate ceramics are made from calcined powder and flux grown powder. Calcined LiNbO_3 powder is prepared by ordinary ceramic processes. Li_2CO_3 and Nb_2O_5 in equal mole fraction are mixed for 8 hrs and then calcined at 950°C for 1 hr. Flux-grown LiNbO_3 powder is crystallized from a mixture of salts. LiCl and KCl in equal mole fraction are used as flux. Li_2CO_3 and Nb_2O_5 are mixed in a ball mill with salts for 8 hrs, and then heated at 950°C for 1 hr.

X-ray diffraction patterns of both calcined powder and flux-grown powder are the same as the JCPDF standard pattern for LiNbO_3 . No extra diffraction peaks have been found.

The average size of calcined powder estimated from SEM pictures is around $1 \cdot 10^{-6}$ m with irregular shapes. The average size of flux-grown powder is around

$5 \cdot 10^{-6}$ m with regular crystal shape, as shown in Figure 1.

Both ordinary sintering and uniaxial hot pressing are used to prepare ceramic samples. The sintering temperature is around 1080°C . A uniaxial compressive stress of 10^6 n/m^2 is used for hot pressing. The sintering of LiNbO_3 ceramic is rather difficult. The sintering temperature range is very narrow. Higher temperature causes serious recrystallization to form very large crystal grains. An SEM picture of LiNbO_3 ceramics is shown in Figure 1.

III. Experimental Measurement

The measurements of high frequency dielectric spectra of lithium niobate ceramics were carried out within the frequency range of 1-1000 MHz at room temperature. The HP 4191A RF impedance analyzer was used over this frequency range. In order to get more accurate results, measurements were divided into three bands: 1-10, 10-100, 100-1000 MHz. The impedance analyzer was calibrated in each band by 0Ω , 0 S , and 50Ω standards at 51 frequency calibration points arranged in logarithm steps just before the measurement runs. The measuring points and the calibration points are the same. Reproducibility of measurements is quite good.

Figure 2 is the dielectric spectrum of a LiNbO_3 ceramics from calcined powder produced by conventional sintering. There is a very high dielectric dissipation peak around $3.35 \cdot 10^8 \text{ Hz}$. In the same frequency range the dielectric constant K increases slightly at first and then drops down quickly as the frequency rises. Hot pressing shifts the loss peak to higher frequency and narrows its band width as shown in Figure 3. The dielectric spectrum of LiNbO_3 ceramics prepared by flux-grown powder has similar characteristics. In this case, the loss peak appears around $7 \cdot 10^8 \text{ Hz}$.

IV. Evidence of Grain Resonance

Strong evidence suggests that the huge loss peak around 10^8 Hz range originates from grain resonance in LiNbO_3 ceramics.

The dielectric spectra of LiNbO_3 ceramics as shown in Figure 2 and 3 have the similar characteristics of the piezoelectric resonant spectra of LiNbO_3 single crystal and bicrystal as shown in Figure 4. The spectra of single crystal and bicrystal are mostly governed by piezoelectric resonance of longitudinal thickness mode from d_{33} coupling. The resonant nature is clearly shown. In the resonant frequency band the capacitance increases at first and then drops down to the clamped value, while the dissipation factor passes through its maximum. The dielectric constant of LiNbO_3 ceramics also exhibits a slight increase and then a big drop - down around the loss tangent maximum. Therefore, the spectrum of LiNbO_3 ceramics is closer to a resonant process than to a relaxation process.

The result of piezoelectric effect in LiNbO_3 bicrystal reveals, that in encountering bicrystals, crystal wafers always resonate separately. The bicrystal sample in Figure 4 was made from the same wafers as the single crystal sample. Despite the fact that the bicrystal is twice as thick as the single crystal, they have almost the same fundamental and overtone resonant frequencies. This suggests that the crystal wafers of the bicrystal must vibrate separately. The frequency constant of thickness vibration mode of single crystal and bicrystal of LiNbO_3 is $3.84 \cdot 10^3 \text{ M} \cdot \text{Hz}$. Since the loss tangent maximum of LiNbO_3 ceramics appears at $3 \cdot 10^8$ -- $7 \cdot 10^8$ Hz, the average grain size of LiNbO_3 ceramics calculated from the frequency constant should be around 5.5 -- $12 \cdot 10^{-6} \text{ M}$. This value is consistent with the SEM picture of the LiNbO_3 ceramics.

As mentioned above, the loss peak of hot pressed ceramics shifts to a higher frequency. From the point of view of grain resonance, it can be easily understood. Since the hot pressed ceramics exhibit a smaller grain size and a

narrower size distribution, the shift and the shrinkage of the loss peak is the logical consequence of hot pressing.

V. Equivalent Circuit Model of Grain Resonance

It is possible to estimate the dielectric spectrum of LiNbO_3 ceramics based on the concept of grain resonance. The result is quite close to the experimental data. Figure 5 is the equivalent circuit of a LiNbO_3 grain around its resonant frequency. The series branch L_1, C_1, R_1 represents the mechanical resonance of the grain, where R_1 represents the mechanical damping of vibration. The parallel branch C_0 represents the clamped high frequency capacitance of the grain. The value of these components can be related to grain size, grain orientation and material constants. As a first approximation, assume a cubic grain, then the value of these components are given as below:

$$C = K_0^S d \quad (1)$$

$$C_1 = (K^T - K^S) \epsilon_0 d \quad (2)$$

$$L_1 = \frac{\rho d S^E}{\pi^2 (K^T - K^S) \epsilon_0} \quad (3)$$

$$R_1 = \frac{D \sqrt{\rho S}}{\pi (K^T - K^S) t_0} \quad (4)$$

where d is the grain size, K^T and K^S are dielectric constant under constant stress and constant strain respectively, S^E is the mechanical compliance of LiNbO_3 crystal under constant electric field, ρ is the density, ϵ_0 is the permittivity of free space, D is the damping factor of mechanical resonance. C_0, C_1 and L_1 are all linear functions of grain size d , whereas R_1 is independent of grain size.

The resonant frequency f_r of grain is given as,

$$f_r = \frac{1}{2\sqrt{L_1 C_1}} \quad (5)$$

Figure 6 is the relation between f_r and d (through d_{33} coupling).

The IBM 1620 Electric Circuit Analysis Program (ECAP) is designed to calculate the DC, AC and the transient response of any linear electrical network with up to twenty nodes. Using a modification of ECAP it is possible to calculate both real and imaginary components of the impedance for a number of piezoelectric equivalent circuits connected to represent the coupled resonant behavior of grains of different size and orientation in a ceramic. For a given block of elements with up to twenty nodes, ECAP can be used at a fixed frequency to calculate a single equivalent circuit and by iteration at a sequence of frequencies the different equivalent at each frequency can be found. Repeating this procedure for twenty more blocks, the equivalents may then be folded together using ECAP to define a new fixed frequency equivalent at each frequency for the 20x20 block.

Using the block by block procedure described above, a series of simplified models which break the grain size distribution into a sequence of parallel connected block distributions have been solved, and with increasing detail in the model approach closely to the observed relaxation spectra.

From these model studies, it becomes clear that the dominant features of the effective permittivity and loss are in major part controlled by the majority of grains near the peak of the grain size distribution in this case in the range $4-6 \cdot 10^{-6}$ M size giving the possibility of a much simplified approach.

In the simplified calculation 44.4% of the volume is assumed to contain cubic encountering type (head to head) grains with orientation of polar c axis occurring with equal probability along 1, 2, and 3 direction. To obtain effective mixing grains with different orientation are assumed to be connected in series and in parallel respectively, and then the two blocks connected in parallel. For the remainder, 33.3% of the volume is assumed to be in larger or link type grains where resonant frequency is below and outside the band of interest and

22.3% are assumed to be small or encountering types with resonances above the band of interest.

In each case these blocks can be represented by single capacitors whose permittivities are controlled by ϵ^S and ϵ^T respectively. For the 5 μ meter grains only longitudinal vibrations along 2 and 3 directions and shear vibrations about the 2 axis are taken into account. The mechanical damping factor D in Equation 4 is taken to be larger than in the single crystal to take account of the mutual intercoupling. Apart from this adjustment, unperturbed single crystal parameters are used for all calculations.

The model structure and its equivalent circuit are given in Figure 7, and the calculated response for the model compared to experiment in Figure 8.

VI. Discussion

From the block calculations, by using the folding method in the ECAP computer program it is possible to calculate the impedance of very complex series and parallel interconnection of equivalent resonator circuits. The results of such detailed simulation show that the mixing of series and parallel connections smooths out the very sharp single grain resonance so that the overall response becomes dominated by grains of the mean grain size, padded by the off resonant response of the smaller and larger fractions. Anisotropy of the individual grain response in itself contributes a spreading of the elementary resonances and permits a much simplified model to describe the impedance with fair quantitative accuracy.

Relative independence of the result upon the fine detail of the model structure gives confidence that piezoelectric resonance is the major contributor to the high frequency dielectric dispersion in LiNbO_3 .

The attempt to apply similar models to the perovskite dielectrics based on BaTiO_3 must be tempered by the much more complicated domain structure in

such unpoled ceramics. Clearly, one 90° twin wall across the body diagonal of a cubic grain will make a continuous change in length of the effective resonant element from the grain size down to zero, with a corresponding spreading of the dispersive region. Based, however, on the clear evidence of the major piezoelectric contribution to dispersion in the LiNbO_3 ceramic, it is probable that the higher piezoelectric coupling in the titanate will also contribute strongly to high frequency dispersion. For the perovskite families an interesting experiment would be to compare dispersion in ferroelectric and antiferroelectric species of similar permittivity level since in the latter type no piezoelectric effect can occur.

VII. Summary

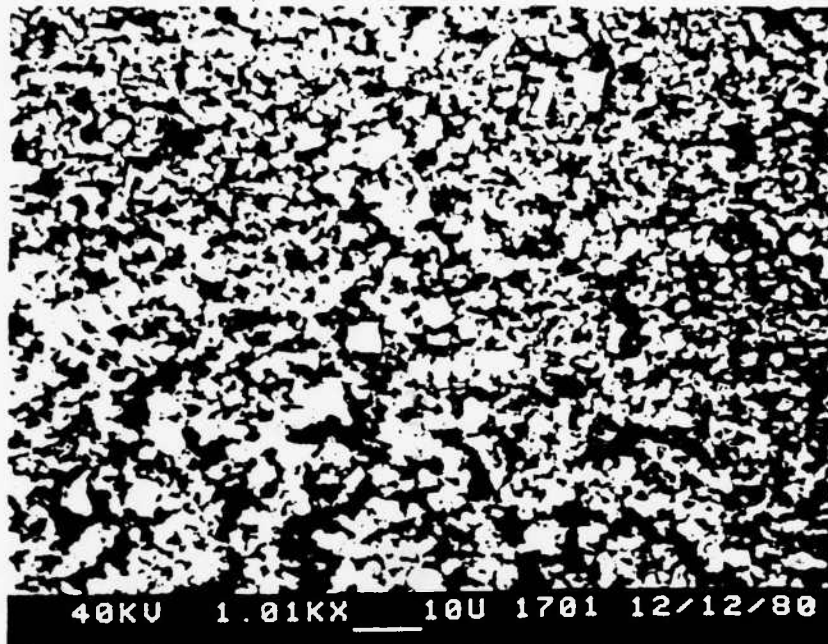
1. The dispersion of dielectric constant and the huge peak of loss tangent of LiNbO_3 around 10^8 Hz originate from the coupled individual grain resonance.
2. For coupled individual grain resonances, the frequency dependence of both real and imaginary components can be quantitatively simulated by using a modified ECAP program and the piezoelectric equivalent circuit model.

REFERENCES

1. J.G. Powles and W. Jackson, Dielectric Properties and Applications of Barium Titanate Ceramics, Proc. IEEE, 96:383-391 (1949).
2. A. Von Hippel, Ferroelectricity, Domain Structure, and Phase Transitions of Barium Titanate, Rev. Mod. Phys., 22:221-228 (1950).
3. M.E. Drougard and D.R. Young, Domain Clamping Effect in Barium Titanate Single Crystals, Phys. Rev., 94:1561-1564 (1954).
4. J. Fousek, On the Problems of the Permittivity Dispersion of Barium Titanate, Czech. J. Phys., 9:172-185 (1959).
5. A.V. Turik, K.R. Chernyshov, D.V. Komarov, Dielectric Dispersion in Ferroelectrics with Perovskite Structure Over the Meter-Wave Range, Ferroelectrics, 6:45-47 (1973).
6. A. Von Hippel, Piezoelectricity, Ferroelectricity and Crystal Structure, Zs. Phys., 133:158-173 (1952).
7. W.P. Mason and B.T. Matthias, Theoretical Model for Explaining the Ferroelectric Effect in Barium Titanate, Phys. Rev., 74:1622-1636 (1948).
8. V.A. Ginzburg, Non-linear Barium Titanate Crystal, UFN, 38:490-501 (1949).
9. C. Kittel, Domain Boundary Motion in Ferroelectric Crystals and the Dielectric Constant at High Frequency, Phys. Rev., 83:458 (1951).
10. J. Fousek, The Dielectric Properties of Single Crystals of BaTiO_3 at a Frequency of 1000 MC/S, Czech. J. Phys., 8:254-263 (1958).
11. A.V. Turik and E.I. Bondarenko, Effect of Domain Structure on Physical Properties of Ferroelectrics, Ferroelectrics, 7:303-305 (1974).
12. A.V. Turik and G.I. Khasabova, Dielectric Properties of BaTiO_3 Polydomain Crystals, Ferroelectrics, 18:91-93 (1978).
13. Yao Xi and L.E. Cross, Lithium Niobate Bicrystal, Ferroelectrics, 38:829-832 (1981).

List of Figures

- Figure 1. SEM picture of LiNbO_3 powder and ceramic (a) calcined powder, (b) flux-grown powder, (c) ceramic from calcined powder (d) ceramic from flux-grown powder.
- Figure 2. Dielectric spectra of LiNbO_3 ceramic from calcined powder and conventional sintering.
- Figure 3. Dielectric spectra of LiNbO_3 ceramic from calcined powder and hot-press sintering.
- Figure 4. Piezoelectric resonant spectra of LiNbO_3 single crystal (a), and bicrystal.
- Figure 5. Electrical equivalent circuit of a piezoelectric resonator around resonant frequency.
- Figure 6. Resonant frequency of LiNbO_3 single cube-shaped grain.
- Figure 7. Connection pattern (a) and equivalent circuit (b) for simulating grain resonant spectra of LiNbO_3 ceramic.
- Figure 8. Calculated spectra of dielectric constant K and dissipation factor D of LiNbO_3 ceramic.



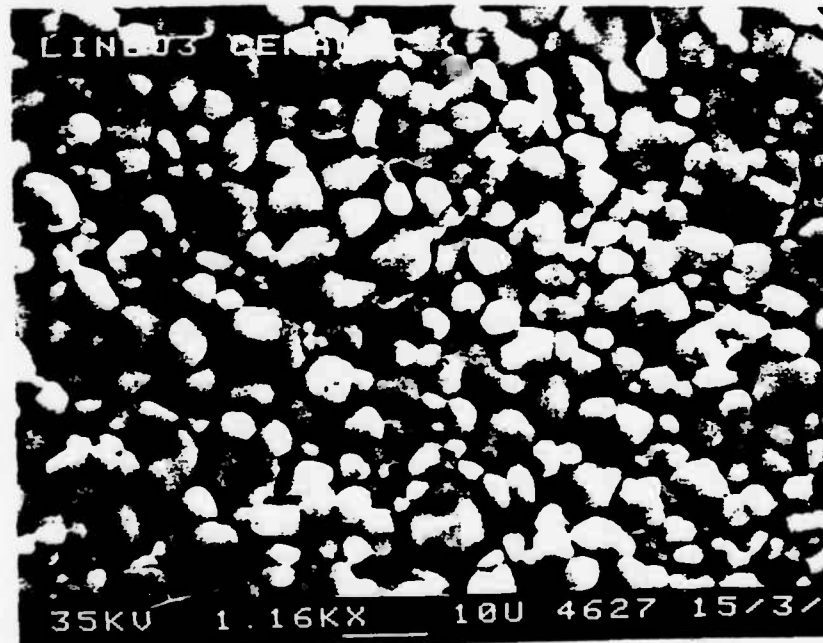
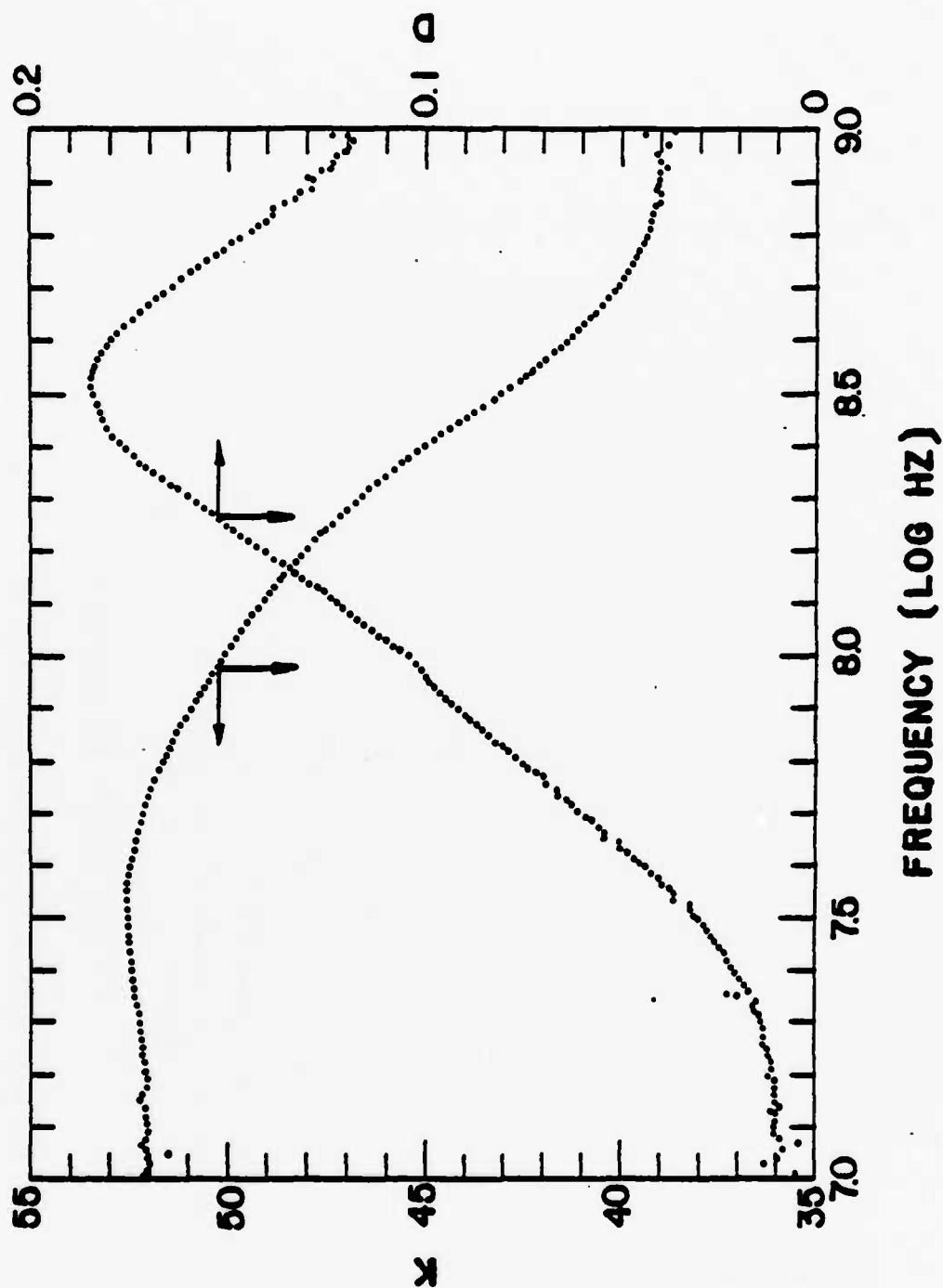
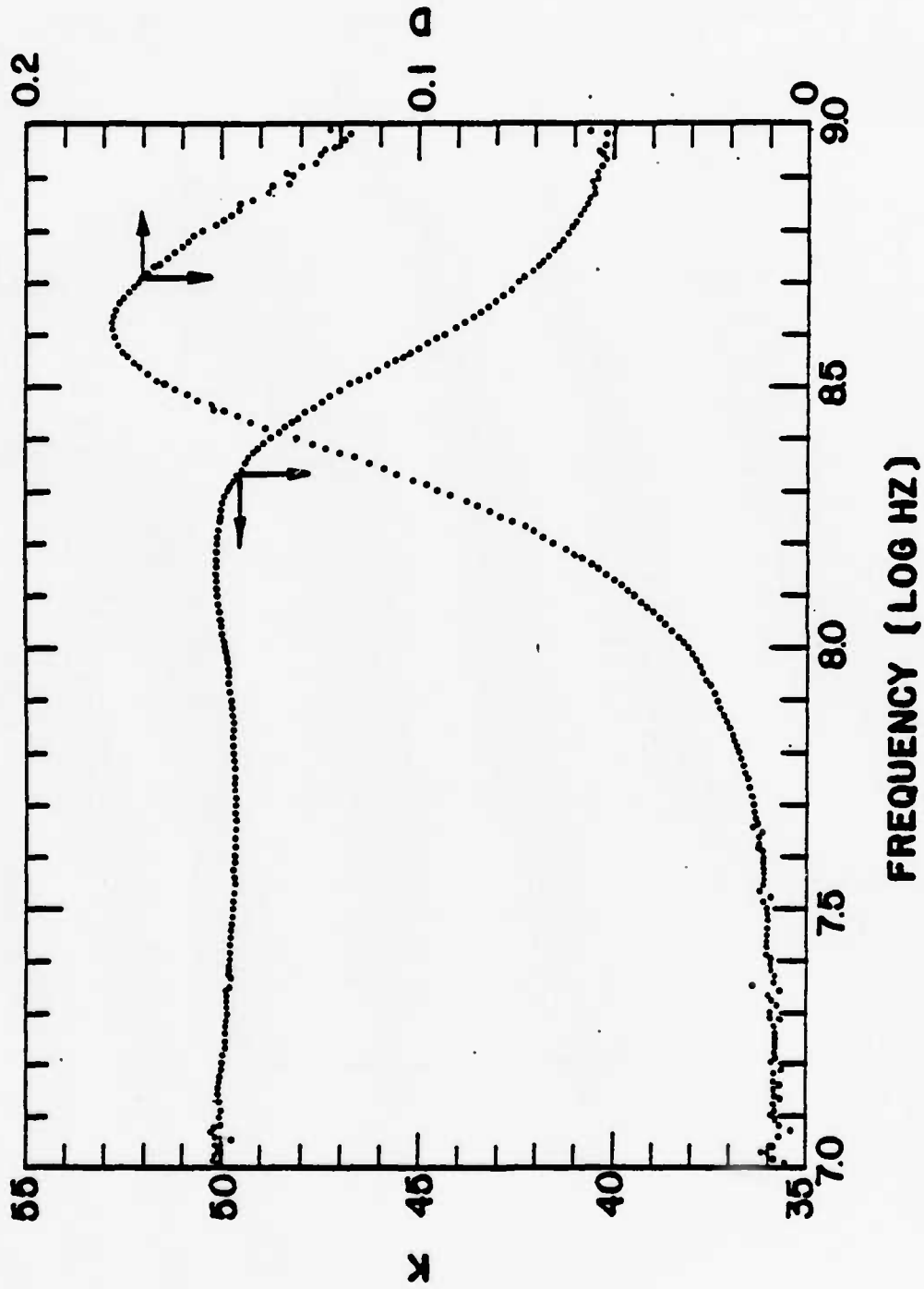


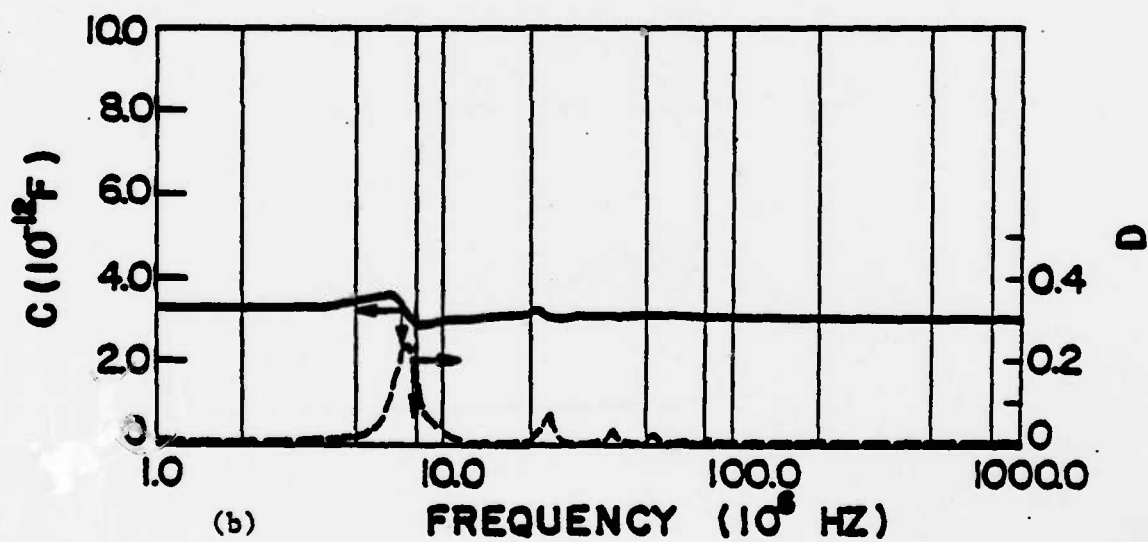
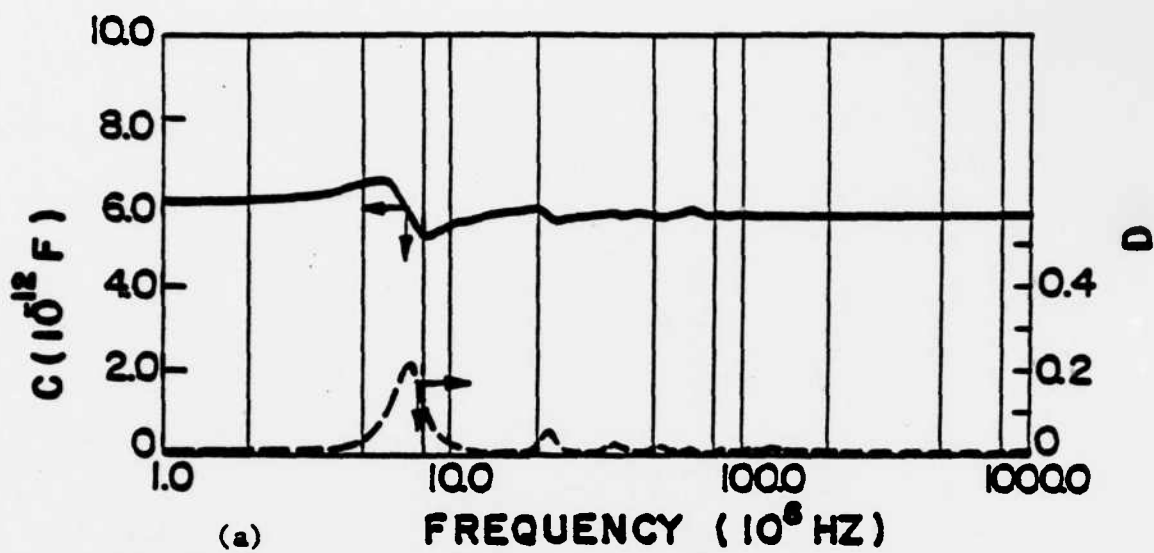
fig 10.1

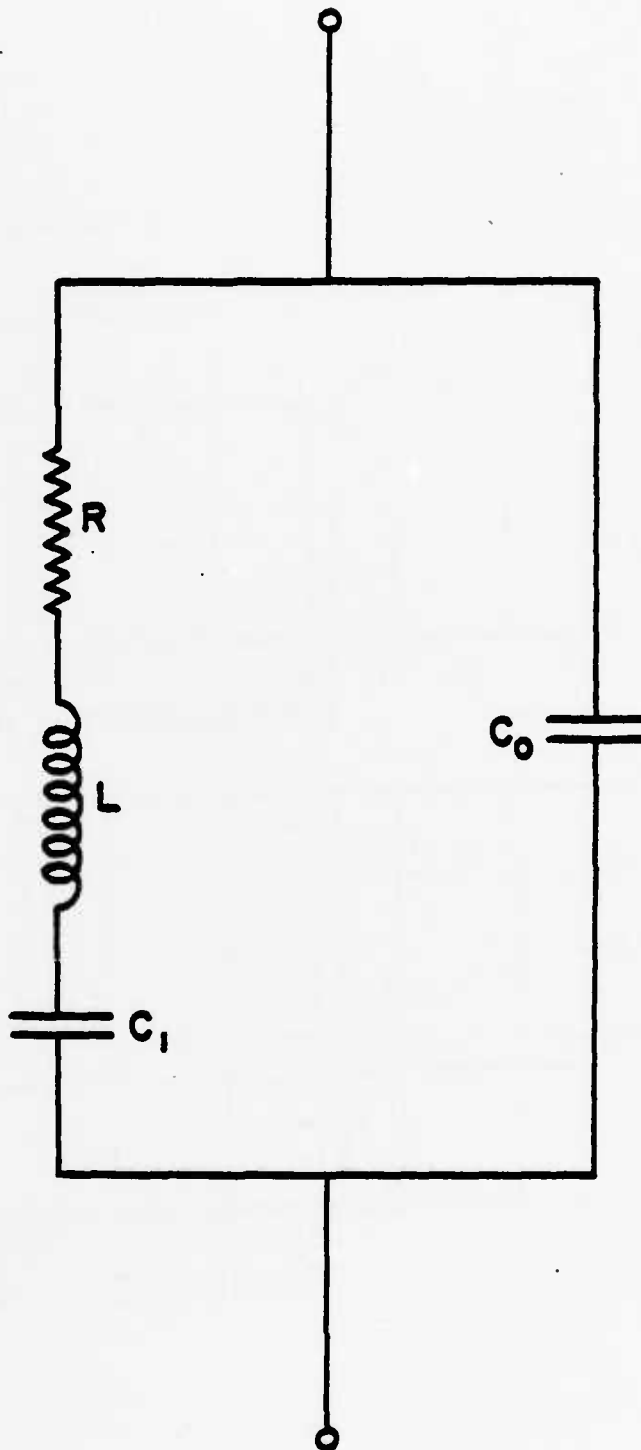


Dielectric spectra of LiNbO₃ ceramic from calcined powder and conventional sintering.

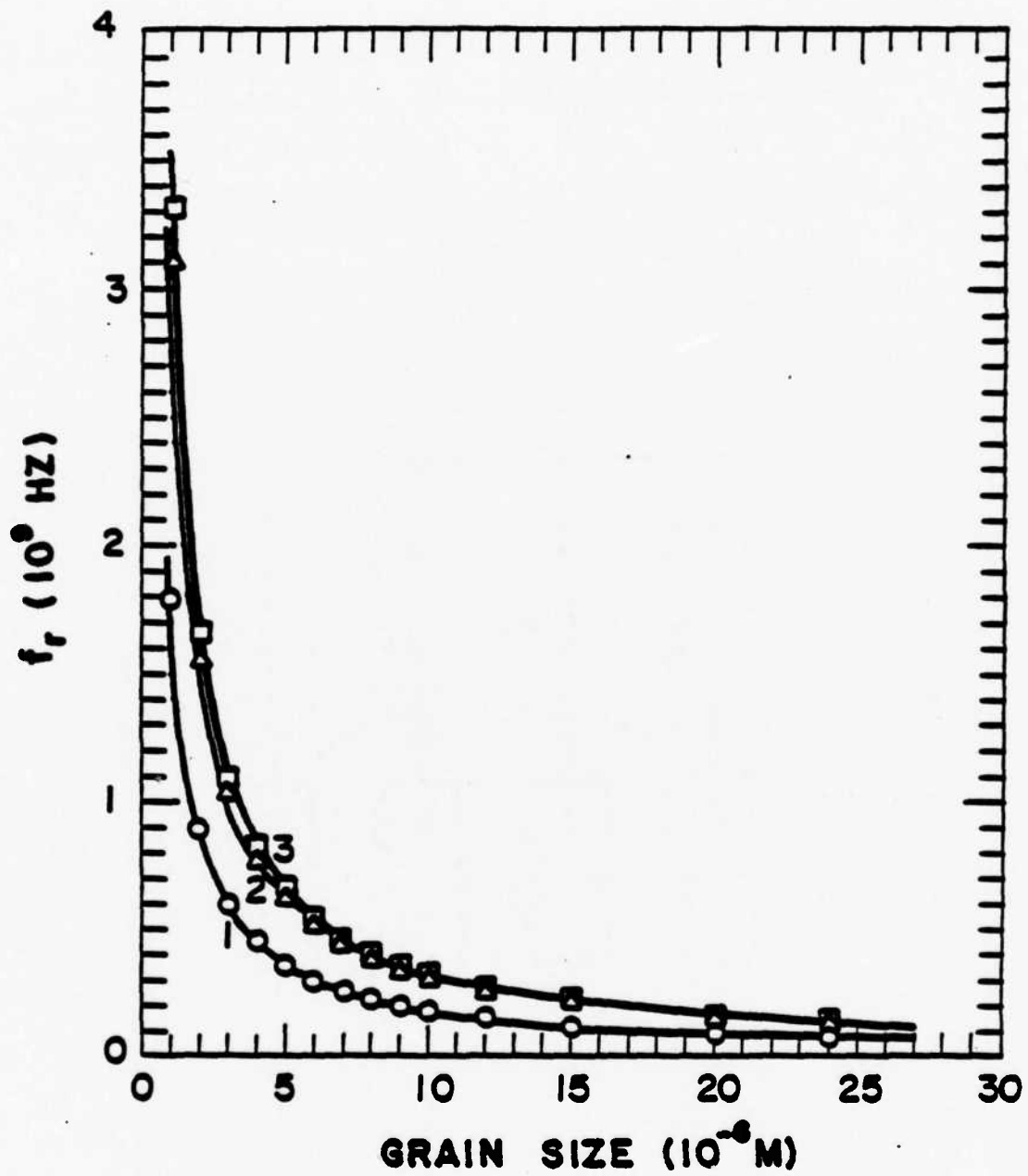


Dielectric spectra of LiNbO₃ ceramic from calcined powder and hot-press sintering.

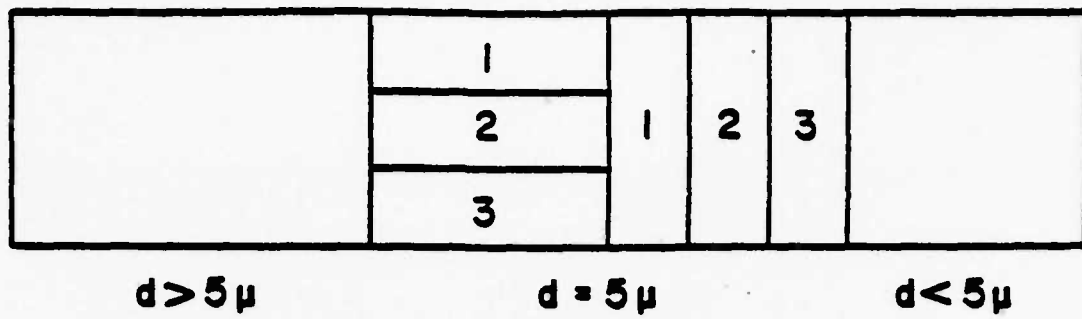




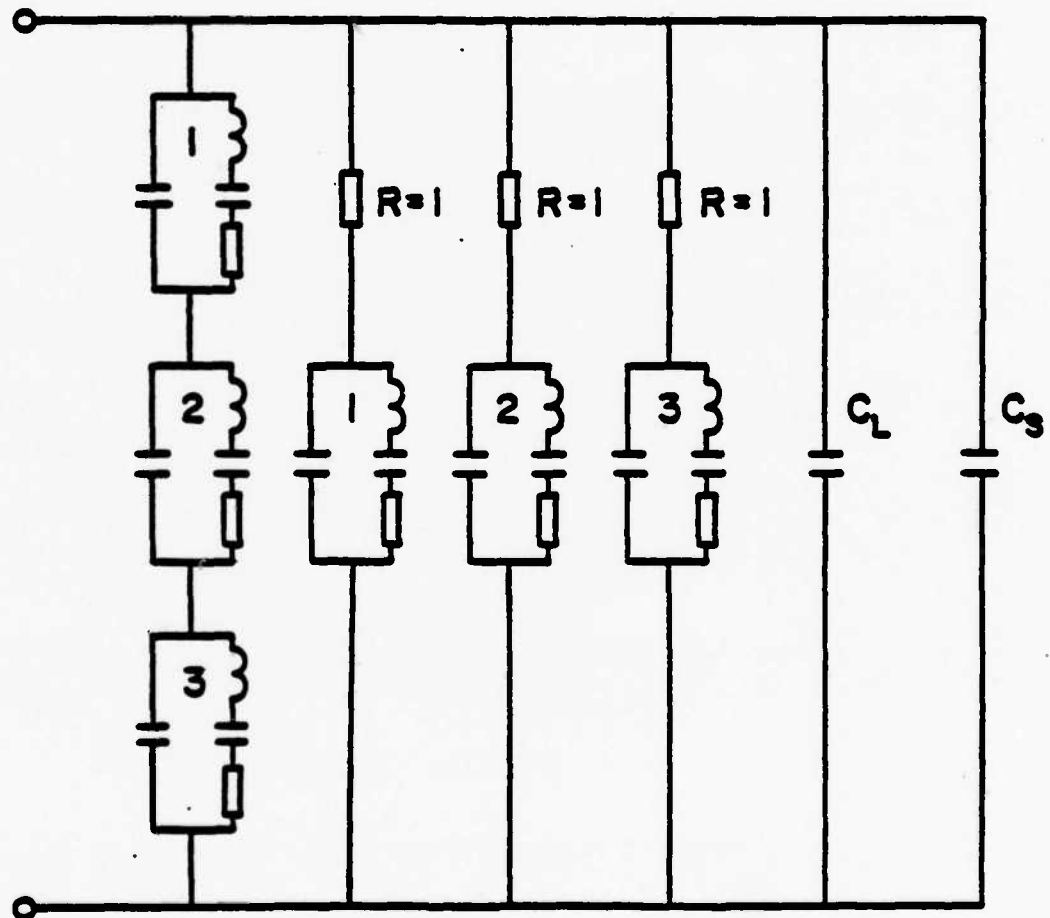
Electrical equivalent circuit of a piezo-
electric resonator around resonant
frequency.



Resonant frequency of LiNbO_3 single cube-shaped grain.

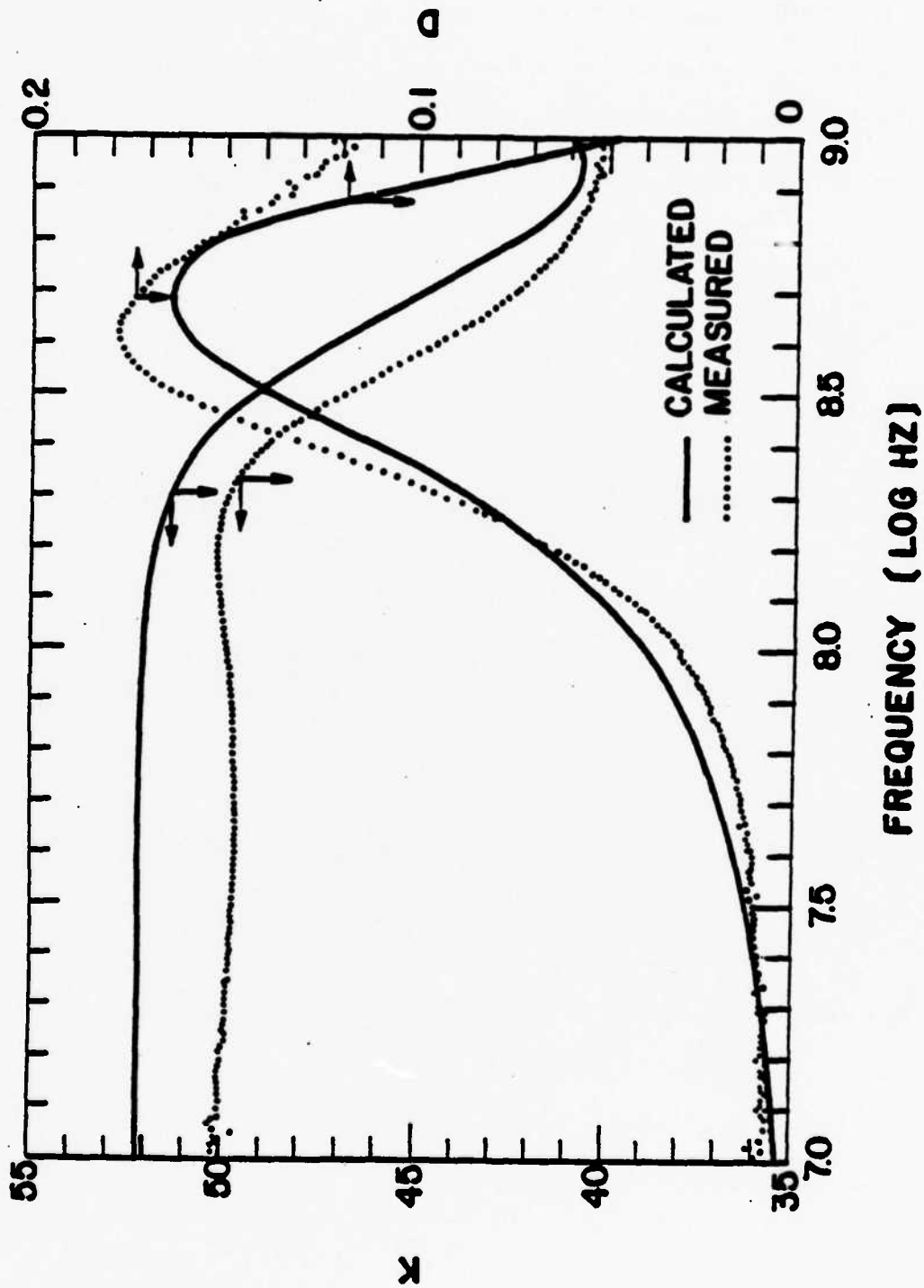


(a)



(b)

Connection pattern (a) and equivalent circuit (b) for simulating grain resonant spectra of LiNbO_3 ceramic.



Calculated spectra of dielectric constant K and dissipation factor D of 1.1NbO_3 ceramic.

APPENDIX 2.9

SHAPE-MEMORY EFFECT IN PLZT FERROELECTRIC CERAMICS

Shape-Memory Effect in PLZT Ferroelectric Ceramics

T. KIMURA, R. E. NEWNHAM and L. E. CROSS

*Materials Research Laboratory, The Pennsylvania State University,
University Park, Pennsylvania 16802, U.S.A.*

(Received April 30, 1981)

The shape-memory effect in PLZT (Lead Lanthanum Zirconate Titanate) ceramics with composition $x/65/35$ ($4.0 \leq x \leq 8.0$) has been investigated using bending experiments and temperature cycling. Relationships between load and the degree of bending, together with their temperature dependence, have been determined, and characteristic temperatures associated with the onset and disappearance of the pseudo-plastic shape change are compared with the observed dielectric anomalies. Effects of mechanical stress and electric field on the shape-memory temperatures and the magnitude of strain have also been investigated. It is concluded that domain alignment and the temperature-dependence of spontaneous strain are important factors governing the shape-memory effect in ferroelectrics. Preferred-orientation effects have been confirmed by X-ray diffraction analysis.

1 INTRODUCTION

The recovery of a plastically deformed material to its original shape by heating is called the shape-memory effect. This effect has been extensively studied in metallic alloys and is generally associated with martensitic phase transformations (Warlimont, 1976; Delaey, Krishnan, Tas, and Warlimont, 1974). Phase transformations in ferroelectric materials are not martensitic, but Schmidt and Boczek (1978) observed apparently similar effects in PLZT ceramics. Details of the phenomena occurring in PLZT are not clear.

Applications for PLZT ceramics include a number of different optical devices (Haertling and Land, 1971; Maldonado and Meitzler, 1970, 1971; Maldonado and Anderson, 1971). The materials of interest are conventionally referred to in the $x/y/z$ notation, where x gives the atomic percentage of La and y/z is the Zr to Ti ratio. Attention has generally been concentrated

T. KIMURA; R. E. NEWNHAM AND L. E. CROSS

on materials of composition $x/65/35$. Those with $x > 4.5$ exhibit an interesting phenomenon called *piezoelectricity* (Mcitzler and O'Bryan, 1973), *quasi-ferroelectricity* (Carl and Geisen, 1973) or $\beta \rightarrow \alpha$ phase transformation (Keve and Annis, 1973). PLZT specimens with $x = 8.0$ show relaxor behavior with a diffuse phase transition.

This paper describes the shape-memory effect in PLZT ceramics with La concentrations between 4.0 and 8.0 at. %. Because of their simplicity, bending experiments were used to investigate the shape change. The effects of stress and La content on the magnitude of bending strain, and on the memory effect were determined. The characteristic temperatures associated with the shape-memory effect were compared with the dielectric anomalies, and it was concluded that ferroelectric domains are the main cause of the shape-memory effect in ferroelectric ceramics.

2 EXPERIMENTAL

Five hot-pressed PLZT ceramic wafers with compositions $x/65/35$ ($x = 4.0, 6.5, 7.0, 7.5$ and 8.0) were obtained from Dr. William Harrison at Honeywell Inc. The wafers were cut and polished into rectangular bars of width 2 mm, thickness 0.35 mm and length 15 mm, and then annealed at 600°C for 15 h.

Bending experiments were used to measure the shape change. The specimen was positioned on two knife-edge supports separated by 12 mm, and surrounded by a small brass box. A heater placed under the box could raise the temperature up to 270°C , as measured by a thermocouple positioned near the sample. One end of a glass rod was placed at the center of the sample and the other end attached to a dilatometer probe. Movement of the probe was measured with a differential transformer. To apply load to the sample, lead weights were placed on a shelf attached to the glass rod.

The sample was heated to a selected temperature above the Curie temperature, and the load was then applied. The sample was then cooled to room temperature under constant load. At room temperature the load was removed (except for the 8.6 g weight of the measurement probe) and the sample was then reheated. During the reheating cycle, the glass rod and dilatometer probe maintained contact with the sample to measure the amount of bending.

Stress and strain were calculated assuming a circular arc. Since both stress and strain are functions of position throughout the cross-section of the bar, the calculated values are for the maximum stress and strain present on the outside surface of the bar.

Dielectric properties were measured at frequencies of 1, 10, 100 and 1000 kHz. The major face of the bar was electroded by Au-evaporation and poled with a DC field of 15 kV/cm at room temperature. Dielectric constant and

SHAPE-MEMORY EFFECT IN PLZT

loss factor were measured by a capacitance bridge at a constant heating rate of $2^\circ/\text{mm}$.

The samples with $x = 4.0$ and 7.0% La (width 2 mm, thickness 1 mm and length 12 mm) were squeezed at 400 kg/cm^2 (equivalent to the bending load of 86 g) at 310°C and 800°C , respectively, and cooled to room temperature. Sample faces, perpendicular and parallel to the stress direction, were examined by X-ray diffraction using Ni-filtered $\text{CuK}\alpha$ radiation and compared with a diffraction pattern recorded before squeezing.

3 STRESS-STRAIN-TEMPERATURE RELATIONSHIPS

Figure 1 shows the typical behavior of the bending strain with temperature under several different loads. Application of a load at high temperature bent the sample bar elastically, and the bending returned to zero upon removal of the load. The magnitude of elastic bending agreed with the value calculated using the reported values of s_{11} (Schmidt and Boczek, 1978; O'Bryan, 1973). On cooling under load, the magnitude of bending did

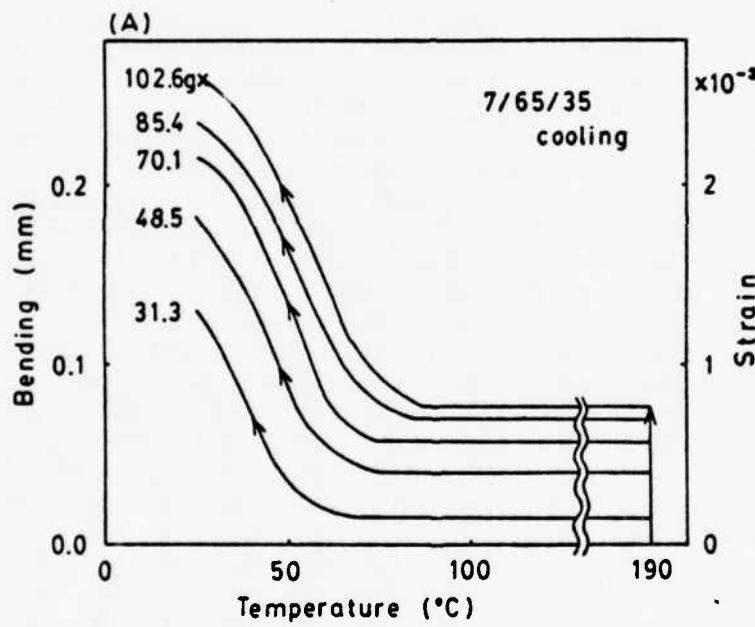


FIGURE 1(A) Bending behavior of a 7.0/65/3.5 ceramic as a function of temperature during cooling under several fixed loads. A load of 102.6 g caused fracture of the sample during cooling as indicated by X.

T. KIMURA, R. E. NEWNHAM AND L. E. CROSS

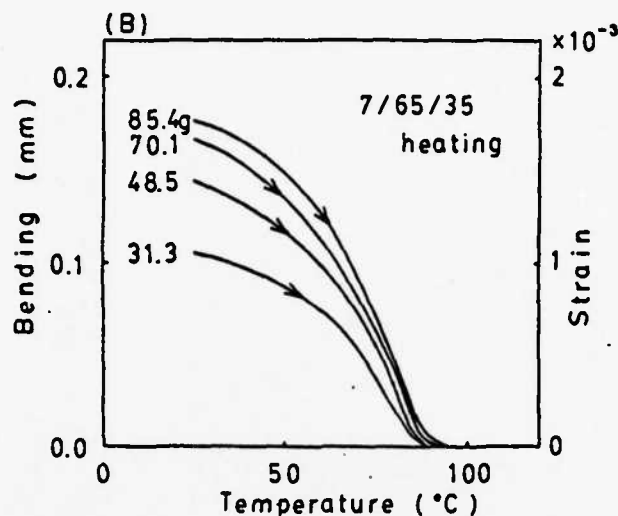


FIGURE 1(B) Bending behavior of a 70/65/35 ceramic during heating without load. The weights used to produce deformation during the preceding cooling cycle are given beside each curve.

not change appreciably down to a certain temperature T_s , at which bending began to increase rapidly, and continued increasing to room temperature. When the weight was removed at room temperature, there was a slight reduction in the amount of bending. The reduction in bending agreed with the value calculated from the s_{11} coefficient, indicating that this part of the strain was elastic. Reloading without load decreased the plastic portion of bending until it became zero at temperature T_f . The original shape was completely recovered by heating.

The elastic part of the bending increased linearly with the increase in load, but the plastic contribution tended to saturate. The amount of load also affected the characteristic temperature T_s . The initial deformation temperature T_s shifted to higher values under larger loads, but the shape-recovery temperature T_f did not depend noticeably on the size of load applied during cooling. Further increase in the load caused fracture of the sample during cooling, as indicated in Figure 1(A).

4 EFFECT OF La CONTENT ON THE STRAIN-TEMPERATURE RELATION

Figure 2 shows the effect of La content on the strain-temperature relation under various loads. Data showing maximum bending for each composition were selected; further increases in load caused fracture of the samples.

SHAPE-MEMORY EFFECT IN PLZT

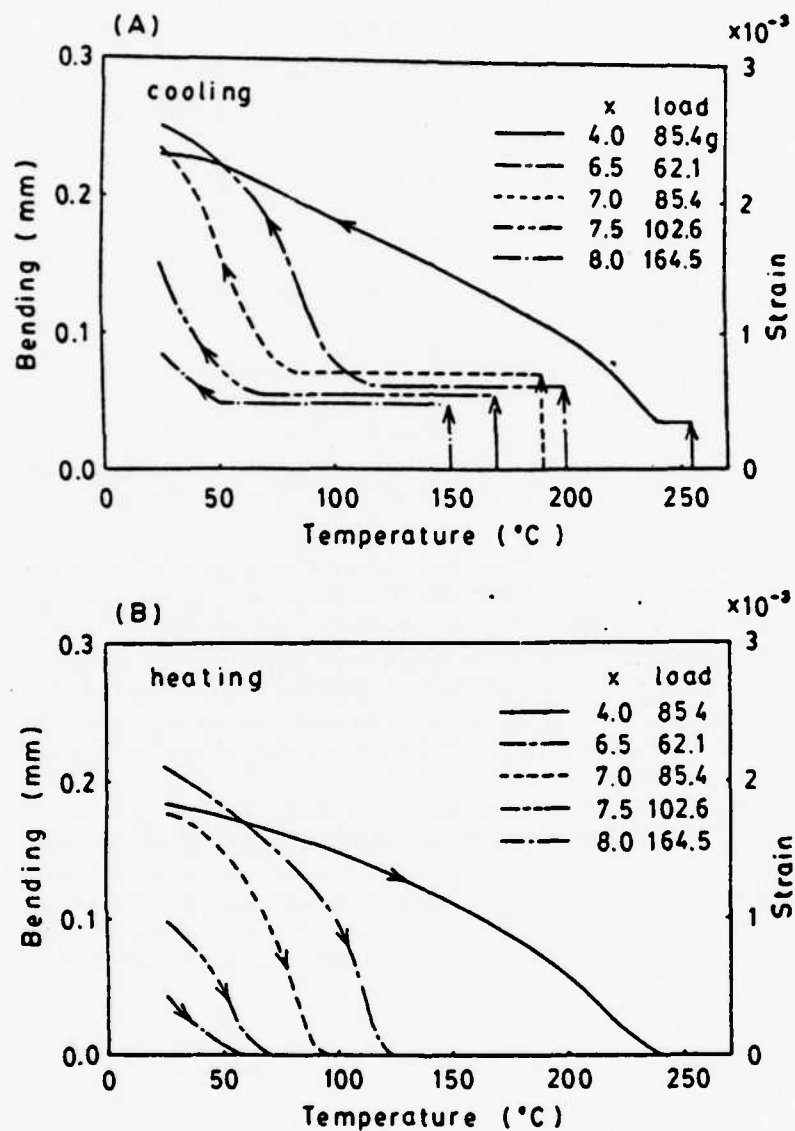


FIGURE 2 Effects of La content on the temperature-dependence of bending during (A) cooling under constant load and (B) heating without load.

T. KIMURA, R. E. NEWNHAM AND L. E. CROSS

Figure 3 shows the relations between temperatures T_s and T_f and the amount of load, as well as the load which caused fracture.

As judged from the amount of bending and dependence of T_s on load, the shape-memory behavior of the sample with $x = 4.0$ was different from that in the composition range $6.5 \leq x \leq 8.0$. For samples with $6.5 \leq x \leq 8.0$, those of higher La content showed less bending at room temperature as well as lower deformation temperatures T_s and restoration temperatures T_f . Larger loads were required to produce an equivalent bending in samples with high La content. The deformation temperature T_s was significantly lower than T_f . Furthermore, T_s increased appreciably with increasing load but T_f did not depend strongly on load. For the sample with $x = 4.0$, the characteristic temperatures T_s and T_f were the highest within the composition range examined, but the magnitude of bending at room temperature was about the same as the other samples. Furthermore, T_s and T_f were equal for the 4% sample and did not depend on the load applied.

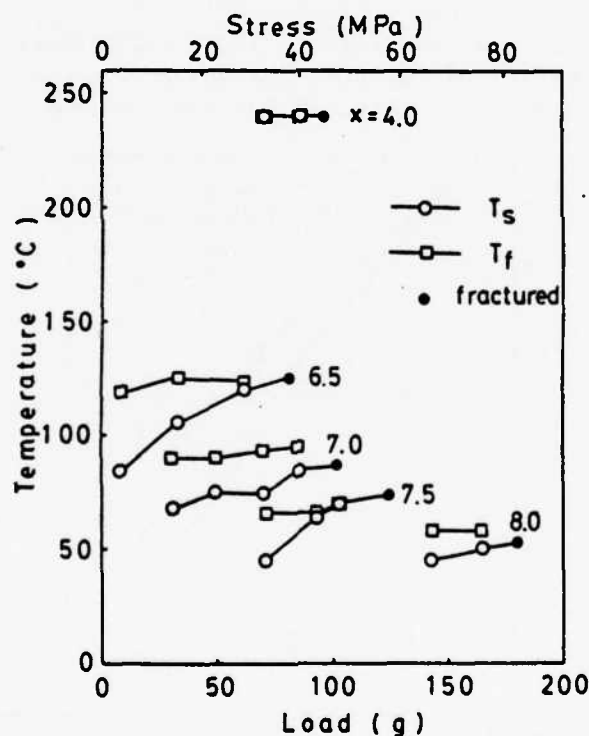


FIGURE 3 Relationships between characteristic temperatures T_s and T_f and the amount of load.

SHAPE-MEMORY EFFECT IN PLZT

Another difference in the $x = 4.0$ sample was the behavior of bending during temperature-cycling under no load. After the samples were cooled under constant load, they were reheated to a certain temperature below T_f and then recooled without load. The bending increased as the temperature was lowered. For the $x = 4.0$ sample, the relation between bending and temperature was the same as that observed originally when cooled under stress, when the sample was reheated up to 10°C below T_f . Reheating above T_f and cooling without load caused no bending. In samples with $6.5 \leq x \leq 8.0$, the amount of bending observed during recooling was smaller than that of the initial cooling under load, and room-temperature bending was dependent on the temperature at which recooling was begun. For example in the case of the $x = 7.0$ sample deformed at 85.4°C ($T_f = 96^\circ\text{C}$), recooling from 56°C reduced the room-temperature bending to 70% of the original value, and from 74°C the amount was 400%.

5 RELATION BETWEEN DIELECTRIC AND MECHANICAL PROPERTIES

The dielectric constant of poled samples with $6.5 \leq x \leq 8.0$ showed relaxor behavior in which the temperature of the dielectric maximum T_c depended on the measuring frequency. Furthermore there was a pre-maximum peak

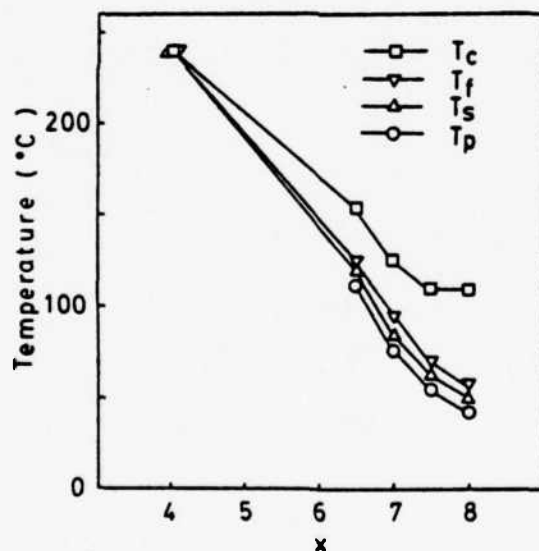


FIGURE 4 Curie temperature T_c , pre-maximum temperature T_p , deformation temperature T_f , and restoration temperature T_s as a function of La content x .

T. KIMURA, R. E. NEWNHAM AND L. E. CROSS

associated with the disappearance of ferroelectric domains. The temperature of the pre-maximum peak T_p did not depend strongly on measuring frequency. In the case of $x = 4.0$, there was no pre-maximum peak and T_c did not depend on measuring frequency.

Figure 4 shows the relationship between La content and the characteristic temperatures T_c , T_p , T_s and T_f . The values of T_s and T_f were collected from the data shown in Fig. 2, and the T_c values correspond to those measured at 1 kHz. The T_s and T_f temperatures of the sample with $x = 4.0$ coincide with T_c , but those of the sample with $6.5 \leq x \leq 8.0$ lay between T_c and T_p . The dependence of T_s and T_f on La content more closely resembles that of T_p rather than T_c .

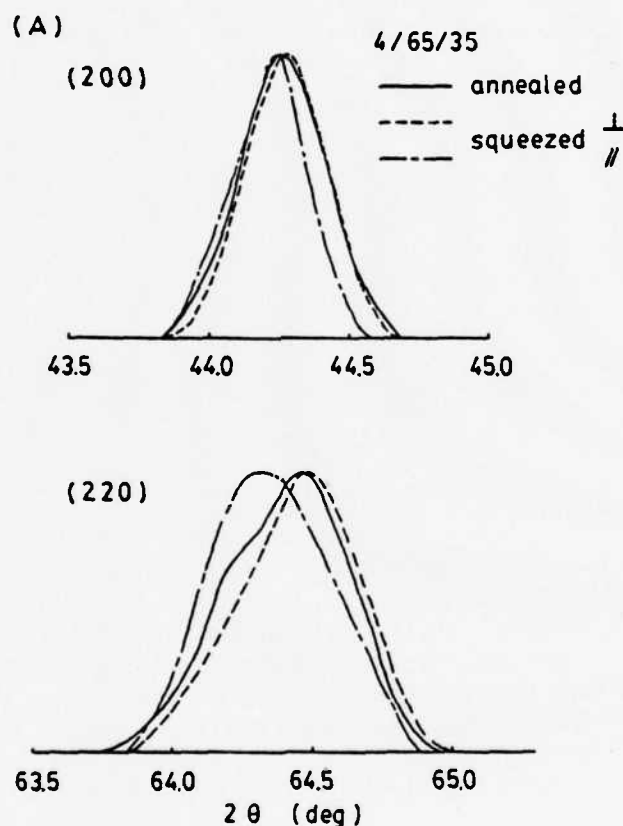
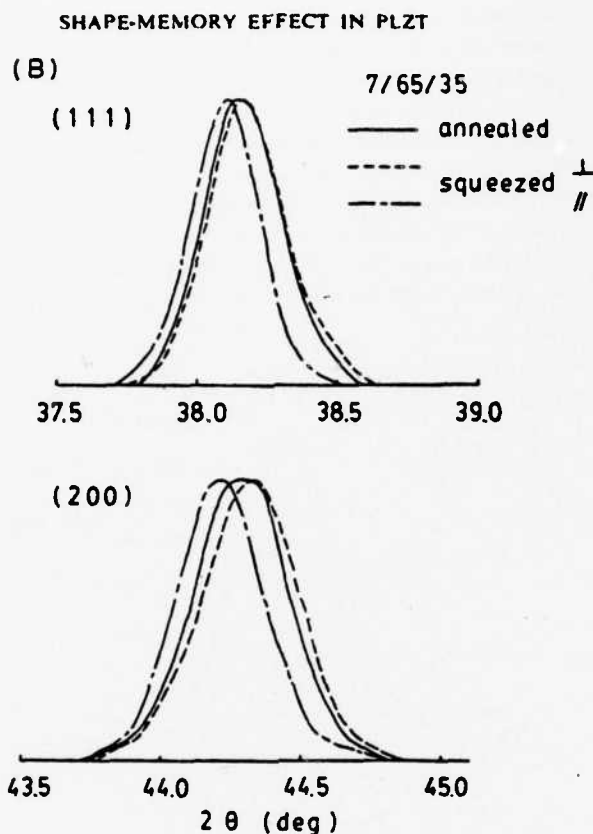


FIGURE 5 X-ray diffraction profiles of annealed (—) and compressed PLZT (---) face perpendicular, and — — — face parallel to stress direction) for (A) $x = 4.0$.

FIGURE 5 (contd.) for (B) $x = 7.0$.

6 X-RAY MEASUREMENT

Seven strong diffraction lines (110, 111, 200, 210, 211, 220 and 310) of annealed and compressed samples were examined. Figure 5 shows a few peak profiles and Table I lists the diffraction angles. The unit cell of the annealed samples was either rhombohedral ($x = 4.0$) with $a = 4.094$ Å and $\alpha = 89.76^\circ$, or cubic ($x = 7.0$) with $a = 4.086$ Å, in good agreement with the reported structures and cell size (Keve and Bye, 1975; O'Bryan and Meitzler, 1972).

Peaks from the compressed samples shifted to higher values for faces cut perpendicular to the stress direction, and to lower angles for faces parallel to the stress. As expected for compression, the d -spacings of the faces oriented perpendicular to the stress direction were smaller than those of the faces

T. KIMURA, R. E. NEWNHAM AND L. E. CROSS

cut parallel to the stress. Peaks from the faces perpendicular to the stress were similar to those of the annealed sample.

Quantitative determination of phases present in the compressed samples was difficult because good high-angle diffraction data were not available. Because the largest differences in d -spacings between mutually perpendicular faces were between (220) and (200) for the $x = 4.0$ sample and between (200) and (111) for the $x = 7.0$ specimen, the structures were judged to be rhombohedral ($x = 7.0$).

7 DISCUSSION

For compositions with $x \leq 4.0$, the samples behave like normal ferro-electrics, but for those in the range $8 \geq x \geq 6.5$, domains are not observed on cooling through T_c , nor do they disappear at T_c on heating. Ordered domains in a poled ceramic disappear at T_p in this composition range. The close relationship between the shape-memory temperatures T_s and T_f , and T_c and T_p suggests that the domain process plays an important role in the shape-memory effect. Mechanical stress orders the domains at T_c ($x = 4.0$) or at T_p ($6.5 \leq x \leq 8.0$) during cooling, which results in a large pseudo-plastic strain at room temperature. Heating eliminates the domains and restores the original shape.

X-ray diffraction measurements on the compressed samples (Figure 5 and Table I) gave the largest d -spacings from sample faces oriented parallel

TABLE I
Diffraction angles of annealed and compressed PLZT x 65/35 with
 $x = 4.0$ and 7.0

hkl	Angle of peak maximum, 2θ ($^\circ$)					
	$x = 4.0$			$x = 7.0$		
	Annealed	Compressed \perp	Compressed \parallel	Annealed	Compressed \perp	Compressed \parallel
110	30.91	30.92	30.89	30.94	30.96	30.90
111	38.13	38.14	38.10	38.15	38.16	38.11
200	44.26	44.28	44.24	44.28	44.33	44.22
210	49.79	49.80	49.72	49.84	49.86	49.78
211	55.00	55.01	54.90	55.01	55.05	54.93
220	64.46	64.48	64.30	64.47	64.51	64.39
310	73.14	73.18	73.07	73.16	73.24	73.07

\perp Faces perpendicular to stress.

\parallel Faces parallel to stress.

SHAPE-MEMORY EFFECT IN PLZT

to the stress direction. This means that the polar directions are preferentially aligned perpendicular to the compressional stress.

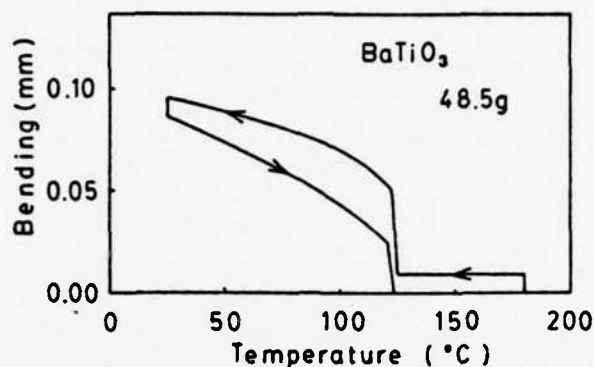
For samples with La content $6.5 \leq x \leq 8.0$, the deformation temperature T_d depends on load, but the restoration temperature T_r does not (Figure 3). Electrically, the discontinuity temperature in polarization shifts to higher values when the dc bias field increases (Keve and Annis, 1973). This abrupt change in polarization with temperature is associated with the domain phenomena occurring at T_p . This effect is analogous to the shift in T_d and T_r under mechanical stress. Since no mechanical stress was applied during heating, however, the restoration temperature T_r was not influenced by the stress applied during cooling. Apparently, mechanical stress has similar effects to an electric field in aligning domains. The anisotropic thermal expansion coefficients (O'Bryan and Meitzler, 1972) observed in hot-pressed PLZT ($x = 8.0$) further supports this view. Radial stresses developed during cooling in the hot-pressing procedure cause domain alignment below the Curie temperature. Thermal expansion coefficients parallel to the direction of the compressional stress are higher than in annealed material, while negative coefficients are observed in the direction of tensile stresses.

These facts show that the polar direction can be easily aligned by stress when the sample is cooled through the temperature at which the domains form. Tensile stress aligns the polar direction parallel to the stress direction, and compressive stress favors domains in the perpendicular direction.

The relationship between bending and temperature shown in Figures 1 and 2 differs from the results reported by Schmidt and Boczek (1978), especially with regard to the shape of the cooling curve and the magnitude of bending. They observed a large bending at high temperature, and an elastic compliance about 300 times larger than the value determined by resonance measurement. This discrepancy might be attributed to the method of supporting the sample. Schmidt and Boczek used a cantilever method, in which one end of the sample was fixed, but this results in a rather complicated stress state. In our experiment, the samples were freely held by two supports. Under these circumstances, the stress state at a supporting position is not as complicated. Since stress levels strongly affect the shape-memory effect, the discrepancy in the results may be attributable to the experimental method.

Schmidt and Boczek (1978) postulated, on the basis of their data, that the relaxor or diffuse phase transformation was essential to obtain the shape-memory effect in ferroelectrics. The PLZT sample with $x = 4.0$, however, is not a relaxor. The fact that this sample shows a shape-memory effect indicates that the relaxor behaviour is not an essential property. To confirm this idea, BaTiO₃ ceramic bar with the same shape and size as the PLZT samples was examined. Figure 6 shows the bending-temperature relation. Upon cooling from 180°C under constant stress, bending increased

T. KIMURA, R. E. NEWNHAM AND L. E. CROSS

FIGURE 6 Temperature-dependence of bending of BaTiO_3 .

abruptly between 125° and 122°C and more slowly below 122°C . When the sample was reheated after removing the load at room temperature, bending decreased gradually up to 121°C and then fell sharply to zero between 121° and 123°C . This abrupt change in shape near the Curie temperature (126°C) coincides with the discontinuity in the lattice parameters, and indicates that domain formation and disappearance are likely causes of the shape-memory effect in ferroelectrics.

The maximum room-temperature strain obtained in these experiments was 2.1×10^{-3} in the sample with $x = 6.5$. The stress field is complicated in the bending test and it is difficult to understand which of the stresses, tension or compression, govern the strain. However, the observed strain can be compared with electrically-induced strain. In the sample with $x = 7.0$, the strains parallel and perpendicular to the electric field at room temperature are 2.1×10^{-3} and 0.5×10^{-3} , respectively (Smith, 1973). In our experiment the plastic part of the strain at room temperature in such a sample was 1.8×10^{-3} (Figure 1), which is comparable to the strain parallel to the electric field. Table II lists the values calculated from the data in Table I. The strains were calculated by comparing the d -spacings between compressed and annealed samples. In both samples, the strains observed in the faces parallel to the stress direction were larger than those in perpendicular faces. In the compressed samples, the polar axes are nearly perpendicular to the stress direction as discussed previously. The large strains observed parallel to the stress direction coincide with the large strains measured parallel to the electric field.

Large strains under tensile stress have been observed in samples with $x = 1.3$ and 6.0 (Meitzler and O'Bryan, 1971). At room temperature, the maximum strain in the $x = 6.0$ sample was 2.5×10^{-3} , which is almost the same strain observed in the present experiments. A structural phase change

SHAPE-MEMORY EFFECT IN PLZT

TABLE II

Differences of d -spacing between annealed and compressed samples

hkl	$\frac{d \text{ compressed} - d \text{ annealed}}{d \text{ annealed}} \times 10^3$			
	$x = 4.0$		$x = 8.0$	
	\perp	\parallel	\perp	\parallel
110	-0.3	0.7	-0.7	1.4
111	-0.2	0.8	-0.3	1.0
200	-0.4	0.4	-1.1	1.3
210	-0.2	1.3	-0.4	1.1
211	-0.2	1.7	-0.7	1.3
220	-0.3	2.2	-0.6	1.1
310	-0.5	0.9	-0.9	1.1

accompanied by a high degree of preferred orientation parallel to the direction of the applied tensile force is the cause of the large strains.

Figure 7 shows the temperature-dependence of the plastic part of the strain plotted with reduced temperature T/T_s and T/T_f . In the case of cooling under stress, the relationship between strain and the reduced temperature can be expressed by a single curve, except for the $x = 4.0$ sample. For the heating cycle, the relations for $x = 6.5$ and 7.0 coincide but others do not; all lie under the curve for $x = 6.5$ and 7.0 . The behavior of the $x = 4.0$ ceramic might be attributed to differences in crystal structure. The structures of the compressed samples were rhombohedral ($x = 4.0$) and tetragonal or of mixed phases ($x = 7.0$). The single curve relating strain and the reduced temperature shown in Figure 7(A) would imply that the crystal structures of $6.5 \leq x \leq 8.0$ are the same. In perovskites, the strain associated with a tetragonal distortion is generally larger than that of a rhombohedral distortion. Inversion of the magnitude of strain between $x = 4.0$ and 6.5 might result from such a difference in crystal structure.

Disagreement of the relation between strain and reduced temperature in the heating cycle for samples with $6.5 \leq x \leq 8.0$ might be attributed to the temperature at which the load was removed. To confirm this conjecture, two additional experiments were undertaken. In the first experiment, the weight was removed at various temperatures during the cooling. Figure 8 shows the result for $x = 7.0$. When unloaded at high temperatures (but below T_s), the reduction in bending was larger than that observed at room temperature.

In the second experiment, the sample was loaded at room temperature and then heated. Room-temperature bending was almost the same as that observed when the cooled sample was unloaded at room temperature (Figure 1). Bending increased during heating up to a certain temperature, and then

T. KIMURA, R. E. NEWNHAM AND L. E. CROSS

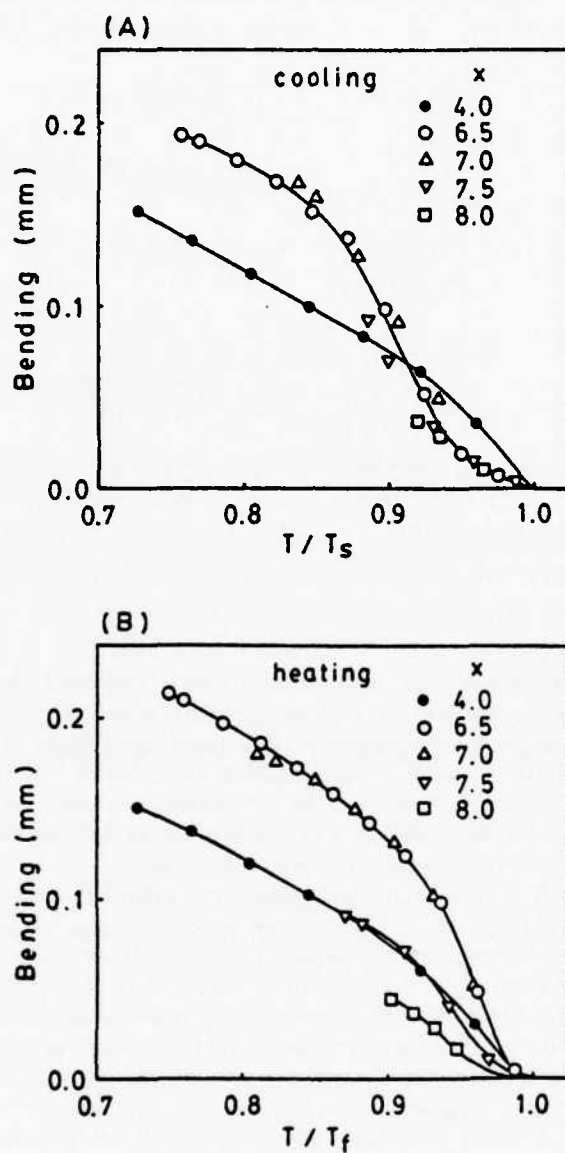


FIGURE 7 Relations between bending and reduced temperatures (A) T/T_s during cooling under constant load and (B) T/T_f during heating without load.

SHAPE-MEMORY EFFECT IN PLZT

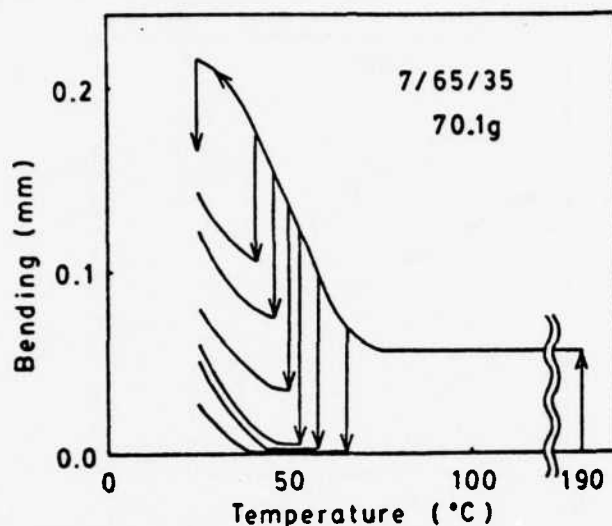


FIGURE 8 Reduction of bending by removal of the load at different temperatures in the sample 7.0/65/35.

decreased at higher temperatures, as shown in Figure 9. This result indicates that below T_p the stresses caused a phase transformation to a distorted structure with an aligned polar direction. The magnitude of the bending up to the temperature at which bending became a maximum is indicative of the ease of domain wall motion, i.e., the mechanical coercivity decreases with increasing temperature. Decrease in the bending at still higher temperature results from a reduction of the spontaneous strain.

Based on these two additional experiments, the following explanation appears feasible. The presence of mechanical stress forces domain alignment, so that a single curve expresses the relationship between strain and reduced temperature in the cooling cycle, as shown in Figure 7(A). Removal of the stress at room temperature releases the external constraint, and the internal stresses developed during cooling under stress tend to stabilize the structure. Since the difference between T_p and room temperature are large for $x = 6.5$ and 7.0 , the domain walls cannot move, and the only reduction in bending during unloading is elastic in nature. For $x = 7.5$ and 8.0 , on the other hand, T_p is low and some of the domains reorient to a more stable configuration during stress removal at room temperature. In other words, the mechanical relaxation time at room temperature decreases with increasing La content (Esaklul, Gerberich and Koepke, 1980). The reduction of bending accompanying unloading at room temperature has both elastic and domain

T. KIMURA, R. E. NEWNHAM AND L. E. CROSS

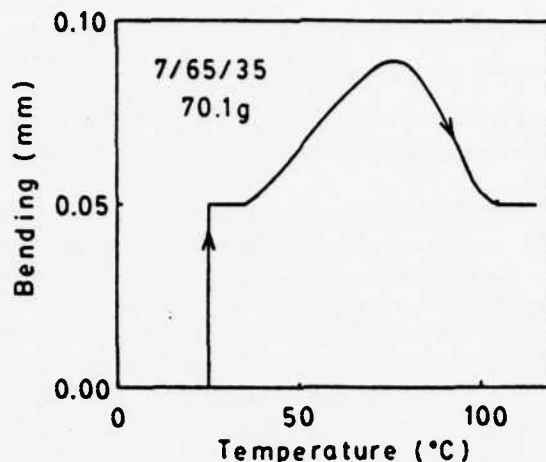


FIGURE 9 Temperature-dependence of bending during heating under constant load of 70.1 g.

contributions for $x = 7.5$ and 8.0 , resulting in the different curves in Figure 7(B).

The anomalous behavior caused by temperature cycling without load can also be explained by this idea. For $x = 7.0$, heating to high temperatures just below T_f causes domain re-orientation, resulting in smaller strains when recooled to room temperature. But several cycles between room temperature and 10°C below T_f did not lead to appreciable domain re-orientation.

8 CONCLUSION

The strains associated with the shape-memory effect in ferroelectric ceramics can be explained as follows. Above T_c the crystallites are cubic, and domains form when the sample is cooled through the transition temperature under stress. Mechanical stress causes partial alignment of the polarization directions (but not the absolute sense). The degree of alignment is determined by the magnitude of the stress, as in the case of electrical poling. In the perovskite structures, the polar axis is longer than the other axes. Polar axes tend to align parallel to a tensile stress. Domains with polarization vectors perpendicular to the stress direction are favored for compressional stresses. The alignment in a ceramic is not complete, however, because of random grain orientation and because of internal stresses between neighboring grains. After the domain pattern is formed, further cooling has little

SHAPE-MEMORY EFFECT IN PLZT

effect on the domain walls. But cooling increases the spontaneous strain of the distorted unit cell, and therefore the total strain increases as the temperature is decreased.

When the lattice parameters change discontinuously at the ferroelectric transition temperature, an abrupt change in shape takes place, as in the case of BaTiO_3 . When the lattice parameters change continuously, a gradual shape-change temperature-change is observed, as in the case of PLZT.

When stress is removed at room temperature, the total strain is reduced by an amount equivalent to the elastic contribution. If domain walls can move at room temperature, further reduction in total strain occurs by domain re-orientation as in the case of PLZT samples with $7.5 \leq x \leq 8.0$.

Upon heating without load, the decrease in spontaneous strain causes a gradual reduction in total strain. Domain re-orientation near the transition temperature contributes a further decrease in strain. Finally the spontaneous strain disappears at T_f , and the total strain goes to zero. In other words the shape-memory effect in ferroelectrics is caused by domain alignment together with the temperature-dependence of spontaneous strain.

Acknowledgements

This work was sponsored by the U.S. Army Research Office (DAAG29-80-C-0008). We also wish to thank Dr. William Harrison for supplying the samples, and Mr. James Laughner for his assistance with the experiments.

References

- Carl, K. and K. Geisen (1973). Dielectric and optical properties of a quasi-ferroelectric PLZT ceramic. *Proc. IEEE*, 61, 967.
- Delaey, L., R. V. Krishnan, H. Tas and H. Warlimont (1974). Thermoelasticity, pseudoelasticity and the memory effects associated with martensitic transformations. *J. Mater. Sci.*, 9, 1521, 1536, 1545.
- Esaklul, K. A., W. W. Gerberich and B. G. Koepke (1980). Stress relaxation in PZT. *J. Amer. Ceram. Soc.*, 63, 25.
- Haertling, G. H. and C. E. Land (1971). Hot-pressed (Pb, La) (Zr, Ti)O₃ ferroelectric ceramics for electrooptic applications. *J. Amer. Ceram. Soc.*, 54, 1.
- Keve, E. T. and A. D. Annis (1973). Studies of phase transformations and properties of some PLZT ceramics. *Ferroelectrics*, 5, 77.
- Keve, E. T. and K. L. Byc (1975). Phase identification and domain structure in PLZT ceramics. *J. Appl. Phys.*, 46, 810.
- Maldonado, J. R. and L. K. Anderson (1971). Strain-biased ferroelectric-photoconductor image storage, and display devices operated in a reflection mode. *IEEE Trans. Electron Devices*, 18, 774.
- Maldonado, J. R. and A. H. Meitzler (1970). Ferroelectric ceramic light gates operated in a voltage-controlled mode. *IEEE Trans. Electron Devices*, 17, 148.
- Maldonado, J. R. and A. H. Meitzler (1971). Strain-biased ferroelectric-photoconductor image storage and display devices. *Proc. IEEE*, 59, 368.
- Meitzler, A. H. and H. M. O'Bryan, Jr. (1971). Ferroelastic behavior of PLZT ceramics when subjected to large tensile strains. *App. Phys. Letters*, 19, 106.

T. KIMURA, R. E. NEWNHAM AND L. E. CROSS

- Meitzler, A. H. and H. M. O'Bryan, Jr. (1973). Polymorphism and penferroelectricity in PLZT ceramics. *Proc. IEEE*, 61, 959.
- O'Bryan, Jr., H. M. and A. H. Meitzler (1972). Enhanced ordering of ferroelectric domains in PLZT ceramics. *Bull. Amer. Ceram. Soc.*, 51, 459.
- O'Bryan, Jr., H. M. (1973). Phase relations in (Pb, La) $Zr_{0.65}Ti_{0.35}O_3$. *J. Amer. Ceram. Soc.*, 56, 385.
- Schmidt, G. and I. Boczek (1978). Pseudoelasticity and shape memory of PLZT ceramic. *Phys. Stat. Sol. (a)* 50, K109.
- Schulze, W. A., J. V. Biggers and L. E. Cross (1978). Aging of dielectric dispersion in PLZT relaxor ceramics. *J. Amer. Ceram. Soc.*, 61, 46.
- Smith, W. D. (1973). Electrically-controlled secondary phase in PLZT ceramics. In L. E. Cross (Ed), *Phase Transitions*. Pergamon Press, New York, pp. 71.
- Warlimont, H. (1976). Shape-memory effects. *Mater. Sci. Engineering*, 25, 139.

APPENDIX 2.10
POLAR GLASS CERAMICS

POLAR GLASS CERAMICS

A. HALLIYAL, A.S. BHALLA, R.E. NEWNHAM, L.E. CROSS
Materials Research Laboratory, The Pennsylvania State University, University
Park, PA 16802, USA

Abstract—Pyroelectric-piezoelectric glass ceramics of polar materials like $\text{Li}_2\text{Si}_2\text{O}_5$, $\text{Ba}_2\text{TiGe}_2\text{O}_8$, $\text{Ba}_2\text{TiSi}_2\text{O}_8$, and various compositions in the systems $\text{Li}_2\text{O}-\text{B}_2\text{O}_3$, $\text{Li}_2\text{O}-\text{SiO}_2-\text{ZnO}$, $\text{Li}_2\text{O}-\text{SiO}_2-\text{B}_2\text{O}_3$ have been prepared by oriented recrystallization of the glasses under a strong temperature gradient, providing a simple inexpensive process for preparing piezoelectric and pyroelectric materials. High pyroelectric responses were observed in these glass-ceramics. Values of piezoelectric d_{33} coefficients, frequency constants, electromechanical coupling coefficients and dielectric properties of glass-ceramics were in close agreement with the values of respective single crystals.

INTRODUCTION

In recent years there has been a growing interest in the study of ferroelectricity in glassy state and recrystallized ferroelectric glasses¹⁻¹⁰. Dielectric and pyroelectric measurements have been reported in glasses of stoichiometric compositions of LiTaO_3 , LiNbO_3 , $\text{Pb}_5\text{Ge}_3\text{O}_{11}$ and PbTiO_3 ¹⁻³.

Electro-optic properties, dielectric and pyroelectric measurements and switching behavior have been reported for glass ceramics containing ferroelectric microcrystals of BaTiO_3 , NaNbO_3 , LiTaO_3 , PbTiO_3 , $\text{Pb}_5\text{Ge}_3\text{O}_{11}$ and several other materials in a silica or borate rich glass matrix⁴⁻¹⁰. Effect of heat treatment process on porosity, grain size and on ferroelectric properties of the recrystallized glasses has been studied. All these studies on glass ceramics are limited to the ferroelectric glass ceramics where piezoelectric and pyroelectric properties are induced by electric poling of the domain structure of the microcrystals. Not much attention has been given to studies for inducing polar orientation in the microcrystals in nonferroelectric glass ceramics. Recently it has been shown that by controlled crystallization of glasses having compositions of pyroelectric-piezoelectric materials in a strong normal temperature gradient it is possible to obtain glass ceramics with both crystallographic and polar orientations^{11,12}. This paper describes the piezoelectric and pyroelectric measurements done on several glass-ceramic compositions. Advantages of glass ceramics for various device applications are discussed.

EXPERIMENTAL DETAILS

Glasses of compositions $\text{Ba}_2\text{TiGe}_2\text{O}_8$, $\text{Ba}_2\text{TiSi}_2\text{O}_8$, $\text{Li}_2\text{O}-2\text{SiO}_2$ and several compositions in the systems $\text{Li}_2\text{O}-\text{B}_2\text{O}_3$, $\text{Li}_2\text{O}-\text{SiO}_2-\text{ZnO}$ and $\text{Li}_2\text{O}-\text{SiO}_2-\text{B}_2\text{O}_3$ were prepared by mixing reagent grade chemicals in the desired molar ratios and melting in a global furnace. The compositions of the glasses and the crystallization temperatures determined from DTA runs are given in Table 1. Crystallization of glasses was carried out in a temperature

TABLE I

Properties of Glass-Ceramic Samples Prepared in a Temperature Gradient

	ϵ_r	$T_{cr} (^{\circ}\text{C})^a$	Crystalline Phases ^b	Piezo ^c d33 pC/N	Chynoweth responded pyro mV
2BaO-2GeO ₂ -TiO ₂	15	800	B ₂ TG ₂	+6	(-) 20
BaO-1.8SiO ₂ -TiO ₂	12	860	B ₂ TS ₂ +Q	+3	(+) 35
Li ₂ O-2SiO ₂		585	LS ₂	-1	(-) 20
Li ₂ O-2SiO ₂ -0.1ZnO	5	570	LS ₂ +LSZ+Q	-3	(-) 70
Li ₂ O-2SiO ₂ -0.2ZnO	6	580	LS ₂ +LSZ+Q	-4	(-) 100
Li ₂ O-2SiO ₂ -0.25ZnO		585	LS ₂ +LSZ+Q	-4	(-) 80
Li ₂ O-2SiO ₂ -0.4ZnO	8	590	LS ₂ +LSZ+Q	0	(-) 4
Li ₂ O-3B ₂ O ₃		580	LB ₂ +LB ₃	+3	(-) 70
Li ₂ O-1.8SiO ₂ -0.2B ₂ O ₃	8	605, 680	LS ₂ +LB ₂ +LS	+6	(-) 200
Li ₂ O-1.33SiO ₂ -0.66B ₂ O ₃	8	670	LS ₂ +LB ₂ +LS	+3	(-) 85
Li ₂ O-1.8SiO ₂ -0.1ZnO-0.1B ₂ O ₃	7	580, 670	LS ₂ +LSZ	-2	(-) 20

^a T_{cr} is the crystallization temperature determined from DTA runs.^bAbbreviation for phases.B₂TG₂ = Ba₂TiGe₂O₈LSZ = Li₂ZnSiO₄B₂TS₂ = Ba₂TiSi₂O₈LS = Li₂SiO₃Q = SiO₂ (quartz)LB₂ = Li₂B₄O₇LS₂ = Li₂Si₂O₅LB₃ = Li₂B₆O₁₀^cMeasured on the surface facing the higher temperature end of the temperature gradient axis.^d(±) indicates the sign of pyroelectric coefficient p.

gradient by placing the polished glass samples, in the form of thick disks, on a microscope hot stage (E. Leitz, Inc.). A detailed procedure for the preparation of glass-ceramic samples can be found in references 11-14. The crystalline phases in the glass-ceramic samples were identified from x-ray powder patterns. The piezoelectric constants were measured using a d33 meter. For resonance studies, samples in the shape of circular disks were prepared, polished and gold electrodes were sputtered. Measurements were made both in the radial and the thickness mode of resonance by resonance and antiresonance method using a Hewlett Packard 3585A spectrum analyzer¹⁴. Pyroelectric responses from thin samples (250 μm) were measured by the dynamic Chynoweth technique¹⁵ at a modulating frequency of 4 Hz.

MICROSTRUCTURE OF RECRYSTALLIZED SAMPLES

Glass-ceramics prepared from recrystallization of the glasses in a temperature gradient showed a high degree of crystallographic orientation. Studies on the degree of preferred orientation of the crystallites as a function of depth from the hot face revealed that the oriented crystallites region extends deep in the glass-ceramic samples and then tapers off (Figure 1). Needle-like crystals grow from the hot face into the sample along the direction of the temperature gradient. The depth of the oriented region was 400 to 600 μm . The width of the crystallites estimated from the optical microscope is in the range 2-5 μm .

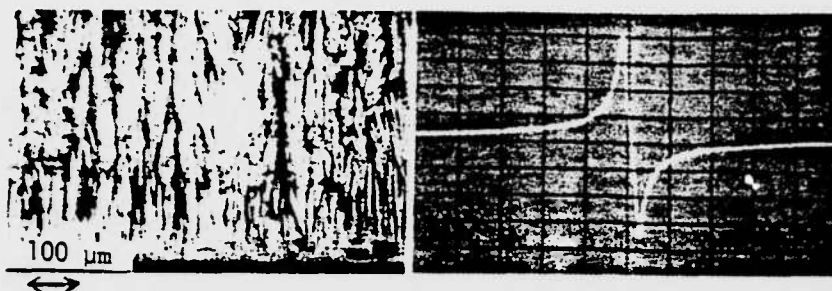


FIGURE 1

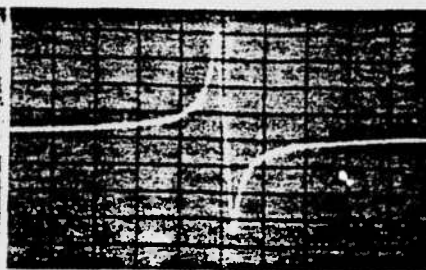


FIGURE 2

Fig. 1.

Optical photomicrograph of oriented crystallized region in $\text{Li}_2\text{O}-2\text{SiO}_2-0.2\text{ZnO}$ glass-ceramics ($\times 100$).

Fig. 2.

Resonance spectrum for $\text{Li}_2\text{O}-1.8\text{SiO}_2-0.2\text{B}_2\text{O}_3$ glass-ceramic (horizontal scale = 6.8 kHz; vertical scale = 5 dB).

PIEZOELECTRIC PROPERTIES

The piezoelectric d_{33} coefficients and their signs measured on the surface facing the higher temperature gradient end are given in Table 1. For $\text{Ba}_2\text{TiGe}_2\text{O}_8$ and $\text{Ba}_2\text{TiSi}_2\text{O}_8$ glass-ceramics, the sign of d_{33} was positive. For $\text{Li}_2\text{Si}_2\text{O}_5$ the sign of d_{33} was negative and remained the same in samples containing small amounts of ZnO in the composition. However, the magnitude of d_{33} increased for compositions containing even a small amount of ZnO . Addition of small amounts of B_2O_3 in $\text{Li}_2\text{Si}_2\text{O}_5$ reversed the sign and increased the magnitude of d_{33} . This indicated that both the crystallization behavior and the polar orientation were influenced strongly by the various ionic species present in the parent glass.

A typical resonance spectrum observed in glass-ceramic samples is shown in Fig. 2. The electromechanical properties of some of the glass-ceramic compositions are given in Table 2.^{14,16} The coupling coefficients k_p and k_t of $\text{Ba}_2\text{TiGe}_2\text{O}_8$ glass-ceramics are comparable to the corresponding values of single crystals. The values for mechanical quality factor Q are comparatively higher. The TCR values for $\text{Li}_2\text{O}-\text{SiO}_2-\text{B}_2\text{O}_3$ glass-ceramics are comparable to the values of commonly used piezoelectric materials like LiTaO_3 and LiNbO_3 . In this system, the strong dependence of TCR on the composition of the parent glass suggests that it might be possible to reduce TCR further by a suitable choice of the composition of the parent glass. In addition, by employing proper heat treatment cycles for crystallization, it is possible to prepare glass ceramics with oriented crystallites of more than one phase from the glass matrix. Hence, in such glass-ceramic systems, composition and processing parameters are the extra controlling factors, which can be exploited to tailor the properties of piezoelectric resonators.

TABLE 2
Electromechanical Properties of Glass Ceramics

Composition	N_p m-Hz	N_t m-Hz	k_p %	k_t %	Q	TCR ppm/ $^{\circ}\text{C}$
$2\text{BaO}-2\text{GeO}_2-\text{TiO}_2$	3100	2500	4.4	7.5	700	95 (0° - 100°C)
$\text{Ba}_2\text{TiGe}_2\text{O}_8$ (single crystal)	2900	2150	6.2	10.0	650	50 (0° - 100°C)
$\text{Li}_2\text{O}-1.8\text{SiO}_2-0.2\text{B}_2\text{O}_3$	4500	--	14	--	1000	60 (0° - 100°C)
$\text{Li}_2\text{O}-1.33\text{SiO}_2-0.66\text{B}_2\text{O}_3$	4200	--	9	--	400	30 (30° - 60°C)

PYROELECTRIC PROPERTIES

The pyroelectric voltage response of the samples measured by the Chynoweth technique are given in Table 1. Pyroelectric responses from grain oriented glass-ceramics were typically 50% of the responses from the corresponding single crystals. Lithium borosilicate glass-ceramics seem very promising for pyroelectric applications. A strong pyroelectric response was measured from glass ceramics of composition $\text{Li}_2\text{O}-1.8\text{SiO}_2-0.2\text{B}_2\text{O}_3$ and was comparable to the signal from a commercial pyroelectric such as LiTaO_3 .

For pyroelectric detectors and vidicon, the figure of merit is given by $P/\epsilon\rho C_p K$ where p is the pyroelectric coefficient, ϵ the dielectric constant, ρ the density, C_p the specific heat and K is the thermal conductivity of the material. The dielectric constants of the glass-ceramics listed in Table 1 are in the range 5 to 10 and the densities are about 2-3 gms/cc. A high figure of merit could be possible in glass-ceramic pyroelectric detectors.

SUMMARY

Several piezoelectric and pyroelectric materials can be prepared in the glassy phase, and it is possible to prepare large area, inexpensive polar glass ceramics by recrystallizing the glasses under a strong normal temperature gradient. Electrical properties of glass ceramics are less sensitive to the chemical impurities and the defects in the samples. The piezoelectric and pyroelectric properties of the glass ceramics can be tailored to the desired requirements by recrystallizing the multicomponent glasses using a proper temperature cycle. Pyroelectric and electromechanical properties of glass ceramics are comparable to their properties in the single crystal form. Such composite elements may be useful for device applications based on flexural resonance mode, in pyroelectric detectors, for resonators, and in SAW devices. The process for preparing glass ceramics is amenable to mass production.

ACKNOWLEDGMENTS

This work was sponsored by the U.S. Army Research Office (DAAG 29-80-C-0008) and the Advanced Research Project Agency (DARPA Project No. P-15124-MS).

REFERENCES

1. A.M. Glass, M.E. Lines, K. Nassau, J.W. Shiever, *Appl. Phys. Lett.* 31, 249 (1977).
2. A.M. Glass, K. Nassau, J.W. Shiever, *J. Appl. Phys.* 48, 5213 (1977).
3. M. Takashige, T. Mitsui, T. Makagura, Y. Aikawa, M. Jang, *Jpn. J. Appl. Phys.* 20, L159 (1981).
4. A. Herzog, *J. Amer. Ceram. Soc.* 47, 107 (1964).
5. N.F. Borrelli, *J. Appl. Phys.* 38, 4243 (1967).
6. M.E. Lines, *Phys. Rev.* B15, 388 (1977).
7. T. Kokubi, H. Nagao, M. Tashiro, *Yogyo-Kyokai-shi* 77, 293 (1969).
8. C.G. Bergeron and C.K. Russell, *J. Amer. Ceram. Soc.* 48, 115 (1965).
9. K. Takahashi, L.E. Cross, R.E. Newnham, *Mat. Res. Bull.* 10, 599 (1975).
10. M.M. Layton, J.W. Smith, *J. Amer. Ceram. Soc.* 58, 435 (1975).
11. G.J. Gardopée, R.E. Newnham, A.G. Halliyal, A.S. Bhalla, *Appl. Phys. Lett.* 36, 817 (1980).
12. G.J. Gardopée, R.E. Newnham, A.S. Bhalla, *Ferroelectrics* 33 (1981) (accepted).
13. A. Halliyal, A.S. Bhalla, R.E. Newnham, L.E. Cross, *J. Mater. Sci.* 16, 1023 (1981).
14. A. Halliyal, A.S. Bhalla, R.E. Newnham, L.E. Cross, *J. Mater. Sci.* (accepted).
15. A.G. Chynoweth, *J. Appl. Phys.* 27, 78 (1956).
16. A. Halliyal, A.S. Bhalla, R.E. Newnham, L.E. Cross, *J. Appl. Phys.* (submitted).

APPENDIX 2.11

$\text{BaTiGe}_2\text{O}_8$ AND $\text{Ba}_2\text{TiSi}_2\text{O}_8$ PYROELECTRIC GLASS-CERAMICS

Ba₂TiGe₂O₈ and Ba₂TiSi₂O₈ pyroelectric glass-ceramics

A. HALLIYAL, A. S. BHALLA, R. E. NEWNHAM, L. E. CROSS

Materials Research Laboratory, The Pennsylvania State University, University Park, Pennsylvania 16802, USA

Pyroelectric glass-ceramics of composition Ba₂TiGe₂O₈ and Ba₂TiSi₂O₈ were prepared by crystallizing the glasses in a temperature gradient. High pyroelectric responses up to 50% of the single-crystal values were observed because of the high degree of orientation of the crystallites in the glass-ceramic samples. The piezoelectric and dielectric properties of the glasses and the glass-ceramics are also consistent with the properties of the single crystals.

1. Introduction

Pyroelectric lithium disilicate glass-ceramics have recently been prepared by growing highly orientated surface layers of lithium disilicate crystals by crystallizing the glasses of stoichiometric glass compositions Li₂O · 2SiO₂ in a temperature gradient [1]. This technique provides a method of fabricating large and inexpensive pyroelectric devices. However, one difficulty encountered in working with the lithium disilicate pyroelectric glass-ceramic was that thin targets (of thickness, $d < 200 \mu\text{m}$) cut perpendicular to the growth direction (the polar c -axis of Li₂Si₂O₅) were extremely fragile and could not be prepared routinely.

In this study pyroelectric glass-ceramics of barium titanium silicate (BTS: Ba₂TiSi₂O₈ or fresnoite) and barium titanium germanate (BTG: Ba₂TiGe₂O₈) are described, the physical properties of which are superior to Li₂Si₂O₅. Thin sections of these glass-ceramics, less than 100 μm in thickness, can easily be prepared since they are mechanically much stronger. Glass-ceramics of BTG and BTS were prepared by crystallizing glasses of stoichiometric compositions of BTG and a silica-rich composition (64SiO₂–36BaTiO₃) of BTS in a thermal gradient. The dielectric and pyroelectric properties were measured and compared with the properties of single crystals.

In the single-crystal form fresnoite belongs to

the crystallographic point group 4mm and is pyroelectric [2]. Ba₂TiGe₂O₈ is reported to be a ferroelastic [3, 4] below 810°C and belongs to the orthorhombic polar point group mm2. In the paraelastic phase above the transition temperature, T_c , BTG also belongs to the tetragonal point group 4mm.

Glass-ceramics in the BaTiO₃–SiO₂ system have been previously investigated. Herczog [5] studied the crystallization of BaTiO₃ in a silicate glass matrix. Dielectric and electro-optic measurements on transparent glass-ceramics containing ferroelectric BaTiO₃ in a glass matrix have also been reported [6]. However, the primary interest in these materials has been concerned with the dielectric and electro-optic properties of the glass-ceramics, and in the ferroelectric nature of BaTiO₃ crystallites surrounded by a glass matrix. In these studies no efforts have been made to develop glass-ceramics containing orientated crystallites. The present study describes the preparation and characterization of glass-ceramics containing orientated crystallites of the pyroelectric (but non-ferroelectric) BTS and BTG phases.

2. Experimental details

Glasses of composition 64SiO₂ · 36BaO · 36TiO₂ were prepared by mixing reagent-grade silicic acid*, barium carbonate† and titanic oxide‡.

*J. T. Baker Chemical Co., Phillipsburg, NJ, USA.

†Fisher Scientific Co., Phillipsburg, NJ, USA.

‡Eagle-Picher Industries, Inc., Quapaw, Oklahoma, USA.

followed by melting in a global furnace. Fresnoite has a high melting point (1400°C) and thus, it was difficult to obtain bubble-free glasses of the stoichiometric composition. To avoid this problem, a composition was selected which lies near the eutectic point on the silica-rich side of the $\text{BaTiO}_3\text{--SiO}_2$ binary phase diagram [7]. This composition lies well within the range of glass formation in the $\text{BaTiO}_3\text{--SiO}_2$ system.

In the case of BTG, reagent-grade barium carbonate, germanium oxide* and titanic oxide were mixed and melted in the furnace. In both cases, the melts were maintained at 1375°C for 24 hours for fining and homogenization. Transparent samples were obtained by pouring the melt into a graphite mould. The samples which crystallized during pouring of the melt were remelted and poured again into the graphite mould in order to ensure transparent glass samples. All the glass samples were annealed at 600°C for 12 hours and then cut and polished in the form of thick disks in preparation for the crystallization studies. To determine the crystallization temperatures of the glass compositions, differential thermal analysis (DTA) measurements were performed on the glass samples. Exothermic peaks were observed at 860°C in the case of BTS and at 800°C in the case of BTG, as shown in Fig. 1.

Crystallization was carried out in a temperature gradient by placing the polished glass samples, in the form of thick disks, on a microscope hot stage.[†] The temperature gradient near the hottest temperature zone was perpendicular to the surface of the sample and it was estimated to be about $100^{\circ}\text{Cmm}^{-1}$. Typical heating cycles used for glass crystallization are shown in Fig. 2. The heating cycle consisted of an initial rapid rise in temperature to minimize volume nucleation, followed by a slow increase in temperature at a rate of about $3^{\circ}\text{Cmin}^{-1}$. After reaching the maximum crystallization temperature (1100°C for BTS and 1000°C for BTG), the samples were held at this temperature for 24 hours. The temperature was then decreased rapidly to room temperature. The thicknesses of the crystallized portions of the glasses ranged from 1 to 2 mm, depending on the heating cycle.

The degree of preferred orientation of the

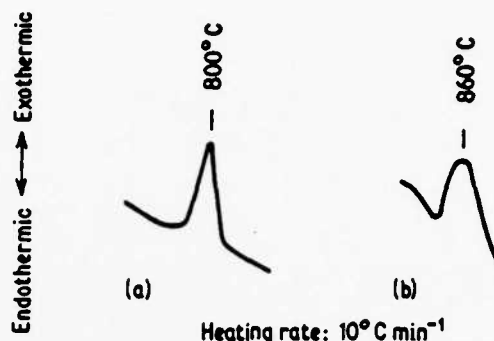


Figure 1 DTA heating curves of (a) BTG and (b) BTS glasses.

glass-ceramic was evaluated from X-ray diffractometer patterns. X-ray diffraction (XRD) patterns were recorded on surfaces normal to the direction of the temperature gradient (Fig. 3). The XRD patterns were compared with the standard powder diffraction patterns to determine the relative degree of orientation. The dielectric constants of glass and glass-ceramic disks were measured with a capacitance bridge. The piezoelectric behaviour parallel to the crystallization direction was studied using a d_{33} -meter.[‡] The samples were thinned down to about $200\mu\text{m}$ in thickness and the pyroelectric response was measured by the dynamic Chynoweth technique [8] at a modulating frequency of 4 Hz. The pyroelectric signals on glass-ceramics were compared with the responses from single crystals of the BTG and BTS. The densities of BTG, BTS glasses and glass-ceramic samples were determined by a mercury porosimeter[§] and compared with the densities of single crystals.

3. Results and discussion

Table I summarizes the data for the glass and glass-ceramic samples. Single-crystal values are also listed for comparison.

X-ray powder diffraction patterns of the crystallized samples showed that the principal crystallized phases were fresnoite in the BTS glass-ceramics and $\text{Ba}_2\text{Ge}_2\text{TiO}_8$ in the BTG glass-ceramic samples. A few low-intensity peaks of an unidentified phase were observed in the powder diffraction patterns of both compositions. The samples showed highly orientated crystal growth

*Eagle-Picher Industries, Inc., Quapaw, Oklahoma, USA.

[†]Model No. 493, manufactured by E. Leitz, Inc., Rockleigh, NJ, USA.

[‡]Model CPDT 3300, manufactured by Channel Products, Chesterland, OH, USA.

[§]Model JS-7146, manufactured by American Instrument Co., Silver Spring, MD, USA.

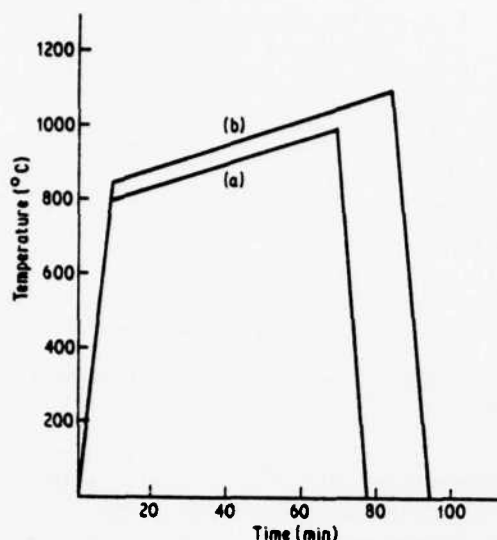


Figure 2 Heating cycles used for crystallizing (a) BTG and (b) BTS glasses.

in a direction parallel to the temperature gradient, with the polar c -axis perpendicular to the hot surface of the sample. As shown in Fig. 4, the 002 reflection was the strongest in the X-ray patterns of the crystallized surfaces. The ratio of the intensity of the 002 peak to that of the 211 peak was taken as a measure of the relative degree of orientation. The intensity ratios are given in Table I. Comparison of the intensity ratios in the glass-ceramic samples with the intensity ratios of a standard powder pattern, showed a high degree of orientation of the crystallites in the glass-ceramics. An even higher degree of orientation was obtained in the samples with good surface finish.

The degree of preferred orientation in crystallized samples of BTS and BTG was similar to that observed previously [1] in $\text{Li}_2\text{Si}_2\text{O}_5$. It was observed that the degree of orientation of the crystallites in the isothermally crystallized glass-ceramics was poor compared to the samples crystallized in a temperature gradient. In addition, detailed studies of the microstructure of the crystallized samples showed that the thickness of the well-orientated region was larger in the case of samples crystallized in a temperature gradient, indicating that thermal gradient crystallization is preferable for obtaining well orientated glass-ceramics.

The main reason for the orientation of the crystallites is surface-nucleated crystallization which takes place in both the isothermal and temperature-gradient crystallization. A higher degree of electrical and crystallographic orientation is obtained in the temperature-gradient crystallization method due to the absence of volume nucleation; however, in the case of isothermal crystallization, the orientation of the crystallites is limited to a layer only a few micrometers thick due to the simultaneous occurrence of volume nucleation. Atkinson and McMillan [9] attempted to produce a $\text{Li}_2\text{Si}_2\text{O}_5$ glass-ceramic with an aligned microstructure by a hot-extrusion method. They were partially successful in obtaining glass-ceramic samples with the disilicate crystal crystallographically-aligned parallel to the extrusion axis. However, the degree of orientation of the crystallites was less than that obtained in glass-ceramic samples prepared by crystallizing the glasses in a temperature gradient [1].

The density of BTG glass was about the same as

TABLE I Summary of data for glass and glass-ceramic samples.

Sample	X-ray intensities, $I(002)/I(211)$	Dielectric constant, ϵ^*	Dissipation factor*	Density (g cm^{-3})	d_{33} ($\times 10^{12} \text{ C N}^{-1}$)	Pyroelectric response
BTG glass	—	17	0.003	4.74	—	50% to 60% of single- crystal value
BTG glass-ceramic	85	15.0	0.002	4.56	5 to 7	
$\text{Ba}_3\text{Ge}_2\text{TiO}_8$ single crystal	0.2 (standard powder pattern)	$\epsilon_{11} = 20$ $\epsilon_{22} = 20$ $\epsilon_{33} = 13$	0.003	4.84	8	
BTS glass	—	15	0.002	4.01	—	50% to 60% of single- crystal value
BTS glass-ceramic	15	12.5	0.002	3.90	2 to 3	
$\text{Ba}_2\text{Si}_2\text{TiO}_8$ single crystal	0.2 (standard powder pattern)	$\epsilon_{11} = \epsilon_{22} = 15$ $\epsilon_{33} = 11$	0.003	4.45	3.8	

*Measurements were made at 1 MHz for the glass and glass-ceramic and at 1 kHz for single crystals.

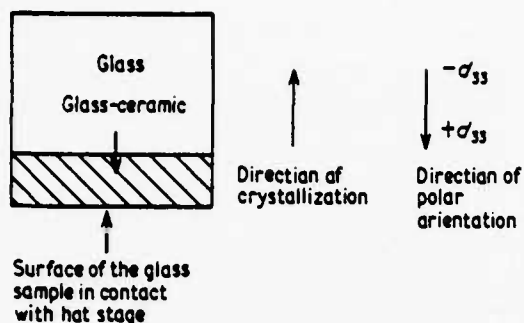


Figure 3 The direction of polar orientation in glass-ceramic samples.

the single-crystal form (Table I), while that of BTS glass was slightly lower than the density of ferroite single crystals because of the excess silica used in the BTS composition. Only a small decrease in density occurred on crystallization of the glass phases, indicating a low concentration of voids in the glass-ceramic samples. Samples as thin as $100\mu\text{m}$ could be prepared without difficulty because of the absence of pores and cracks.

The dielectric constants of BTS and BTG glasses measured at 1 MHz are very close to the mean dielectric constant, $(\epsilon_{11} + \epsilon_{22} + \epsilon_{33})/3$, of the corresponding crystalline phases. On crystal-

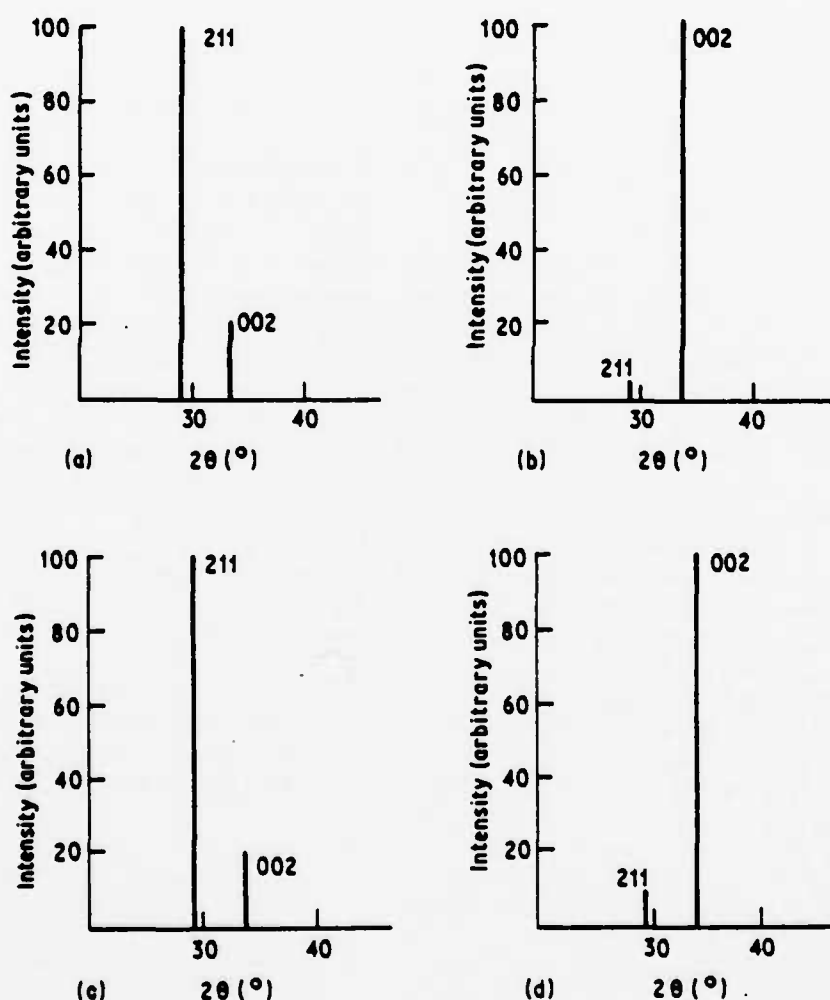


Figure 4 X-ray diffraction patterns of (a) $\text{Ba}_2\text{Ge}_2\text{TiO}_7$, standard powder diffraction pattern, (b) BTG glass-ceramic, (c) $\text{Ba}_2\text{TiSi}_2\text{O}_{10}$, standard powder diffraction pattern, and (d) BTS glass-ceramic.

lization, the dielectric constants of the glass-ceramic samples show a slight decrease; the dielectric constant measured in the crystallization direction is closer to the ϵ_3 -values of the single crystals. This is consistent with the fact that the c -axis is the preferred orientation direction in the glass-ceramic, as indicated by X-ray diffraction analysis.

The loss tangent factors of the glass-ceramics were similar to those measured on single crystals.

Piezoelectric coefficients, d_{33} , measured in the crystallization direction in glass-ceramics were comparable to the single-crystal d_{33} coefficient values reported [2-4] for BTS and BTG. Opposite faces of the sample gave opposite signs for the piezoelectric constant. The large magnitude of d_{33} -values and its sign reversal suggest that the crystallites in the glass-ceramics are not only orientated along the c -axis in the crystallization direction, but that most of the crystallites have the same polarity as well. The fact that the d_{33} -values remained constant over the entire surface of the glass-ceramic testifies to the uniformity and the homogeneity of the samples.

As in the previous study of lithium disilicate [1], it was observed that the temperature gradient dictated both the electrical and crystallographic alignment. In all samples the polar orientation was antiparallel to the direction in which crystallization proceeds into the glass, with the positive end of the dipole pointing toward the high-temperature end of the sample, as depicted in Fig. 3. There may be several causes for the polar alignment of the crystallites. One possible cause is the existence of high local electric fields resulting from surface pyroelectric charges [10]. These local electric fields might dictate the orientation of the dipoles as crystallization proceeds into the glass. A second possible cause is the nature of the surface chemistry. It is known that low charge cations such as Li^+ or Ba^{2+} migrate to the surface upon heating [11]. This higher surface concentration of cations could influence the nature of both the crystallization and polar orientation. It is possible that as the crystallization proceeds into the bulk of the glass, starting from a cation-rich surface, the positive end of the dipole moments in the crystallites will be directed toward the hot surface.

The pyroelectric response on the glass ceramics was studied by the dynamic Chynoweth method. Pyroelectric voltage responses of between 50 and 60% of the single-crystal values were obtained

reproducibly with the glass-ceramic samples. The sign of the pyroelectric coefficient is negative for BTG single crystals and positive for BTS. A similar difference in sign was observed with glass-ceramics. For a simple pyroelectric detector, the figure of merit is given by p/ϵ , where p is the pyroelectric coefficient and ϵ is the dielectric permittivity. The pyroelectric coefficients of single crystals of $\text{Ba}_2\text{TiGe}_2\text{O}_8$ and $\text{Ba}_2\text{TiSi}_2\text{O}_8$ are 3 and $10 \mu\text{C m}^{-2} \text{ } ^\circ\text{C}^{-1}$, respectively [12]. Since the dielectric constants of the glass-ceramics are comparable with those of single crystals, it can be concluded that the pyroelectric coefficients of the glass-ceramics are of the same order of magnitude as those of the single crystals. Specimens of 100 to $500 \mu\text{m}$ in thickness were studied during pyroelectric tests. Samples of large surface area and less than $100 \mu\text{m}$ in thickness were mechanically strong and gave reproducible results, suggesting their use as pyroelectric detectors.

4. Conclusions

Glass-ceramics of composition $\text{Ba}_2\text{TiGe}_2\text{O}_8$ and $\text{Ba}_2\text{TiSi}_2\text{O}_8$ were prepared by crystallizing the glasses in a temperature gradient. The glass-ceramics show preferred orientation, with the polar c -axis parallel to the temperature gradient. Pyroelectric responses up to 50% of the single-crystal values were observed on these glass-ceramic samples. Measurement of the density, dielectric constant, and piezoelectric constant gave results comparable to the reported single-crystal properties.

Acknowledgement

We wish to thank our colleagues at the Materials Research Laboratory for their advice and assistance. This work was sponsored by the U.S. Army Office of Research and Development (Contract Grant No. DAAG29-78-0033) and by Defense Advanced Research Projects Agency (Contract DARPA Project No. P-15124-MS).

References

1. G. J. GARDOPEE, R. E. NEWNHAM, A. G. HALLIYAL and A. S. BHALLA, *Appl. Phys. Lett.* **36** (1980) 817.
2. M. KIMURA, Y. FUGINO and T. KAWAMURA, *ibid.* **29** (1976) 227.
3. M. KIMURA, K. DOI, S. NANAMATSU and T. KAWAMURA, *ibid.* **23** (1973) 531.
4. M. KIMURA, K. UTSUMI and S. NANAMATSU, *ibid.* **47** (1976) 2249.

5. A. HERCZOG, *J. Amer. Ceram. Soc.* 47 (1964) 107.
6. N. F. BORRELLI and M. M. LAYTON, *J. Non-Cryst. Sol.* 6 (1971) 197.
7. D. E. RASE and R. ROY, *J. Amer. Ceram. Soc.* 38 (1955) 393.
8. A. G. CHYNOWETH, *J. Appl. Phys.* 27 (1956) 78.
9. D. I. H. ATKINSON and P. W. McMILLAN, *J. Mater. Sci.* 12 (1977) 443.
10. P. E. BLOOMFIELD, I. LEFKOWITZ and A. D. ARONOFF, *Phys. Rev. B* 4 (1971) 974.
11. G. E. RINDONE, in Proceedings of the Symposium on Nucleation and Crystallization in Glasses and Melts, edited by M. K. Roser, G. Smith and H. Insley (American Ceramic Society, Columbus, Ohio, 1962) pp. 63-69.
12. A. S. BHALLA, unpublished work.

Received 4 July and accepted 22 September 1980.

APPENDIX 2.12
DENSIFICATION IN PZT

DENSIFICATION IN PZT

S. VENKATARAMANI, J.V. BIGGERS

Materials Research Laboratory, The Pennsylvania State University, University Park, PA 16802, USA

The reaction sequence of PZT formation from the mixture of $\text{PbO-ZrO}_2\text{-TiO}_2$ has been extensively studied¹⁻³. However, there have been no studies on the morphological changes occurring during the calcination process. The dependence of the characteristics and properties of the ceramic on the calcining conditions though has been well noted⁴⁻⁵, no systematic explanations have been given for the reasons of such dependencies.

Inhomogeneous sintering has been observed in PZT tapes and disks⁶ and was attributed to packing characteristics and chemical inhomogeneities. Earlier efforts to reactively sinter PZT ceramics from uncalcined oxide mixtures were in vain due to the "anomalous" expansion of the compacts during the sintering process⁷.

The purpose of this study was to investigate the dilatometric behavior of the compacts during calcining and its influence of sintering and properties of PZT ceramics.

EXPERIMENTAL

The PZT 60/40 ($\text{PbZr}_{0.6}\text{Ti}_{0.4}\text{O}_3$) composition was prepared from the reagent grade oxides via the usual processing steps—ball milling and drying. Four different calcinations were carried out with varying temperature/time conditions to produce different phase assemblages: (i) uncalcined (as mixed); (ii) calcines at 600° for 3 hours; (iii) calcined at 700°C/3 hours and (iv) calcined at 800° for 6 hours. Calcining was done by placing the ZrO_2 Saggers containing the PZT mix into an electric muffle furnace preheated to the required temperature for the specified period of time.

The calcined powders were characterized for (i) surface area by a BET technique; (ii) particle size and shape distribution by CESEMI and (iii) qualitative and quantitative phase analysis by x-ray diffraction. For details of the analyses see Table I. Sintered alumina rods covered with platinum foil with a LVDT attachment were used for the dilatometric studies. The samples were heated at a constant rate of 200°C/hr from room temperature to 1300°C and cooled back at the same rate.

Isothermal studies were carried out by introducing the crucibles containing the PZT samples and the PbO source pellets into a muffle furnace maintained at specific temperatures (1000, 1100, 1200 and 1300°C) and quenching after a stipulated period of soak (1 min-12 hrs). Sintering studies were also done on all samples at constant rate of heating (200°C/hr) up to 1300°C.

Studies on reactive sintering were done on (PZT 60/40, PZT 401, PZT 501) compositions calcined to 840°C, the temperature at which the expansion maximum was noted. Dilatometric and isothermal studies (at 700, 800, 900, 1000 and 1150°C) were done with pellets as mentioned earlier. Dense pellets (>97% theoretical) were obtained by sintering at 1150°C for 1/2 hour. The physical, microstructural and electromechanical characteristics of these were compared with standard samples of PZT 60/40 obtained by sintering at 1300°C for half-hr; pellets made from completely calcined single phase PZT calcines.

S. VENKATARAMANI, J.V. BIGGERS

TABLE 1. PZT 60/40 calcines-characterization data.

Nomenclature	Calcining Conditions	Phase
MO UNC	Uncalcined	PbO ZrO ₂ TiO ₂
MO 600/3	600°C/3 hr	PbO PbTiO ₃ ZrO ₂ PbO _{ss} ^a
MO 700/3	700°C/3 hr	PbO PbO _{ss} PbTiO ₃ 'PZT' ^b ZrO ₂
MO CAL	800°C/6 hr	PZT

^aA tetragonal PbO solid solution containing PbTiO₃ phase.^bA PZT phase of varying Zr/Ti ratios.

Geometric densities of fired samples were obtained from weight and dimension measurements. Microstructural analysis was done on polished and fractured surfaces. The dielectric and electromechanical properties were obtained 24 hrs after poling which was accomplished by applying a 25-30 kV/cm DC field at ~120°C for 5 min across the silver electroded samples in an oil bath. The dielectric constant, k , and the loss factor, $\tan\delta$ were obtained using a Hewlett-Packard automatic capacitance bridge. The piezoelectric coefficient, d_{33} , was measured in a Berlincourt d_{33} meter. Resonance techniques described in IRE Standards (1961) were used to obtain the coupling coefficient, k_p , and the quality factor Q .

RESULTS AND CONCLUSIONS

Figure 1 is the dilatometric behavior of the compacts from the various calcines as a function of temperature. The two distinct regions of expansion in the uncalcined sample correspond to the two different stages of reaction as was seen from the x-ray analysis.

(i) The formation of PbTiO₃ around 450-600°C and (ii) the formation of PbO_{ss} containing some PbTiO₃ dissolved into a tetragonal PbO

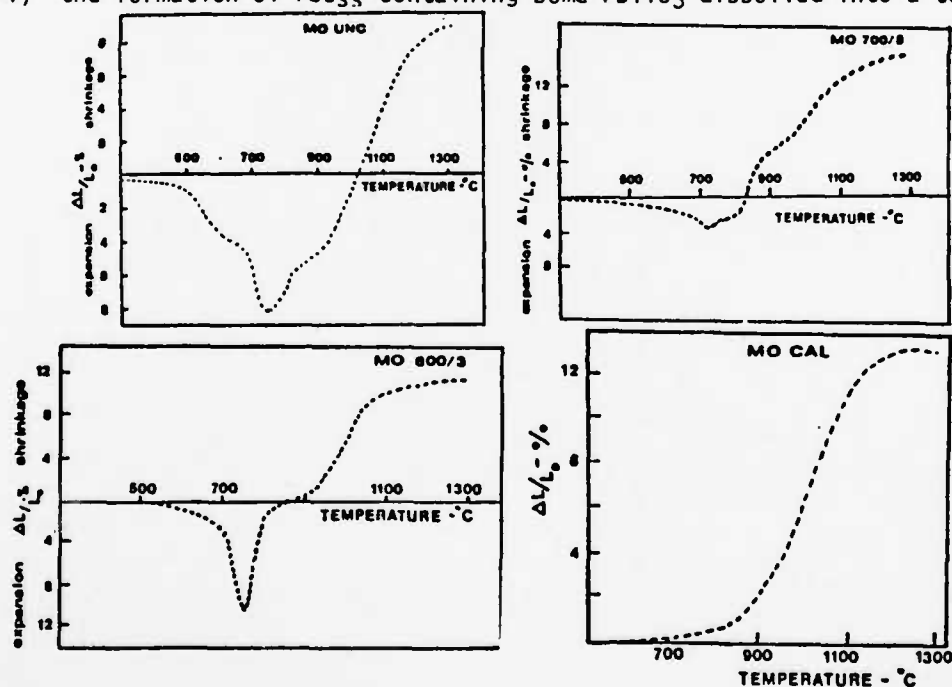


FIGURE 1. Dilatometric behavior of PZT during calcining.

DENSIFICATION IN PZT

and (PZT) compounds of varying Zr/Ti ratios. The final stages of the stoichiometric PZT formation is accompanied by a rapid shrinkage above 800°C up to 900°C above which densification starts to occur. The SEM micrographs of the fractured surfaces of compacts quenched at various temperatures during calcining also showed interesting changes in the microstructure as a function of temperature. Dense platey regions richer in PbO and TiO₂ were noted around 700-750°C from the selected area x-ray energy emission analyses of these regions. These are possibly the reaction products PbTiO₃ and PbO_{ss}. The absence of the specific expansion regions—region 1 around 600°C in MO 600/3 samples and region 1 and most of region 2 in MO 700/3 samples which had the corresponding phase distribution of these materials (Table 1) also prove the relationship between the expansions and the reaction sequences. The expansion is due to (i) the topological nature of the reactions—diffusion of PbO into TiO₂ particles and the formation of PbTiO₃ on the TiO₂ skeletal regions and (ii) the differences in the molar volumes of the product PbTiO₃ (38 ml) and TiO₂ (20.8 ml). Further reactions involving ZrO₂ also occur in a similar manner at the P/Z and P/T and P/PT/Z interfaces, causing expansion of the compact. The rapid shrinkage during the final stages of PZT formation is due to particle coarsening, higher product densities and phase transformations.

INHOMOGENEOUS DENSIFICATIONS

The results of the isothermal sintering at 1100°C studies on the pellets from the different calcines are shown in Figure 2. At all the sintering temperatures the uncalcined and partially calcined specimens initially expand as PZT formation occurred, resulting in a porous ceramic. On further heating, sintering occurs only within the ceramic regions leaving the large pores unclosed. The values slopes of the log-log plots of the density change vs time curves ($n \approx 0.3$) indicate that sintering occurs through a diffusion process. Higher temperature and/or periods of soak are required for the occurrence large scale of diffusion processes to close the pores. The green density vs fired density characteristics (Fig. 3) showing the linear dependence indicate the inhomogeneous densification phenomenon occurring in these samples. Similar observations have been made earlier⁶ and were attributed to the same phenomenon. The inhomogeneous densification is attributed to the volume changes during calcining and the chemical heterogeneities and reaction sintering in the ceramic regions of the expanded compacts.

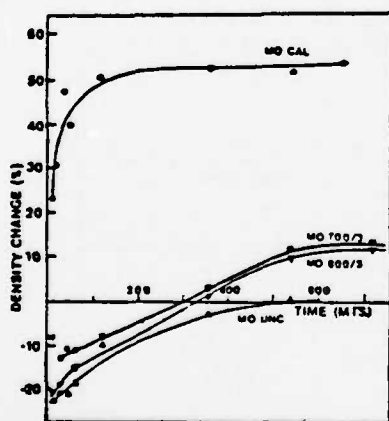


FIGURE 2. Isothermal sintering studies at 1100°C.

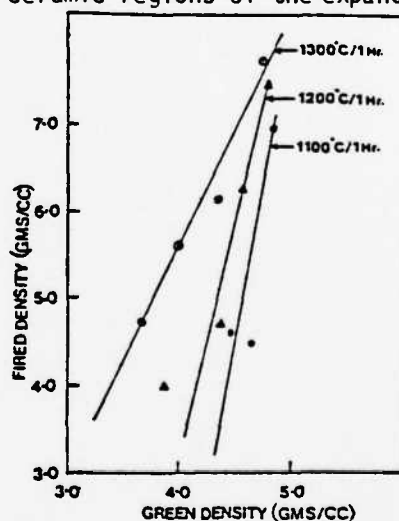


FIGURE 3. Green density vs fired density characteristics.

The percent density change and percent shrinkage as a function of sintering temperature is shown in Fig. 4. It is obvious that the reactive sintered sample undergoes enhanced densification up to $\sim 900^\circ\text{C}$ (15% change in density and 5% linear shrinkage). The x-ray analysis of quenched samples at intermediate temperatures showed the decrease of PbO, PT and ZrO₂ contents and an increase in the PZT content and sharpening of the PZT peaks. The lower value of the activation energy (68 kJ/mole) calculated from the slope of the log shrinkage vs $1000/T$ plots also indicates the enhanced densification. The near zero slope above 1150°C also confirms that densification is complete around that region. The microstructural analyses and isothermal sintering data showed no evidences of fine particle sintering such as rapid particle coarsening and densification within the initial few seconds. Hence, the enhanced densification is possibly in part due to the chemical reactions and phase transitions occurring at the final stages of PZT formation in the partially calcined starting material. Table 2 illustrates the properties of reactive sintered samples in comparison with corresponding standard samples of the same composition. The effect of the finer grain structure as evidenced from the micrographs were obvious in the values of the various electromechanical properties esp dielectric constant, d_{33} and k_p .

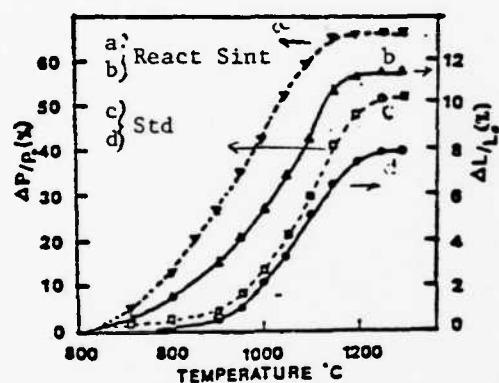


FIGURE 4. Dilatometric and density change characteristics

REFERENCES

1. Y. Matsuo, H. Sasaki, *J. Amer. Ceram. Soc.* 48, 289 (1965).
2. W.M. Speri, D. Eng. Thesis, Rutgers University (1969).
3. D.L. Hankey, Ph.D. Thesis, The Pennsylvania State University (1980).
4. D.A. Buckner, P.D. Wilcox, *Technical Report*, U.S. Atomic Energy Commission (1971).
5. A.H. Webster, T.8. Weston, V.M. McNamara, *J. Canad. Ceram. Soc.* 35, 61 (1966).
6. L.J. Bowen, T.R. Shrout, S. Venkataramani, J.V. Biggers, *Annual Report*, Office of Naval Research (1980).
7. K. Okazaki, *J. Ceram. Assoc. Japan* 13, 17 (1965).

TABLE 2. Reactive Sintering: Electromechanical Properties

Comp.	Calcining and Sintering Conditions	Density (g/cc)		K			Tan δ			d_{33} (pC/N)	k_p	Q
		Green	Fired	1kHz	10kHz	100kHz	1kHz	10kHz	100kHz			
PZT 60/40	CAL: 840 SINT: 1150/1/2	5.05	7.84	450	440	435	.04	.025	.021	100/125	0.35	240
PZT 60/40	CAL: 850/5 SINT: 1150/1/2	4.96	7.45	390	380	386	.008	.009	.010	130/130	0.41	330
401	CAL: 840 SINT: 1150/1/2	4.80	7.70	990	978	970	.015	.013	.013	140/235	0.41	220
401	CAL: 850/5 SINT: 1150/1/2	4.95	7.45	1060	1050	1112	.015	.008	.010	290/310	0.60	215
301	CAL: 840 SINT: 1150/1/2	4.94	6.73	897	896	913	.026	.023	.027	340/345	0.44	75
501	CAL: 850/5 SINT: 1150/1/2	4.83	7.30	1345	1315	1370	.028	.023	.036	340/345	0.59	85

AD-A132 136

TARGETED BASIC STUDIES OF FERROELECTRIC AND
FERROELASTIC MATERIALS FOR PI. (U) PENNSYLVANIA STATE
UNIV UNIVERSITY PARK MATERIALS RESEARCH LA..

4/4

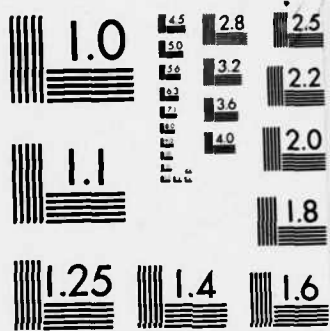
UNCLASSIFIED

L E CROSS ET AL. MAR 83 N00014-78-C-0291

F/G 9/1

NL





MICROCOPY RESOLUTION TEST CHART
NATIONAL BUREAU OF STANDARDS-1963-A

SECTION III

PRACTICAL INDUSTRIAL DEVELOPMENTS BASED ON CONTRACT WORK

1.0 PRACTICAL INDUSTRIAL DEVELOPMENTS BASED ON CONTRACT WORK

1.1 Introduction

Five of the topic areas which have evolved from basic studies under this contract have sparked significant industrial interest and activity towards developing new materials for specific system requirements. Because of the competitive nature of the electronic materials industry, specific company names will not be disclosed except where the activity has built up as a result of published information from our reports and is not directly coupled with this laboratory.

2.0 ELECTROSTRICTIVE CERAMICS

The need for robust ceramic actuators for IR surface deformable mirrors was one of the driving forces for our own work on multilayer ceramic electrostrictors. The evolution of the lead magnesium niobate:lead titanate family of relaxor ferroelectrics provides the large strain capability, low hysteresis, freedom from aging, low thermal expansion and dimensional stability which was required. In cooperation with industry, we have provided advice to build up a capability for tape casting PMN:PT materials in a suitable form for several types of actuator, and devised processing methods which permit reproducible fabrication of the perovskite structure material under industrial conditions.

It is probable that this material will find major use in a number of important IR:optical communication systems of high tactical importance. Prototype systems using PMN have already been constructed and perform to specification.

In parallel with the optical applications, several complementary high strain applications which could exploit the tape cast multilayers are under study for electrostrictive pumping of cryogenic gases, and for low voltage high drive level bimorphs.

3.0 COMPOSITE PIEZOELECTRICS

Several of the ideas for new types of composite structures which have been developed on contract funds are now under advanced development.

(a) In MRL, work is in progress to scale up the 3:1, 1:3 and 2:3 composites in the PZT:polymer materials to provide practical size sheets which can be available for routine evaluation. The exercise is difficult as the composites are of a type which would lend themselves to automatic manufacture, but are exceedingly tedious and time consuming to assemble manually. Development does, however, afford the opportunity to test a wider range of polymer components, and to develop new attacks upon the problem of robust flexible electrodes to retain contact to these highly flexible web structures.

(b) Composites of PZT and polymers are in extensive development in Japan. Following MRL work, Mitsubishi Mining and Cement Company have been developing an interesting fine scale porous PZT with excellent 3:3 connectivity. NGK Spark Plug Division have been using the connectivity concepts developed on this program to explain the performance, and improve the design of their 0:3 ceramic:plastic composites and their recent PbTiO_3 based materials are certainly competitive with PVDF for many applications.

(c) Recently we have been solicited by a major polymer company to undertake joint development of 0:3 and 1:3 composites. This new University:Industry coupled program has just started up and promises to spur development of the composites in the USA to keep better pace with efforts in Japan.

(d) In a cooperative program with Honeywell Corporation sponsored by ONR, the laboratory has been transferring technology for the tape casting and fabrication of PZT multilayers for multimorph structures. The program envisages currently using noble metal integrated electrodes, but will be involved also with the development of materials and processing techniques compatible with high silver and with base metal electrode systems.

(e) Higher frequency application of the 1:3 ceramic:polymer composites are now being jointly explored with industry. The mode structure modification which can be effected by suitable choice of element spacing have been evaluated and with improved fabrication it appears that the composites may have considerable promise in electromedical acoustic applications.

4.0 PIEZOELECTRIC GLASS CERAMICS

The development of techniques for fabricating oriented polar glass ceramics using an active phase which is not ferroelectric opens up the possibility for making a new generation of low permittivity piezoelectric ceramics. Applications for these materials in surface acoustic wave filters and in bimorph structures are now being formulated with a major US electronics company. Initial emphasis will be upon scale up of the fabrication process using a number of innovative new methods to form the glass films and to process the oriented crystal microstructure.

5.0 NEW FERROELECTRIC CRYSTALS FOR ELECTRO-OPTICS

Our basic studies in the $\text{Pb}_{1-x}\text{Ba}_x\text{Nb}_2\text{O}_6$ family of tungsten bronze structure crystals have been focused upon compositions close to the orthorhombic: tetragonal morphotropic phase boundary near the $\text{Pb}_{0.6}\text{Ba}_{0.4}\text{Nb}_2\text{O}_6$ composition. The objective being to develop the full thermodynamic phenomenology for the bronze, then to be able to test out the fit with experiments in a system where because of the single crystal character the full tensor forms of ϵ_{ij} , d_{ijk} , Q_{ijkl} , etc. can be explored and the more sophisticated optical methods used to distinguish domain and phase boundary motion under field or stress.

It appears, however, that just as in the PZT family, morphotropy leads to exceptional values of the shear coefficients d_{15} , r_{41} , etc. As in many tungsten bronze family crystals, it appears that $\text{Pb}_{1-x}\text{Ba}_x\text{Nb}_2\text{O}_6$ may have temperature compensated acoustic properties. A joint program to explore these materials and their device applications in electro-optic four wave mixing, electro-optic modulation and acousto-optic applications is now under way with a major US Industrial Research Laboratory.

In general, it has been interesting and exciting for the participants in this ONR sponsored program to observe a strong resurgence of interest in the USA in piezoelectric materials, and an increasing demand for new materials with properties more directly tailored to specific device requirements. We believe that in part, we have helped to spark some of this resurgence. It has been a salutary experience to participate in a small way in some of the development efforts and to realize some of the challenges and frustrations of moving from a well documented carefully tested research proven idea towards a implementation of that idea into a working practical transducer ensemble.

6.0 PATENTS

A further indication of the practical impact of the work may be gauged from the ten invention disclosures which have been submitted. The status of patents on these disclosures is summarized in Table 6.1.

Table 6.1. Navy Patent Position

Navy Case No.	Inventor	Subject	Disposition
63,430	Cross, L.E. Newnham, R.E. Skinner, P.	Flexible Piezoelectric Composite Transducer	U.S. Patent NJ 4,227,111
64,667	Schulze, W.A. Biggers, J.V.	Lead Germanate Bonded PZT Composite Piezoelectrics	Filed 6/2/80 Amendment "A" 6/19/81
64,470	Bowen Schulze Biggers	A Hot Isostatic Pressure Process for Powder	1/31/80
64,996	Schulze, W.A. Biggers, J.V. Bowen, L.J.	Internally Electroded Ceramic Piezoelectric Transformer	Filed - 4/16/81
64,407	Cross, L.E. Uchino, K.	A New Type of Ultra-Sensitive AC Capacitance Dilatometer	Placed in pend. status 1/18/80 Published in Nov.
65,051	Shrout, T.R. Schulze, W.A. Biggers, J.V.	Simplified Fabrication of PZT/Polymer Composites	Authorized w/o search 8/7/80 - Filed 11/12/80 Amendment "A" 8/28/81
65,121	Klicker, K.A. Newnham, R.E. Cross, L.E. Biggers, J.V.	3-1 Phase Connected PZT-Polymer Composites for Transducer Application	Filed 4/26/81
65,463	Gururaja, T.R. Cross, L.E. Newnham, R.E. Bowen, L.J.	Continuous Poling Technique for Piezoelectric Fibers	Authorized -
65,464	Uchino, K. Jang, S.J. Cross, L.E. Newnham, R.E.	Pressure Gauge Using Relaxor Ferroelectrics	Placed in Pend. status - 8/11/81
65,465	Klicker, K.A. Newnham, R.E. Cross, L.E. Bowen, L.J.	Broadband Bandwidth Composite Transducer For Resonance Applications	Evaluated 8/81

SECTION IV-A

TOPICS AND OPPORTUNITIES FOR FUTURE STUDY

1.0 TOPICS AND OPPORTUNITIES FOR FUTURE STUDY

1.1 Introduction

In this section, a number of new opportunities and new areas of study which have been uncovered by work on the current contract will be discussed. From our studies in the composites, an opportunity which clearly must be explored is the possibility of using a ferroic component to add completely new sound damping possibilities. In electrostriction, there is still urgent need for a more complete microscopic theory and a vital requirement for reliable values of electrostrictive parameters in simple crystals. For practical application, the relaxor materials are prime candidates and combinations of relaxors could provide wider temperature ranges of operation. Studies on the present contract point up some new avenues for more detailed understanding of present PZT materials, both theoretical and experimental. The demands for finer scale and exotic shapes in the composites will drive new needs in preparative studies and the urgent need to intercalate electrodes into larger monolithics must require a new focus upon low firing or alternative processing to give compatibility with inexpensive electrode materials. Grain orientation promises an avenue for the exploitation of lower symmetry ferroelectrics and there is need to expand the family of techniques for realizing these fascinating intermediates between single crystals and ceramics. For practical purposes, electrodes are an ever present problem - the need to make reliable low impedance contact to large areas of flexible composites must challenge our present capability and drive new needs. Each of these areas will be briefly discussed in the following sections.

2.0 COMPOSITES STRUCTURES

2.1 Creative Techniques for Scale Reduction

In the 1:3, 1:2:3, 3:1 and 3:2 composites, it has been possible to explore many of the bounds of low frequency operation using scaling which has permitted simple processing and manual assembly of the composite components. For the fiber type structures, it is evident that with reduction in scale the brittle ferroelectric component becomes elastically more tolerant, and the ferroelastic twinning begins to impart a plasticity so that fine fibers can even be shaped in the fingers. Extension to still finer scale may then permit the use of textile techniques like 3-dimensional weaving - already in wide use with carbon fibers, to provide automatic assembly of larger structures. It may be interesting to explore new finer scale extrusion and fiber crystal growth to provide the fiber base for 1:3 and 1:2:3 transverse reinforced composites.

2.2 Alternative Polymer Components

Present studies have focused upon just two families of polymers, namely epoxies and polyurethanes with relatively little attention to bonding, elastic properties, etc. Recent studies have shown that much improved properties can be realized by improving polymer:ceramic bonding and there is real need to extend studies to a more complete series of polymers and polymer alloys.

2.3 Active Matching Layers

The ability which the composite structures afford for the exact control of density and acoustic impedance suggest that as well as the range of "stand alone" transducer applications which have been considered heretofore, it may be most interesting to explore the possibility of using the PZT:polymer composite as an active acoustic matching layer on more conventional ceramic transducers.

2.4 Ferroic Composite Sound Absorbers

It would appear that sound absorbing materials in present use rely primarily upon friction or internal friction losses to convert sound into heat. In the ceramic:plastic composites, some new ways of effecting conversion suggest themselves. For systems involving a ferromagnet, it is well known that moving a magnet through a conductor generates a current. If the conductor is short circuited, the current generates heat, and the high school experiment of short circuiting a ballistic galvanometer, suggests that such heat generation can give rise to strong damping of the mechanical motion. In some ferroelectrics, the piezoelectric coupling K_{33} exceeds 0.8 giving efficient conversion of mechanical to electrical energy - again if the charge generated is short circuit through a good conductor strong damping can be reflected back into the crystal. Finally, in some ferroelastics the coercive stress for wall motion is exceedingly small. Since the wall motion is hysteretic, energy is lost on each stress cycle equivalent to the area of the stress:strain loop. It would be most interesting to explore the efficiency of these potential sound damping mechanisms.

2.5 Model Studies

In the work to date upon composite structures, only the simplest two-dimensional models have been used to give insight into the behavior. It would be most valuable to refine these theoretical guidelines by a more detailed analysis of the stress:strain, polarization and field for the true three-dimensional problem. Using finite element methods, the techniques are available for the study of such problems, both under static and dynamical conditions for the most general case of viscoelastic solids.

3.0 ELECTROSTRICTION

3.1 Microscopic Theory

An achievement of the current program has been the development of a realistic microscopic theory for the room temperature electrostriction in SrTiO_3 . A problem which must be tackled is the temperature dependence of electrostriction, which in the oxide perovskites requires as a prerequisite a quantitative description of the mode softening. With the evolution of the soliton description of the ferroelastic domain wall, an interesting topic for study would be the ferroelastic contribution to piezoelectricity in the perovskite crystals and ceramics.

3.2 Basic Experiments in Electrostriction

The challenge of measuring the true electrostriction in simple solids becomes more intriguing with the evidence of extrinsic frequency dependence, and of the sign contradiction in the first measurements by converse methods. It will be necessary to mount several alternative strategies so as to permit direct measurement by at least two independent dilatometric techniques covering as wide a frequency range as possible, and by careful evaluation of the converse method. One is tempted to wonder whether the charged dislocations in the alkali halides may not be playing a role, and whether the electrostriction measurement may not be a good technique for obtaining new information in this field.

3.3 Practical Electrostrictors

Clearly the new relaxor ferroelectric materials which have been developed for capacitor dielectrics and are compatible with high silver electrodes are a prime topic for future study. The many families of lead based perovskites with complex composition and relaxor character offer interesting possibilities for new low temperature and wider temperature range electrostrictors for micro-positioner and for direct stress measurement.

The outlines of a fresh phenomenological theoretical approach to electrostrictive deformation in antiferroelectrics has been given. It will be most interesting to develop this theory for the full three-dimensional description of the deformations at antiferroelectric:ferroelectric phase transitions, with the strong possibility that these systems may provide the next generation of very high strain electrostrictors.

An experimental challenge which should be taken up is the assessment of the temperature dependence of electrostriction for a wide range of perovskite and of tungsten bronze structure ferroelectrics.

4.0 CONVENTIONAL PIEZOELECTRIC CERAMICS

4.1 Theoretical Description

It will be of major importance for making an effective separation between intrinsic and extrinsic contributions to the elasto-dielectric response in PZT family ceramics to continue to update and improve the thermodynamic phenomenological description of the single domain properties.

Problems which are tractable and could be handled include:

- (a) The role of the relaxor character in PZTs, at compositions near morphotropy in modifying the effective Curie constant C .
- (b) Extension of the theory to include the oxygen octahedron 'crumpling' in the rhombohedral single cell:multicell transitions.
- (c) Development of a two sub-lattice model for the polarization so as to include the description of the antiferroelectric phase compositions near PbZrO_3 .
- (d) The addition of a third dimension in the phase diagram so as to model the interesting PLZT family of phases.

4.2 New Experimental Studies

Recent measurements by Kawabata in Japan suggest that the X-ray line profile in the high temperature cubic phase above T_c may be a sensitive indicator of homogeneity of the Zr:Ti ratio in PZTs.

Two questions now could be answered:

- (a) Can the homogeneity (or otherwise) of the Zr:Ti ratio be used as a "quality indicator" in commercial PZTs.
- (b) Do homogeneous unpoled PZTs show relaxor behavior.

It would appear that at present we have rather good explanations for the mechanisms by which PZTs can be hardened (the coercivity increased and biased) but no good explanation of why donor doped PZTs are soft.

A basic question is why the ferroelastic:ferroelectric domain structure can be so readily modified at low fields while the pure ferroelectric walls are apparently still immobile.

Do the defects due to donor doping order in planar arrays and break up the strong forward coupling? Are relaxor doped PZTs softened in the same manner? Is there short range ordering of Zr:Ti at compositions close to morphotropy? Do all PZTs of the same Zr:Ti ratio freeze out to the same intrinsic electrical and electro-elastic parameters at 4°K.

In spite of their longevity, these and many other questions are still unresolved for the PZT family and clearly require additional experimental study.

5.0 PREPARATIVE STUDIES

5.1 Organic Methods

Additional work on the newer organic methods to prepare PZTs with minimum microstrain above T_c will be most desirable. Extension of these methods to prepare PbTiO_3 and some of the doped PbTiO_3 compositions currently under study in Japan would also be highly desirable.

5.2 Fast Firing Techniques

With the detailed understanding of the calcining reactions in the PbTiO_3 : PbZrO_3 system, and the ability to form a range of metastable phase assemblages by adjustment of the calcining process, it will be interesting now to explore in more detail the later densification stages.

The high microwave losses in PZTs suggest that microwave heating may be an interesting mode for rapid firing, and that internal temperature gradients might be effectively balanced out by combining microwave and radiant heating.

5.3 New PbTiO_3 Based Compositions

The new Ca and Sm doped PbTiO_3 are obviously interesting materials for their remarkably high anisotropy d_{33}/d_{31} . Studies to elucidate the mechanism and improve the performance will require new preparative work in these high PbTiO_3 families.

5.4 Low Firing Relaxor Combinations

The importance of developing new relaxor ferroelectrics compatible with silver or high silver palladium electrodes has already been stressed. Further exploration of $\text{Pb}_5\text{Ge}_3\text{O}_{11}$ and other flux systems to reduce the firing temperature would obviously be of major interest.

5.5 Grain Orientation Methods

Clearly grain orientation offers perhaps the only way of expanding piezoceramics with high coupling beyond the present range of perovskite based compositions.

A major task must be to explore doping schemes in the tungsten bronze and bismuth oxide layer structure families which will reduce conductivity, raise breakdown strength and permit effective poling of these high T_c materials.

6.0 FLEXIBLE ELECTRODES

6.1 Contact to Composite Structures

The high flexibility and large thickness of many of the more interesting composite materials places unusual requirements onto the electrode structure. Most flexible electrodes use polymers which are non-conducting, loaded with carbon, metal particles or semi-conducting grains. The loading must be beyond the critical percolation threshold, but the resulting conductivity depends in a complex manner upon shape, size and shape and size distributions in the conductive phase, upon the bonding to the polymer, etc.

No system that we have so far been able to obtain commercially is completely suitable and clearly additional work is needed to improve the conductivity, the bonding and the flexibility of the systems.

6.2 Electrode:Dielectric Interface

Particularly for high permittivity dielectrics such as the electrostrictive relaxors, the interface between electrode and dielectrics can be a major source of problems. Low impedance surface layers due to polishing or other surface treatments, improper bonding, intervening second phases and similar problems can reduce efficiency markedly.

For internal electrodes, the formation of second phases by interaction with the electrode, delamination, etc. are of major importance.

In view of the many systems which now depend on the efficacy and integrity of both external and internal electrodes, a comprehensive attack on the contact problem is long overdue.

SECTION IV-B

RELEVANCE OF THE WORK TO OTHER AREAS OF ELECTROCERAMICS

1.0 RELEVANCE OF THE WORK TO OTHER AREAS OF ELECTROCERAMICS

1.1 Introduction

Many of the topics which have been the focus of major interest on this contract from the point of view of their relevance to piezoelectric transducer application are also strongly relevant to other areas of both theoretical and practical interest in electronic ceramics. It is the purpose of this short section to outline some of these interesting interconnections and the manner in which they may also assist the 'design' of new materials for other purposes.

2.0 ELECTROSTRICTION

The most pressing reason for our interest in electrostriction is that it is the basic coupling mechanism between dielectric and elastic properties in all ferroelectric systems derived from centric prototypes, like for example the piezoelectric ceramics.

Indirectly, however, one could list a host of ancillary areas in which this basic coupling plays a major role in determining properties which at first sight one might believe to be unrelated. Listing just some of the more important

(1) Grain Size and Internal Stress Effects in Ferroelectric Ceramics

Since lattice strain in an electrostrictor is $x_{ij} = Q_{ijkl} P_k P_l$, spontaneously polarized states are spontaneously deformed. In a randomly axed ceramic sintered in the cubic state, spontaneous strains are mutually incompatible leading to complex twinning and internal stress.

Consequences of these effects are:

- (a) Grain size dependence of the weak field permittivity in BaTiO_3 ceramics.
- (b) Changes in the fracture behavior with temperature and grain size.
- (c) Spontaneous rupture and grain 'pop out' in very coarse grained PTC and barrier layer ceramic capacitors.
- (d) Some of the aging phenomena in dielectric and piezoelectric ceramics.

(2) Domain Stabilization Effects

It is most interesting to observe that in the perovskite family of ferroelectrics all known relaxor compositions have rhombohedral symmetry in the poled 'induced' ferroelectric state.

Since the magnitude of spontaneous strain is dictated by Q_{44} in the rhombohedral symmetry and $Q_{44} < 1/5 Q_{11}$ or Q_{12} it is clear that the stabilization effects leading to first order change in cubic:tetragonal transitions is much reduced for cubic:rhombohedral changes, i.e., it is much easier for large local polar fluctuations to occur.

It may be noted that in tetragonal tungsten bronze structures Q_{33} and Q_{31} are almost an order smaller than in perovskites and in this family relaxor behavior is almost the rule rather than the exception.

(3) Polarization Biased Electrostriction

In multilayer ceramic capacitors, the thin dielectric gives rise to large E fields at low bias levels, thus electrostriction can induce large piezoelectric effects in capacitors under bias. Such unwanted coupling to mechanical behavior could;

- (a) Generate noise from mechanical vibration.
- (b) Propagate cracks in the dielectric under local bias.
- (c) Modify defect distribution under cyclic AC fields.

3.0 COMPOSITE STRUCTURES

The models of phase interconnection, i.e., connectivity give a new insight which may be applied to many problems involving composite materials. Examples which may be cited include;

- (a) Enhanced secondary pyroelectricity in suitably interconnected composites.
- (b) Tailoring materials to exhibit special acoustic or electromagnetic absorption characteristics, as for example in the Marks fluids.
- (c) Modification of magnetoelectric response in composites from non-magnetoelectric separate phases.

4.0 RELAXOR FERROELECTRICS

Application of the empirical rule of constancy of the Curie constant $C \times$ electrostriction constant Q (CQ rule) to perovskite lead to the focus upon relaxor ferroelectrics with large C but small Q for electrostrictive applications since

$$x = QP^2 \approx Q \epsilon^2 E^2$$

thus if CQ (ϵQ) is constant in most materials since ϵ occurs to second power in the strain, it is better to choose crystals with low polarization strain coupling as electrostrictors SINCE MUCH HIGHER POLARIZATIONS CAN BE INDUCED.

Clearly if high polarization can be induced at low fields, relaxors are also prime candidates for capacitor dielectrics. Coupling the fact that these Pb containing compounds can be fired to high density at low temperature and are comparable with silver electrodes, dielectric application appears most likely and is indeed active in Japan and China.

Theoretically, a more detailed understanding of the polarization mechanisms which give rise to relative permittivity values up to 35,000 and Curie constants $\sim 6 \cdot 10^5$ would be highly desirable, as if the mechanism could be understood, fine tuning might be possible to give even more useful dielectric parameters.

5.0 PHENOMENOLOGICAL THEORY

For many ferroelectrics of high practical interest, the microscopic theories to deal in the required detail with the higher order anharmonic properties are not sufficiently developed to be of major practical value in fine tuning parameters for particular application. Phenomenological theories of the Landau:Ginsburg:Devonshire form provide an elegant framework for the description of the single domain intrinsic elasto-dielectric properties from equations whose coefficients often mutate only slowly with composition across wide ranges of solid solution.

Systematic application to the ceramic piezoelectric and dielectric systems can;

- (a) Assist in the separation of intrinsic single domain parameters from extrinsic domain, defect and phase boundary dominated properties.

- (b) Provide insight into the parameter changes which can be achieved by fine tuning compositions close to morphotropic phase boundaries.

- (c) Give basic relations from which to deduce potential piezoelectric, elastic and electro-optic parameters.

The method provides at least a basis for the organization and systematization of the rapidly developing data base for dielectric, piezoelectric and electro-optic solid solution compositions.

6.0 PREPARATION AND CRYSTAL GROWTH

The strong programs in powder preparation, classification, formulation, tape casting, extrusion, calcining, sintering, uniaxial and isostatic hot pressing and other ceramic preparative techniques provided the springboard from which to develop programs covering a wide range of electronic ceramic requirements, and in particular to respond to the needs of the ceramic capacitor industry in the formulation of programs for a National Dielectrics Center.

Single crystal growth is an essential complementary skill required for the development of samples which permit the full panoply of elastic, dielectric, optical and structural evaluation tools to be used to unravel the complex property tensors in the lower symmetry ferroelectric and ferroelastic:ferroelectric species. Both crystal pulling from the melt, and flux growth are essential for the range of oxide and non-oxide ceramics which are of high practical interest for electronic applications.

BASIC DISTRIBUTION LIST

Technical and Summary Reports

November 1979

<u>Organization</u>	<u>Copies</u>	<u>Organization</u>	<u>Copies</u>
Defense Documentation Center Cameron Station Alexandria, VA 22314	12	Naval Air Propulsion Test Center Trenton, NJ 08628 ATTN: Library	1
Office of Naval Research Department of the Navy 800 M. Quincy Street Arlington, VA 22217 ATTN: Code 471 Code 470	1 1	Naval Construction Battalion Civil Engineering Laboratory Port Hueneme, CA 93043 ATTN: Materials Division	1
Commanding Officer Office of Naval Research Branch Office Building 114, Section D 666 Summer Street Boston, MA 02210	1	Naval Electronics Laboratory. San Diego, CA 92152 ATTN: Electron Materials Sciences Division	1
Commanding Officer Office of Naval Research Branch Office 536 South Clark Street Chicago, IL 60605	1	Naval Missile Center Materials Consultant Code 3312-1 Point Mugu, CA 92041	1
Office of Naval Research San Francisco Area Office One Hallidie Plaza Suite 601 San Francisco, CA 94102	1	Commanding Officer Naval Surface Weapons Center White Oak Laboratory Silver Spring, MD 20910 ATTN: Library	1
Naval Research Laboratory Washington, DC 20375 ATTN: Codes 6000 6100 6300 2627	1 1 1 1	Commander David W. Taylor Naval Ship Research and Development Center Bethesda, MD 20084	1
Naval Air Development Center Code 606 Warminster, PA 18974 ATTN: Mr. F. S. Williams	1	Naval Oceans Systems Center San Diego, CA 92132 ATTN: Library	1
		Naval Underwater System Center Newport, RI 02840 ATTN: Library	1
		Naval Postgraduate School Monterey, CA 93940 ATTN: Mechanical Engineering Department	1
		Naval Weapons Center China Lake, CA 93555 ATTN: Library	1

BASIC DISTRIBUTION LIST (cont'd)

<u>Organization</u>	<u>Copies</u>	<u>Organization</u>	<u>Copies</u>
Naval Air Systems Command Washington, DC 20360 ATTN: Codes 52031 52032	1 1	NASA Lewis Research Center 21000 Brookpark Road Cleveland, OH 44135 ATTN: Library	1
Naval Sea System Command Washington, DC 20362 ATTN: Code 05R	1	National Bureau of Standards Washington, DC 20234 ATTN: Metals Science and Standards Division	1
Naval Facilities Engineering Command Alexandria, VA 22331 ATTN: Code 03	1	Ceramics Glass and Solid State Science Division Fracture and Deformation Division	1 1
Scientific Advisor Commandant of the Marine Corps Washington, DC 20380 ATTN: Code AX	1	Director Applied Physics Laboratory University of Washington 1013 Northeast Fortieth Street Seattle, WA 98105	1
Army Research Office P. O. Box 12211 Triangle Park, NC 27709 ATTN: Metallurgy & Ceramics Program	1	Defense Metals and Ceramics Information Center Battelle Memorial Institute 505 King Avenue Columbus, OH 43201	1
Army Materials and Mechanics Research Center Watertown, MA 02172 ATTN: Research Programs Office		Metals and Ceramics Division Oak Ridge National Laboratory P. O. Box X Oak Ridge, TN 37380	1
Air Force Office of Scientific Research/NE Building 410 Bolling Air Force Base Washington, DC 20332 ATTN: Chemical Science Directorate Electronics & Materials Sciences Directorate	1 1	Los Alamos Scientific Laboratory P. O. Box 1663 Los Alamos, NM 87544 ATTN: Report Librarian	1
Air Force Materials Laboratory Wright-Patterson AFB Dayton, OH 45433	1	Argonne National Laboratory Metallurgy Division P. O. Box 229 Lemont, IL 60439	1
Library Building 50, Room 134 Lawrence Radiation Laboratory Berkeley, CA	1	Brookhaven National Laboratory Technical Information Division Upton, Long Island New York 11973 ATTN: Research Library	1
NASA Headquarters Washington, DC 20546 ATTN: Code RRM	1	Office of Naval Research Branch Office 1030 East Green Street Pasadena, CA 91106	1

SUPPLEMENTARY DISTRIBUTION LIST A
Electronic, Magnetic, and Optical Ceramics

032
June 1981

Advanced Research Projects Agency
Materials Science Director
1400 Wilson Boulevard
Arlington, VA 22209

Dr. Don Berlincourt
Channel Products
16722 Park Circle Drive W.
Chagrin Falls, OH 44022

Dr. J. V. Biggers
Pennsylvania State University
Materials Research Laboratory
University Park, PA 16802

Mr. George Boyer
Sensor Systems Program
Office of Naval Research
Code 222
Arlington, VA 22217

Professor R. Bradt
Ceramics Section
Materials Sciences Department
The Pennsylvania State University
University Park, PA 16802

Dr. Dean Buckner
Piezo Products Division
Gulton Industries
P. O. Box 4300
Fullerton, CA 92634

Dr. Robert Callahan
Channel Industries
339 Ward Drive
Box 3680
Santa Barbara, CA 93105

Professor L. E. Cross
The Pennsylvania State University
Materials Research Laboratory
University Park, PA 16802

Mr. N. Coda
Vice President for Engineering
Erie Technological Products
West College Avenue
State College, PA 16802

Dr. Gene Haertling
Motorola Corporation
3434 Vassar, NE
Albuquerque, NM 87107

Dr. W. B. Harrison
Honeywell Ceramics Center
1885 Douglas Drive
Golden Valley, MN 55422

Dr. C. M. Stickley, V. P.
The BDM Corporation
7915 Jones Branch Drive
McLean, VA 22102

Dr. L. L. Hench
Department of Metallurgy
University of Florida
Gainesville, FL 32603

Dr. B. F. Rider
Rockwell International
400 Collins Road NE
Cedar Rapids, IA 52406

Dr. F. Robert Hill
Marine Resources
755 Highway 17 & 92
Fern Park, FL 32730

Dr. Bernard Jaffe
232 Forbes Road
Bedford, OH 44146

Dr. B. G. Koepke
Honeywell, Inc.
Corporate Research Center
10701 Lyndale Avenue South
Bloomington, MN 55420

Dr. R. Lapetina
Edo Western Corporation
2645 South 300 West
Salt Lake City, UT 84115

Mr. C. LeBlanc
Naval Underwater Systems Center
TD 121
Newport, RI 02840

Dr. N. Perrone
Code 474
Office of Naval Research
800 N. Quincy Street
Arlington, VA 22217

Dr. Frank Recny
General Electric Company
Court Street
Plant Building C
Box 1122
Syracuse, NY 13201

Dr. J. H. Rosolowski
General Electric Company
Research and Development Center
P. O. Box 8
Schenectady, NY 02301

Dr. P. L. Smith
Naval Research Laboratory
Code 6361
Washington, DC 20375

Dr. R. W. Timme
Naval Research Laboratory
Code 8275
Underwater Sound Reference Division
P. O. Box 8337
Orlando, FL 32806

Dr. Charles C. Walker
Naval Sea Systems Command
National Center #3
2531 Jefferson Davis Highway
Arlington, VA 20390

Dr. Paul D. Wilcox
Sandia Laboratories
Division 2521
Albuquerque, NM 87115

The State University of New York
at Alfred
Material Sciences Division
Alfred, NY

Dr. R. Rice
Naval Research Laboratory
Code 6360
Washington, DC 20375

Professor R. Roy
The Pennsylvania State University
Materials Research Laboratory
University Park, PA 16802

Dr. N. Tallan
AFML Wright-Patterson AFB
Dayton, OH 45433

Dr. H. E. Bennett
Naval Weapons Center
Code 3818
China Lake, CA 93555

Dr. Michael Bell
Inorganic Materials Division
National Bureau of Standards
Washington, DC 20234

Dr. R. Bratton
Westinghouse Research Laboratory
Pittsburgh, PA 15235

Dr. Joe Dougherty, Dir. Engr.
Gulton Industries
212 Durham Avenue
Metuchen, NJ 08840

Dr. James Pappis
Raytheon Co., Research Division
28 Seyon Street
Waltham, MA 02154

Dr. Perry A. Miles
Raytheon Co., Research Division
28 Seyon Street
Waltham, MA 02154

Dr. P. E. D. Morgan
Rockwell Science Center
1049 Camino Dos Rios
P. O. Box 1085
Thousand Oaks, CA 91360

Dr. G. Ewell
MS6-D163
Hughes Aircraft Company
Centinela & Teale Streets
Culver City, CA 90230

Dr. David C. Hill
Member Technical Staff
Texas Instruments, Inc.
Attleboro, MA 02703

Dr. S. K. Kurtz, V. P.
Clairol, Inc.
2 Blachley Road
Stamford, CT 06902

Dr. Herb Moss
RCA Laboratories
Princeton, NJ 08540

Dr. R. E. Newnham
Materials Research Laboratory
The Pennsylvania State University
University Park, PA 16802

Dr. Charles S. Sahagian, Chief
EM Technology Branch, SSS Division
HQ Rome Air Dev. Center (AFSC)
Deputy for Electronic Technology
Hanscom AFB, MA 01731

Dr. J. Smith
GTE Sylvania
100 Endicott Street
Danvers, MA 01923

Dr. Wallace A. Smith
North American Philips Laboratories
345 Scarborough Road
Briarcliff Manor, NY 10510

Mr. Raymond E. Sparks
Technology Library R220
Delco Electronics Division/GMC
P. O. Box 1104
Kokomo, IN 46901

Dr. Manfred Kahn
Senior Scientist, Prod. Dev.
AVX Ceramics, P. O. Box 367
Myrtle Beach, SC 29577

Mr. G. Goodman, Manager
Corporation of Applied Research Group
Globe-Union Inc.
5757 North Green Bay Avenue
Milwaukee, WI 53201

Dr. George W. Taylor
Princeton Resources, Inc.
P. O. Box 211
Princeton, NJ 08540

Mr. John J. Thiermann
Physics International
2700 Merced Street
San Leandro, CA 94577

Dr. D. Carson
Code 7122
Naval Ocean Systems Center
San Diego, CA 92152

Dr. C. Hicks
Code 631
Naval Ocean Systems Center
San Diego, CA 92152

Dr. R. Smith
Code 7122
Naval Ocean Systems Center
San Diego, CA 92152

Professor R. Buchanan
Department of Ceramic Engineering
University of Illinois
Urbana, Illinois 61801

Professor B. A. Auld
Stanford University
W. W. Hansen Laboratories of Physics
Stanford, CA 94306

Dr. S. Musikant
General Electric Co.
3188 Chestnut Street
Philadelphia, PA 19101

Dr. A. Gentile
Hughes Research Laboratories
3011 Malibu Canyon Road
Malibu, CA 90265

Dr. J. Harrington
Hughes Research Laboratories
3011 Malibu Canyon Road
Malibu, CA 90265

Professor G. Kino
Stanford University
Stanford, CA 94305

Dr. A. E. Clark
Naval Surface Weapons Center
White Oak Laboratory
Silver Spring, MD 20910

Dr. Gordon Martin
2627 Dungeness
San Diego CA 92110

Eric Udd
McDonnell Douglas Astronautics
5301 Bolsa Ave
Huntington Beach CA 92647

Deborah Graves
Ceramic Engineer
Endevco
Rancho Vie Jo Road
San Juan Capistrano, CA 92675

Director
Applied Research Lab
The Pennsylvania State Univ.
University Park, PA 16802

Army Research Office
Box CM, Duke Station
Attn: Met. & Ceram. Div.
Durham, NC 27706

National Bur. Standards
Inorganic Mats. Division
Washington DC 20234

National Bur. Standards
Metallurgy Division
Washington DC 20234

Naval Air Systems Comm.
Code 320
Washington DC 20360

Pacific Missile Test Center
Materials Consultant
Code 4121
Pt. Mugu, CA 93042

Naval Research Lab
Code 6400
Washington DC 20390

Naval Sea System Command
Code 035
Washington DC 20362

Naval Ship Engr. Center
Code 6101, CTR BG #2
3700 East-West Highway
Prince Georges Plaza
Hyattsville, MD 20782

Office of Naval Research
Department of the Navy
Code 102
Arlington, VA 22217

Dr. G. Bansal
Battelle Laboratories
505 King Avenue
Columbus, OH 43201

Dr. George Benthien
Naval Ocean Systems Center
Code 212
San Diego, CA 92152

Mr. N. Coda, VP Engr.
Erie Technol. Products
Res. and Dev.
Erie, PA 16512

Dr. G. Denman, Code LPJ
AFML, Wright-Patterson AFB
Dayton, OH 45433

Sheldon Detwiler, Disp. Mgr.
Adv. Technol. Laboratories
13208 Northrup Way, PO Box 6639
Bellevue, WA 98007

Dr. W.G.D. Frederick
AFML, Wright-Patterson AFB
Dayton, OH 45433

Dr. P. Giellisse
University of Rhode Island
Kingston, RI 02881

Mr. G. Hayes
Naval Weapons Center
China Lake, CA 93555

Dr. R.N. Katz
Army Materials and Mechanics
Research Center
Watertown, MA 02171

Dr. P.L. Lall
Office of Naval Research
666 Summer Street
Boston, MA 02210

Dr. P. Land
AFML, Wright-Patterson AFB
Dayton, OH 45433

Dr. F.F. Lange
Rockwell International
PO Box 1085
1049 Camino Dos Rios
Thousand Oaks, CA 91360

Dr. Eugene A. Larson, Pres.
Blue River Laboratories
PO Box 442
Lewistown, PA 17044

Mr. K. Letson
Redstone Arsenal
Huntsville, AL 35809

Dr. N. Macmillan
Materials Research Laboratory
The Pennsylvania State Univ.
University Park, PA 16802

Mr. F. Markarian
Naval Weapons Center
China Lake, CA 93555

Mr. K.D. McHenry
Yoneywell Corp. Tech. Center
10701 Lyndale Avenue South
Bloomington, MN 55420

Dr. R.R. Neurgaonkar
Rockwell International Science Center
1049 Camino Dos Rios
PO Box 1085
Thousand Oaks, CA 91360

Norton Company - Library
Industrial Ceramics Division
Worcester, MA 01606

James W. Pelli
Manager of Development
Rohe Scientific Corporation
2722 S. Fairview Street
Santa Ana, CA 92704

Dr. R.C. Pohanka
Room 619, Ballston Tower
800 N. Quincy Street
Arlington, VA 22217

Dr. R.A. Queeney
126 Hammond Building
The Pennsylvania State Univ.
University Park, PA 16802

J.J. Rasmussen, Manager
Applied Research Division
Montana Energy and MHD R&D
PO Box 3809
Butte, Montana 59701

Dr. R. Ruh
AFML, Wright-Patterson AFB
Dayton, OH 45433

James Runt
313 Steidle Bldg
The Pennsylvania State Univ.
University Park, PA 16802

Mr. G. Schmitt
AFML, Wright-Patterson AFB
Dayton, OH 45433

Dr. T. Sentementes
GTE Sylvania
100 Endicott Street
Danvers, MA 01923

State University of New York
College of Ceramics
Alfred University
Attn: Library
Alfred, NY 14802

Dr. R.E. Tressler
Ceramic Science Section
226 Steidle Building
The Pennsylvania State Univ.
University Park, PA 16802

Eric Udd
McDonnell Douglas Astron.
5301 Bolsa Avenue
Huntington Beach, CA 92647

Dr. T. Vasilos
AVCO R & Adv. Dev. Division
201 Lowell Street
Wilmington, MA 01887

Mr. J.D. Walton
Engineering Experiment Station
Georgia Institute of Technology
Atlanta, GA 30332

Mr. L.B. Weckesser
Applied Physics Laboratory
Johns Hopkins Road
Laurel, MD 20810

END

FILMED

9-83

DTIC